Thèse

Pour obtenir le grade de

Docteur de L'Université de Lille 1

Discipline : Micro et Nano technologies, Acoustique et Télécommunications

Docteur de Tongji University

Discipline : Mechanics

Présentée par

Yabin JIN

Design of Acoustic Artificial Structured Materials: Piezoelectric Superlattice, Gradient Index Lens, Pillar Based Phononic Crystal Plate

Soutenue Le 17 février 2017 devant le jury composé de:

Rapporteurs :

Abdelkrim Khelif , Directeur de Recherche, Institut FEMTO-ST, CNRS

Yue-Sheng Wang, Professeur, Beijing Jiaotong University

Examinateurs :

Bernard Bonello, Directeur de Recherche, Institut des NanoSciences de Paris, CNRS

Qian Cheng, Professeur Associé, Tongji University

Invités :

Badreddine Assouar, Chargé de Recherche, HDR, Institut Jean Lamour, CNRS

Yong Li, Professeur Recherche, Tongji University

Directeurs de thèse :

Bahram Djafari-Rouhani, Professeur, Université de Lille1

Yongdong Pan, Professeur, Tongji University (co-tutelle)

To my parents
To my family

Acknowledgements

First and foremost, I would like to acknowledge the jury members of my thesis defense, Prof Abdelkrim Khelif, Prof Yue-Sheng Wang, Prof Bernard Bonello, Prof Qian Cheng, Prof Badreddine Assouar and Prof Yong Li, for reviewing my manuscript and attending my defense. Your professional remarks and fruitful discussions with me improve the quality of the manuscript.

I would like to express my deep gratitude towards Prof. Bahram Djafari-Rouhani, my advisor at Universté de Lille 1. Without your expert guidance, persistent on pursuits and infinite patience throughout my studies, my thesis can't come true. I won't forget countless fruitful discussions with you at any time in any day. Your rigorous attitude towards science greatly impressed me. I would also like to thank Prof. Yongdong Pan, my advisor at Tongji University, for your continuous encouragement and professional guidance. It's your knowledgeable and frontier horizon brings me entering the areas of phononic crystals and acoustic metamaterials. Thank you for providing me free academic space and the opportunity of joint doctoral diplomas.

I highly appreciate Prof. Yan Pennec, my co-advisor at Universté de Lille 1, who kindly gave me technical guidance in simulation as well as many professional scientific ideas in discussion. I won't forget our frequent lunches at the RU and wonderful trips to Bruges and Gent.

I would like to offer my special thanks to Dr. Daniel Torrent, my co-advisor as well as my friend, who share active excellent ideas and professional code skills with me. Sometimes we fighted together for new ideas with a lot of coffee really excited me and left me impressive memories.

I am particularly grateful for the assistance given by Prof. Bernard Bonello. It's you who recommended me to Prof Djafari-Rouhani, making my study in Lille as a reality. Since our

first meeting and discussion at your office during my undergraduate exchange study in 2012, you have been cooperating with me in research, especially many times discussion in Lille.

My grateful thanks are also extended to Prof. Gaëtan Lévêque, Prof Léonard Dobrzynski, Prof Abdellatif Akjouj and Prof. Stéphanie Hemon. As members of Group EPHONI, we shared many discussions and talks in coffee time, lunchtime and other times in the Lab. I also would like to thank Prof Zheng zhong, Prof. Jinfeng Zhao, Prof Libin Li, for giving me many helps in Tongji.

Special thanks should also be given to Prof Aihua Yan, Prof Yan Li, Prof Xiangrong Zhang, Prof Zejun Li, who assisted me a lot during the application for my study in France. Thank you China Scholar Council for financially supporting me to complete my study in France.

I wish to thank Dr. Said El-Jallal, Dr. Rayisa Moiseyenko, Dr. Montacer Dridi, Abdellatif Gueddida, Abdelali Mrabti, Nabil Mahi, Nicolas Fernez, my colleagues in Lille together with Dr. Xuehang Song, Dr. Lei Liu, Gen Chen, Song Ling, Feng Yang, Wei Wang, Xixi Li, Lei Jin, Dongbo Zhang, Fenglin Zhang, colleagues in Tongji, for aiding me a lot in daily life.

I would like to thank David Veganzones, Tiago Mendes, Zhijun Wu, Huan Chen, Chen Chen, Lei Li, Haifeng Yuan, my friends in Lille, and Kui Li, Xin Cai, Xu Zhang, my friends in Tongji, for sharing so many happy and impressive moments together. Special thanks are given to Yingjiao Kong.

Last but not least, I wish to express my deepest gratitude to my parents for their continuous support and unconditional love.

Abstract

Phononic crystals and acoustic metamaterials are artificial structured materials which provide a promising way to manipulate acoustic/elastic waves with many novel potential applications. The aim of this work is to design new acoustic artificial structured materials and discover new properties. After an introduction to the state of the art, the second chapter designs actively controlled multilayers with piezoelectric resonant structures. The corresponding transmission and effective properties can be tuned by changing the electric boundary conditions of the piezoelectric materials. The third chapter develops homogenization methods for phononic crystal plates and demonstrates for the first time the possibility of controlling simultaneously all the fundamental Lamb waves. The full control method developed here is applied to the design of various gradient index lenses that can exhibit several functionalities such as wave focusing or wave beaming. A new elastodynamic homogenization theory, known as Willis constitutive theory, is also investigated which can offer more precise description of wave behaviors in periodic inhomogeneous media than the classical elasticity theory. The forth chapter designs a new type of phononic crystal/metamaterial plate with hollow pillars that exhibits several new localized modes, such as whispering-gallery modes, inside both Bragg and low frequency band gaps. These modes can be actively tuned by filling the hollow parts with a liquid for which the height or the temperature is controlled. The fifth chapter proposes acoustic metasurface consisting of a single pillar or one line of pillars deposited on a thin plate. Local resonances of dipolar and monopolar symmetries can be characterized which are very sensitive to the pillar's geometric parameters. We study the amplitude and phase of the waves resulting from the scattering of an incident wave by the pillars and show that they can be described as dipolar or monopolar waves emitted by the pillar resonators as acoustic sources.

Résumé

Les cristaux phononiques et métamatériaux acoustiques sont des matériaux structurés artificiels qui fournissent un moyen prometteur pour manipuler les ondes acoustiques/élastiques avec de nombreuses applications potentielles nouvelles. Le but de ce travail est de concevoir de nouveaux matériaux structurés artificiels acoustiques et découvrir de nouvelles propriétés. Après une introduction à l'état de l'art, le chapitre 2 propose des multicouches actives à base de structures piézoélectriques résonnantes. Leur transmission et leurs propriétés effectives peuvent être contrôlées activement en changeant les conditions limites électriques des matériaux piézoélectriques. Le chapitre 3 développe des méthodes d'homogénéisation pour une plaque de cristal phononique et montre pour la première fois la possibilité de contrôler simultanément la propagation de toutes les ondes fondamentales de Lamb. La méthode est appliquée à la conception de lentilles à gradient d'indice avec plusieurs fonctionnalités pour les phénomènes de focalisation et transmission directive. De plus, une nouvelle théorie élastodynamique d'homogénéisation, connus sous le nom de théorie de Willis, est développée pour permettre une description plus précise des ondes dans les milieux inhomogènes périodiques que la théorie classique d'élasticité. Le chapitre 4 propose un nouveau type de cristal phononique en plaque à base de piliers creux qui met en évidence de nouveaux modes fortement localisés, tels que les modes de galerie, aussi bien dans le gap de Bragg que dans un gap à basse fréquence. Ces modes peuvent être activement accordés en remplissant les parties creuses des piliers avec un liquide dont on contrôle la hauteur ou la température. Le chapitre 5 propose une métasurface acoustique comportant un pilier unique ou une ligne de piliers déposés sur une plaque mince. Ces piliers ont des modes de résonance dipolaires et monopolaires qui sont très sensibles aux paramètres géométriques des piliers. Nous étudions en détail l'amplitude et la phase des ondes émises lorsqu'une onde incidente est diffusée par les piliers et montrons qu'elles peuvent être décrites comme des ondes dipolaires et monopolaires émises par les piliers résonnants comme sources d'ondes acoustiques.

Content

Chapter 1

General Introduction

1.1 Phononic crystals

Light and sound are two of the most important carriers of information for our society and daily lives[1]. In recent decades, technological revolutions enable us to manipulate and control two particles, photons and phonons, with functionalities beyond discoveries found in nature realized by man-made materials. Initially inspired by an analogy with the quantum mechanical band theory of solids in which electronic waves interact with a periodically arranged atomic lattice to form energy bands separated by bandgaps[2], photonic crystals were proposed by Yablonovitch[3] and John[4] in 1987 in which the atoms are replaced by macroscopic media with differing dielectric constants and the periodic potential is replaced by a periodic dielectric function. Photonic crystals with band gaps can prevent light from propagating in certain directions. Differing from electromagnetic waves which only have transverse polarization, elastic waves propagating in a solid have both longitudinal and transverse polarizations, being harder to design band gap. The search for structures with elastic band gaps began with theoretical work by Sigalas and Economou[5] at the University of Heraklion in Greece in 1992, considering in-plane elastic wave propagation in periodic structures consisting of identical spheres placed periodically within a host homogeneous material. Later, they used gold cylinders embedded in a beryllium host and incorporated out of plane shear waves[6]. The term "phononic crystals" was first proposed by Kushwaha, Halevi, Dobrzynski and Djafari-Rouhani[7] at the University of Lille in France in 1993 when studied out of plane waves in a periodic array of nickel alloy cylinders in an aluminum alloy matrix.

Phononic crystals are artificial materials consisting of periodic inhomogeneous elastic medium that can manipulate the flow of sound in air, of acoustic waves in fluids and of elastic waves in solids. The notion "phonon" may be interpreted as a discrete particle-like quantity of acoustic wave in a solid[8]. In fact, an atom will exerts a force on its neighbors when it is

displaced from its equilibrium position, which causes a special wave of lattice distortion that propagates through the solid, as a "phonon"[9]. The propagation of acoustic waves in a phononic crystal is governed by the Bloch or Floquet theorem from which one can compute the band structure (dispersion relationship) in the corresponding Brillouin zone[10]. In their band structure, phononic crystals can exhibit band gaps which prohibit the propagation of waves. In periodic systems, the origin of a band gap is so-called Bragg mechanism, based on the destructive interference of the scattered waves by the inclusions, which needs the path difference between the interfering waves must be equal to an integer multiple of their wavelength[9]. As the path difference depends on the lattice constant of a crystal, when the wavelength is comparable to the lattice constant, such Bragg scattering mechanism occurs. In addition, band gaps can also come from the avoided crossing of two bands of the same symmetry in the low frequency range, at least one of the two bands originates from localized resonance modes of the individual particles, named as hybridization gaps[11]. In some degrees, such band gap is in the field of acoustic metamaterial, which originates from the concept of locally resonant sonic materials induced by Sheng and his colleagues[12]. From Fig. 1.1, one can easily figure out the difference between the mechanisms of Bragg band gap and hybridization band gap. Bragg band gaps require structural periodicity, however, hybridization band gap can persist with structural disorder[13].

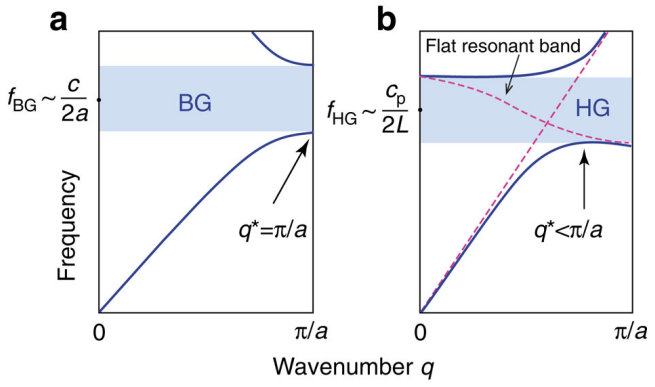

Figure 1.1 Schematic representation of Bragg and hybridization gaps[11]

The position and width of the band gap depend on the direction of the waves since the path difference relies on the angle of incidence[9]. Gaps may occur for particular directions of the wave vector, but they can also span the whole Brillouin zone so that for any polarization and any incidence angle, the propagation of waves is forbidden[10]. Endeavors are taken to seek the absolute band gaps in the past two decades. Generally, to open a wide acoustic band gap, it requires two main conditions: one is a large contrast in physical properties (density and acoustic velocity) between the inclusions and the host matrix; the other is a sufficient filling ratio of inclusions[14]. The type of lattice[15] and the choice of solid and liquid component as matrix and inclusions will also affect the band gaps.

Phononic and photonic crystals share many analogies: the elastic parameters and density of phononic crystals are the analogue of dielectric and magnetic constants of photonic crystals. In photonic crystal devices, the manipulation of the electromagnetic spectrum is achieved by wide range of frequencies (over 14 orders of magnitude) control, ranging from position emission tomography (PET) scanning at frequency 10^{20} Hz to amplitude-modulation (AM) radios at 10^{6} Hz. In phononic crystal devices, it would be valuable to achieve a similar degree of control[16]. As the band structure is scalable with the dimensions of unit cell, phononics play a role in a wide range from Hz to THz, shown in Fig. 1.2. A great deal of works has been devoted to the propagation of waves in the range of sonic (kHz) and ultrasonic (MHz) frequencies in the past two decades [8, 17-19]. In the range of infrasound (Hz) frequency, surface elastic wave (Rayleigh wave) can be controlled to improve soil seismic performances[20]. Recently, the challenge has been to fabricate phononic crystals in nano-meter scale to control hypersound in GigaHertz regime, known as hypersonic crystals[21-23]. In such frequency range, the wavelength of electromagnetic wave is comparable to that of acoustic wave. The study of simultaneous control of photonic and phononic band gap in the same frequency zone attracts increasing attention, which leads to the term phoXonic crystals[24-28]. By reducing the

periodicity to the nanometer scale, phononic crystals can be applied to control heat [29, 30], since heat vibrations oscillate at TeraHertz regime. Phononic crystals fabricated with periodicities ranging from meter to nanometer, are able to manipulate the phonon spectrum in the frequency range from 1 Hz to 10^{12}Hz, a range of 12 orders of magnitude.

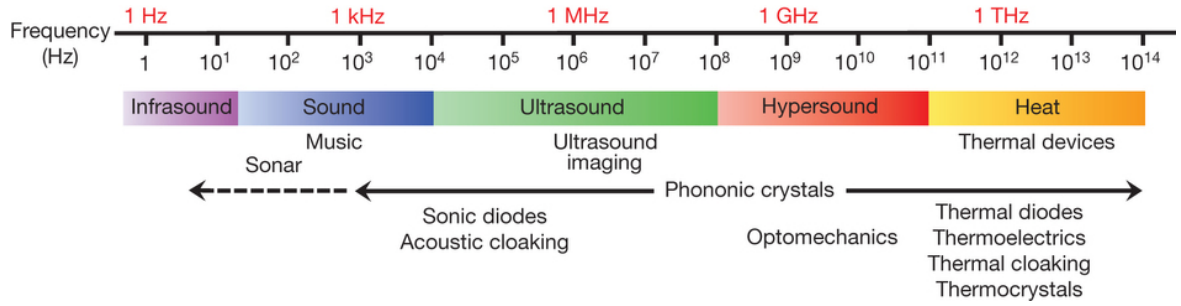

Figure 1.2 The phononic spectrum[16]

Phononic crystals make it possible to control and manipulate acoustic/elastic waves with many potential applications: I) Negative refraction and superlens. Generally for common materials, it is impossible to design a lens to offer an image with details better than half a wavelength. A superlens with negative refraction effect can overcome this limit, which can be realized if the phase velocity and group velocity have opposite directions in phononic crystals[31, 32]. In fact, by analyzing band structures and equifrequency surfaces, positive, zero and negative refractions are possible depending on the angle of incidence[33]. Backward propagation can also be observed when phase and group velocities are anti-parallel[34]; II) acoustic diode. With counterpart of the electronic diode, acoustic diode also allows waves passing in one direction but not in the opposite direction[35, 36], which opening novel applications such as biomedical ultrasound imaging and noise reduction; III) waveguide and filtering. Any route of waveguide[37-39] and any frequency of filter[40, 41] can be designed by well choosing passing frequencies located at the band gap of the background phononic crystals; IV) acousto-optic interaction devices. In the same wavelength range of acoustic and electromagnetic waves, both "blind" and "deaf" material can be designed[25]. Opto-mechanical on-chip device is also possible with the connectivity of phononic and photonic

propertites[42, 43]. V) heat control. With the help of periodically nanostructured phononic crystals, one can use coherent band structure effects to control phonon thermal conductance [29, 44, 45].

1.2 Acoustic metamaterials

Phononic crystals with Bragg scattering mechanism has band gaps where the wavelength is comparable to the lattice constant. In the audible regime, the wavelength of sound ranges from centimeter to meter, which requires the unit cell size of phononic crystals has the same scale, that limits its applications due to the bulky samples. The emergence of acoustic metamaterials not only solved the problem of sample size but also introduced new functionalities not found previously[2].

Acoustic metamaterials are not well defined until now. From a point of common sense, acoustic metamaterials are engineered materials whose properties derive from their structure rather than from their composition. For normal materials in nature, their mass density and bulk modulus are positive, known as right-handed material. If one may imagine both of mass density and bulk modulus are negative simultaneously, the wave equation still allows wave propagation, but in the left handed coordinate system, named as left-handed material or metamaterial. In such case, its refractive index is also negative, which has a different original mechanism from negative refraction of phononic crystals as explained before.

The first work on acoustic metamaterial dates back to 2000, when Sheng and his colleagues designed a matrix of silicon-coated metallic spheres embedded in epoxy and realized a transmission dip at very low frequency zone resulted from local resonance[12]. The local resonance is characterized by relative motions of constituents internal to the background matrix. The effective mass density at local resonance either diverges to an extreme large value or turns to a negative value, so that waves are strongly attenuated causing near-total

reflection[46]. In contrast, if the deformations involves relative compression-extensional motion, it's the effective bulk modulus becomes frequency-dependent, which was first demonstrated by Fang et al on ultrasound by a waveguide shunted by a chain of Helmholtz resonators[47]. The effective mass density and bulk modulus behaviors are associated with the symmetry of motions. Li and Chan first figured out that dipolar mode contributes to the inertial response and monopolar mode generates compressive/expansive motion[48]. By combining these two resonant modes, it is able to realize negative effective mass density and bulk modulus simultaneously [49-52].

Different from the Bragg scattering mechanism, the relevant wavelength at the local resonance can be orders of magnitude larger than the size of unit cell, as shown in Fig. 1.3A, which especially helps manipulate acoustic waves in liquids more efficiently. Metamaterial moves to the left when pushed toward the right if the effective mass density is negative and expands upon compression when the compressibility gets negative, as illustrated in Fig. 1.3B and C. In liquids, acoustic wave is longitudinal wave. Owing to the same mathematical form with electromagnetic wave, two constitutive parameters can be mapped as $\rho \to \varepsilon$ and $\kappa^{-1} \to \mu$, where ρ, κ are mass density and bulk modulus for acoustic longitudinal wave, respectively, ε, μ are dielectric constant and magnetic permeability for electromagnetic wave, respectively. The extraordinary phenomena of electromagnetic metamaterials can also be developed for acoustic metamaterials hand in hand, such as negative refraction[53, 54], superlensing[55] and cloaking[56, 57].

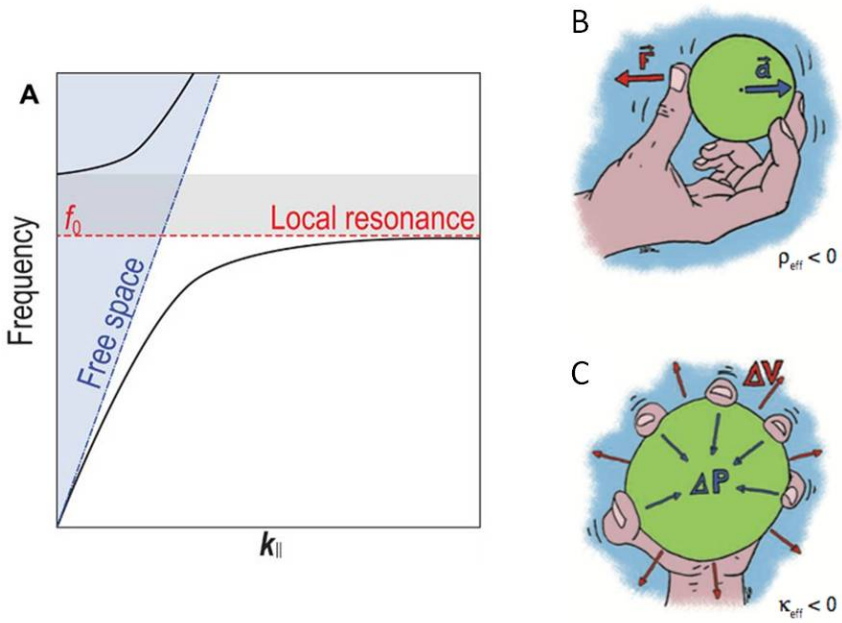

Figure 1.3 (A) Schematic representation of local resonance[2], (B) and (C) Schematic illustration of the dynamic behaviors of locally resonant metamaterials with negative effective mass density and bulk modulus[58]

One of the acoustic metamaterial family is acoustic metasurface. Liang and Li proposed a space-coiling structure consisting of complex labyrinth passages which is deep subwavelength in their cross sections[59]. The coiled-up passages introduce larger phase delays, and can be properly designed to exhibit novel effects, such as negative refraction[59, 60], near-zero index[61, 62], Dirac-like dispersion[63, 64]. However, these coiled-up structures are impedance mismatch to incident wave, causing some challenges for the transmission configuration. By designing horn-like structure[65-67] or using resonance[68, 69], one can improve the impedance coupling. Li, Qi and Assouar[70] proposed a metascreen-based acoustic passive phased array which keeps impedance matching and provides a fully shifting phase for sub-wavelength spatial resolution. Li and Assouar further designed metasurfaces for perfect absorber with deep subwavelength thickness[71] and acoustic collimated self-accelerating beam[72].

Some modern concepts such as topological matter and parity-time symmetry can also be realized by acoustic meta-crystals. Topologic states in electronic materials include the quantum Hall effect and topological insulators. A phase transition associated with phonon

Hall effect is observed in dielectrics with Raman spin-phonon coupling[73]. Phononic crystals with topologically nontrivial band gaps through the breaking of time-reversal symmetry, can result in protected one-way elastic edge waves[74-76].Topological notions can also characterize the topological phase of mechanical isostatic lattices[77] or periodic acoustic systems[78-80].

1.3 GRIN and pillar type acoustic artificial structures

In a specific case, both Bragg and low frequency band gaps can be found in one type of acoustic metamaterials, which consists of a periodic array of pillars on a plate[81, 82]. Because of the dual aspect, great deals of efforts have been devoted to such structural system in the past few years. Wang, Laude and Wang[83] proposed a 1D structure made of acoustic pillar resonantors grafted onto a waveguide, which can also exhibit both Bragg and low frequency band gaps. To enhance the local resonance, Assouar and Oudich[84] used double-sides stubbed plate. Bilal and Hussein[85] designed pillars on a plate patterned by a periodic array of holes to enlarge low frequency gap. Assour *et al*. studied hybrid phononic crystal plates composed of periodic stepped pillars and periodic holes which can also generate lower and wider acoustic gap because the acoustic waves are scattered by both of the pillars and holes[86]. Coffy *et al.*[87] tailored a pillar-based plate displaying an extra wide band gap starting at very low frequency together with an extreme low frequency band gap. Shu *et al*. designed a double tubular pillars showing an enlargement of band gap[88]. The feature of local resonance pursues many different objectives. Zhao *et al* numerically and experimentally focused the lowest anti-symmetric Lamb waves with a gradient index lens enhanced by local resonance of silicon pillars[89]. Addouche *et al* demonstrated super resolution imaging for surface acoustic waves using pillar-based structure displaying negative refractive index[90]. Colombi *et al* showed a locally resonant metamaterial made of pillars arranged on a sub-wavelength scale whose dynamic properties are similar to those of forest-trees and can induce large frequency

bandgaps for Rayleigh waves at tens of Hz[20]. Davis and Hussein found that thermal conductivity can be reduced by local resonance of nanopillars using molecular simulations[45]. Alonso-Redondo *et al* demonstrated that the hybridization gap is less sensitive to periodicity and can even persist with structural disorder of colloidal particles[11]. Therefore, the topics of pillar structures and low frequency band gaps have become an active domain for diverse fundamental and applied studies in the field of phononic crystals and acoustic metamaterials.

The field of phononic crystals and acoustic metamaterials provides a promising background for the realization of artificial inhomogeneous materials, as has been widely demonstrated in the literatures [12, 47, 91-94]. The propagation of mechanical waves can be tailored by means of gradient index (GRIN) devices consisting of locally inhomogeneous materials in which the refractive index is a function of the spatial coordinates. Therefore, waves follow curved trajectories that can be properly designed if the position-dependent parameters of the medium are chosen according to specific laws. GRIN devices, which are well known in optics[95], are recently receiving increasing attention in the field of phononic crystals and metamaterials, since the artificial nature of these structures allows for an easy design of inhomogeneous materials.

By locally changing the filling fraction in phononic crystal, gradient index flat lens was designed[96] and experimentally characterized[97] in a plate or air[98]. Coupling the flexural resonant mode of pillars and the vibration mode in phononic crystal, GRIN metalens can focus a spot less than half a wavelength[89]. Omnidirectional broadband acoustic absorber or acoustic black hole with acoustic impedance matching can also be realized[99-102]. Some other omnidirectional lenses, e.g. Luneburg lens, Maxwell lens, Eaton lens, are also designed for acoustic and elastic waves[103-105].

The major drawback for the realization of these inhomogeneous devices for elastic waves is that, unlike acoustic waves, the propagation of elastic waves, either in bulk materials or plates,

presents three polarizations, which propagate at different speeds. Their design has been done so far for only one of these polarizations, which obviously hinders the full functionality of the devices for applications like cloaking, absorption or even energy harvesting. The dispersion characteristics of these polarizations are in general different, so that the design of refractive index working for all of them, even in the low frequency limit, is obviously a challenging problem.

Phononic crystals and acoustic metamaterials are rapidly evolving new physical understandings and diverse functions in the coming years, especially new discoveries in photonic crystals and electromagnetic metamaterials. Given the progress over the past decades, the future of acoustic artificial structured materials is promising.

1.4Thesis organization

The central theme of this thesis is to design and characterize acoustic artificial structured materials for potential applications in acoustic/elastic control. The thesis is organized into six chapters. Besides the current chapter which presents a general introduction of phononic crystals and acoustic metamaterials, the other five chapters are organized as following:

The second chapter proposes a resonant structure of a hard-core coated by piezoelectric composite materials as an acoustic metamaterial, in which negative effective mass density and elastic modulus are simultaneously achieved. The double negativity, appearing within a certain range of the filling ratio, is numerically demonstrated by the switch of the electric boundary from open to close. The bandwidth of the negative effective elastic modulus is sensitive to the piezoelectric constant e_{33}. The multi-unit acoustic metamaterial offers the advantages of broadening the double-negativity domain and of reducing the primary frequency, while the cut-up frequency remains the same as that of the single unit cell.

The third chapter first presents two methods for the design of gradient index devices for elastic waves in plates, despite the fact that for different Lamb modes, their dispersion relations are managed by different elastic constants. The first method allows the simultaneous control of the anti-symmetric and symmetric Lamb modes, depending on an effective medium theory developed for the anti-symmetric mode working with Kirchhoff equation; the second method allows the design of devices to control the three fundamental Lamb modes, based on the homogenization of the bulk phononic crystal with Plane Wave Expansion (PWE) method. Then, developing the latter PWE method, we demonstrate the realization of the so-called "Willis" medium in the local approximation by breaking the symmetry in the unit cell. The properties of "Willis" medium plate are further explored.

The forth chapter first investigates the properties of a phononic crystal plate with hollow pillars and introduces the existence of quadrupolar whispering-gallery modes (WGMs). By tuning the inner radius of the hollow pillar, these modes can merge inside both of Bragg and low frequency band gaps, deserving phononic crystal and acoustic metamaterial applications. These modes can be used as narrow pass bands for which the quality factor can be greatly enhanced by the introducation of an additional cylinder between the hollow pillar and the plate. Then, filling the hollow parts with a fluid gives rise to new localized modes, which depend on the physical properties and height of the fluid. These modes can be actively controlled by several parameters, such as the physical properties of liquid, liquid's height, temperature. We further propose a new type of phononic crystal plate consisting of hollow pillars on a bar-connected plate, whose Bragg band gap can be tuned to be much wider and extended to sub-wavelength region and low frequency gap can be moved to extreme low frequency range. Such a structure can generate quadrupolar, hexapolar and octopolar WGMs inside the band gaps with very high confinement. We discuss the functionality of these

phononic crystal plates for the purpose of multiplexer devices, sensing the acoustic properties of liquid and wireless communication.

The fifth chapter investigates an acoustic metasurface, considering a single pillar and a line of identical pillars on a thin plate, and studies their interaction with anti-symmetric Lamb wave. Local resonances are exhibited as bending and compression modes, which are sensitive to the geometric parameters of the pillars. The amplitude and phase of scattering waves emitted by the pillars at resonances are studied for the cases when bending and compression modes are separated or superposed. Especially, the analysis of amplitude and phase of transmitted wave for one line of pillars at the superposed resonant frequency demonstrates a new transmission with phase shift π as induced by out of phase emitted wave.

The last chapter summaries all works in this thesis and gives some perspectives.

Chapter 2

Tunable Acoustic Metamaterials with Piezoelectric Resonant Structures

The content of this chapter was published in:

Yabin Jin, Bernard Bonello, Yongdong Pan. *Acoustic metamaterials with piezoelectric resonant structures*. Journal of Physics D: Applied Physics. 47 (24), 245301, 2014.

2.1 Introduction

Acoustic metamaterials (AMs) are engineered materials whose properties derive from their structure rather than from their composition[106]. They are of particular interest in terms of both basic science and applications since they could exhibit novel phenomena including acoustic cloaking[107-112], sound attenuation[113-115] and acoustic superlens[116-119]. Realizing negative acoustic parameters is one of the primary goals of the researches on AMs[60]. In this context, the concept of negativity of the effective properties relies both on the dynamic response of an effective medium and to the phase changes of the dynamic response induced by the resonances. The most attractive structures for AMs, are composite systems with resonant structural units. They are usually formed from a hard-core material coated by a soft material and they can exhibit negative effective bulk modulus and/or negative effective mass density in certain frequency ranges[12]. However, the dimensions of the resonators must be much less than the wavelength of the incident acoustic wave in the host media so that both mass density and bulk modulus can be defined through homogenization theories[120]. Several methods have been developed to study these hetero-structures, including the plane wave expansion method[7], the multiple scattering theory[121], the finite difference time domain[122], and the method for retrieving the effective acoustic properties from reflection and transmission coefficients that both can be measured experimentally[123]. The key features of AMs can be captured for a one-dimensional (1D) multilayered medium[124], because it can provide an excellent model for the rigorous and physical analysis of the dynamic properties.

However, most of the works that have been made on this topic were focusing on the study of the passive AMs with fixed material properties whose double negative effective properties are inherently dispersive and negative only over a narrow frequency band, resulting in limited applications, e.g. acoustic cloaking and sub-wavelength focusing. To overcome the inherent limit of the frequency bandwidth, active AMs with tunable material properties have been

proposed to achieve the double negative properties in a large frequency range[125, 126]. The active AMs, consisting of an array of fluid chambers with piezoelectric wall, have tunable homogenized properties through the variation of the applied electrical voltage. Moreover, it can overcome the frequency bandwidth limitation of passive techniques[127]. AMs consisting of layers of electrically charged nano or micro particles exposed to an external magnetic field are designed with tunable properties by controlling both the magnetic field and/or the electrical charges[128]. Another design of active AMs controlled by an actuator has been presented to have a stable response with a tunable double negative frequency band[129-131]. Recently, a cell architecture of active acoustic metafluids has been shown to be allowed for the independent tune of the effective material parameters[132]. The effective mass density profile of surface bonded AMs can be tailored from different AM cells, using the piezoelectric actuator to excite acoustic wave[133]. Piezoelectric materials with periodically modulated properties were investigated as examples of Helmholtz resonant metamaterials or metafluid. However, less attention has been paid to the active control of effective material parameters using resonant structures and piezoelectric materials. It was found that the electrical boundary of the piezoelectric material may significantly affect the propagation of the elastic waves due to the introduction of the piezoelectricity[134]. The band gaps can be tuned as well, owing to the fact that the piezoelectricity allows for the transduction of the energy between acoustic and electric fields. PZT based materials are components of ultrasound transducers, ceramic capacitors and surface acoustic wave actuators.

In this chapter, an active AM of hardcore coated by piezoelectric composite materials is proposed to exhibit negative effective mass density and elastic modulus simultaneously. A single unit of this active AM is first supposed to be a 1D structure of a lead plate sandwiched by the piezoelectric composite materials. A modified recursively algorithm[135] is applied to calculate the transmission and reflection coefficients of the incident acoustic wave, and the

equivalent theory of wave propagation in homogeneous media is applied to retrieve the effective acoustic properties. The double-negativity can be achieved through the switch of the electric circuit from open to close, and the resonances are excited through the vibration of the piezoelectric layers for a certain filling ratio. It is further demonstrated that the resonances may be enhanced by stacking AM units, which in turn leads to the broadening of the frequency band where the negative properties arise. This approach provides some interesting applications, which may be realized over a fixed narrow band, such as acoustic cloaks and sub-wavelength resolution lenses. AMs being still at an early stage of development, no experimental data are available to date. Numerical methods like FEM could be very useful to verify the theoretical findings of this work, and it is planned as the next step of our research.

2.2 Theoretical formulations

For the ease of understanding, a steady pressure wave (P) is considered propagating through single- or multi- units of 1D AMs along z coordinate, as shown in Fig. 2.1. It is supposed that the AMs are multilayered media, and that the P wave is excited in the layer (I) at normal incidence along the z coordinate. The wave propagates through the AMs, and is then detected in the layer (II). Both layers I and II are made of the same fluid material, e.g. water. It is further supposed that the AM unit is made of layers with different thicknesses and materials, both layers A and C are made of the same piezoelectric material and have identical thicknesses whereas layer B is made of lead. The elastic wave propagating within the medium (A+B+C) could resonantly excite the inclusions into vibration only if the sound velocity of material A and C is smaller than the sound velocity of material B by at least two orders of magnitude. Therefore, the sound velocity of material A and C must be considered to be no more than a few m/s. The most common and realistic choice of the soft material is silicone rubber, which has phase speed two orders of magnitude lower than those of typical solids.

Effort has been tried to assemble the existing piezoelectric materials with this type of AMs, including PZT and PVDF, but no observable difference is found when changing the electric conditions. Thus, the piezoelectric material is supposed to be a composite material, whose elastic constants are those of silicone rubber and whose piezoelectric constants are those of PZT4 polarized along the z coordinate (see table 2.1). It should be possible to elaborate this soft piezoelectric material studied in our article by embedding piezoelectric ceramic PZT particles into the silicone rubber matrix. The total thickness of the AM unit cell is $h=h_A+h_B+h_C$, and the filling ratio of the hardcore is $\beta=h_B/h$.

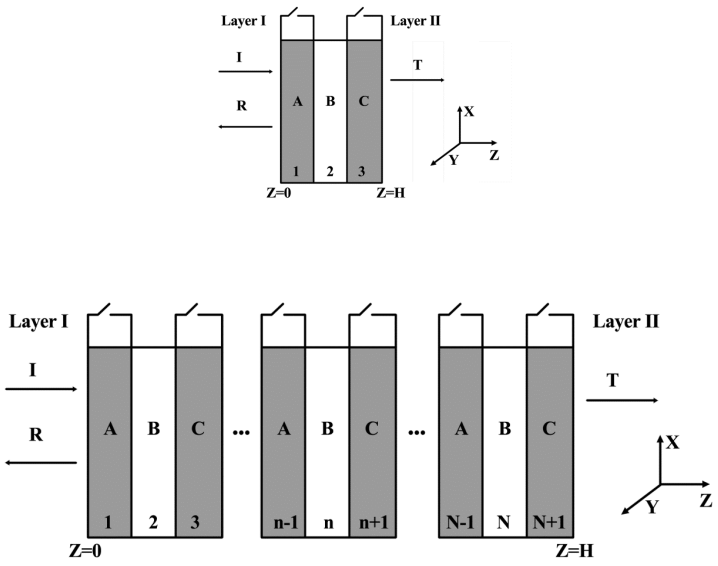

Figure 2.1 Scheme of P wave propagating through single-unit (a) and multi-unit (b) actively switched AMs, where layers in grey are piezoelectric materials and layers in white are lead

Properties	Piezoelectric material	Lead
$\rho(10^3\ \mathrm{kg\,m^{-3}})$	1.300	11.600
$c_{11},c_{33}(10^9\ \mathrm{N\,m^{-2}})$	6.800×10^{-4}	53.190
$c_{55},c_{13}(10^9\ \mathrm{N\,m^{-2}})$	4.000×10^{-5}	8.430
$e_{31}\ (\mathrm{C\,m^{-2}})$	−5.200	0
$e_{33}\ (\mathrm{C\,m^{-2}})$	15.080	0
$e_{15}(\mathrm{C\,m^{-2}})$	12.720	0
$\varepsilon_{11}\ (10^{-9}\ \mathrm{C^2/(N\,m^2)^{-1}})$	1.306	∞
$\varepsilon_{33}\ (10^{-9}\ \mathrm{C^2\ (N\,m^2)^{-1}})$	1.115	∞

Table 2.1. Material properties of piezoelectric material and lead

The constitutive equations of the transversely isotropic piezoelectric or elastic materials can be written as[136]

$$\begin{cases} \sigma_{pq} = c_{pqrs}(u_{r,s} + u_{s,r})/2 - e_{pqr}\varphi_{,r} \\ D_r = e_{pqr}(u_{p,q} + u_{q,p})/2 + \varepsilon_{rs}\varphi_{,s} \end{cases} \tag{2.1}$$

where $p, q, r, s = x, y, z$; c_{pqrs}, e_{pqr}, ε_{rs} are the elastic, piezoelectric and the dielectric constants respectively; φ stands for the electric potential; D_r is the electric displacement; σ_{pq} is the stress; u_r is the displacement; a comma followed by the subscript s means the space differentiation with respect to the s coordinate. The corresponding constitutive equations for layers A, B, C can be found just by replacing the material properties. Since the considered P wave shows its invariance along y coordinate, we have $u_y=0$, $\sigma_{yz}=\sigma_{zy}=\sigma_{xy}=\sigma_{yx}=\sigma_{yy}=0$.

A. Single layer

For the transversely isotropic piezoelectric or elastic materials, the displacement and electric potential satisfy the general forms of the dynamic differential equations as followings:

$$\begin{cases} \rho \dfrac{\partial^2 u_p}{\partial t^2} = \sigma_{pq,q} \\ D_{p,p} = 0 \end{cases} \tag{2.2}$$

The polarized direction of the piezoelectric material is parallel to the direction of layer's thickness, so that the components of the displacement field u_x, u_z and the electric potential φ are assumed to have the forms $u_x(x,z,t) = u_x(z)e^{i(k_x x - \omega t)}$, $u_z(x,z,t) = u_z(z)e^{i(k_x x - \omega t)}$, $\varphi(x,z,t) = \varphi(z)e^{i(k_x x - \omega t)}$, where $u_x(z)$, $u_z(z)$ and $\varphi(z)$ are the corresponding amplitude of u_x, u_z and φ; i is the unit imaginary number; ω is the angular frequency; k_x is the wave number along the x coordinate.

For the electrically closed circuit boundary, the electric potential φ is zero everywhere on the interfaces and hence $\varphi^{+}=\varphi^{-}=0$, where the superscripts "+" and "-" stand for the propagation along the positive and negative z directions, respectively. Generalized displacement vector $\mathbf{U}^{close}=(u_x,u_z,D_z)^T$ and stress vector $\Sigma^{close}=(\sigma_{xz},\sigma_{zz},\varphi)^T$ are further defined. Therefore, the state-vector equation could be derived as[137]

$$\frac{\partial}{\partial z}\begin{pmatrix}\mathbf{U}\\ \mathbf{\Sigma}\end{pmatrix}=\mathbf{A}(k_x,\omega)\begin{pmatrix}\mathbf{U}\\ \mathbf{\Sigma}\end{pmatrix} \tag{2.3}$$

where $\mathrm{A}^{close}(k_x,\omega)$ is the system matrix

$$\mathrm{A}^{close}(k_x,\omega)=\begin{pmatrix} 0 & -ik_x & 0 & 1/c_{55} & 0 & -ik_x e_{15}/c_{55} \\ -ik_x\Omega_1 & 0 & e_{33}/\Delta & 0 & \varepsilon_{33}/\Delta & 0 \\ 0 & 0 & 0 & -ik_x e_{15}/c_{55} & 0 & -k_x^2(\varepsilon_{11}+e_{15}^2/c_{55}) \\ k_x^2\bar{c}-\rho\omega^2 & 0 & ik_x\Omega_2 & 0 & ik_x\Omega_1 & 0 \\ 0 & -\rho\omega^2 & 0 & -ik_x & 0 & 0 \\ -ik_x\Omega_2 & 0 & -c_{33}/\Delta & 0 & e_{33}/\Delta & 0 \end{pmatrix} \tag{2.4.1}$$

and $\bar{c}=c_{11}-(c_{31}\Omega_1+e_{31}\Omega_2)$, $\Omega_1=(e_{31}e_{33}+c_{13}\varepsilon_{33})/(e_{33}^2+c_{33}\varepsilon_{33})$, $\Delta=c_{33}\varepsilon_{33}+e_{33}^2$,

$\Omega_2=(c_{13}e_{33}-c_{33}\varepsilon_{31})/(e_{33}^2+c_{33}\varepsilon_{33})$.

For the electrically open circuit boundary, the electric displacement D is zero on the interfaces and hence $D_z^{+}=D_z^{-}=0$. Generalized displacement and stress vectors $\mathbf{U}^{open}=(u_x,u_z,\varphi)^T$ and $\Sigma^{open}=(\sigma_{xz},\sigma_{zz},D_z)^T$ are thus defined. The corresponding matrix system is

$$\mathrm{A}^{open}(k_x,\omega)=\begin{pmatrix} 0 & -ik_x & -ik_x e_{15}/c_{55} & 1/c_{55} & 0 & 0 \\ -ik_x\Omega_1 & 0 & 0 & 0 & \varepsilon_{33}/\Delta & e_{33}/\Delta \\ -ik_x\Omega_2 & 0 & 0 & 0 & e_{33}/\Delta & -c_{33}/\Delta \\ k_x^2\bar{c}-\rho\omega^2 & 0 & 0 & 0 & -ik_x\Omega_1 & -ik_x\Omega_2 \\ 0 & -\rho\omega^2 & 0 & -ik_x & 0 & 0 \\ 0 & 0 & -k_x^2(\varepsilon_{11}+e_{15}^2/c_{55}) & -ik_x e_{15}/c_{55} & 0 & 0 \end{pmatrix} \quad (2.4.2)$$

B. Multilayer of A-B-C units

To the solid sandwich structures shown in Fig. 2.1, the transfer matrix between different layers has to been derived. The general solution of Eq. (2.3) is

$$\begin{pmatrix} \mathbf{U}^{n+1} \\ \Sigma^{n+1} \end{pmatrix} = \mathbf{M}^n(k_x,\omega)\begin{pmatrix} \mathbf{U}^n \\ \Sigma^n \end{pmatrix} = \begin{pmatrix} \mathbf{M}_1 & \mathbf{M}_2 \\ \mathbf{M}_3 & \mathbf{M}_4 \end{pmatrix}\begin{pmatrix} \mathbf{U}^n \\ \Sigma^n \end{pmatrix} \quad (2.5)$$

with $\mathrm{M}^n(k_x,\omega)$ being the transfer matrix from n th layer to (n+1)th layer. Here, the superscript denotes the position along the z coordinate of the general displacement and stress, and $\mathbf{M}^n(k_x,\omega)=\mathbf{X}^n\mathbf{E}^n(\mathbf{X}^n)^{-1}$ is a 6×6 propagator matrix; $\mathbf{M}_g$ (g=1, 2, 3, 4) is the 3×3 sub-matrix at left top, right top, left bottom and right bottom of $\mathbf{M}^n(k_x,\omega)$; $\mathbf{E}^n=diag(e^{\lambda_\alpha d^n})$ is the diagonal matrix and λ_α is the eigenvalues of the matrix $\mathbf{A}^n(k_x,\omega)$, $\mathbf{X}$ is the corresponding eigenvector; and d^n is the width of nth layer. Eq. (2.5) can be rewritten as

$$\begin{pmatrix} \mathbf{U}^n \\ \mathbf{U}^{n+1} \end{pmatrix} = \mathbf{S}^n\begin{pmatrix} \mathbf{\Sigma}^n \\ \mathbf{\Sigma}^{n+1} \end{pmatrix} = \begin{pmatrix} -\mathbf{M}_3^{-1}\mathbf{M}_4 & \mathbf{M}_3^{-1} \\ \mathbf{M}_2-\mathbf{M}_1\mathbf{M}_3^{-1}\mathbf{M}_4 & \mathbf{M}_1\mathbf{M}_3^{-1} \end{pmatrix}\begin{pmatrix} \mathbf{\Sigma}^n \\ \mathbf{\Sigma}^{n+1} \end{pmatrix} \quad (2.6)$$

where $\mathbf{S}^n$ is the compliance matrix for nth layer.

Assume the total layer number for the sandwiched acoustic mematerial is n+1. If we get the total compliance matrix for n layers, then the total 6×6 compliance matrix $\mathbf{ST}^{n+1}$ for $n+1$ layers is derived as[138]

$$\mathbf{ST}^{n+1}=\begin{pmatrix}\mathbf{S}_1^{n+1}+\mathbf{S}_2^{n+1}\left(\mathrm{ST}_1^{n}-\mathbf{S}_4^{n+1}\right)^{-1}\mathbf{S}_3^{n+1} & -\mathbf{S}_2^{n+1}\left(\mathbf{ST}_1^{n}-\mathbf{S}_4^{n+1}\right)^{-1}\mathbf{ST}_3^{n}\\ \mathbf{ST}_3^{n}\left(\mathbf{ST}_1^{n}-\mathbf{S}_4^{n+1}\right)^{-1}\mathbf{S}_3^{n+1} & \mathbf{ST}_4^{n}-\mathbf{ST}_3^{n}\left(\mathbf{ST}_1^{n}-\mathbf{S}_4^{n+1}\right)^{-1}\mathbf{ST}_2^{n}\end{pmatrix} \tag{2.7}$$

where $\mathbf{ST}_g$ (g=1,2,3,4) is the 3×3 sub-matrix in left top, right top, left bottom and right bottom of $\mathbf{ST}^{n+1}$. Until now, through the above compliance matrix, one can calculate the displacements from the first layer to the last layer of AM. As seen in Fig. 2.1, the AM is embedded in the liquid lays I and II, so that it needs further to match the normal displacement equivalent condition at the solid-liquid interface.

C. Transmission and reflection from liquid layer I and II

For the structure depicted in Fig. 2.1, the pressure in the semi-infinite spaces I and II can be expressed as

$$\begin{cases}p^{0}=(a_{+}e^{-\eta z}+a_{-}e^{\eta z})e^{i(k_x x-\omega t)}=(a_{+}+a_{-})e^{i(k_x x-\omega t)}\\ p^{H}=b_{+}e^{-\eta z}e^{i(k_x x-\omega t)}=b_{+}e^{-\eta H}e^{i(k_x x-\omega t)}\end{cases} \tag{2.8}$$

The corresponding displacements for media I and II can be derived from Eq. (2.8) as

$$\begin{cases}u^{0}=-\dfrac{\eta(a_{+}-a_{-})}{\omega^{2}\rho_{I}}e^{i(k_x x-\omega t)}\\ u^{H}=-\dfrac{\eta b_{+}e^{-\eta H}}{\omega^{2}\rho_{II}}e^{i(k_x x-\omega t)}\end{cases} \tag{2.9}$$

in which $\eta=\sqrt{k_x^2-\omega^2/c_f^2}$ is the wave number along the z coordinate; a_+ and a_- are the amplitudes of the pressure wave along positive and negative z directions (including z=0), respectively; b_+ is the amplitude of the pressure wave at $z=H$ along positive z direction.

Considering Eq. (2.6), the normal displacements on the left and right interfaces of the AM unit cell satisfy

$$\begin{pmatrix} u_z^0 \\ u_z^H \end{pmatrix}=\begin{pmatrix} st_{22} & st_{25} \\ st_{52} & st_{55} \end{pmatrix}\begin{pmatrix} \sigma_{zz}^0 \\ \sigma_{zz}^H \end{pmatrix} \tag{2.10}$$

where st_{gl} (g, l=2, 5) is the gth row and lth column element of the total compliance matrix **ST**.

Acknowledging the boundary conditions that the displacement u_z is continuous along the interfaces between AM unit and fluid, the following equations can be found:

$$\begin{cases} u^0 = u^0{}_z \\ u^H = u_z{}^H \end{cases} \tag{2.11}$$

Then, substituting Eq. (2.9) and (2.10) into Eq. (2.11) leads to the relations:

$$\begin{cases} -\eta(a_+-a_-)/\left(\omega^2\rho_I\right)=st_{22}(a_++a_-)+st_{25}b_+e^{-\eta H} \\ -\eta b_+e^{-\eta H}/\left(\omega^2\rho_{II}\right)=st_{52}(a_++a_-)+st_{55}b_+e^{-\eta H} \end{cases} \tag{2.12}$$

The transmission and reflection coefficients being $T=b_+/a_+$ and $R=a_-/a_+$ respectively, they can be obtained from Eq. (2.12) as

$$\begin{pmatrix} T \\ R \end{pmatrix}=\begin{pmatrix} e^{\eta H} & 0 \\ 0 & 1 \end{pmatrix}\begin{pmatrix} st_{25} & st_{22}-\eta/\omega^2\rho_I \\ st_{55}+\eta/\omega^2\rho_{II} & st_{52} \end{pmatrix}^{-1}\begin{pmatrix} -\eta/\omega^2\rho_I-st_{22} \\ -st_{52} \end{pmatrix} \tag{2.13}$$

D. Effective elastic parameters

The acoustic impedance Z and refractive index n are derived as[123]

$$Z = \alpha \Big/ \left(1 - 2R + R^2 - T^2\right), \qquad n = \left(-\mathrm{i}\log\gamma + 2\pi m\right) \Big/ k_x H \tag{2.14}$$

where $\alpha = \mathrm{m}\sqrt{\left(R^2 - T^2 - 1\right)^2 - 4T^2}$, $\gamma = \left(1 - R^2 + T^2 + \alpha\right) \Big/ 2T$; m is the branch number of the $\cos^{-1}$ function.

According to the theory of acoustics in homogeneous media, the effective dynamic properties of the AMs can be obtained from n and Z, and are expressed as[139]

$$E_{eff} = Zv, \;\; \rho_{eff} = Z / v \tag{2.15}$$

where $v = \mathrm{c}_p / n$ is the effective velocity of the elastic wave and c_P is the velocity of the P wave.

2.3 Effective properties of acoustic metamaterials

First to confirm the theoretical formulation, the effective properties are calculated for the single unit cell with the thickness h_A=h_C=1mm, h_B=0.5mm, and the filling ratio β=20%. The amplitude and the phase of the transmission coefficient are shown in Fig. 2.2. It can be observed that the transmission coefficient has an amplitude peak value near 1 and a 180-degrees phase shift at fh=5.675 kHzmm for electrically closed condition, while they nearly remain the same over their respective frequency range for electrically open condition. The 180-degrees phase shift gives an evidence of a resonance. The effective mass density and the elastic modulus are further displayed in Fig. 2.3 for the electrically closed or open conditions. The real parts of effective mass density and elastic modulus are normalized to volume average values ρ_0 and E_0, respectively. Under the electrically closed condition, both real parts of the

effective mass density and the elastic modulus are negative at *fh*=5.675 kHzmm and remain less than zero in the frequency ranges (5.675, 14.000) kHzmm and (5.675, 5.825) kHzmm respectively (blue lines in Fig. 2.3a and 2.3b). The corresponding imaginary parts are also displayed in the lower panel as Fig. 2.3c and 2.3d. However, the double negativity does not appear under the electrically open condition (red lines in Fig. 2.3a and 2.3b). This clearly demonstrates that the effective mass density and elastic modulus can be easily controlled by switching the electrical boundaries and that the AM can be actively switched on and off easily. However, it should be noticed that the effective mass density and elastic modulus are obtained for the wave propagation perpendicular to the layered structures only. For the focus of this work, the resonances in the high frequency range are not presented, as they are more complicated and less important than the primary resonance. It is the same for the mechanical resonances of the interleaved rubber and lead layers, as they are also in the high frequency range.

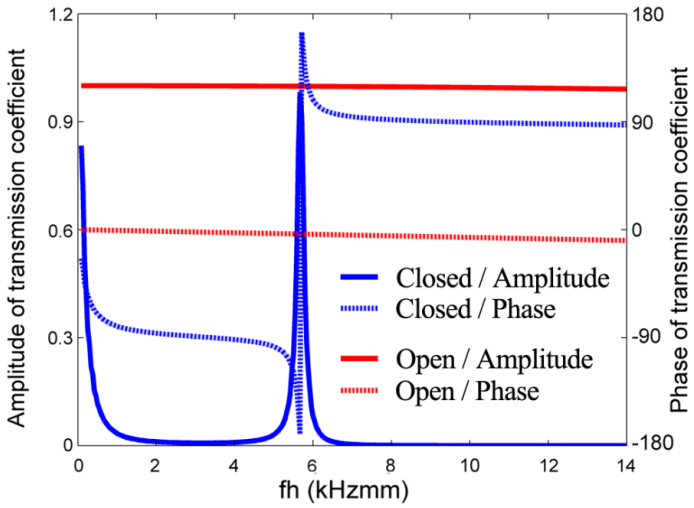

Figure 2.2 Amplitude (solid) and phase (dotted) of the transmission coefficient under the electrically open (red) or closed (blue) status for a single unit AM

The electrical boundary of the piezoelectric material can significantly affect the propagation of the elastic waves. More generally, integrating a piezoelectric material in an AM would have many advantages. Indeed, similarly to the phononic crystals whose filling ratio and band gap can both be tuned by applying an electrical field, the lateral dimensions and the resonant frequencies of the resonators could be externally controlled. Actually, the elastic constants of the material are strengthened by the piezoelectric tensor components and the sound velocity along certain directions can be affected by a few percent. However, this is not the main reason why incorporating a piezoelectric material in an AM deserves special attention. Indeed, since the negative properties of an AM relate to the relative movement of the inclusions and the matrix, controlling the phase of the displacement is of primary importance. The propagation of an elastic wave in a piezoelectric material goes along with the propagation of an electromagnetic field, which, under some conditions of polarization, can couple with the elastic field. Under the electrically closed status, in the piezoelectric material the D_z and c_{33} are coupled, which means that along z direction, the electric field is coupled with elastic field. As a result of this coupling, a phase shift, that could be realized by simply short-circuiting the electrodes on the piezoelectric element, affects the propagation of the elastic wave and produces a resonance. On the contrary, this coupling disappear when the electric boundary is open as D_z=0. In the context of the investigation of AM, this makes the effective properties different from the conventional passive AMs since they could be actively controlled in the former case.

It is important to notice that the frequency domain of negative effective elastic modulus is very narrow, only 0.150 kHzmm. This can be explained by both phases of the effective mass density and the elastic modulus as shown in Fig. 2.3. At the resonance frequency, an about 100 degrees phase shift instead of 180 degrees is observed. This will be discussed below when the multi-unit AM will be investigated.

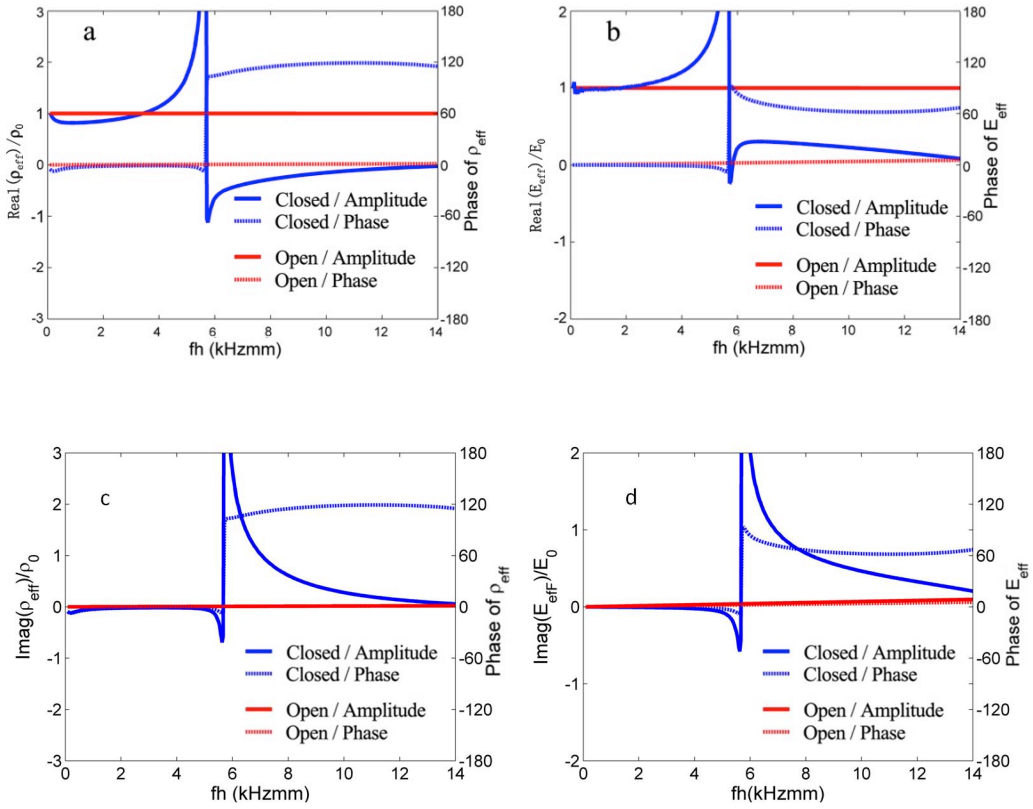

Figure 2.3 Upper panel: normalized real part (solid) and phase (dotted) of the effective mass density (a) and elastic modulus (b) under the electrically open (red) or closed (blue) status for a single unit AM; lower panel: the same as upper panel but for imaginary part

In contrast to the effective mass density, negative effective elastic modulus can only be obtained for certain filling ratio. As shown in Fig. 2.4, the effective properties are related to the filling ratio. When the filling ratio increases from 0.1 to 0.5, the minimum real parts of both effective mass density and elastic modulus increase up to the maximum values of ~-0.9 and ~0.2 respectively. The real part of the effective elastic modulus becomes positive when the filling ratio β is 30%. It is well known that Q factor characterizes the bandwidth of the resonator[24]. The high filling ratio brings high Q factor, indicating a lower relative rate of energy loss as compared to the stored energy of the oscillating system and a narrow range of frequencies at the resonant frequency, the vibration of the piezoelectric material plays an important role in the phase shift of the effective properties. When the filling ratio β is large

enough, the piezoelectric material structure cannot realize the resonance as required by the negative effective elastic modulus.

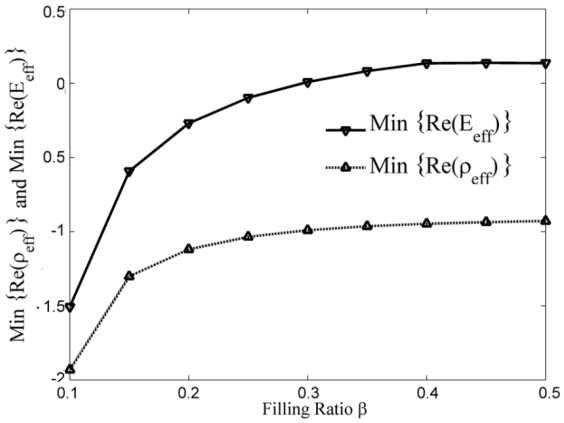

Figure 2.4 The minimum real part of effective mass density (solid) and elastic modulus (dotted) for different filling ratios

It is to be noted that the piezoelectric constants have a significant effect on the negative bandwidth of the effective properties. We have investigated the influence of the piezoelectric constants e_{13}, e_{33} and e_{15} to outline this sensitivity. We found that the bandwidth of the negative effective elastic modulus can be changed by the variation of e_{33} when the filling ratio is 20%, as shown in Fig. 2.5. The blue lines correspond to the frequency regions where the effective elastic modulus is negative. We varied e_{33} from 10 to 60 C/m^2, with a step of 10 C/m^2. The bandwidth when e_{33} is 10, 20 or 30 C/m^2 remains the same as that obtained with the original real value of 15.080 C/m^2, *i.e.* (5.675, 5.825) kHzmm. The bandwidth enlarges at $e_{33} = 40$ C/m^2 and narrows at $e_{33} = 50$ C/m^2, and even it splits into two parts at $e_{33} = 60$ C/m^2. This result shows how sensitive is the negative bandwidth of the effective elastic modulus to the piezoelectric constant e_{33}.

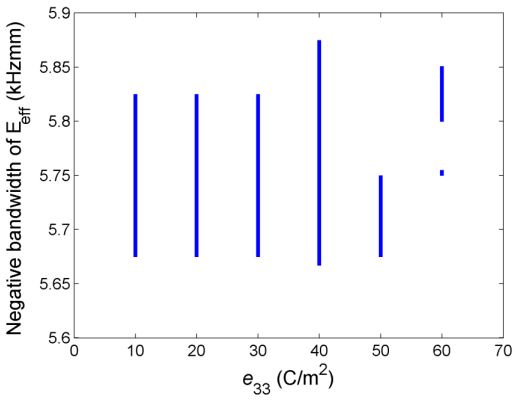

Figure 2.5 Effect of the piezoelectric e_{33} on the negative bandwidth of effective elastic modulus E_{eff}

Actually, if only single unit AM is inserted in the path of the elastic wave propagation, the phase shift of the effective properties at resonance is less than 180 degrees, which leads to a narrow frequency domain of double negativity. One efficient way to enlarge this frequency domain is to construct a multi-units AM. The effective mass density and elastic modulus of such a multi-units AM are displayed in Fig. 2.6. The computations were done for two (blue lines), three (black lines) and ten (green lines) stacked units. The frequency range of the negative effective mass density for two-units AM extends in the interval (3.750, 14.000) kHzmm, as shown in Fig. 2.6a. It is larger than the range (5.675, 14.000) kHzmm (red lines) that was calculated for the single unit AM. For the three-units AM, the effective mass density is negative for two frequency ranges, (2.583, 4.667) and (5.675, 14.000) kHzmm. The frequency range of the negative effective elastic modulus for two- or three- units AM extends to (3.750, 5.750) kHzmm and (2.667, 4.833) kHzmm, respectively (see Fig. 2.6b). As mentioned before, the resonance of the single unit AM is weak, because the phase shift of effective properties is less than 180 degrees at resonant frequency. When stacking the AM units, the phase shift at the first resonance is 180 degrees. The stacking of several AM units

contributes to the new resonances, which are demonstrated by the phase shifts in Fig. 2.6c and 2.6d. It is also interesting to note that the number of resonances is equal to the number of unit cells due to mutual interactions and dynamic response among them.

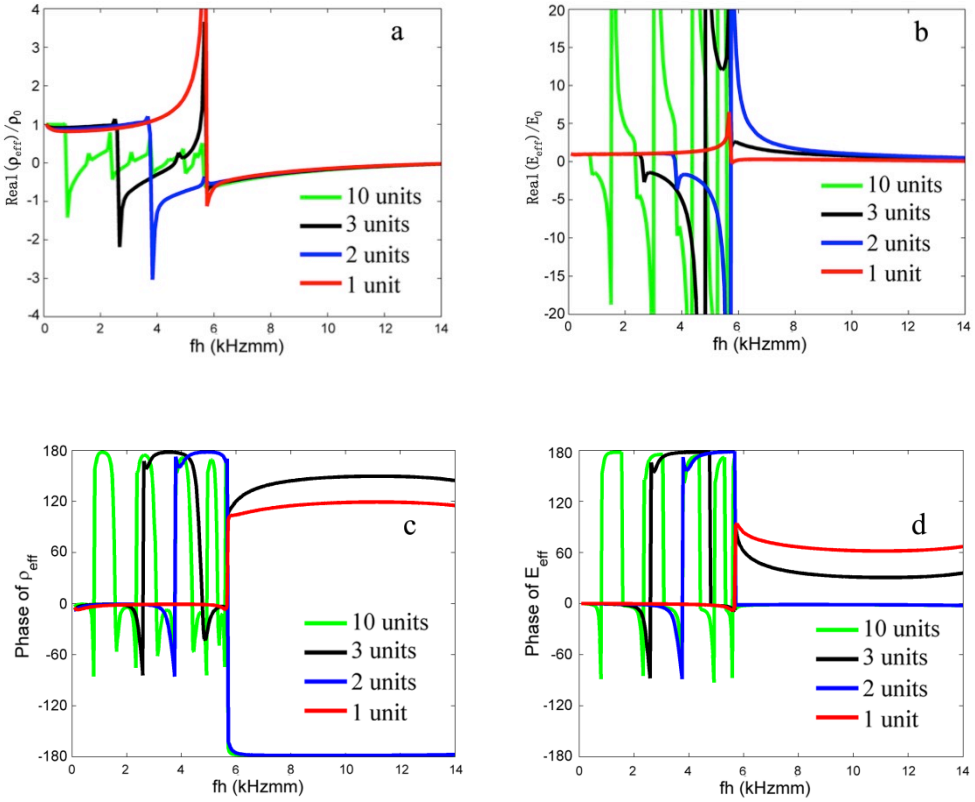

Figure 2.6 Under the electrically closed status for one- (red), two- (blue), three- (black) and ten- (green) unit AM: real part of the effective mass density (a) and elastic modulus (b); phase of the effective mass density (c) and elastic modulus (d)

In addition, increasing the number of AM units will reduce the frequency of the first resonance whereas the frequency of the last resonance remains unchanged. Since several AM units are coupled, the multi-unit AM, has multi resonances the first of which is strictly defined and the followings get attenuated as the phase shift may be less than 180 degrees. Figure 2.6 also implies that the intrinsic resonance mechanism of a single unit AM defines the cut-up resonant frequency width of multi-units AM. The multi resonances broaden the frequency range of negative effective properties and reduce the frequency of the first resonance at the

same time, as shown in Fig. 2.6 and 2.7. Figure 2.7 indicates that the double negative bandwidth divides into more parts and turns into lower frequency with the increase of the number of stacked unit.

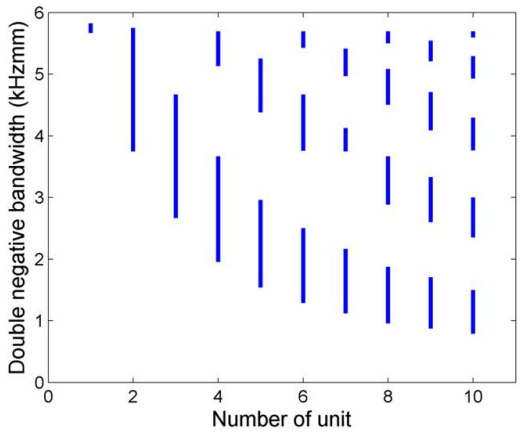

Figure 2.7 Effect of the number of unit on the double negative bandwidth

2.4 Conclusions

In this chapter, an active AM with resonances is proposed to exhibit double negativity over a certain frequency range by switching the electrical boundaries of the piezoelectric material. Analytical models were developed and analyzed. When the filling ratio β exceeds a certain value, the negative effective elastic modulus cannot be achieved. The piezoelectric constant e_{33} has an influence on the negative bandwidth of effective elastic modulus. The resonance could be strengthened to broaden the frequency band of the negative effective properties, through the stacking of the multi AM units. The proposed multi-units AMs are found to lower the first resonant frequency, while the cut-up frequency of the last resonance remains unchanged. The number of resonances and segments of double negative bandwidth increase with the number of stacked unit cells.

Chapter 3

Homogenization Method and Full Control of Lamb Modes

The content of this chapter was published in:

Yabin Jin, Daniel Torrent, Yan, Pennec, Yongdong Pan, Bahram Djafari-Rouhani. *Simultaneous control of the S0 and A0 Lamb modes by graded phononic crystal plate*. Journal of Applied Physics. 117(24), 244904, 2015.

Yabin Jin, Daniel Torrent, Yan, Pennec, Yongdong Pan, Bahram Djafari-Rouhani. *Gradient index devices for the full control of elastic waves in plates*. Scientific Reports. 6, 24437, 2016.

Yabin Jin, Daniel Torrent, Yan, Pennec, Gaëtan Lévêque, Yongdong Pan, Bahram Djafari-Rouhani. *Multimodal and omnidirectional beam splitter for Lamb modes in elastic plates*. AIP Advances. 6(12), 121602, 2016.

3.1 Introduction

The control of the propagating characteristics of mechanical (acoustic and elastic) waves in linear media is a challenging problem with a wide variety of applications, since this control allows the design of acoustic or elastic lenses[96, 97, 105, 140-142], omnidirectional absorbers[99, 103, 143], cloaking devices[107, 112, 144] or hyperlenses[117]. The propagation of mechanical waves can be tailored by means of inhomogeneous materials, as it is well known that in these media waves follow curved trajectories that can be properly designed if the position-dependent parameters of the medium are chosen according to specific laws. However, it is obvious that natural materials cannot provide these specific position-dependent parameters. Therefore, their realization has to be achieved artificially.

In this context, the field of phononic crystals[145, 146] and metamaterials[147] provides a promising background for the realization of artificial inhomogeneous materials, as has been widely demonstrated in the literature[46, 47, 91-94].

Gradient index (GRIN) devices consist of locally inhomogeneous materials in which the refractive index is a function of the spatial coordinates; therefore, waves follow curved trajectories that can be properly designed to focus the energy at a specific point. GRIN devices, which are well known in optics[95], are recently receiving increasing attention in the field of phononic and sonic crystals, since the artificial nature of these structures allows for an easy design of inhomogeneous materials.

Effectively, phononic crystals are essentially periodic arrangements of solid inclusions in an elastic matrix (fluid background for sonic crystals). They behave, in the low frequency limit, as homogeneous materials with effective constitutive parameters which depend mainly on the filling fraction of the inclusions[91]. Then, by locally changing this parameter according to some specific law, we can create an artificially inhomogeneous material which will work as a gradient index device. Following this approach, a wide variety of inhomogeneous devices

have been proposed, such as GRIN flat lenses[94, 96, 98, 140, 141], acoustic beam modifiers[148], omnidirectional refractive devices[105, 142] or absorber[99, 143], and acoustic or elastic cloaks[107, 144], which are indeed a new type of advanced gradient index device.

In the case of GRIN devices for solids, the main applications arise in the propagation of guided waves, such as Lamb or Love waves in plates and substrates[149]. However, these systems present several propagation modes and polarizations, whose dispersion relations are different in general. The main effort so far in this domain has been focused on the design of GRIN devices for the control of the lower order Lamb mode in thin plates, i.e., for the control of flexural waves, based on either non-resonant[97, 133, 150] or resonant[151-153] structures, and less attention has been given to the other vibrational modes.

The focusing of elastic waves in plates or substrates is interesting for applications such as vibration detection or energy harvesting, in which the interest remains in collecting all the possible energy carried out by these waves. However, it must be taken into account that the excitation of a vibration in a plate will be composed of a linear combination of all the vibrational, so that the design of refractive devices for an individual polarization only will have limited efficiency or utility. The dispersion characteristics of these polarizations are in general different, so that the design of refractive devices working for all them, even in the low frequency limit, is obviously a challenging problem.

In the second section of this chapter, a step towards this full control of vibrational modes is given, by exploiting an interesting property of the two lower order Lamb modes, which is the fact that they are connected by means of the so called “plate velocity.” It is found that this relationship is valid not only for isotropic plates but also for phononic crystal plates in the low frequency limit. Therefore, it is shown that it is possible to design GRIN devices for the simultaneous control of these two modes in a broadband frequency region. Since the dispersion relation of flexural modes is dependent on the plate thickness h, in contrast to the

dispersion relation of the first symmetric Lamb mode, the realization of the GRIN devices is based on the simultaneous variation of the filling fraction of the phononic crystal and the thickness of the plate in space.

Two devices are proposed and numerically studied: A flat GRIN lens and a Luneburg lens. The objective of these two devices is similar, which is focusing an incoming plane wave at a specific point. The design of these devices working for the two lower order Lamb modes suggests that any low frequency Lamb wave generated in a thin plate will be focused at the same point, so that these structures have potential applications for energy harvesting or small vibration detection.

The method developed in the second section allows the simultaneous control of two of the three fundamental plate modes[154], namely the anti-symmetric (A_0) and symmetric (S_0) Lamb modes. This simultaneous control was based on an effective medium theory developed for the A_0 mode[153] working with Kirchhoff equation[155], which is a two-dimensional equation describing the propagation of flexural waves in thin plates. The mentioned theory can be applied as well to the control of the S_0 mode given that the refractive indexes of these two modes are related by means of the same elastic constants and the thickness of the plate, however the refractive index of the third plate mode, named the shear horizontal (SH_0) mode, cannot be controlled by this approach, given that it depends on different elastic constants that, in general, cannot be changed independently. Due to the extraordinary difficulty required to work on homogenization using plate theories including the shear mode[156], we propose in the third section an alternate approach, based on the homogenization of the bulk phononic crystal.

In the third section a homogenization theory for phononic crystals is developed and applied to the homogenization of phononic crystal plates, which provides the solution of the refractive indexes of the three modes. It is shown then that by means of a complex unit cell, consisting of a circular inclusion with a hole in its center, it is possible to design

independently the refractive index of the three fundamental plate modes. The method is applied to the design of a flat gradient index lens, a Luneburg lens and a Maxwell lens working identically for the three modes. Finally, to illustrate the advantage of the method, a more advanced multi-lens device is designed, which works as a Luneburg lens for the S_0 and the SH_0 modes while it works as a Maxwell lens for the A_0 mode. Numerical simulations by COMSOL support their functionality in a broadband frequency region.

In the forth section, beam splitters are proposed for the control of the vibration of elastic plates. These devices have been widely studied in photonics[157-159] or atom optics[160, 161], and have been also designed for acoustic waves by using phononic crystals, utilizing the so-called self-collimation effect[162-164]. Beam splitters have also been proposed for flexural waves[105] based on graded phononic crystals, but their generalization to control the other two fundamental modes (the symmetric and shear modes) requires a more complicated approach, since the propagation of these waves is managed by different elastic constants.

Effectively, the propagation of elastic waves in a homogeneous plate is composed of three polarizations, namely anti-symmetric, symmetric and shear-horizontal modes, with different propagation velocities for each polarization. Gradient index devices typically are designed for only one of these polarizations, which hinder the full functionality of them for some specific applications. Also, while the flexural mode typically can be scattered and controlled in a plate without mode conversion, the symmetric and shear modes are in general coupled together, therefore the design of gradient index devices for only one of them will result in an important loss of efficiency, since some energy will be converted to the other mode. This inconvenience can be avoided by means of the design of multimodal devices.

In the fifth section, we investigate the elastodynamic homogenization theory, or known as "Willis" constitutive theory, which was exhibited by J. R. Willis[165-168] and offers more precise description of wave behaviors in periodic inhomogeneous media[169-172]. In theory, the

Willis material properties can be realized by designing microstructures with internal spring-mass-gyroscopes[168] or material with inhomogeneous pre-stresses[173]. However, proposed methods of calculating these proper dynamic effective medium parameters are very complicated[171, 174-176]. The PWE method[177] implemented in the last section for phononic crystal homogenization obtains the "Willis" term, which includes tensorial mass density and stiffness, and an additional coupling tensor, in a simpler way. Mathematically, we also demonstrate the realization of a "Willis" medium by breaking the symmetry in unit cell, e.g. chiral unit cell. Despite the non-zero value of "Willis" term, it is found that the "Willis" term does not play a role in the bulk phononic crystal dispersion. By introducing boundary conditions, we explore the non-classical dispersion properties of a "Willis" plate.

3.2 Simultaneous control of the S_0 and A_0 Lamb modes

3.2.1 Refractive devices for the S_0 and A_0 modes

Phononic crystals are periodic arrangements of solid inclusions in an elastic matrix, and phononic crystal plates are a special case of these structures in which a finite "slide" of the phononic crystal is taken. Fig. 3.1 shows an illustration of these two structures: In blue and at the left, a two dimensional arrangement of elastic cylinders embedded in an elastic matrix; at the right, we can see how a finite slide of this infinite periodic system has been taken.

In the low frequency limit, phononic crystals behave like homogeneous materials with some effective parameters, and the same is expected for phononic crystal plates, as it is illustrated in the lower part of Fig. 3.1. Therefore, it is expected that the effective parameters of the phononic crystal and the phononic crystal plate are the same.

The above statement has a non-trivial implication in terms of symmetry: A two-dimensional phononic crystal like the one shown in Fig. 3.1 will behave, in the low frequency limit, as an anisotropic solid, with tetragonal anisotropy in the most general case or transversal isotropy in the case of a triangular arrangement of inclusions. Therefore, the homogenization of phononic crystal plates has to be done taking into account that the effective plate will be a "slice" of a tetragonal material[149].

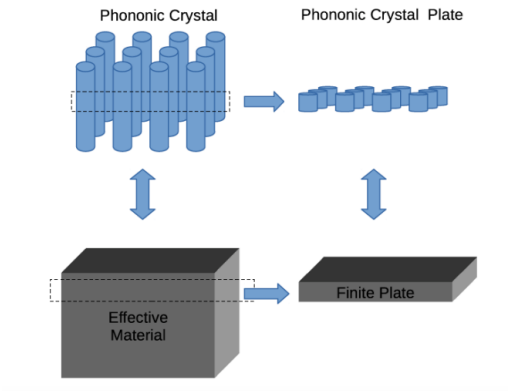

Figure 3.1 Schematic view of the homogenization procedure for phononic crystals and its relationship with phononic crystal plates

This work is focused on controlling the propagation of the two lower order Lamb modes of a plate, the S_0 mode and the A_0 mode (also named the flexural mode). In Ref[153], it was developed an effective medium theory for the propagation of the A_0 mode in a phononic crystal plate, and in this work it is shown that, given the special relationship between the propagation properties of the S_0 and the A_0 mode, the mentioned theory can be applied to both modes.

The dispersion relation of Lamb waves in elastic plates can be found in Ref[149]. It is shown that in the low frequency limit, defined by means of wavelengths $k > h$, where h is the thickness of the plate, the dispersion relation for the S_0 mode is linear and given by

$$\omega = v_p k_S \tag{3.1}$$

while for the A_0 mode it is parabolic and given by

$$\omega = \frac{v_p h}{\sqrt{12}} k_A^2 \tag{3.2}$$

with v_p being the so called "plate velocity." These expressions show the interesting property that the dispersion relation of the A_0 mode depends on the plate's thickness h, and it is directly related with the dispersion relation of the S_0 mode by means of the plate velocity v_p. In this work, this relationship between the dispersion relation of the two modes will be exploited, and homogenized two-dimensional phononic crystals will be employed for that purpose.

The above expressions are valid for the vibrations of a homogeneous and isotropic plate. It must be figured out if they can also be applied to phononic crystal plates in the low frequency limit. The analysis of Lamb waves in anisotropic plates is complex, but in the specific case of tetragonal materials, which is the case considered here, it can be demonstrated (see Appendix A) that expressions (3.1) and (3.2) are valid but the plate velocity must be given by

$$v_p^2 = \frac{c_{11}}{\rho}\left(1 - \frac{c_{13}^2}{c_{11}c_{33}}\right) \tag{3.3}$$

where c_{ij} stands for the ij element of the stiffness tensor of the plate.

In Ref.[153] , the effective parameters for the propagation of flexural waves in plates with a periodic arrangement of inclusions were obtained. It was found the dispersion relation in terms of the effective rigidity D^* and mass density ρ^*

$$\omega^2 = \frac{D^*}{\rho^* h_b} k^4 = \frac{\bar{D}^*}{\bar{\rho}^*} \frac{D_b}{\rho_b h_b} k^4 = \frac{\bar{D}^*}{\bar{\rho}^*} \frac{E_b}{\rho_b (1-v_b^2)} \frac{h_b^2}{12} k^4 \tag{3.4}$$

where the quantities with the bar mean that they are relative to the background. The above expression allows identifying

$$v_p^2 = \frac{\bar{D}^*}{\bar{\rho}^*} \frac{E_b}{\rho_b (1-v_b^2)} \tag{3.5}$$

so that by means of the effective medium theory we can obtain the effective plate's velocity. Usually, the dispersion relation is given as a function of $\omega a / 2\pi c_t$ as a function of ka, with a being the lattice constant and $c_t^2 = \mu_b / \rho_b$. In that case, knowing that $\mu_b = E_b / 2(1+v_b)$, we get, for the antisymmetric mode,

$$\frac{\omega a}{2\pi c_t} = \frac{h_b}{2\sqrt{3}a} \frac{1}{\pi} \sqrt{\frac{\bar{D}^*}{\bar{\rho}^*}} \sqrt{\frac{1}{2(1-v_b)}} k^2 a^2 \tag{3.6}$$

And for the symmetric one

$$\frac{\omega a}{2\pi c_t} = \frac{1}{\pi} \sqrt{\frac{\bar{D}^*}{\bar{\rho}^*}} \sqrt{\frac{1}{2(1-v_b)}} ka \tag{3.7}$$

Figures 3.2 shows the dispersion curves obtained by the FEM method (red dots) of a square and triangular arrangement of inclusions in an Aluminum plate, respectively. The upper panels show results for holes and the lower panels show results for lead inclusions (see Ref.[153] for material's parameters). The radius of the inclusions is $R_a = 0.3a$ and the thickness of the plate is $h = 0.1a$, where a is the lattice constant. The blue-continuous line shows the dispersion curves employing Eqs. (3.6) and (3.7). It is clear that there is a perfect agreement between the homogenization theory and the numerical calculation.

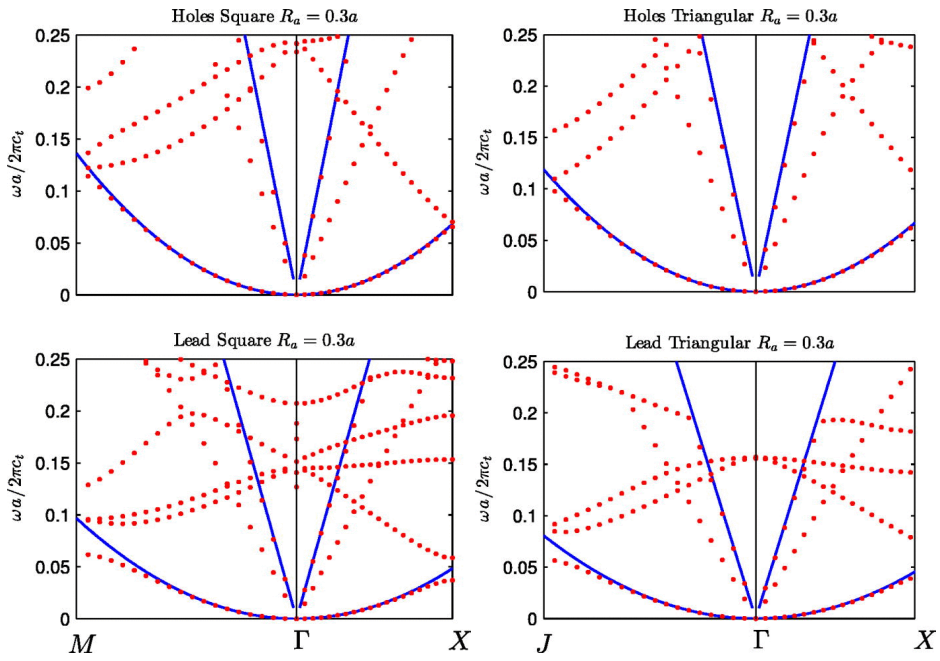

Figure 3.2 Left Panel: Dispersion curves for a phononic crystal plate consisting of a square lattice of holes (upper panel) and of lead inclusions (lower panel) of radius *Ra=0.3a* in an Aluminum plate of thickness *h*=0.1*a* , where *a* is the lattice constant. Red dots show the curves computed by finite element method and blue lines show the dispersion relation of the homogenized plate, which is tetragonal for this geometry; Right Panel: Same as in left panel but in this case the inclusions are in a triangular arrangement. The effective medium is transversely isotropic now

The propagation of waves in a medium is determined by the dispersion relation, but the refraction of waves when passing from one medium to another one is determined by the ratio between the wavenumbers in the two media, which defines the index of refraction. Then, according to Eqs. (3.7) and (3.6), it is easy to check that if a wave propagating in medium 1 (plate of thickness h_1) changes to medium 2 (plate of thickness h_2), the refractive index for the S_0 mode will be

$$n_S = \frac{v_{p1}}{v_{p2}} \tag{3.8}$$

while for the A_0 mode will be

$$n_A^2 = \frac{v_{p1}}{v_{p2}} \frac{h_1}{h_2} \tag{3.9}$$

which shows that n_S and n_A are related as

$$n_A^2 = n_S \frac{h_1}{h_2} \tag{3.10}$$

It has been assumed that the two media are two different plates, with different materials and thickness. The above expression shows that, although the dispersion relation for the two modes is different, with different frequency dependence, their refractive indices are closely related, with the remarkable result that, if the thickness of the two media is chosen as $h_1 = h_2 n_S$, it will be found that the refractive index of the S_0 and the A_0 mode is the same.

This interesting property will be exploited here to design of a refractive device identically for the two modes. Equation (3.9) was exploited in Ref[142] for the design of GRIN devices for the A_0 mode based on thickness variations, and in Ref[153] for the design of GRIN devices for the same mode but based on filling fraction variations. In this work, a combination of these two effects, together with Eq. (3.10), will be employed to design GRIN devices for the A_0 and the S_0 mode, simultaneously.

Two devices, a gradient index lens and a Luneburg lens, are proposed in this work based on the combination of graded phononic crystals and thickness variations. These devices have been already studied for flexural waves, and here it is proposed their design to work simultaneously for the two fundamental Lamb modes.

A GRIN lens consists in a rectangular device in which the refractive index is a function of the distance to the lens' axis, and it is given by[96]

$$n(y) = n_0 \mathrm{sech}(\alpha y) \tag{3.11}$$

If the variation of the index is along the y direction, a wave travelling along the x axis and arriving to the device is focused at a distance $f = \pi/2\alpha$. Similarly, a Luneburg lens consists in a circular device in which the refractive index is a function of the distance to the center of the lens and given by[95]

$$n(r) = \sqrt{2 - (r / R_L)^2} \tag{3.12}$$

where R_L is the radius of the lens. The Luneburg lens is an omnidirectional device in which any plane wave arriving at its surface is focused on the diametrically opposed border of the lens.

Phononic crystal based GRIN devices consist in the realization of the above variations of the refractive index by varying the physical properties of the inclusions. In the low frequency limit, phononic crystals behave like homogeneous materials with some effective parameters which are function of the inclusions' properties and sizes, and then a rectangular or circular region of a phononic crystal can be properly designed to satisfy the above position-dependent refractive indices.

The design of this type of devices requires of a proper effective medium theory which gives the effective refractive index of the phononic crystal as a function of the physical properties of the inclusions. In the present case, this theory is the recently developed homogenization theory for flexural waves (A_0 mode) which can be used to obtain the refractive index of the A_0 mode[153]. In the framework of this theory, the propagation of waves is described in terms of the rigidity D_b of the plate and its mass density ρ_b. If in the plate there is a phononic crystal, the theory gives the effective rigidity $\bar{D}^*$ and mass density $\bar{\rho}^*$ relative to those the background D_b and ρ_b. Recall Eq. (3.5), it has been shown that the plate's velocity in the phononic crystal region is related with this theory by

$$v_p^2 = \frac{\bar{D}^*}{\bar{\rho}^*} \frac{E_b}{\rho_b (1-\nu_b^2)} \tag{3.13}$$

so that from the homogenization theory for flexural waves it is possible to deduce the plate's velocity, and consequently, the refractive index not only for the A_0 mode but also for the S_0 mode.

The design procedure for the GRIN lens is as follows. First, an inclusion located at $R_i = (x_i, y_i)$ is selected, and the expected refractive index at that position is computed by means of Eq.

(3.11). Then by means of Eq. (3.8), it is obtained the corresponding plate velocity. Equation (3.13) relates the plate velocity with the filling fraction of the inclusion, thus from this equation we solve for the required filling fraction at the given position, which automatically defines the radius of the inclusion. The procedure is repeated to all the inclusions in the plate, so that the design of the full GRIN lens is finally completed. Notice that it has been employed the effective medium theory for flexural waves to obtain the effective parameters, but taking Eq. (3.8) for the design of the lens means that the GRIN designed works only for the S_0 mode.

The key point in this work is that, after having designed the refractive device for the S_0 mode, it is possible to modify the plate's thickness in the region of the device in a way that the refractive device works also for the A_0 mode. This can be done by means of a position dependent thickness of the plate as $h_2(y) = h_b/n_S(y)$, where h_b is the thickness of the plate in the background (i.e., outside the lens region). Following Eq. (3.10), this condition implies that $n_A(y) = n_S(y)$, so that the refractive index of the two modes is identical and, therefore, the GRIN lens will work properly for the two modes.

3.2.2 Numerical results

The designed flat GRIN lens consists of a square arrangement of lead inclusions with lattice constant a in a silicon plate of thickness $h=a$, with ρ_a = 11.34 kg/m^3, E_a=16 GPa, and ν_a = 0.44 being the mass density, Young's modulus, and Poisson's ratio, respectively, for lead and ρ_b = 2.33 kg/m^3, E_b=150 GPa, and ν_b = 0.28 being the corresponding parameters for silicon. The rectangular region of the phononic crystal is selected as having N_y=15 rows and N_x=30 columns, which defines a lens of height L_y = 15a and length L_x =30a.

Figure 3.3 shows COMSOL simulations of the interaction of the GRIN lens with the S_0 and A_0 polarizations. Upper panels show the expected GRIN design in which the thickness of the plate in the rectangular phononic crystal region is position-dependent, while mid panels

show the GRIN lens without the mentioned thickness variation. Left panels correspond to the normalized z component of the displacement field for the A_0, and the right ones to the S_0 mode, where it is plotted the normalized x component of the displacement field. Given that the performance of the device depends on the wavelength of the field rather than on the frequency, simulations are shown for frequencies that the two modes have the same wavenumber ka=1, which corresponds to $\omega a/c_t = 1/ sqrt(12)$ for the A_0 mode and $\omega a/c_t = 1$ for the S_0 one. It can be seen that the device works properly for the two modes and the focusing point is identical in both situations. It can also be seen that the field distribution is not the same for the two modes, given that, although the A_0 mode can be scattered almost without interaction with other Lamb modes, the S_0 mode tends to excite SH_0 waves, hence the displacement field is not the same. In other words, this theory provides the refractive index for the two modes, but not the mode's dynamics. Simulations in the mid panels, where the thickness variation has been removed and the plate has a constant thickness h_b, show that although the S_0 mode is not affected (as expected), the A_0 mode it is, given that the field distribution is different now.

Figure 3.3, lower panel, shows the normalized field distribution along the central axis of the lens and for the four situations described before. It is clear that the field profile and focusing point are nearly the same for the two modes when the thickness of the plate is position-dependent, but when the thickness is kept constant the A_0 mode is different, which clearly verifies the role of the thickness variation.

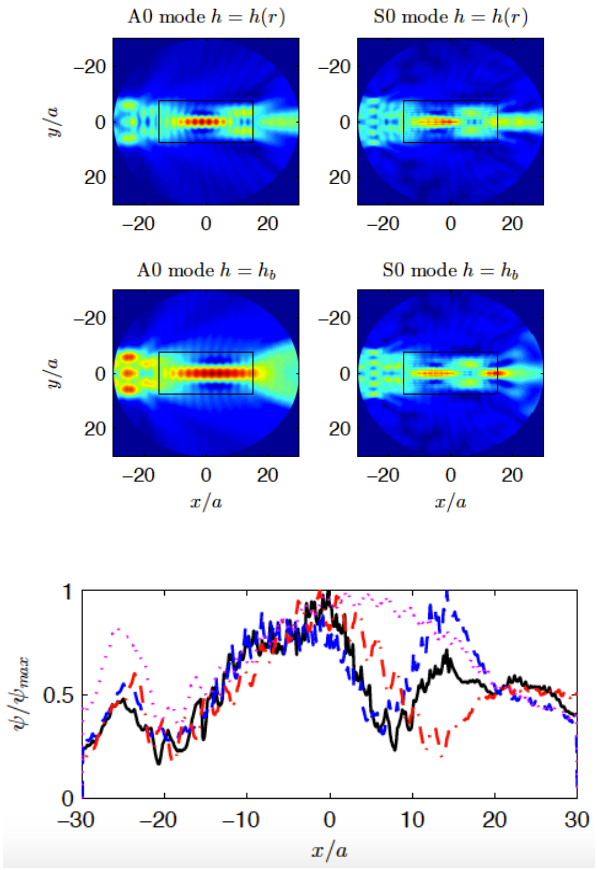

Figure 3.3 Upper panels: Field distribution for ka=1 for a A_0 polarized (left) and a S_0 (right) polarized plane waves interacting with the gradient index lens where the thickness of the plate is designed for the simultaneous focusing of the two Lamb modes. Middle panels: Same as the left-upper panels but now the thickness of the plate is constant throughout the lens, so that the focusing of the A_0 mode is different than for the S_0 mode. Lower panels: Normalized field distribution along the x axis and for y=0 (central axis of the lens) for the S_0 mode with thickness variation (black continuous line) and without thickness variation (blue dashed line), and for the A_0 mode with thickness variation (red dashed-dotted line) and without thickness variation (magenta dotted line). It is seen that the thickness variation does not affect the S_0 mode, while for the A_0 mode it changes the focusing point, making it identical to that of the S_0 mode

For some applications, we may expect the waves arriving from all directions for which an omnidirectional device can be more efficient. The Luneburg lens described in Eq. (3.12) is a good example of an omnidirectional refractive device. Figure 3.4 shows the performance of a Luneburg lens of radius $R_L = 10a$, designed in the same way as the GRIN lens to work for the two modes (inclusions are now arranged in a triangular lattice, which is more suitable for circular clusters). The upper-left panel shows the real part of the normalized z component for the A_0 polarization and the upper-right panel shows the real part of the normalized x component for the S_0 polarization. The lower panel shows the absolute value of these fields

along the axis of the lens. As before, the wavelength for the two fields is ka=1. From all the plots, it can be seen how a focusing point near the border of the lens occurs, as expected.

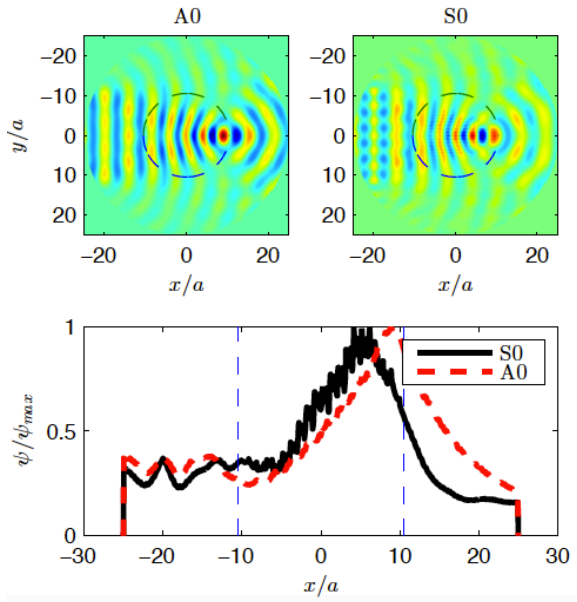

Figure 3.4 Upper panel: Real part of the field distribution for the A_0 (left) and S_0 (right) polarizations interacting with a Luneburg lens designed by means of phononic crystal with a thickness variation. Lower panel: Absolute value of the field distribution along the y=0 line. Vertical dashed lines show the radius of the lens

In the previous simulations, it has been shown the performance of the two devices when working at the same wavenumber, but different frequencies, for the two modes. However, for a practical application it is necessary to see the performance of the lens at the same frequency. Figure 3.5 shows a COMSOL simulation of the GRIN lens working at the frequency $\omega a/c_t$ = 1.22, left panel for the A_0 mode and right panel the S_0 one. We can see how the focusing point is nearly the same for the two modes, while it is better defined for the A_0 mode where the wavelength is $\lambda \approx 3.6a$, while for the S_0 mode this wavelength is $\lambda \approx 7.7a$. Similar results were also found for the Luneburg lens.

It must be pointed out that this type of devices is typically limited by two wavelengths. In the lower limit, it is found that for wavelengths larger than the typical size of the device the diffraction dominates over refraction, and the device's focusing properties are altered. In the upper limit, it is found that for wavelengths shorter than 3 or 4 times the lattice constant, the

phononic crystal is no longer homogeneous, and the effective medium model cannot be applied. Given that this wavenumber region is well defined, but that the corresponding frequency region is not the same for the two modes, the frequency region in which the device works properly for the two modes will be shorter than that in which it works individually. The lower panel of Figure 3.5 shows the dispersion relation for the S_0 mode (red-dashed line) and for the A_0 mode (blue-continuous line). The two vertical lines define the wavenumber region in which the performance of the device is expected. The frequency region in which the device will work properly for the two modes is limited: below for the mode which has the larger wavelength, that is, the S_0 mode; above for the A_0 mode, given that it has the shorter wavelength. These limits are shown in the figure by the red-dashed and blue-continuous horizontal lines, respectively. The horizontal black-dotted-dashed line shows the frequency at which the simulations were performed. It is seen that there is still a broadband frequency region in which the device can work properly for the two modes.

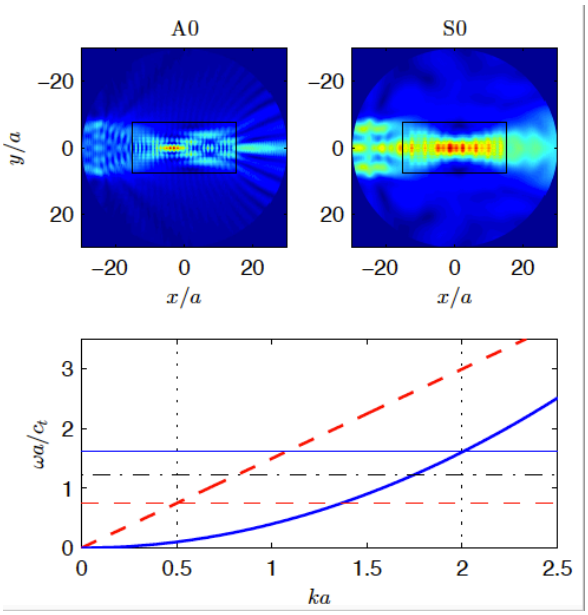

Figure 3.5 Field distributions for the interaction of A_0 mode (upper-left) and the S_0 mode (upper-right) working at the same frequency but different wavenumbers. Lower panel: Dispersion relation $\omega - k$ for the A_0 (blue-continuous line) and the S_0 (red-dashed line). Vertical lines show the wavenumber region in which the GRIN lens would work properly; horizontal red-dashed and blue-continuous lines show the frequency region in which the device will work properly for the two modes. The horizontal dotted line shows the frequency at which the simulations in the upper panels have been performed

These refractive devices have applications by themselves, but their design for several modes suggests their application for energy harvesting or vibration detection. Effectively, any perturbation excited in a plate will be composed of all the possible modes, so that the efficient conversion or detection of this energy will require of a multimodal device. The above results show that the simultaneous control of two different vibrational modes is possible in a broadband frequency region. Although the mechanism exploited in this work is unique for Lamb waves given their special relationship, it suggests that other methods can be applied for more vibrational modes. For instance, a unit cell with two inclusions could be designed to simultaneously control the refractive index of the S_0 and SH_0 modes by locally changing the radius of each inclusion, although new effective medium theory including all Lamb waves should be developed in this case, which is beyond the objective of the present work.

3.3 Full Control of Elastic Waves in Plates

3.3.1 PWE Homogenization method

Recall the basic PWE method from literature[177]. The equation of motion of an inhomogeneous solid is given by the classic elastodynamic equation[149], with harmonic time term ignored

$$-\rho\omega^2 u_i = \partial_j c_{ijkl} \partial_k u_l \tag{3.14}$$

with u_i as the components of the displacement field and c_{ijkl} as the components of the stiffness tensor. If the solid is homogeneous, the dispersion relation can be obtained by assuming plane-wave propagation with wave vector $\boldsymbol{k}=k\boldsymbol{n}$, with k being the wave number and $\boldsymbol{n}$ being the unit vector paralleling to the propagating direction. Thus the equation of motion becomes

$$\rho\omega^2 u_i = k^2 n_{iI} C_{IJ} n_{Jj} u_j \tag{3.15}$$

Now u_i and C_{IJ} are in Voigt notation. The dispersion relation is the root of the determinant of the matrix $\bar{\Gamma}$ defined as

$$\bar{\Gamma}_{ij} = \rho\omega^2 \delta_{ij} - k^2 n_{iI} C_{IJ} n_{Jj} \tag{3.16}$$

Phononic crystals consist of periodic arrangements of inclusions in an elastic matrix, with $\rho(r)$ and $c_{ijkl}(r)$ being periodic functions of the spatial coordinates. By applying the Bloch theorem and using the plane wave expansion method, the dispersion relations are the solutions of the eigenvalue equation

$$\omega^2 \rho_{G-G'} \left(u_{G'}\right)_i = \left(k+G\right)_{iI} C_{IJ}^{G-G'} \left(k+G'\right)_{Jj} \left(u_{G'}\right)_j \tag{3.17}$$

where the terms with G in subscript and superscript are the Fourier components. The $\boldsymbol{G}$ is the reciprocal lattice vector. The above equation can be expressed as

$$\omega^2 N_{GG'} \boldsymbol{u}_{G'} = M_{GG'} \boldsymbol{u}_{G'} \tag{3.18}$$

Where

$$\left(N_{GG'}\right)_{ij} = \rho_{G-G'}\delta_{ij} \tag{3.19}$$

$$\left(M_{GG'}\right)_{ij} = \left(k+G\right)_{iI} C_{IJ}^{G-G'} \left(k+G'\right)_{Jj} \tag{3.20}$$

The average of the displacement vector is given by the $\boldsymbol{G}$=0 component of $\boldsymbol{u}_G$, therefore it can be derived by

$$\omega^2 N_{00}\boldsymbol{u}_0 + \omega^2 N_{0G'}\boldsymbol{u}_{G'} = M_{00}\boldsymbol{u}_0 + M_{0G'}\boldsymbol{u}_{G'} \tag{3.21}$$

$$\omega^2 N_{G0}\boldsymbol{u}_0 + \omega^2 N_{GG'}\boldsymbol{u}_{G'} = M_{G0}\boldsymbol{u}_0 + M_{GG'}\boldsymbol{u}_{G'} \tag{3.22}$$

Hereafter, the matrix elements labeled with G do not include the term G=0, as extracted from the above equations. Re-write the second equation as

$$\boldsymbol{u}_{G'} = -\left(M_{GG'} - \omega^2 N_{GG'}\right)^{-1}\left(M_{G0} - \omega^2 N_{G0}\right)\boldsymbol{u}_0 \tag{3.23}$$

Then substitute into the first equation, we have

$$\left[\omega^2 N_{00} - \omega^2 N_{0G'}\chi_{G'G}\left(M_{G0} - \omega^2 N_{G0}\right) - M_{00} + M_{0G'}\chi_{G'G}\left(M_{G0} - \omega^2 N_{G0}\right)\right]\boldsymbol{u}_0 = 0 \tag{3.24}$$

With

$$\chi_{lm}^{G'G}\left(\omega,k\right) \equiv \left(M_{G'G} - \omega^2 N_{G'G}\right)_{lm}^{-1} \tag{3.25}$$

So that the dispersion relation is obtained from the zeros of the determinant of the matrix Γ defined as

$$\Gamma = \omega^2 N_{00} - \omega^2 N_{0G'}\chi_{G'G}\left(M_{G0} - \omega^2 N_{G0}\right) - M_{00} + M_{0G'}\chi_{G'G}\left(M_{G0} - \omega^2 N_{G0}\right) \tag{3.26}$$

The matrix Γoffers more suitable description about the composite of phononic crystals, from which we can find one set of elements independents on wave vector

$$\left(N_{00}\right)_{ij} = \bar{\rho}\delta_{ij} \tag{3.27}$$

$$\left(N_{0G'}\right)_{ij} = \rho_{-G'}\delta_{ij} \tag{3.28}$$

$$\left(N_{G0}\right)_{ij} = \rho_{G}\delta_{ij} \tag{3.29}$$

With $\bar{\rho} = \rho_{G=0}$ being the mass density average value of the unit cell. Meanwhile, another set of elements contains wave vector,

$$\left(M_{00}\right)_{ij} = k_{iI}\bar{C}_{IJ}k_{Jj} \tag{3.30}$$

$$\left(M_{0G'}\right)_{ij} = k_{iI}C_{IJ}^{-G'}\left(k+G'\right)_{Jj} \tag{3.31}$$

$$\left(M_{G0}\right)_{ij} = \left(k+G\right)_{iI}C_{IJ}^{G}k_{Jj} \tag{3.32}$$

With $\bar{C} = C_{IJ}^{G=0}$ being the average value of the components of the stiffness tensor in the unit cell. By re-organizing the dependence of the wave vector and frequency, the matrix Γ can be expressed in the form

$$\Gamma_{ij} = \omega^2\rho_{ij}^{*} - k^2 n_{iI}C_{IJ}^{*}n_{Jj} - \omega k\left(n_{iI}S_{Ij} + S_{iJ}^{\dagger}n_{Jj}\right) \tag{3.33}$$

With

$$\rho_{ij}^{*}\left(\omega,k\right) = \bar{\rho}\delta_{ij} + \omega^2\rho_{-G'}\chi_{ij}^{G'G}\left(\omega,k\right)\rho_{G} \tag{3.34}$$

$$C_{IJ}^{*}\left(\omega,k\right) = \bar{C}_{IJ} - C_{IL}^{-G'}\left(k+G'\right)_{Ll}\chi_{lm}^{G'G}\left(\omega,k\right)\left(k+G\right)_{mM}C_{MJ}^{G} \tag{3.35}$$

$$S_{Ij}\left(\omega,k\right) = \omega C_{IL}^{-G'}\left(k+G'\right)_{Ll}\chi_{lj}^{G'G}\left(\omega,k\right)\rho_{G} \tag{3.36}$$

These expressions are valid for all frequency and wave number. It is well known that for low frequencies phononic crystals behave like homogeneous materials with some effective parameters (mass density ρ^{*} and stiffness tensor C_{IJ}^{*}). In the low frequency and local limit, $\omega \to 0$ and $k \to 0$, thus the effective elastic constants are simplified as

$$\rho^{*} = \bar{\rho} \tag{3.37}$$

$$C_{IJ}^{*} = \bar{C}_{IJ} - \sum_{G,G'\neq 0}\sum_{L,l,m,M} C_{IL}^{-G'}G'_{Ll}\chi_{lm}^{G'G}G_{mM}C_{MJ}^{G} \tag{3.38}$$

It must be pointed out that the above theory is valid for 1, 2 or 3-dimensional phononic crystals, being the dimensions of the ***G*** vector the only difference for each periodicity.

A phononic crystal plate is a two-dimensional periodic arrangement of inclusions in an elastic plate, and it has also been shown that for low frequencies these structures behave like homogeneous elastic plates. However, the analysis of the dispersion relations of these structures is more complex than that of their bulk counterparts, given that we require additional equations to satisfy boundary conditions, therefore the homogenization of these structures is a more complicated problem[178]. The authors have recently studied the focalization of the symmetric and antisymmetric Lamb modes in a phononic crystal plate[154] assuming that, in the low frequency limit, this plate can be considered a "finite slice" of a two-dimensional phononic crystal, and an excellent agreement was found in the comparison of the respective dispersion curves. Therefore, it is possible to homogenize the bulk phononic crystal by means of equations (3.37) and (3.38), and analyze the vibrations of homogeneous plates with the given effective parameters. Although this study was done for the antisymmetric (A_0) and symmetric (S_0) Lamb modes, here its validity will be demonstrated for the three fundamental Lamb modes.

As an example, let us consider a triangular arrangement with lattice constant a of gold shell-hole structure, with inner radius $R_a = 0.2a$ and outer radius $R_b = 0.4a$, in an Aluminum matrix (see elastic parameters in Table 3.1 and schematics of the unit cell in Fig. 3.6). In the low frequency limit this arrangement of inclusions behaves like a transversely isotropic solid whose effective parameters can be computed using equations (3.37) and (3.38) and are given in Table 3.1. If we take a plate of thickness h of such an effective solid, the dispersion relation of the three fundamental modes in the low frequency limit is isotropic and given by the following equations[154]

$$\rho^* \omega^2 = C_{66}^* k_{SH}^2 \tag{3.39}$$

$$\rho^* \omega^2 = C_{11}^* \left(1 - \frac{C_{13}^{*2}}{C_{11}^* C_{33}^*}\right) k_S^2 \tag{3.40}$$

$$\rho^* \omega^2 = C_{11}^* (1 - \frac{C_{13}^{*2}}{C_{11}^* C_{33}^*}) \frac{h^2}{12} k_A^4 \tag{3.41}$$

with k_X being the wavenumber of the X mode, for $X = SH, S, A$. Figure 3.7 shows the comparison of the full dispersion relation of the phononic crystal plate computed with COMSOL (black dots) with the dispersion relation obtained by means of equation (3.39)-(3.41) (red lines) for plate's thickness $h = 0.1a$, $0.5a$ and $h = a$ in left, center and right panels, respectively. It is clear how in the low frequency limit the plate can be described by the effective medium theory developed for bulk phononic crystals, which in turns simplifies considerably the calculations and also allows for the design of refractive devices, as will be shown in the following section.

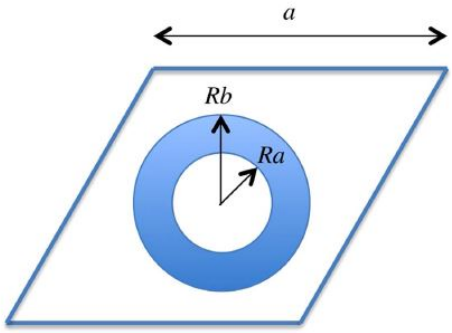

Figure 3.6 Unit cell employed in the design of GRIN devices, consisting of a triangular arrangement of gold inclusions of radius R_b with holes of radius R_a in an Aluminium matrix

Material	ρ (Kg/m^3)	C_{11} (GPa)	C_{12} (GPa)	C_{33} (GPa)	C_{13} (GPa)	C_{66} (GPa)
Aluminum	2.7E3	108.2	51.2	C_{11}	C_{12}	$(C_{11} - C_{12})/2$
Gold	19.5E3	190	161	C_{11}	C_{12}	$(C_{11} - C_{12})/2$
Effective Material	9.63E3	61.1	32.3	79.2	36.6	$(C_{11} - C_{12})/2$

Table 3.1 Elastic parameters of the materials used in the text

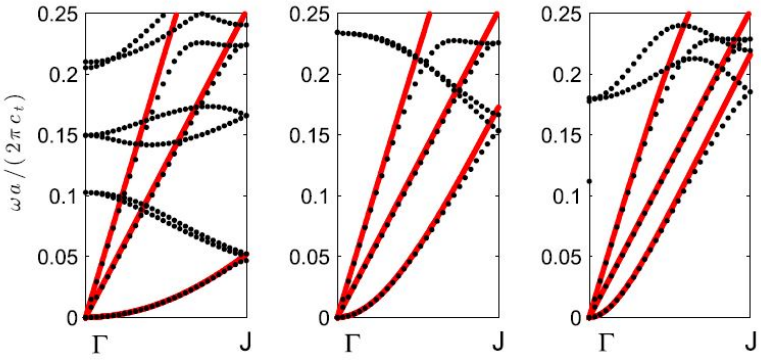

Figure 3.7 Dispersion relations for a phononic crystal consisting of a triangular lattice of gold shell - hole structure with inner radius $R_a = 0.2a$and outer radius $R_b = 0.4a$ in an aluminum plate of thickness $h = 0.1a$, $h = 0.5a$ and $h = a$, corresponding to the left, middle and right panels, respectively. Black dots show the curves calculated by COMSOL and red lines show the dispersion relations obtained by equations (3.39)-(3.41) with effective parameters in Table 3.1

3.3.2 Simultaneous Control of the Fundamental Plate Modes

When a wave passes from a given medium I to a different one II it suffers refraction. The condition for refraction is derived by imposing conservation of the wavenumber in the direction parallel to the plane dividing the two media, and this condition defines the refractive index as the ratio between the wavenumber in the two media[179]. From expression (3.39)-(3.41) we find that the refractive indexes of the three fundamental modes are therefore given by

$$n_{SH} = \frac{k_{SH}^{II}}{k_{SH}^{I}} \tag{3.42}$$

$$n_{S} = \frac{k_{S}^{II}}{k_{S}^{I}} \tag{3.43}$$

$$n_{A}^{2} = n_{S}\frac{h^{I}}{h^{II}} \tag{3.44}$$

where it has been assumed that medium I(II) is a plate with elastic parameters labeled by I(II) and thickness h_I (h_{II}). We can see therefore that the thickness of the plate can be used to control the refractive index of the A_0 mode independently of the other two modes. Besides, we

see that while the elastic constants defining the refractive index of the A_0 and S_0 mode are the same, the refractive index SH_0 mode depends on the C_{66}^* component of the stiffness tensor.

The design of gradient index devices is typically done by choosing one material for the background, another for the inclusions, and then the refractive index is a function of the filling fraction (radius) of the inclusions, that is, $n = n(R_0)$. In this work we have three refractive indexes to design, however the refractive index of the A_0 mode will be designed by changing the relative thickness of the plate and using equation (3.44), so that actually we have to design only n_S and n_{SH}. If we had only one degree of freedom, that is, the radius of the inclusion R_0, we could choose for instance n_S and then determine the corresponding value of R_0, since $n_S = n_S(R_0)$, but then the refractive index of the SH_0 mode would be imposed, so that we need an additional degree of freedom to choose independently n_S and n_{SH}.

We propose the structure shown in Fig. 3.6, in which an Aluminum matrix is perforated by a triangular arrangement of gold inclusions of radius R_b with a hole at its center of radius R_a (see materials' parameters in Table 3.1). The effective parameters of such a phononic crystal will therefore be a function of both R_b and R_a, which will allow us, as will be explained later, the independent tuning of the three refractive indexes.

Figure 3.8 shows the "phase diagram" of this material, in which we make a sweep of $R_b \in (0, 0.5a)$ and $R_a \in (0, R_b)$, with a being the lattice constant of the arrangement. All the possible values that take n_S and n_{SH} are shown in this diagram. This diagram can be used as an inverse design tool: We choose a given value for the desired refractive index for the two modes lying in the diagram, then we find the corresponding values for R_a and R_b, to later use expression (3.44) to determine the thickness of the plate that give us the desired value for n_A, so that we are capable of independently tune the three refractive indexes, obviously under the limitations given by the phase diagram depicted in Fig. 3.8.

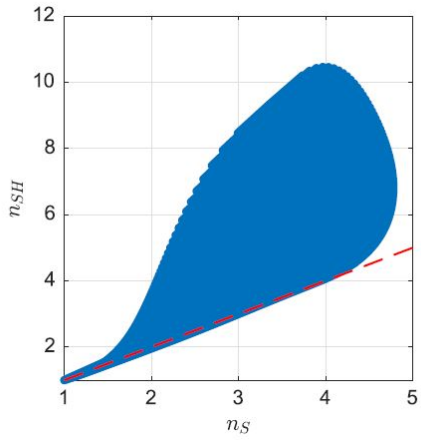

Figure 3.8 Phase diagram showing all the possible values for the effective refractive indexes for the SH_0 and S_0 modes obtained by varying the radius of the holes and the inclusions. The red-dashed line shows the condition $n_{SH} = n_S$, showing that it is possible the design of refractive devices identical for these two modes

3.3.3 Numerical Examples

This part is devoted to illustrating the power of the presented method to design gradient index devices working simultaneously for all three fundamental plate modes. The design procedure is identical for all these devices: First we decide the device, defined by means of a position-dependent refractive index; second, we define the positions of a cluster of inclusions, according to the device's geometry (a square slab for a flat GRIN and a circular cluster for a Luneburg or Maxwell lenses), with a large enough number of inclusions to avoid diffractive effects (see discussion below); third, we select the inclusion α and compute the desired radii R_a and R_b. For the computation of these values we need to know the desired refractive indexes for the S_0 and SH_0 modes at the position $\boldsymbol{r}_\alpha$, and then use the data of the phase diagram shown in Fig. 3.8 which relates the refractive index with the radius of the hole and inclusion. Finally, once we have selected R_a and R_b, by means of equation (3.44) we choose the thickness of the plate at that position to obtain the desired refractive index for the A_0 mode. It has to be noticed that this design method allows for creating refractive devices for the three modes, but not necessarily the same device for the three modes, given that it can be used to tune independently the three indexes. Therefore, although from the practical point of view it

appears better to design devices focusing all the energy at the same point for one kind of lens, we propose in our last example the realization of a multi-lens device working as a Luneburg lens for the S_0 and SH_0 modes and as a Maxwell lens for the A_0 mode.

Figure 3.9 shows a COMSOL simulation of the first example considered in this work. It consists in a long GRIN flat lens as described in several works[96, 154], in which the refractive index is a function of the distance y to the center of the lens and it is given by

$$n(y) = n_0 \operatorname{sech}(\alpha y) \tag{3.45}$$

In this specific case, the lens is made of 15 rows and 34 columns of inclusions arranged in a triangular lattice, oriented in such a way that the vertical distance between inclusions equals the lattice constant a, therefore it has a height $L_y = 15a$ and a width $L_x = 17\sqrt{3}\,a$. The plate has a thickness $h = a$ in the background (recall that the device has a position-dependent thickness). The simulations show the total displacement field when an external plane wave of a given polarization propagates through the x axis and it arrives to the device. Results shown in the left, central and right panels correspond to the S_0, SH_0 and A_0 modes, respectively, and they are computed at the same frequency $\omega a/2\pi c_t = 0.178$, which corresponds to wavenumbers $k_S a = 0.65$, $k_{SH} a = 1.11$ and $k_A a = 1.5$. The dotted red lines display the size of GRIN flat lens, where the focusing points are demonstrated near the center as expected for all three modes.

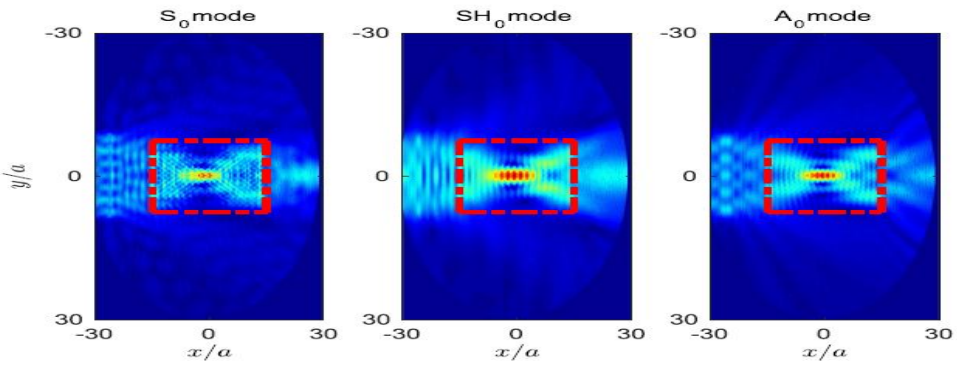

Figure 3.9 GRIN flat lens made with a slab of 15 rows and 34 columns of gold-hole inclusions in an Aluminum plate of thickness $h = a$. Simulations are shown at the same frequency $\omega a/2\pi c_t = 0.178$, which corresponds to wavenumbers $k_S a = 0.65$, $k_{SH} a = 1.11$ and $k_A a = 1.5$, whose corresponding field distributions are shown in left, central and right panels

We can see how the quality of the focusing point depends on the wavenumber of the incident field, given that it will be limited by diffraction and size effects. Effectively, it is commonly assumed in phononic crystals based devices that the limit of validity is the "low frequency limit", however in those situations in which we have more than one mode propagating through the material, this limit has to be properly analyzed. The homogenization limit is indeed a propagation regime in which the wavelength of the propagating field is larger than the typical distance between scatterers, so that the field actually detects an average medium and cannot distinguish individual scatterers. Therefore, it is the wavelength of the field and not its frequency the relevant quantity, for this reason, for the same frequency, the different modes will have different wavelengths, and therefore different responses.

In general, there are two physical phenomena relating the validity of the functionality of the device. The upper limit in wavelength is limited by the fact that this wavelength should be smaller than the size of the device, so that the refraction effect dominates over diffraction, this limit can obviously be controlled by increasing the size of the device and, therefore, the number of inclusions; The lower limit in wavelength is determined by the validity of the homogenization theory, which requires a wavelength typically larger than at least 3 or 4 times the lattice constant. These limits are not strictly defined and are only approximate; however it is obvious that for the same device they will be at different frequencies for the three modes, although it is clear that there will be a frequency region in which these conditions hold for the three modes.

The second example considered in this work is a Luneburg lens, which consists of a circular lens in which the refractive index depends on the position to the center of the lens as[95]

$$n(r)=\sqrt{2-(r/R_c)^2} \tag{3.46}$$

This refractive index is designed in such a way that any plane wave arriving to the lens is focused at the diametrically opposed border of it. It is therefore an omnidirectional device, as it is isotropic and radially symmetric. Its realization is identical to that of the GRIN lens, but this time we use a circular cluster of inclusions of radius $R_c = 10a$. Figure 3.10 shows a COMSOL simulation in which a plane wave of a given polarization impinges the cluster from the left, and it is therefore focused at the opposite side of the cluster. The simulations show the real part of the component of the displacement field dominant for each polarization (u_x for the S_0 mode, u_y for the SH_0 mode and u_z for the A_0 mode) and they are performed as in the previous example at the same frequency $\omega a/2\pi c_t = 0.24$, corresponding to $k_S a = 0.87$, $k_{SH} a = 1.5$, and $k_A a = 1.74$, shown in left, central and right panels, respectively. From the simulations it is clear the path followed by the wavefront which is finally focused at the border of the lens, as expected.

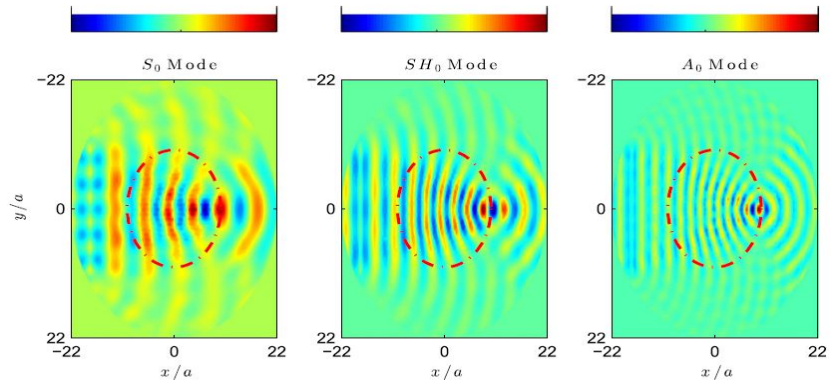

Figure 3.10 Luneburg lens of radius $Rc = 10a$ with about 300 inclusions. Simulations are shown at $\omega a/2\pi c_t = 0.24$, which corresponds to wavenumbers $k_S a = 0.87$, $k_{SH} a = 1.5$, and $k_A a = 1.74$, whose corresponding field distributions are shown in left, central and right panels

The following example is similar to the previous one, but this time the proposed omnidirectional device is a Maxwell lens[95], whose refractive index is given by

$$n(r) = 2/\left(1+\left(r/R_c\right)^2\right) \tag{3.47}$$

The Maxwell lens is designed in a way that a point source excited at one border of the lens is focused at the opposite side of it. The design method is the same as for the Luneburg lens,

and Fig. 3.11 shows the real part of the results of the simulations performed with COMSOL. The point source for each polarization is excited as a body force in the x, y and z direction for the S_0, SH_0 and A_0 modes, respectively.

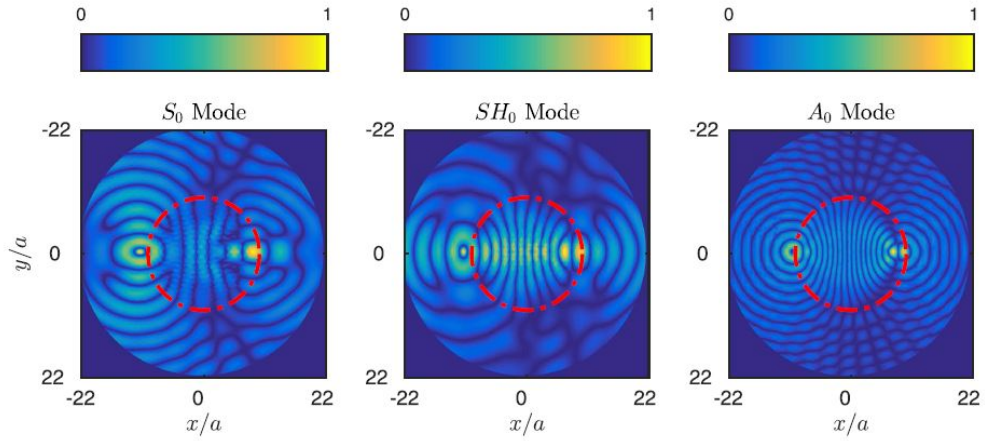

Figure 3.11 Maxwell lens of radius $Rc = 10a$ with about 300 inclusions. Simulations are shown at $\omega a/2\pi c_t = 0.178$, which corresponds to wavenumbers $k_S a = 0.65$, $k_{SH} a = 1.11$, and $k_A a = 1.5$, whose corresponding field distributions are shown in left, central and right panels

As before, the plots show the real part of the dominant component of the displacement field for each polarization. The source is excited at $x = -10a$ at the same frequency $\omega a/2\pi c_t = 0.178$, corresponding to $k_S a = 0.65$, $k_{SH} a = 1.11$ and $k_A a = 1.50$, shown in left, central and right panels, respectively. The focusing points are identically located at the $x = 10a$ border for the three modes, which shows the good performance of the device.

The above simulations show the performance of the method for the simultaneous control of the three fundamental modes, although the three devices work identically for the three modes. However, the method does not require that the refractive index profile be the same for the three modes, since each refractive index can be tuned independently, which means that a device can be designed as working as one type of lens for one mode and as different one for another mode.

To demonstrate the power of the present method, a multi-lens device is designed to behave as a Luneburg lens for the S_0 and SH_0 modes and as a Maxwell lens for the A_0 mode. Figure 3.12 shows the real part of the dominant component of the displacement field for each

polarization, but this time the simulations were made at the same wavenumber ka = 1.5, in this way it is easier to compare the field distributions and performance of the device. This wavenumber corresponds to reduced frequencies $\omega a/2\pi c_t$ of 0.41, 0.24 and 0.17 for the S_0, SH_0 and A_0 modes respectively. We see how the device behaves as a Luneburg lens for the S_0 and SH_0 modes while it behaves as a Maxwell lens for the A_0 polarization.

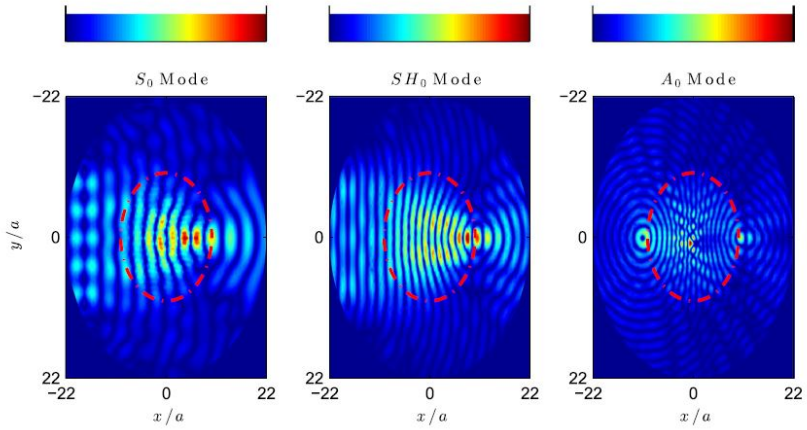

Figure 3.12 Luneburg and Maxwell lens working at the same wavenumber for the three modes ka = 1.5 which corresponds to the frequencies $\omega a/c_t$ = 0.41, 0.24 and 0.17 for the S_0, SH_0 and A_0 polarizations, respectively

3.4 Multimodal and omnidirectional beam splitter

3.4.1 Design of beam splitters for all the fundamental Lamb modes

We focus on beam splitters, consisting in circular lenses of radius R_c in which the refractive index depends only on the distance to the center of the lens. The profile of the refractive index of beam splitters is designed in such a way that when a plane wave arrives at the device it is divided into two beams, each one propagating with a deflection angle θ or -θ with respect to the initial incident direction. The refractive index profile as a function of the distance r to the lens' center is obtained from the solution of the equation[95]

$$(r/R_c) - 2n^{\alpha-1} + (r/R_c)n^{2\alpha} = 0 \tag{3.48}$$

where α defines the deflection angle as $\theta=\pi/\alpha$, and R_c is the radius of the lens.

The solution of equation (3.48) with α=2, 3, and 6, which corresponds to deflection angles of θ=90°, 60°, and 30°, respectively, are shown in the left panel of Fig. 3.13. The refractive index is 1 at the border of the lens, and it increases towards the center. For a given position, the refractive index of a smaller deflection angle is less than that of bigger deflection angle, and it is clear that as we move to the center of the lens the device becomes more "demanding", in the sense that a higher refractive index is required. The horizontal line in the figure shows the maximum refractive index that can be achieved with our complex unit cell, and it is clear from this figure that for 60° and 90° the inner part of the lens will not be properly designed, since the required index cannot be achieved. The numerical simulations presented within the next section will show that the effect of these imperfections is not important for the performance of the lens.

Finally, in order to design $n_A = n_{SH} = n_S$, the variation of the thickness of the lens requires $h_{lens} = h_b/n_S$, where h_b is the thickness of the homogeneous plate. In the right panel of Fig. 3.13 it is shown the relative thickness h_{lens}/h_b as a function of the radial coordinate for deflection

angle θ=90°, 60°, and 30°. The lens requires a reduction between the 50% and 20% of its thickness, which is something achievable in practice although it obviously depends on the scale of fabrication.

Next part shows some numerical simulations for a beam splitter of deflection angle of 60°, designed according to the method presented before.

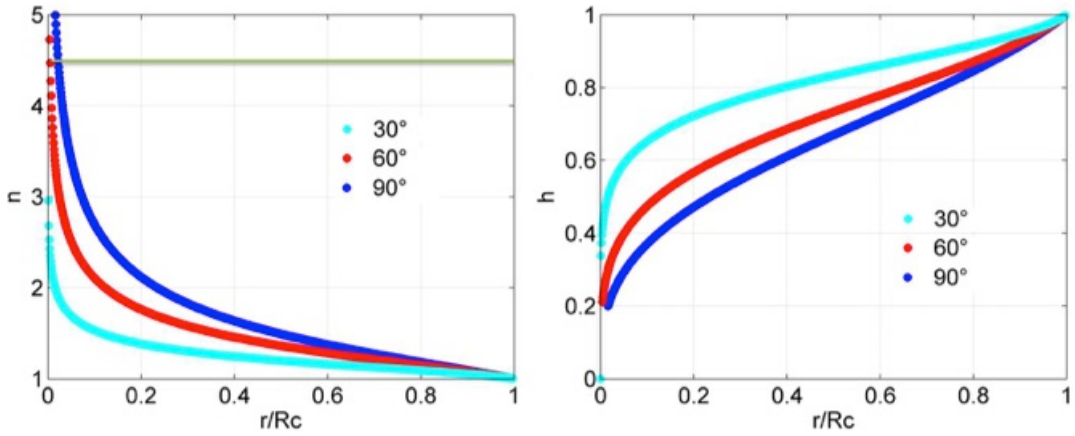

Figure 3.13 Left Panel: the refractive index as a function of the radial coordinate for beam splitters with deflection angles 30° (cyan dotted line), 60° (red dotted line), and 90° (blue dotted line). Right panel: the corresponding plate's thickness as a function of the radial coordinate for these three deflection angles

3.4.2 Numerical Simulations

The realization of the beam splitter is done by means of a circular cluster of hole-gold-shell inclusions embedded in a triangular lattice of lattice constant a. The circular cluster has a radius R_c =10.5a and a background thickness h_b=0.5a. Inside the lens the position-dependent thickness and inner-outer radius are designed so that the refractive indexes of the three modes meet the profiles of the selected deflection angle shown in Fig. 3.13. Therefore we follow the design procedure explained in our previous work for the Luneburg and Maxwell lenses.

The performance of the beam splitter is studied numerically by the commercial FEM software COMSOL Multiphysics®. The plane wave for each polarization is excited as a boundary force in the x, y, z directions for the S_0, SH_0, and A_0 modes, respectively, while the propagating direction is set along the x-axis. The excitation of the field is selected so that the

three modes present the same wavenumber $k_S a = k_{SH} a = k_A a = 1$, which corresponds to reduced frequency $\omega_S a/(2\pi v_t) = 0.307$, $\omega_{SH} a/(2\pi v_t) = 0.157$, $\omega_A a/(2\pi v_t) = 0.068$, respectively, where $v_t = 3249$m/s is the transverse bulk velocity of Aluminum.

Figure 3.14 shows the results for the 60° beam splitter working for the A_0 mode. Since this mode is not coupled to others, only the z component of the displacement field is different than zero. The left panel shows the real part of the displacement when a boundary force in the z direction is applied. It is clear from the figure that there is a splitting of the field towards the +/-60° directions, although the interference pattern in the near field can hinder the effect.

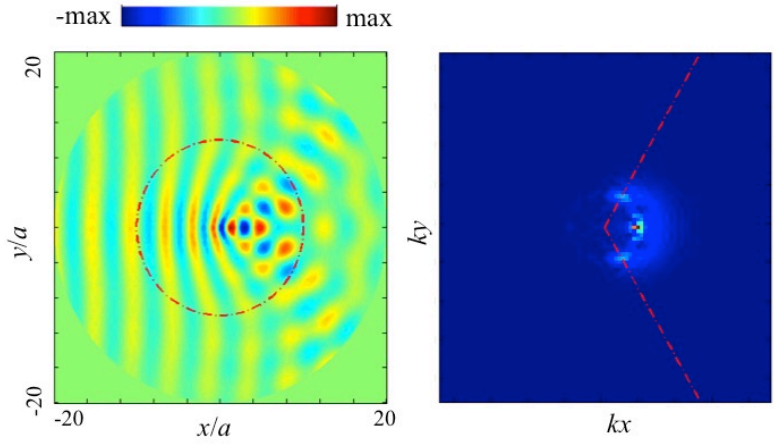

Figure 3.14 Real part of u_z component (left) and the corresponding Fourier Transform (right) for A_0 mode excitation. In the left panel, the red dotted line is the domain of beam splitter; in the right panel, two red dotted lines stand for the 60° deflection angle

The splitting effect can be better seen in the Fourier Transform of the field depicted in the right panel of Fig. 3.14. It is clear that in the k_x - k_y space a hot spot appears for the angles +/-60°, plus the hot spot in the forward direction. The latter cannot be avoided since it is a result of the optical theorem[105].

In Fig. 3.15, left panels show the real field of the u_x (upper) and u_y (bottom) components when the boundary force is excited along the x, which corresponds to the S_0 mode excitation. The right panels show the Fourier transforms of the u_x (upper) and u_y (bottom) components. The upper panels show the same result for the x component as for the z component shown in Fig. 3.14. However we can see how the y component of the displacement field is also

deflected towards the +/-60° directions. The reason for this effect is that since the displacement field is bent 60°, now the S_0 polarization is not predominantly located along the x direction, but it will have two components u_x and u_y. However for the u_y component there is no "incident" field, so that the scattered field is purely along the deflection angle, without the forward field predicted by the optical theorem.

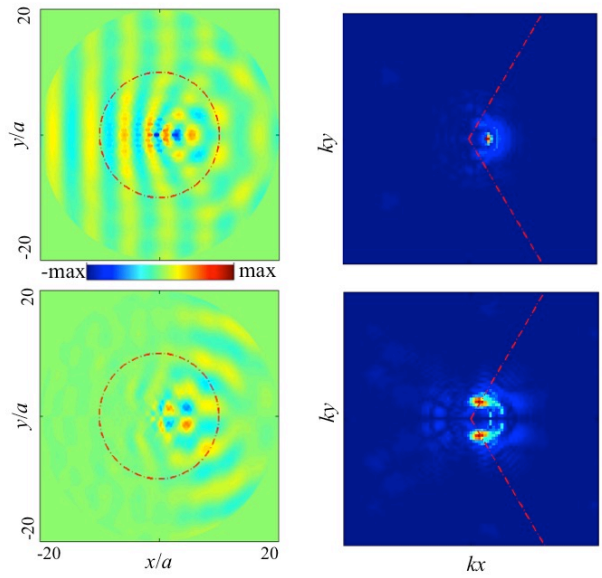

Figure 3.15 Real part of u_x component (upper-left) and the corresponding Fourier Transform (upper-right) for S_0 mode excitation; Real part of u_y component (lower-left) and the corresponding Fourier Transform (lower- right) for the same S_0 mode excitation. In the left column, the red dotted line is the domain of beam splitter; in the right column, two red dotted lines stand for the 60° deflection angle

Similar results are also observed for SH_0 polarization excitation, as seen in Fig. 3.16. The upper panel is the real part of u_x in the left and its Fourier transform in the right, while in the lower panel the results are shown for u_y component of displacement. The deflected SH_0 waves are dominated by both of u_x and u_y, in which u_x mainly originates from the scattering effect as directed along the 60° deflection angle.

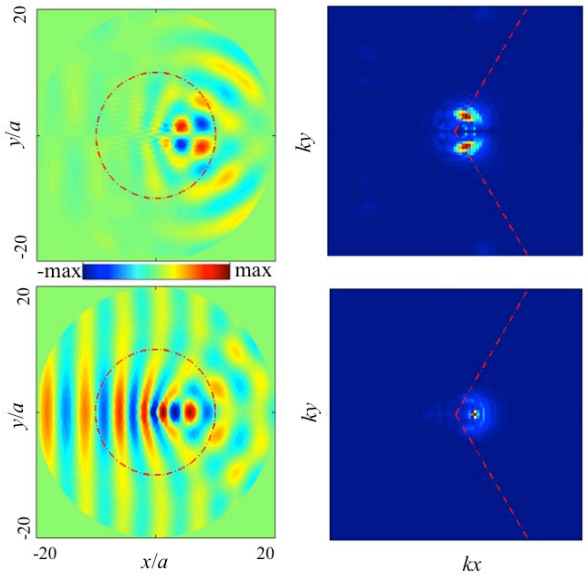

Figure 3.16 shows the same effect but for the SH_0 polarization, so that we have to exchange the x and y components in the interpretation of the field

Therefore the designed device works as a beam splitter for the three fundamental plate modes, as can be seen from the Fourier transform of the near field patterns. Additionally, due to the vectorial nature of the excited field, when excited by the S_0 or SH_0 fields we obtain a split beam with no forward scattered field in the y and x directions, respectively, which are different from the GRIN devices for flat lens, Luneburg lens or Maxwell lens. The latters focus wave energy in the same direction as incident angle. The presented beam splitter in this work is to diverge wave energy in different angles with respect to incident wave, exhibiting new behaviors as shown above and bringing better understandings of the full control of waves. The multimode beam splitter shows great potentials in energy harvesting application.

3.5 Theory of 'Willis' medium

3.5.1 Basic introduction of Willis medium

The constitutive equation and the equation of equilibrium for classic elastic materials are

$$\boldsymbol{\sigma} = C\boldsymbol{\varepsilon} \tag{3.49}$$

$$\mathrm{div}\boldsymbol{\sigma} + \rho\omega^2\boldsymbol{u} = 0 \tag{3.50}$$

Where $\boldsymbol{\sigma}$, $\boldsymbol{\varepsilon}$ and, $\boldsymbol{C}$ are stress, strain and stiffness tensors, respectively.

For Willis medium, the two equations are modified as

$$\boldsymbol{\sigma} = C\boldsymbol{\varepsilon} + i\omega S\boldsymbol{u} \tag{3.51}$$

$$\mathrm{div}\boldsymbol{\sigma} + \rho\omega^2\boldsymbol{u} + i\omega S^{\dagger}\boldsymbol{\varepsilon} = 0 \tag{3.52}$$

With *S* as a coupling Willis form, which provides more precise description of wave behaviors in periodic inhomogeneous media. In periodic structures, the PWE method developed in Sec. 3.5.2 offers a full expression of the Willis form, as

$$S_{Ij}(\omega,k) = \omega C_{IL}^{-G'}\left(k+G'\right)_{Ll}\chi_{lj}^{G'G}(\omega,k)\rho_G \tag{3.53}$$

In the epoxy-rubber-lead infinite medium, the elements of Willis form are zero in the local case when *k*=0, however, they will behave as a resonant component in non-local situation[177].

In this section, we will demonstrate that in the local ($k \to 0$) and low frequency ($\omega \to 0$) limit, if the geometry of the unit cell is symmetric, the values of elements in Willis form are zero, $S \equiv 0$. On the contrary, if break the geometric symmetry in the unit cell, the Willis form becomes non-zero, $S \neq 0$, so that we can realize a Willis medium in the local and low frequency limit.

However, if the Willis medium with non-symmetric geometry, e.g. chiral structure, is infinite in two-dimensional system, the Willis form *S* appears with its conjugate form $S^{\dagger}$, and the summation of them is always zero, $S + S^{\dagger} = 0$, indicating that the Willis form won't affect

the corresponding dispersion curves. By introducing boundary conditions for this infinite Willis medium, as a Willis plate, the Willis form will has influence on the corresponding dispersion curves, from which it is shown the realization of a Willis plate by breaking the symmetry in the unit cell.

The realization of a Willis plate makes it interesting to investigate its vibrating properties, which will be demonstrated in details in the Sec. 3.5.3.

3.5.2 Realization of a" Willis" plate by non-symmetric phononic crystals

The wave equation in a general phononic crystal is given by

$$-\rho\omega^2 u_i = \partial_j C_{ijkl} \partial_k u_l \tag{3.54}$$

where both ρ and *Cijkl* are periodic functions of the spatial coordinates. In Ref[169, 177] it was demonstrated that a phononic crystal can be described, in the low frequency limit, as a Willis medium, in which the wave equation is given by

$$\omega^2 \rho_{ij}^* u_j = \left[k^2 n_{iI} C_{IJ}^* n_{Ji} + \omega k \left(n_{iI} S_{Ij} + S_{iJ}^\dagger n_{Jj} \right) \right] u_j \tag{3.55}$$

with the mass density ρ_{ij}^* being a tensorial quantity and where the additional coupling tensor S_{Ij} has been introduced.

It is found that these parameters can be easily computed by means of the Fourier coefficients of the periodic functions defining the crystal, and the expressions found are as follows

$$\rho_{ij}^* = \bar{\rho}\delta_{ij} + \omega^2 \sum_{G,G' \neq 0} \rho\left(-G'\right) \chi_{ij}^{G'G}\left(\omega\right) \rho\left(G\right) \tag{3.56}$$

$$C_{IJ}^* = \bar{C}_{IJ} - \sum_{G,G' \neq 0} \sum_{L,l,m,M} C_{IL}^{-G'} G_{Ll}' \chi_{lm}^{G'G}\left(\omega\right) G_{mM} C_{MJ}^G \tag{3.57}$$

$$S_{Ij} = \omega \sum_{G,G' \neq 0} \sum_{L,l} C_{IL}^{-G'} G_{Ll}' \chi_{lj}^{G'G}\left(\omega\right) \rho\left(G\right) \tag{3.58}$$

with the bar quantities being the average in the unit cell, ρ (G) and C_{IL}^{G} the Fourier components of the mass density and the stiffness tensor, respectively, G_{Ll} the matrix associated to the reciprocal lattice vector $\boldsymbol{G}$, following Voigt notation, and $\chi_{lm}^{G'G}(\omega)$ the interaction matrix defined as

$$\chi_{lm}^{G'G}(\omega)=\left(M_{G'G}-\omega^2 N_{G'G}\right)_{lm}^{-1},\forall G,G'\neq 0 \tag{3.59}$$

where M and N are given by

$$\left(N_{GG'}\right)_{ij}=\rho\left(G-G'\right)\delta_{ij} \tag{3.60}$$

$$\left(M_{GG'}\right)_{ij}=G_{iI}C_{IJ}^{G-G'}G'_{Jj} \tag{3.61}$$

The χ matrix is the quantity giving the resonant effective parameters. It must be pointed out that, in the static limit this χ matrix is simply the reciprocal of the matrix M. In this limit also the mass density becomes the average in the unit cell and the S tensor is zero. However, near a resonance the term $\omega^2 N$ makes this quantity singular for specific values of ω, that is, resonant. Let us try to understand the nature of these resonances.

Assume that we know the eigenvalues λ_k and eigenvectors υ_k of the matrix $M-\omega^2 N$. We know then that the inverse of this matrix can be expanded by means of the eigen-decomposition theorem, thus we have that

$$\chi=\left(M-\omega^2 N\right)^{-1}=\sum_k \frac{\upsilon_k^{\dagger}\otimes\upsilon_k}{\lambda_k} \tag{3.62}$$

Given that $M-\omega^2 N$ is actually a Hermitian matrix. It was shown that[177], since for low frequencies this matrix is actually a perturbation of the M matrix, perturbation theory can be used to relate the eigenvalues λ_k with frequency. Thus, defining u_k and C_k/a^2 as the eigenvectors and eigenvalues of the M matrix, respectively,

$$Mu_k=C_k/a^2 u_k \tag{3.63}$$

If $-\omega^2 N$ is a perturbation of the matrix M, we have that the eigenvalues and eigenvectors λ_k and υ_k are given by

$$\lambda_k \approx C_k / a^2 - \omega^2 \rho_k \tag{3.64}$$

$$\upsilon_k \approx u_k - \omega^2 \sum_l a_{kl} u_l \tag{3.65}$$

where (assuming $u_k^\dagger \cdot u_k = 1$)

$$\rho_k = u_k^\dagger N u_k \tag{3.66}$$

$$a_{kl} = \frac{u_k^\dagger N u_l}{C_k / a^2 - C_l / a^2} \delta_{kl} \tag{3.67}$$

which ensures as well that $u_k^\dagger \cdot u_k = 1$. The above results allow us to approximate χ as

$$\chi(\omega) \approx \sum_k \frac{u_k^\dagger \otimes u_k}{C_k / a^2 - \omega^2 \rho_k} \tag{3.68}$$

This interesting result shows that the resonant frequencies ω_k are determined by the ratio of the eigenvalues C_k / a^2 of the matrix M and by the perturbation term ρ_k. Also, the coupling of these resonances with the different constitutive parameters is defined by the symmetry of the eigenvectors u_k of the matrix M. Effectively, near the kth resonance we have that

$$\chi_{lm}^{G'G}(\omega) \approx \frac{\left(u_{lG'}^*\right)_k \left(u_{mG}\right)_k}{C_k / a^2 - \omega^2 \rho_k} \tag{3.69}$$

We can now define

$$(A_i)_k = \sum_{G \neq 0} \rho(G) (u_{iG})_k \tag{3.70}$$

$$(B_I)_k = \sum_{G \neq 0} C_{IL}^G G_{Ll} (u_{lG})_k \tag{3.71}$$

and then near the kth resonance the effective parameters are given by

$$\rho_{ij}^{*}(\omega) \approx \frac{\omega^2}{C_k / a^2 - \omega^2 a^2 \rho_k} (A_i^{*})_k (A_j)_k \tag{3.72}$$

$$C_{IJ}^{*}(\omega) \approx \frac{1}{C_k / a^2 - \omega^2 a^2 \rho_k} (B_I^{*})_k (B_J)_k \tag{3.73}$$

$$S_{Ij}(\omega) \approx \frac{\omega}{C_k / a^2 - \omega^2 a^2 \rho_k} (B_I^{*})_k (A_j)_k \tag{3.74}$$

Let us assume a non-chiral phononic crystal. Given the symmetry of these systems, we know that the Fourier components satisfy $F_{-G} = F_G$, then it is easy to demonstrate (see the Appendix B) that the eigenvectors u_G satisfy

$$u_{-G} = \pm u_G \tag{3.75}$$

which implies two types of solutions, $(A_i)_k \neq 0$ and $(B_I)_k = 0$ when $u_{-G} = u_G$, and $(A_i)_k = 0$ and $(B_I)_k \neq 0$ when $u_{-G} = -u_G$. The former induces a resonant mass density, while the latter induces a resonant stiffness tensor. The two cases imply that the Willis tensor S_{Ij} is equal to zero.

Therefore, in this approximation, that is, in the low frequency limit and the local approximation, to have $S_{Ij} \neq 0$ we need both $(A_i)_k \neq 0$ and $(B_I)_k \neq 0$, which is only possible if we break the symmetry of the lattic in such a way that $F_{-G} \neq F_G$, that is, if the lattice is non-symmetry, such as chiral.

For symmetric unit cell, $S_{Ij} = 0$. Both of 2D infinite medium and a finite plate medium, at the low frequency, the shear-horizontal mode only depends on the effective c_{66}^{*} (see Eq. (A5) in Appendix A), bringing the same shear-horizontal dispersion curves. Here, c_{66}^{*} is the effective value of c_{66} in the limit of homogenization. As shown the unit cell in Fig. 3.17, the square inclusion is made of rubber ($\rho = 1300 kg/m^3$, E=2.7e-4GPa, v=0.499), which is embedded in an epoxy matrix ($\rho = 1180 kg/m^3$, E=4.35GPa, v=0.37). From the comparison

of dispersions, we can observe that the branches of shear-horizontal mode for infinite medium and a finite plate are superposed before deviation as they depend on the same elastic constant without Willis term, as indicated by the black arrow.

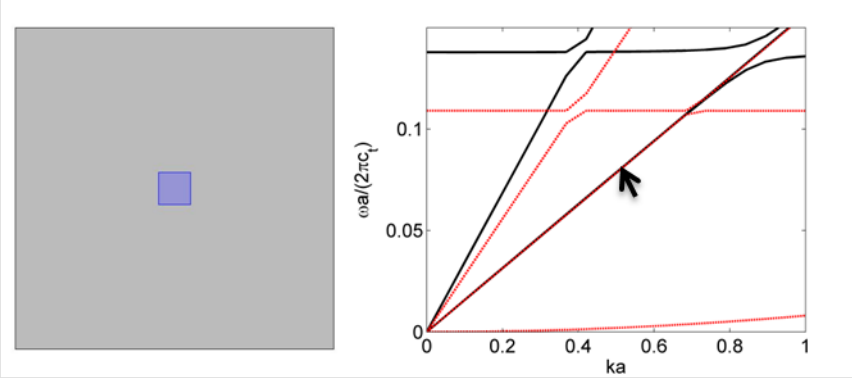

Figure 3.17 Left: unit cell in square array, with the square inclusion as rubber embedded in the epoxy matrix; Right: dispersion curves of 2D infinite medium (black line) and a finite plate medium with a thickness h=0.1a (red dot)

In Fig 3.18, the unit cell is typical chiral geometry as demonstrated widely[180-182], with the blue chiral inclusion made of rubber embedded in an epoxy matrix. Now the Willis term $S_{lj} \neq 0$. For infinite Willis medium, the Willis term does not affect dispersion curves, as demonstrated in Appendix C, which means the shear-horizontal mode, at the low frequency range, still depends on the effective c_{66}^{*}. However, for a finite Willis plate, the Willis term will change the dispersion curves due to the existing of boundary conditions (see Eq.(3.111) and more details in Appendix D), so that at the low frequency range, the shear-horizontal dispersion is different from that of infinite medium, as shown the black arrows in Fig 3.18.

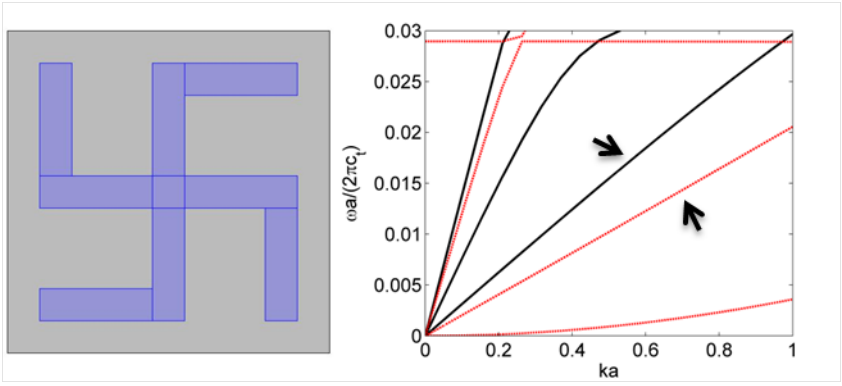

Figure 3.18 Left: chiral unit cell in square array, with the chiral inclusion as rubber embedded in the epoxy matrix; Right: dispersion curves of 2D infinite medium (black line) and a finite plate medium with a thickness h=0.1a (red dot)

3.5.3 The properties of 'Willis' plate

As the Willis plate can be realized by breaking the symmetry in the phononic crystal plate unit cell, it deserves further investigation about the properties of Willis plate. The generalized constitutive equations and the equation of equilibrium in Willis form for infinite medium are

$$\boldsymbol{\sigma} = C\boldsymbol{\varepsilon} + i\omega S\boldsymbol{u} \tag{3.76}$$

$$\mathrm{div}\boldsymbol{\sigma} + \rho\omega^2\boldsymbol{u} + i\omega S^{\dagger}\boldsymbol{\varepsilon} = 0 \tag{3.77}$$

Substitute the constitutive equation into the equation of equilibrium, we have (see the Appendix C)

$$c_{11}\frac{\partial^2 u_1}{\partial x_1^2} + c_{12}\frac{\partial^2 u_2}{\partial x_1 \partial x_2} + c_{13}\frac{\partial^2 u_3}{\partial x_1 \partial x_3} + c_{66}\left(\frac{\partial^2 u_2}{\partial x_1 \partial x_2} + \frac{\partial^2 u_1}{\partial x_2^2}\right) + c_{44}\left(\frac{\partial^2 u_3}{\partial x_1 \partial x_3} + \frac{\partial^2 u_1}{\partial x_3^2}\right) + \rho\omega^2 u_1 = 0 \tag{3.78}$$

$$c_{66}\left(\frac{\partial^2 u_2}{\partial x_1^2} + \frac{\partial^2 u_1}{\partial x_1 \partial x_2}\right) + c_{12}\frac{\partial^2 u_1}{\partial x_1 \partial x_2} + c_{11}\frac{\partial^2 u_2}{\partial x_2^2} + c_{13}\frac{\partial^2 u_3}{\partial x_2 \partial x_3} + c_{44}\left(\frac{\partial^2 u_3}{\partial x_2 \partial x_3} + \frac{\partial^2 u_2}{\partial x_3^2}\right) + \rho\omega^2 u_2 = 0 \tag{3.79}$$

$$c_{44}\left(\frac{\partial^2 u_3}{\partial x_1^2} + \frac{\partial^2 u_1}{\partial x_1 \partial x_3}\right) + c_{44}\left(\frac{\partial^2 u_2}{\partial x_2 \partial x_3} + \frac{\partial^2 u_3}{\partial x_2^2}\right) + c_{13}\frac{\partial^2 u_1}{\partial x_1 \partial x_3} + c_{13}\frac{\partial^2 u_2}{\partial x_2 \partial x_3} + c_{33}\frac{\partial^2 u_3}{\partial x_3^2} + \rho\omega^2 u_3 = 0 \tag{3.80}$$

From the above equation, one can find that the Willis term $S, S^{\dagger}$ do not affect the equation of motion for infinite medium. Thus, we consider the equation of motion for a finite plate with upper and lower boundary conditions in the following.

Let us consider the wave propagation in a plate along x_1 direction and assume that

$$\frac{\partial}{\partial x_2} = 0, k_2 = 0 \tag{3.81}$$

Assume the material is transversely isotropic, the general equations of motion are

$$-\rho\omega^2 u_1 = c_{11}\frac{\partial^2 u_1}{\partial x_1^2} + c_{44}\frac{\partial^2 u_1}{\partial x_3^2} + \left(c_{13} + c_{44}\right)\frac{\partial^2 u_3}{\partial x_1 \partial x_3} \tag{3.82}$$

$$-\rho\omega^2 u_2 = c_{66}\frac{\partial^2 u_2}{\partial x_1^2} + c_{44}\frac{\partial^2 u_2}{\partial x_3^2} \tag{3.83}$$

$$-\rho\omega^2 u_3 = c_{33}\frac{\partial^2 u_3}{\partial x_3^2} + c_{44}\frac{\partial^2 u_3}{\partial x_1^2} + (c_{13}+c_{44})\frac{\partial^2 u_1}{\partial x_1 \partial x_3} \tag{3.84}$$

Define $u_2(x_1,x_3) = A_2 e^{i(k_1 x_1 + k_3 x_3)}$ and substitute into eq. (3.83), we obtain

$$k_3^2 = \alpha^2 = \frac{\rho}{c_{44}}\omega^2 - \frac{c_{66}}{c_{44}}k_1^2 \tag{3.85}$$

So that u_2 can be re-written as

$$u_2(x_1,x_3) = (A_2 e^{ik_3 x_3} + B_2 e^{-ik_3 x_3}) e^{ik_1 x_1} \tag{3.86}$$

Now define $u_1(x_1,x_3) = A_1 e^{i(k_1 x_1 + k_3 x_3)}$ and $u_3(x_1,x_3) = A_3 e^{i(k_1 x_1 + k_3 x_3)}$, substitute into Eq. (3.82) and (3.84), then

$$\begin{pmatrix} \rho\omega^2 - c_{11}k_1^2 - c_{44}k_3^2 & -(c_{13}+c_{44})k_1 k_3 \\ -(c_{13}+c_{44})k_1 k_3 & \rho\omega^2 - c_{33}k_3^2 - c_{44}k_1^2 \end{pmatrix}\begin{pmatrix} A_1 \\ A_3 \end{pmatrix} = 0 \tag{3.87}$$

where

$$k_3^2 = \frac{-b \pm \sqrt{b^2 - 4c_{33}c_{44}\left(\rho\omega^2 - c_{11}k_1^2\right)\left(\rho\omega^2 - c_{44}k_1^2\right)}}{2c_{33}c_{44}} \tag{3.88}$$

$$b = -c_{33}\left(\rho\omega^2 - c_{11}k_1^2\right) - c_{44}\left(\rho\omega^2 - c_{44}k_1^2\right) - (c_{13}+c_{44})^2 k_1^2 \tag{3.89}$$

k_3^2 has two solutions, which can be defined as β^2 and γ^2. On the other hand, the relationship between A_1 and A_3 is

$$A_3 = f(k_3)A_1 = \frac{\rho\omega^2 - c_{11}k_1^2 - c_{44}k_3^2}{(c_{13}+c_{44})k_1 k_3} A_1 \tag{3.90}$$

where

$$k_3 = \pm\beta, \pm\gamma \tag{3.91}$$

The general form of u_1 and u_3 can be expressed as

$$u_1(x_1, x_3) = (A_1 e^{i\beta x_3} + B_1 e^{-i\beta x_3} + C_1 e^{i\gamma x_3} + D_1 e^{-i\gamma x_3}) e^{ik_1 x_1} \tag{3.92}$$

$$u_3(x_1, x_3) = (A_3 e^{i\beta x_3} + B_3 e^{-i\beta x_3} + C_3 e^{i\gamma x_3} + D_3 e^{-i\gamma x_3}) e^{ik_1 x_1} \tag{3.93}$$

with

$$A_3 = f_\beta(k_3 = \beta) A_1 \tag{3.94}$$

$$B_3 = f(k_3 = -\beta) B_1 = -f_\beta B_1 \tag{3.95}$$

$$C_3 = f_\gamma(k_3 = \gamma) C_1 \tag{3.96}$$

$$D_3 = f(k_3 = -\gamma) D_1 = -f_\gamma D_1 \tag{3.97}$$

Instead of exponential function, displacements can be transformed as trigonometric function, as

$$u_1(x_1, x_3) = \left((A_1 + B_1)\cos\beta x_3 + (C_1 + D_1)\cos\gamma x_3 + i(A_1 - B_1)\sin\beta x_3 + i(C_1 - D_1)\sin\gamma x_3\right) e^{ik_1 x_1} \tag{3.98}$$

$$u_2(x_1, x_3) = \left((A_2 + B_2)\cos\alpha x_3 + i(A_2 - B_2)\sin\alpha x_3\right) e^{ik_1 x_1} \tag{3.99}$$

$$u_3(x_1, x_3) = \left((A_3 + B_3)\cos\beta x_3 + (C_3 + D_3)\cos\gamma x_3 + i(A_3 - B_3)\sin\beta x_3 + i(C_3 - D_3)\sin\gamma x_3\right) e^{ik_1 x_1} \tag{3.100}$$

The above three displacements can be arranged into symmetric and anti-symmetric forms.

For symmetric form, we have

$$u_1(x_1, x_3) = \left((A_1 + B_1)\cos\beta x_3 + (C_1 + D_1)\cos\gamma x_3\right) e^{ik_1 x_1} = \left(A_1^{'}\cos\beta x_3 + C_1^{'}\cos\gamma x_3\right) e^{ik_1 x_1} \tag{3.101}$$

$$u_2(x_1, x_3) = ((A_2 + B_2)\cos\alpha x_3) e^{ik_1 x_1} = (A_2^{'}\cos\alpha x_3) e^{ik_1 x_1} \tag{3.102}$$

$$u_3(x_1, x_3) = \left(i(A_3 - B_3)\sin\beta x_3 + i(C_3 - D_3)\sin\gamma x_3\right) e^{ik_1 x_1} \tag{3.103}$$

also

$$u_3(x_1,x_3)=\left(if_\beta(A_1+B_1)\sin\beta x_3+if_\gamma(C_1+D_1)\sin\gamma x_3\right)e^{ik_1x_1}=\left(if_\beta A_1^{'}\sin\beta x_3+if_\gamma C_1^{'}\sin\gamma x_3\right)e^{ik_1x_1} \tag{3.104}$$

where

$$A_1^{'}=A_1+B_1, C_1^{'}=C_1+D_1, A_2^{'}=A_2+B_2 \tag{3.105}$$

For anti-symmetric form, we have

$$u_1(x_1,x_3)=\left(i(A_1-B_1)\sin\beta x_3+i(C_1-D_1)\sin\gamma x_3\right)e^{ik_1x_1}=\left(iB_1^{'}\sin\beta x_3+iD_1^{'}\sin\gamma x_3\right)e^{ik_1x_1} \tag{3.106}$$

$$u_2(x_1,x_3)=\left(i(A_2-B_2)\sin\alpha x_3\right)e^{ik_1x_1}=\left(iB_2^{'}\sin\alpha x_3\right)e^{ik_1x_1} \tag{3.107}$$

$$u_3(x_1,x_3)=\left((A_3+B_3)\cos\beta x_3+(C_3+D_3)\cos\gamma x_3\right)e^{ik_1x_1} \tag{3.108}$$

also

$$u_3(x_1,x_3)=\left(f_\beta(A_1-B_1)\cos\beta x_3+f_\gamma(C_1-D_1)\cos\gamma x_3\right)e^{ik_1x_1}=\left(f_\beta B_1^{'}\cos\beta x_3+f_\gamma D_1^{'}\cos\gamma x_3\right)e^{ik_1x_1} \tag{3.109}$$

The boundary conditions of the plate at $x_3=\pm h$ are

$$\sigma_{33}=c_{13}\frac{\partial u_1}{\partial x_1}+c_{33}\frac{\partial u_3}{\partial x_3}+i\omega\left(s_{31}u_1+s_{32}u_2+s_{33}u_3\right)=0 \tag{3.110}$$

$$\sigma_{23}=c_{44}\frac{\partial u_2}{\partial x_3}+i\omega\left(s_{41}u_1+s_{42}u_2+s_{43}u_3\right)=0 \tag{3.111}$$

$$\sigma_{13}=c_{44}\left(\frac{\partial u_3}{\partial x_1}+\frac{\partial u_1}{\partial x_3}\right)+i\omega\left(s_{51}u_1+s_{52}u_2+s_{53}u_3\right)=0 \tag{3.112}$$

Obviously, one can see that by introducing the boundary conditions, the Willis terms can affect those stresses in the above equations, which further results in a change in dispersion relation.

Substitute the symmetric displacements into boundary conditions,

$$\sigma_{33}\big|_{x_3=h}=Q_1^sA_1^{'}+Q_2^sA_2^{'}+Q_3^sC_1^{'}=0 \tag{3.113}$$

$$\sigma_{23}\Big|_{x_3=h}=Q_4^s A_1^{'}+Q_5^s A_2^{'}+Q_6^s C_1^{'}=0 \tag{3.114}$$

$$\sigma_{13}\Big|_{x_3=h}=Q_7^s A_1^{'}+Q_8^s A_2^{'}+Q_9^s C_1^{'}=0 \tag{3.115}$$

The eigen equation for symmetric mode is (see the Appendix D for details)

$$D^s=\begin{vmatrix} Q_1^s & Q_2^s & Q_3^s \\ Q_4^s & Q_5^s & Q_6^s \\ Q_7^s & Q_8^s & Q_9^s \end{vmatrix}=0 \tag{3.116}$$

D^s=0 is the eigen equation with ω and k_1. The zero values of the eigen equation gives the dispersion relationship $(\omega-k_1)$ of the symmetric mode of this Willis plate.

Substitute the anti-symmetric displacements into boundary conditions,

$$\sigma_{33}\Big|_{x_3=h}=Q_1^a B_1^{'}+Q_2^a B_2^{'}+Q_3^a D_1^{'}=0 \tag{3.117}$$

$$\sigma_{23}\Big|_{x_3=h}=Q_4^a B_1^{'}+Q_5^a B_2^{'}+Q_6^a D_1^{'}=0 \tag{3.118}$$

$$\sigma_{13}\Big|_{x_3=h}=Q_7^a B_1^{'}+Q_8^a B_2^{'}+Q_9^a D_1^{'}=0 \tag{3.119}$$

Similarly, the eigen equation for anti-symmetric mode is (see the Appendix D for details)

$$D^a=\begin{vmatrix} Q_1^a & Q_2^a & Q_3^a \\ Q_4^a & Q_5^a & Q_6^a \\ Q_7^a & Q_8^a & Q_9^a \end{vmatrix}=0 \tag{3.120}$$

The zero values of the eigen equation gives the dispersion relationship $(\omega-k_1)$ of the anti-symmetric mode of this Willis plate.

First for non Willis plate, such as a Silicon plate($c_{11}=16.6\times10^{10}\text{Nm}^{-2}$, $c_{12}=6.4\times10^{10}$ Nm^{-2}, $c_{44}=7.96\times10^{10}$ Nm^{-2}), we can get the dispersion curves from COMSOL (black dots)and compare with the ones which by solving $D^a=0, D^s=0$ (red dots from $D^s=0$, blue dots from $D^a=0$). As shown in Figure 3.19, the results of COMSOL simulations and analytical calculations are exactly the same.

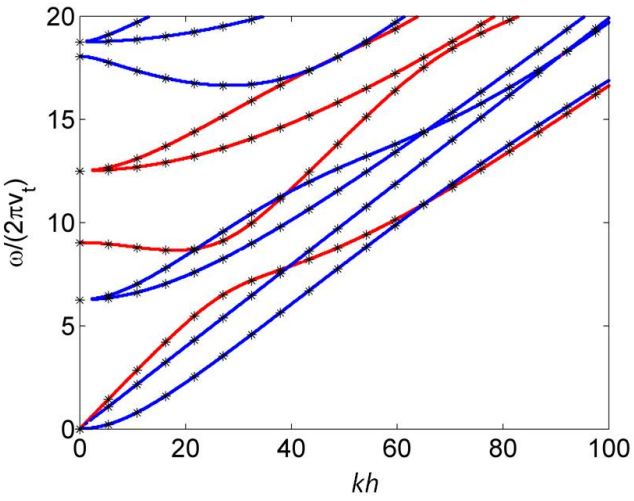

Figure 3.19 Dispersion of Silicon plate. Black dots are results computed by COMSOL; Blue and red lines are calculated by solving the eigen equations (3.116) and (3.120), respectively

As illustrated in the previous part, Willis medium can be realized by constructing a non-symmetric unit cell, especially a chiral structure. Now we assume that a Willis medium has a Willis term $S_{ijk}=S\varepsilon_{ijk}$, with ε_{ijk} as the Levi-Civita symbol. ε_{ijk} is 1 if (i, j, k) is an even permutation of (1, 2, 3), is -1 if it is an odd permutation, and is 0 if any index is repeated. If we define different Willis values in the eigen equations (3.116) and (3.120), the results shown in Fig. 3.20 demonstrate how Willis term affects the dispersion curves. When Willis term has a small value $s/c_{44}=i0.01\text{sm}^{-1}$, the dispersions almost keep the same. When Willis term increases from $s/c_{44}=i0.1$ sm^{-1} to $s/c_{44}=i0.7$ sm^{-1}, significant changes happen to the dispersion curves, as shown the evolution in Fig 3.20.

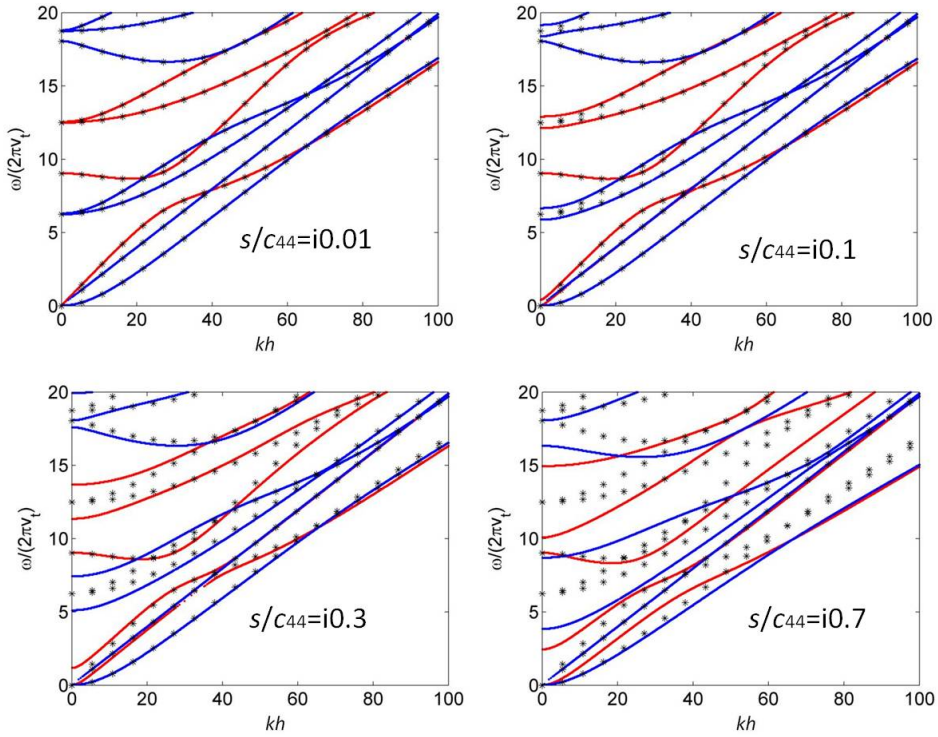

Figure 3.20 Dispersion comparisons for $s/c_{44}=i0.01$ sm^{-1} (upper left), $i0.1$ sm^{-1} (upper right), $i0.3$ sm^{-1} (lower left), $i0.7$ sm^{-1} (lower right). Black dots are dispersions of Silicon plate computed by COMSOL; Blue and red lines are calculated by solving the eigen equations (3.116) and (3.120) with Willis terms, respectively

3.6 Conclusion

In this chapter, we first showed that simultaneous control of the S_0 and A_0 Lamb modes by means of a graded index phononic crystal, combined with a properly designed thickness variation of the plate, is possible. This control has been done here by designing a GRIN flat lens and a Luneburg lens, and it has been shown a good performance of these devices when interacting with both S_0 polarized wave and A_0 one. These devices work properly in a broadband frequency region for the two modes, so that it is in this frequency region where most of the applications are expected. Other gradient index devices are easily envisioned, and its extension to the control of the *SH0* mode or other type of guided modes is also likely.

Secondly, we presented a method for the design of refractive devices working simultaneously for the three fundamental Lamb modes in thin plates. The method is based on the PWE homogenization of phononic crystal plates, studied here as finite slices of phononic crystals. A complex unit cell is employed to simultaneously control the refractive index of the three modes, together with thickness variations of the plate, the system has therefore enough degrees of freedom to independently tune the refractive indexes of the three modes. The performance of the method is demonstrated by means of the design of a flat gradient index (GRIN) lens and a circular Luneburg and Maxwell lens working simultaneously for the three modes. Also, a more advanced device is shown which consists in a circular lens working as a Luneburg lens for the S_0 and SH_0 polarizations and as a Maxwell lens for the A_0 one.

Then, we implemented this method to design beam splitters working simultaneously for all fundamental plate modes. These devices consist of circular lenses in which the refractive index is a function of the distance to the center of the lens, designed in such a way that a plane wave is deflected a given angle independently of its initial direction, therefore the device is omnidirectional. The inhomogeneous refractive index is implemented by means of graded phononic crystals, and the multimodal operation is achieved by a combination of a complex

unit cell and thickness variations of the plate. Numerical simulations are performed for a beam splitter of 60° of deflection angle, and it is shown that the device properly deflects the incoming wave independently of its initial polarization.

The performance of these gradient index devices is broadband, since it is designed in the framework of a homogenization theory in the quasi-static limit. The presented method can be efficiently employed to the design of devices for the control or harvesting of mechanical energy, since it allows the full control of vibrations excited in a finite elastic plate. Additionally, given the scalable nature of the presented method, this work can be applied to beam forming and energy harvesting in nano or micro scale.

In the last section, we showed that the PWE homogenization method for phononic crystals includes the so-called “Willis” term. Mathematically and numerically, it is further proved that “Willis” medium can be realized by breaking the symmetry in the unit cell. The “Willis” term does not affect the dispersion in bulk medium, but in finite plates. The dispersion properties of “Willis” plate are also derived and analytically studied. By gradually increasing the value of “Willis” term, we demonstrate how the plates’ dispersions change.

Chapter 4

Phononic Crystal Plates with Hollow Pillars

The content of this chapter was published in:

Yabin Jin, Nicolas Fernez, Yan, Pennec, Bernard Bonello, Rayisa P Moiseyenko, Stephane Hémon, Yongdong Pan, Bahram Djafari-Rouhani. *Tunable waveguide and cavity in a phononic crystal plate by controlling whispering-gallery modes in hollow pillars*. Physical Review B. 93 (5), 054109, 2016

Yabin Jin, Yan Pennec, Yongdong Pan, Bahram Djafari-Rouhani. *Phononic crystal plate with hollow pillars actively controlled by fluid filling*. Crystals. 6 (6), 64, 2016

Yabin Jin, Yan Pennec, Yongdong Pan, Bahram Djafari-Rouhani. *Phononic crystal plate with hollow pillars connected by thin bars*. Journal of Physics D: Applied Physics. 50(3),035301,2016

4.1 Introduction

Phononic crystals (PCs)[6, 7, 17, 18], or acoustic band gap materials, constituted of a periodic arrangement of inclusions embedded in a matrix, are receiving increasing attention for elastic/acoustic wave control and have found several fields of applications such as waveguiding[183, 184], filtering[185], acoustic lensing[96, 154, 186, 187], fluid sensing[188, 189]…. Beside the two dimensional infinite crystal and the control of bulk elastic waves, the interest of the phononic community has turned to the control of waves confined on the surface of a half infinite PC[190, 191] or propagating in finite PC plates. The latter geometry has been studied by considering either periodic inclusions[192, 193], in particular holes, in a slab or a periodic array of pillars on top of the plate[81, 82]. It has been shown that the pillar structure exhibits two types of band gaps resulting either from Bragg scattering when the wavelength is in the order of the lattice parameter (Bloch theorem[194]) or from local resonances of the pillars at large wavelength[81, 82, 195]. It can then be described respectively as a PC or as an acoustic metamaterial. In acoustic metamaterials[2, 196], the band gap known as low frequency or hybridization band gap originates from the avoided crossing of two bands in the low frequency range or sub-wavelength, where at least one of the two bands come from localized resonant modes of inclusions. The presence of local resonances can generate dynamic responded behaviors, negative effective mass density or elastic modulus, which do not exist in natural materials. Because of their novel properties, acoustic metamaterials become an active field of research with various potential applications, such as super-resolution and focusing[197-199], absorption[114, 200], and cloaking[107, 112, 201].

Because of this dual aspect, a great deal of works has been devoted to these structures, and different objectives have been pursued. Playing with the nature of the constitutive material, Oudich et al.[202] have shown the opening of very low resonant absolute band gaps in

a plate covered with one or two layers of stubs made of soft rubber. Assouar and Oudich[84] reported that by using double-sides stubbed phononic plates locally resonant band gap could be enlarged. Bilal and Hussein[85] designed pillars on a plate patterned by a periodic array of holes which can enhance the local resonance. Assour *et al*. studied hybrid phononic crystal plates composed of periodic stepped pillars and periodic holes which can also generate lower and wider acoustic gap because the acoustic waves are scattered by both of the pillars and holes[86]. Coffy *et al*. [87] designed a strip consisting of periodic pillars deposited on a tailed beam, enabling the generation of a ultra-wide band gap resulting from both Bragg scattering and local resonance. Midtvedt *et al*. [203] considered a graphene membrane that is deposited on top of a square lattice of cylindrical pillars to exhibit coupled localized modes with nonlinear dynamics. Changing the geometry of the pillar, Hsu[204] investigated numerically the propagation of Lamb waves through an array of stepped resonators on a thin slab. Experimentally, Achaoui et al.[205] reported on the propagation of surface guided waves in a periodic arrangement of pillars on a semi-infinite medium. Using Brillouin light scattering experiments, Graczykowski *et al*.[206] showed significant changes in the hypersonic phonon propagation due to the presence of local resonances in phononic crystal made of square lattice of holes and pillars in/on silicon membrane. The negative properties of the low frequency modes have also been considered[89, 90, 207, 208] for focalization applications. El Hassouani et al.[209] studied theoretically the simultaneous existence of phononic and photonic band gaps in a periodic array of silicon pillars deposited on a homogeneous thin silica plate for potential optomechanical applications. Finally, Davis et al.[45] introduced the concept of a locally resonant nanophononic metamaterial for thermoelectric energy conversion. Therefore, since the early papers in this topic[81, 82], pillar structures have become a useful platform for many fundamental and applied investigations in the frame of phononic crystals and acoustic metamaterials.

In the second section, we theoretically explore the existence and some functionalities of the pillar structure when the latter are constituted by hollow cylinders. Indeed, the hollow cylinders can display whispering gallery modes (WGM) whose quality factors can be greatly enhanced when the slab is separated from the hollow pillar by a second thin cylinder. Thus, the pillar is constituted by two layers and the WGM confined in the upper layer interacts very weakly with the modes propagating in the slab. Let us mention that whispering gallery modes date back to the works of Rayleigh[210] in the field of acoustics followed the observation in St. Paul's Cathedral. The recent interest in the literature is about high Q optical WGM resonators which can play a very significant role in photonics for applications in sensing[211] or photovoltaic[212]. Recent studies report the potentiality of these modes in the field of phononic crystal. Li et al[213] immersed an isolated tube in liquid medium and showed that WGMs can exhibit a narrow periodic transmission dip with a high quality factor while Kaproulias[214] considered the disk geometry for sensing application. The main recent interest in WGMs is related to the excitation of acoustic modes in optical WGM resonators via stimulated backward Brillouin scattering (SBS)[215, 216]. In this context, acoustic whispering gallery modes have been recently investigated in spherical and cylindrical resonators within the theory of elasticity[217]. The displacement fields of the modes studied in this work have similar shapes as the one reported in those previous papers, hence the denomination of whispering gallery modes we adopted here. As mentioned above, the novelty of the modes proposed here is to allow a strong degree of confinement inside the pillars and a high quality factor, hence allowing several applications related to the manipulation of the acoustic waves such as guiding and filtering, both in the range of the Bragg and low frequency gaps.

Additionally, hollow pillars on a plate give rise to the possibility of filling the hollow parts with a liquid, which creates new modes for the manipulation of acoustic waves, in particular allowing their active control by changing the height of the fluid or its temperature.

Jin *et al*.[218] and Popa *et al*. [219] reported that the acoustic properties of PCs and acoustic metamaterials can be actively tuned by piezoelectric structures. Wang et al.[220] used nonlinear pre-deformation to tune the band gap with local resonant structures. With infiltrated liquids in the hollow pillars, another actively controlled phononic crystal can be proposed since for instance the mass density and acoustic velocity of the liquids change with temperature, which will be shown in the third section.

In forth section, we investigate several novelties of a structure with hollow pillars on a membrane. First of all, we assume that the pillars are connected by thin bars instead of being deposited on a full plate. This produces both a significant widening and lowering of the Bragg gap as well as a decrease in the frequency of the low frequency gap. Then, the utilization of hollow pillars allows the occurrence of several new types of WGM with quadrupolar, hexapolar and octopolar symmetries falling in the band gap. Some of these modes can easily reach very high quality factors. Finally, new localized modes appear in the band gaps when the hollow pillars are filled with a liquid opening the way to sensing and filtering applications.

4.2 Control whispering-gallery modes in hollow pillars

4.2.1 Whispering-gallery modes

We consider a structure made of a square lattice of hollow pillars deposited on a thin homogeneous plate with a periodicity in the (*x, y*) plane. The *z*-axis direction is chosen perpendicular to the plate. The elementary unit cell is presented Fig.4.1 in which the geometrical parameters are the lattice constant *a*, the height *h* of the hollow pillars and the thickness *e* of the plate. *r* and r_i correspond respectively to the outer and inner radius of the hollow pillar. The complete structure is made of silicon, assuming a cubic symmetry with the crystallographic axes oriented along the coordinate axes *x*, *y* and *z*. The elastic constants are c_{11} = 166 GPa, c_{12} = 64 GPa and c_{44} = 79.6 GPa, and the mass density is ρ = 2330 kg/m^3.

All dispersion and transmission curves have been computed using the finite element code COMSOL Multiphysics®. Periodic boundary conditions are applied on each side of the unit cell, in the (*x*, *y*) plane. The dispersion and transmission curves will be presented as a function of the reduced frequency, $\omega a/2\pi v_t$ where v_t = 4678 m/s is the transverse bulk velocity of silicon along *x*.

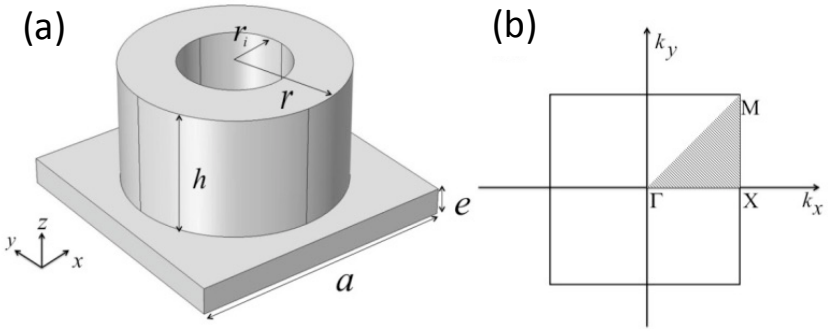

Figure 4.1 (a) 3D-schematic view of the elementary unit cell constituting the phononic crystal (PC) made of finite hollow pillars deposited on a thin homogeneous plate. The lattice constant is *a* and the thickness of the plate is *e*. The hollow pillar has a height *h* and an inner and outer radius respectively denoted r_i and *r*. (b) Periodic boundary conditions are applied in the (x, y) plane on each side of the unit cell, constituting a periodic crystal with a square array symmetry for which the first Brillouin zone and its irreducible part is presented

Before presenting the results for the hollow pillars on plate, we have calculated as a reference the band structure of the native phononic crystal containing filled cylinders of silicon ($r_i = 0$). The choice of the geometrical parameters is done in order to obtain two wide absolute band gaps, one at the Bragg frequency regime and the second in the low frequency range[81]. In figure 4.2(a), we present the dispersion curves calculated along the direction ΓX of the Brillouin zone with $e/a = 0.1$, $h/a = 0.55$ and $r/a = 0.42$. With this set of parameters, we obtain two wide absolute band gaps around the respective reduced frequency 0.2 (red area) and 0.6 (blue area). The low frequency band gap is due to local resonances of the pillars at a wavelength almost 10 times larger than the lattice constant a. The Bragg gap comes from the periodicity of the crystal and the collective scattering effects between the pillars. These reduced geometrical parameters (e/a, h/a, and r/a) will be kept fixed in the rest of the paper.

Figure 4.2 shows the evolution of the dispersion curves as a function of the inner radius. The introduction of the hollow cylinders gives rise to two new dispersion branches labeled '1' and '2' that do not exist in the native phononic crystal. By increasing r_i/a from 0 to 0.35 they move towards lower frequencies.

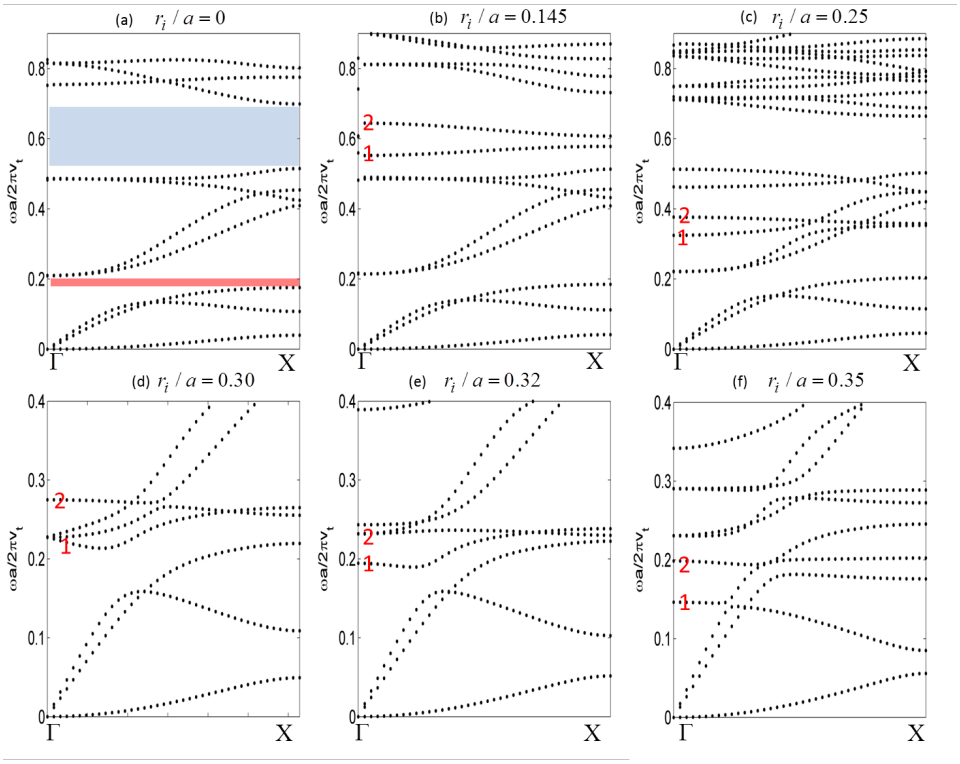

Figure 4.2 Dispersion curves of the hollow pillars on a thin silicon plate in the ΓX direction of the first irreducible Brillouin zone in two reduced frequency ranges ([0; 0.9] for (a, b, c) and [0; 0.4] for (d, e, f)) with different inner radii (a) r_i/a = 0, (b) r_i/a = 0.145, (c) r_i/a =0.25, (d) r_i/a = 0.30, (e) r_i/a = 0.32, (f) r_i/a = 0.35. The thickness of the plate is e/a = 0.1, the outer radius r/a = 0.4 and the height h/a = 0.45. The hatched areas correspond to the low (red) and Bragg (blue) absolute band gaps of the native crystal. The '1' and '2' branches come from the hollow pillar structure

At r_i/a = 0.145 (figure 4.2(b)) the two branches appear inside the Bragg gap while the gap boundaries and the branches below are almost unaffected. When increasing r_i/a to 0.25 (figure 4.2(c)), the two branches cross the lower edge of the Bragg gap and the branch labeled 1 interacts with the Lamb waves situated just below the reduced frequency 0.40. For higher values of r_i/a, the two branches still move downwards while new modes progressively appear at higher frequencies. At higher r_i/a (not shown) the Bragg gap gets closed. For r_i/a = 0.30 to 0.35, the frequencies of the two branches continue decreasing and cross the low frequency gap. However, at these low frequencies, the modes interact with the Lamb waves of the plate and do not give rise to isolated branches as it was the case in the Bragg gap. We shall see in the next section how to make them flat by a better confinement of the modes and therefore make the structure useful for both phononic crystal and acoustic metamaterial applications.

Despite the fact that these branches are slightly dispersive due to their interaction with the Lamb waves in the plate, they still remain nearly flat (i.e. with a small group velocity) and one can recognize that they are essentially WGM modes of the hollow cylinders as shown in the displacement field maps of Figure 4.3(a) corresponding to r_i/a = 0.145. For such modes, the acoustic path around the hollow pillar should be a multiple integer of the wavelength, here equal to 2 for both modes. Figure 4.3(b) represents a top view of the component U_z of the displacement field. It brings to light the main difference between the two modes that explain the existence of two separates frequencies. While mode '2' is almost totally confined inside the hollow pillar, mode '1' strongly interact with the four 'first neighbors' hollow cylinders of the unit cell via the plate.

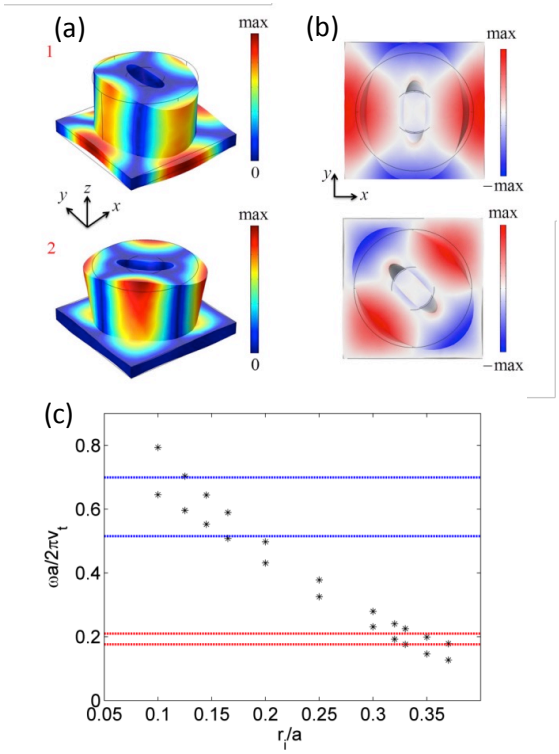

Figure 4.3 (a) Representation of the displacement field distribution and the deformation of the unit cell at the frequency of the Whispering Gallery Mode (WGM) '1' and mode '2' at the Γ point for r_i/a = 0.145. (b) Top view representation of the component U_z of the displacement field for the two modes. (c) Evolution of the frequency of mode '1' and '2' as a function of the inner radius r_i of the hollow pillar. The blue (resp. red) dashed lines represent the boundaries limits of the Bragg (resp. low frequency) band gap

Although the modes studied here have a quadrupolar shape, we have also identified higher frequency modes with hexapolar or octopolar symmetries that fall outside the range of the band gap. Let us mention that modes of dipolar or quadrupolar symmetries have also been studied in other context of acoustic metamaterials[221, 222]. We have also compared the frequencies and shapes of our WGM's with those obtained when the pillars are almost isolated from each other, namely by assuming a period which is 10 times higher than in the above calculations. It is found that the results are insensitive to the pillar separation, not only for quadrupolar but also for higher hexapolar or octopolar modes. Of course the resonance frequencies will change if the membrane at the bottom of the pillar is removed because depending on the WGM, its displacement field is more or less affected by the presence of the membrane.

Figure 4.3(c) summarizes the behavior of the two WGM's as a function of the inner radius of the hollow pillar. Both the WGM's frequencies decrease as the inner radius increases. This behavior can be understood if noticing that higher values of the average radius $\langle r \rangle = (r+r_i)/2$ increases the acoustic path along the perimeter $2\pi\langle r \rangle$ of the cylinder. As a result, when $r_i/a = 0.145$ (resp. 0.35), the whispering eigenmodes '1' and '2' fall in the middle of the Bragg (resp. low frequency) gap.

In order to show the filtering capacity of the structure based on WGM's, we calculate the transmission spectrum through a finite PC plate containing 5 rows of hollow pillars. Perfect matching layers (PML) are applied at the entrance and the exit of the slab to avoid any reflections from the external edges. Periodic boundaries conditions are applied along *y*-direction, on each side of the unit cell. The incident wave is the A_0 Lamb wave of the plate, propagating along the *x*-axis, and launched by applying a harmonic displacement U_z in the (*y*, *z*) plane in front of the crystal. To determine the transmission coefficient, the displacement

field is recorded in the far field behind the PC, and then normalized to the displacement field propagating in the homogeneous plate.

As stated above, the choice of r_i/a = 0.145 appears as the best because of the frequencies of the WGM's being in the center of the Bragg gap. We represent in figure 4.4 the transmission coefficient as a function of frequency, together with the dispersion curves. One can notice a relatively narrow transmission peak associated with WGM '1' while WGM '2' does not transmit. This result can be understood on the basis of symmetry consideration. Indeed, the incident wave A_0 is symmetric with respect to the symmetry plane (x, z). Thus, it can only excite WGM '1' which has the same symmetry and not WGM '2' which is antisymmetric with respect to this plane. Then, the latter appears as a deaf band[223, 224] in the transmission spectrum.

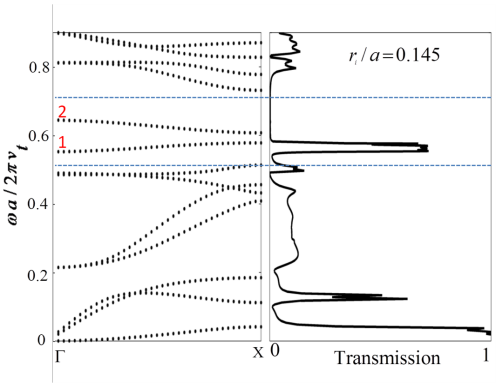

Figure 4.4 Dispersion curve (left) and transmission spectrum of the antisymmetric Lamb wave (right) through the hollow cylinder phononic crystal with inner radius r_i/a = 0.145. The blue dashed lines represent the boundaries of the Bragg gap

4.2.2 Whispering modes with high quality factor and narrow band filtering

In the previous section, we have shown that WGMs can be used as a tunable band filter in the Bragg and low frequency band gaps of the phononic crystal. In this section, we shall show how the quality factor of the WGM-based transmitted wave can be significantly increased. Indeed, the width of the transmission peak, or accordingly the width of the narrow band associated with WGM '1' in Fig. 4.4, are related to its interaction with the Lamb waves of the

plate as can be seen from the maps of the displacement field (Fig. 4.3). To enhance the confinement of the WGM without changing significantly the associated field, we insert a silicon solid cylinder of height *l* at the basis of the hollow pillar (see the red block in the inset of Fig. 4.5(a)).

We show in Fig. 4.5(b) the dispersion curves in the range [0.4; 0.8] as a function of the reduced height *l/h* of the added cylinder when *h/a* = 0.45. We can observe that the two branches associated to the WGM's become more and more flat as *l/h* increases, which is the signature of a better confinement of the modes inside the unit cell. To quantify the role of the added cylinder on the pass band, we have calculated the quality factor $Q = f / \Delta f$ where f is the central frequency of the pass band and Δf the full width at half maximum of the transmission peak. Figure 4.5(a) shows a significant increase in the quality factor with increasing the reduced height *l/h*. For *l/h* = 0.64, the quality factor reaches Q = 280, i.e. more than 10 times the value obtained without the additional cylinder, paving the way to a high resolved narrow pass band device for filtering applications.

Increasing now the inner radius to *ri/a* = 0.35 we shift the two WGMs in the vicinity of the low frequency band gap. As previously, we insert the silicon solid cylinder of height *l* at the basis of the hollow pillar. The Fig. 4.5(c) represents the dispersion curve in the low frequency regime for *l/a* = 0; 0.22 and 0.44. One can see that, when *l/h* increases, the interaction of the branches '1' and '2' with the Lamb modes decreases, reaching finally to a localization of the two WGMs in the middle of the narrow low frequency band gap when *l/h* = 0.54.

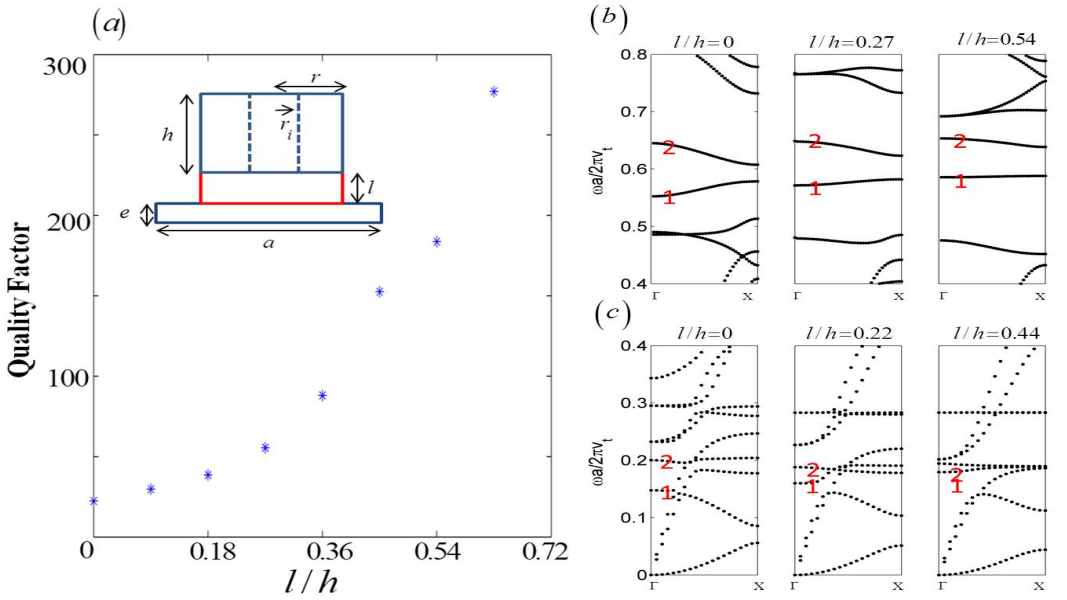

Figure 4.5 (a) (Inset) Schematic cross section of the unit cell with the added full silicon cylinder of height *l* (red block) with *h/a*=0.45, *e/a*=0.1 and *r/a*=0.4. (Graph) Evolution of the quality factor of the narrow pass band based on the WGM '1' as a function of *l/a*, (r_i/a = 0.145). (b) Dispersion curves magnified in the Bragg gap range ([0.4; 0.8]) for different value of *l/a*. (c) Dispersion curves magnified in the low frequency gap range ([0; 0.4]) for different value of *l/a*

4.2.3 Multiplexing devices based on tunable waveguides and cavities

As reported in Fig. 4.3(c), the position of the narrow pass band is very sensitive to the inner radius of the hollow pillar. Actually, the narrow pass band can cover the full Bragg gap (i.e. the reduced frequency range [0.55, 0.7]) when r_i/a is varied from 0.145 to 0.155. For a mixed system composed of different inner radii, different narrow pass bands inside the Bragg gap are expected. We propose to use this property for the design of a new kind of mono and multichannel wavelength division multiplexers by inserting appropriate waveguides and cavities in a PC slab. A similar property was earlier proposed in a 2D phononic crystal constituted by hollow cylinders filled with different liquids[40]. For the sake of computational convenience, the height of the added cylinder is fixed to l/a = 0.2 (l/h = 0.36) in the following calculations, leading to a Q factor of 100.

A. Multichannel wavelength multiplexer

We first consider (inset of Fig. 4.6(a)) a (5×5) supercell with periodic conditions along *y*-axis and PML in the direction of propagation *x*. The phononic plate contains two linear waveguides separated from each other by one row of filled cylinders to prevent significant leakage between the guides. The waveguides are constituted by two rows of hollow pillars with the radius $r_i^{(a)}/a = 0.145$ and $r_i^{(b)}/a = 0.160$ for the waveguides 'a' and 'b' respectively. We probe the transmission of the waveguides by launching the A_0 Lamb wave in front of the PC. The transmission spectrum, displayed in Fig. 4.6(a), features two narrow pass bands occurring at the reduced frequencies 0.543 and 0.581, inside the band gap. These values significantly differ from those obtained with the perfect hollow pillar phononic plate (Fig. 4.3(c)). This means that the effect of confinement inside the waveguide on the transmission peak is far from being negligible while the narrowness of the pass bands is preserved. As seen in the displacement field distributions of Fig. 4.6(b), the two narrow pass bands correspond respectively to the transmitted wave through the waveguide '*a*' and '*b*'. We then have created a multichannel wavelength multiplexer.

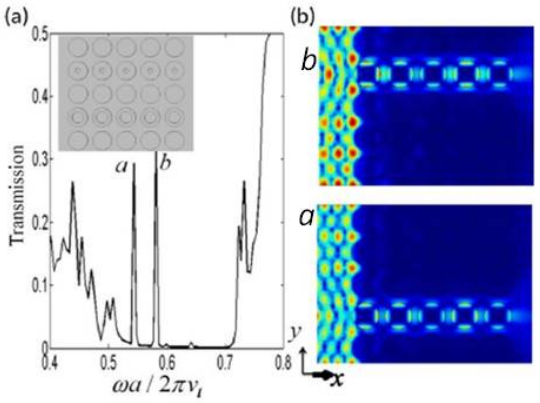

Figure 4.6 (a) (Inset) Schematic representation of the multichannel wavelength multiplexer. (Graph) Transmission spectrum of the antisymmetric Lamb wave when the radius of the hollow pillars inside waveguide '*a*' and '*b*' are $r_i^{(a)}/a = 0.145$ and $r_i^{(b)}/a = 0.160$. (b) Displacement field distributions at the frequency of the two narrow pass bands '*a*' and '*b*'

B. Monochannel wavelength multiplexer

Next, we consider the propagation at the frequencies of two narrow passbands through one single waveguide composed of alternating hollow cylinders with two different radii (see inset in Fig. 4.7(a)) of $r_i^{(c)}/a$ = 0.145 and $r_i^{(d)}/a$ = 0.140. The transmission spectrum is presented Fig 4.7(a) in which one can see the occurrence of two narrow passbands at the reduced frequencies $f^{(c)}$ = 0.571 and $f^{(d)}$ = 0.590. This means that it becomes possible to transport two different wavelengths through the same channel. The elastic wave transmission comes from evanescent waves inside the slab, which in turn allows for the overlapping of the elastic fields between two next nearest neighbors hollow pillars with identical radii. The waveguide then allows for the tunneling, and therefore to the propagation of the elastic wave. Figure 4.7(b) sketches the displacement field at the frequencies $f^{(c)}$ and $f^{(d)}$ where the enhancement of the fields inside the hollow pillars is clearly observable for both radii.

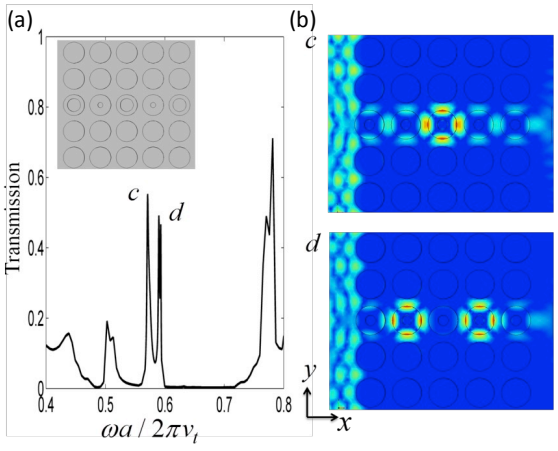

Figure 4.7 (a) (Inset) Schematic representation of the monochanel wavelength multiplexer. (Graph) Transmission spectrum of the antisymmetric Lamb wave when consecutive hollow pillars inside the waveguide have radii of $r_i^{(c)}/a$ = 0.145 and $r_i^{(d)}/a$ = 0.140. (b) Displacement field distributions at the frequency of the two narrow pass bands '*c*' and '*d*'

C. Compact multiplexer based on linear cavity

Another way to obtain high-Q resonators is to create an infinite linear cavity oriented perpendicularly to the direction of propagation. The inset of Fig. 4.8(b) shows the unit cell of

a periodic structure which contains two lines of hollow pillars surrounded from each side by one line of solid cylinders. The unit cell has a finite size along *x*-axis and periodic in the *y*-direction. The cavity is constituted by two different hollow pillars with respective radii $r_i/a^{(e)}$ = 0.145 and $r_i/a^{(f)}$ = 0.140. The transmission of the antisymmetric Lamb wave launched in the *x*-direction and presented in Fig. 4.8(a), shows that the structure supports two narrow pass bands at $f^{(e)}$ = 0.561 and $f^{(f)}$ = 0.578 respectively (Fig. 4.8(b)). Note that the confinement of the elastic energy is achieved by using only one PC layer embedding the cavity region, and leading to an extremely compact multiplexer filter with high *Q* factor.

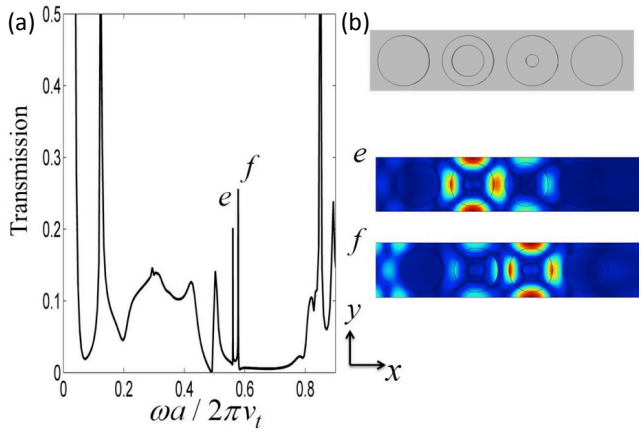

Figure 4.8 (a) Transmission spectrum of the antisymmetric Lamb wave when the radius of the hollow pillars inside waveguide are $r_i^{(e)}/a$ = 0.145 and $r_i^{(f)}/a$ = 0.140. (b) (Inset) Schematic representation of the compact wavelength cavity multiplexer. (Graph) Displacement field distributions at the frequency of the two narrow pass bands '*e*' and '*f*'

4.2.4 Sub-wavelength waveguide

This last section deals with an application of the WGMs inside the low frequency band gap. As established previously, the two modes can be localized inside the narrow low frequency band gap as far as we chose a large inner radius (r_i/a = 0.35). The second condition is to add a solid silicon cylinder of thickness l/h = 0.49 between the hollow pillar and the plate to get the dispersion branches almost flat. Under these conditions and the set of others geometrical parameters h/a = 0.45, r/a = 0.4, and e/a = 0.1, we have obtained the dispersion

curve of the perfect phononic crystal made of hollow pillars on plate presented Fig. 4.9(a). We then built the design of the sub-wavelength waveguide by replacing one row of the perfect phononic crystal with hollow pillars. The transmission spectrum of the anti-symmetric Lamb wave depicted Fig. 4.9(b) shows the transmission of a very narrow peak at the reduced frequency 0.19. As seen Fig 4.9(c), the transmission comes from the excitation of the WGM '1' on top of the hollow cylinders.

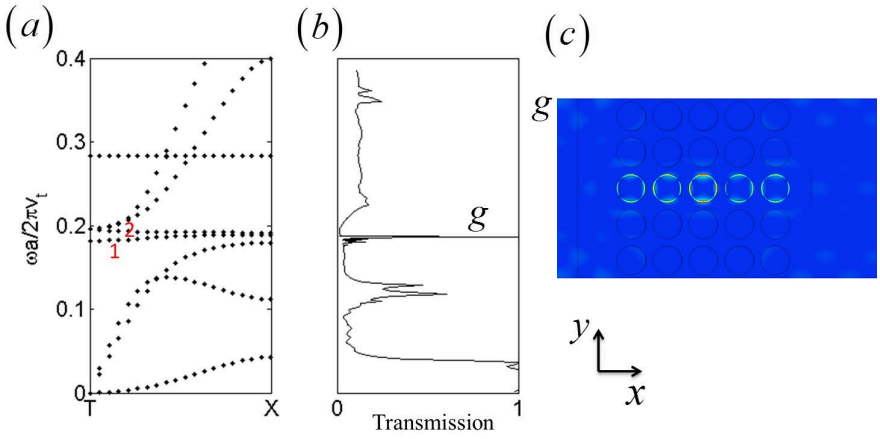

Figure 4.9 (a) Dispersion curve in the low frequency range [0; 0.4] corresponding to the perfect phononic crystal made of hollow pillars on plate with the set of geometrical parameters r_i/a = 0.35, l/h = 0.49, h/a = 0.45, r/a = 0.4, and e/a = 0.1. (b) Transmission spectrum of the antisymmetric Lamb wave through the waveguide of hollow pillars inserted inside a full silicon pillar crystal. (b) Displacement field distributions at the reduced frequency 0.19 corresponding to the narrow pass bands '*g*'

4.3 Localized modes actively controlled by fluid filling

4.3.1Further properties of whispering-gallery modes

A PC of a square lattice with a periodicity a in the (x, y) plane is considered which consists of a periodic array of hollow pillars deposited on a thin plate (Fig. 4.10a). A full cylinder separates the hollow part from the plate in order to increase the confinement of the studied modes. The scheme in Fig. 4.10a shows the geometrical parameters, namely the lattice constant a, the thickness of the plate e, the height of confinement l, the height of the hollow pillar h, its inner radius r_i and outer radius r. The entire structure is made of cubic silicon, with the elastic constants c_{11} = 166 GPa, c_{12} = 64 GPa, c_{44} = 79.6 GPa, the mass density ρ=2330 kg m^{-3}. The crystallographic axis [100] and [010] have been chosen respectively parallel to the phononic crystal axis x and y. In the (x, y) plane, periodic boundary conditions are applied on each side of the unit cell. Dispersion and transmission curves are calculated by the finite element code COMSOL Multiphysics® and presented as a function of the reduced frequency $\omega a/2\pi v_t$ where v_t =Sqrt ($0.5\times(c_{11}- c_{12})/\rho$) is the transverse velocity of sound in silicon along the [110] direction in the (001) plane.

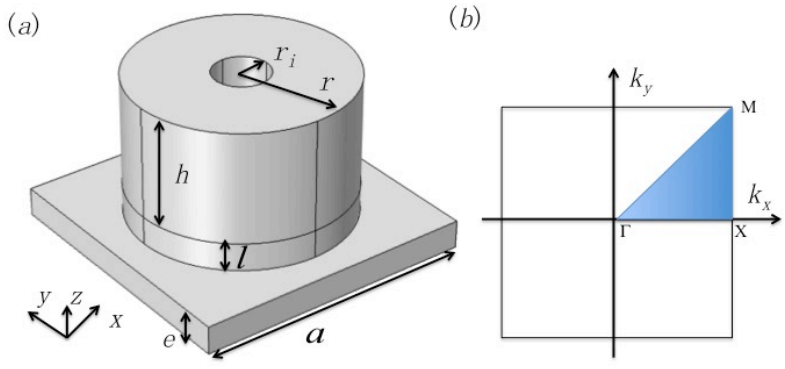

Figure 4.10 (a) Schematic view of PC unit cell in the square array consisting of hollow pillars deposited on a thin homogeneous plate with an additional cylinder of height *l* at the basis to improve the confinement of the modes in the hollow pillars. *a* is the lattice constant, *e* is the thickness of plate, *h* is the height of hollow pillar, r_i and *r* are the inner and outer radius of the hollow pillar, respectively. (b) The irreducible first Brillouin zone of the square lattice

With an appropriate choice of the geometrical parameters (r/a=0.4, h/a=0.45, e/a=0.1), the native PC with full pillars deposited on a thin plate can exhibit two absolute band gaps, one at the Bragg frequency regime and the other at low frequency regime [81]. By introducing an inner hole in the pillar, two new branches of WGMs with quadrupolar shape occur in the dispersion curves that do not appear in the native PC; their fields are localized in the upper part of the pillars, around the hollow. The quality factor of the WGMs can be further increased by adding a full cylinder between the hollow pillar and the plate, so that the elastic energy is better confined in the hollow pillar part [39]. This new structure was first studied in the previous section. In this section we give some additional results.

In Fig. 4.11, we present more detailed properties of the WGMs. In the left panel, the black dotted lines are dispersion curves calculated along the ΓX and ΓM directions of the first Brillouin zone with geometric parameters r_i/a=0.145, r/a=0.4, h/a=0.45, e/a=0.1, l/a=0.2. With this set of parameters, the Bragg and low frequency band gaps still appear along ΓX direction while it only remains a Bragg band gap along ΓM direction. In the Bragg band gap, two branches of WGMs occur, marked as branch '1' and '2'. Two transmission spectra along each direction are associated with two different incident waves, namely the fundamental anti-symmetric A_0 Lamb (blue curve) and the symmetric S_0 (red curve) Lamb waves. Although some mode conversion can occur at the exit of PnC, the transmitted wave keeps essentially its original character. Only WGM1 gives rise to a narrow transmitted pass band in both ΓX and ΓM directions, more significantly with anti-symmetric Lamb wave excitation, marked as peak '*A*' and '*B*'. In the right panel of Fig.4.11, we show the displacement fields of the dominant Uz component (displacement along *z* axis) for peak '*A*' and '*B*'. The excitation inside the PC is symmetric with respect to an *xz* plane, perpendicular to the pillars and parallel to the propagation direction. This is in accordance with the symmetry of the incident wave (either A_0 or S_0) with respect to such a plane. In contrast, to obtain a transmission at the frequency of

WGM2, it would be necessary to have an incident wave which has an antisymmetric profile with respect to this plane, which means -/+ force in the unit cell along the *y* direction. To explain the higher transmission of WGM1 with the A_0 rather than S_0 incident wave, it should be noticed that the *x* and *y* components of its displacement field are mainly localized in the upper part of the pillar, around the hollow part, while the *z* component extends down to the bottom of the pillar and is therefore sensitive to a vertical motion in the membrane. However, in some other frequency ranges such as [0.2; 0.4], the transmission is much higher with S_0 rather than A_0 excitation.

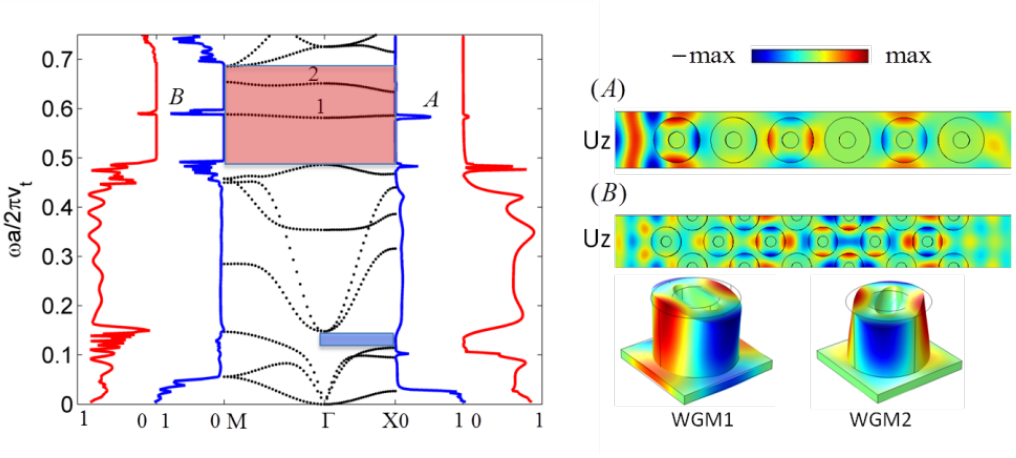

Figure 4.11 Left panel: Dispersion curves of the confined hollow pillars on a thin silicon plate in the ΓX and ΓM directions of the first irreducible Brillouin zone in the reduced frequency range [0; 0.75]. On each side of the dispersion curves we give the corresponding transmission spectra in blue and red respectively for which the incident wave is either anti-symmetric A_0 or symmetric S_0. The Bragg and low frequency band gaps are marked as red and blue rectangular hatched regions, respectively. The geometric parameters are chosen as r_i/a=0.145, r/a=0.4, h/a=0.45, e/a=0.1, l/a=0.2; Right panel: Uz component of the displacement fields with the anti-symmetric A_0 Lamb wave excitation at transmission peak *A* along ΓX direction and peak *B* along ΓM direction; Uz component of the displacement fields of WGM1 and WGM2 at Γ point

Figure 4.12 left panel presents the evolution of the two WGMs as a function of the inner radius of the hollow pillar. Both WGMs' frequencies decrease when increasing the inner radius. Indeed, it is noteworthy that a higher value of the average radius $\langle r \rangle = (r + r_i) / 2$ of the shell around the hollow increases the acoustic path along the perimeter $2\pi\langle r \rangle$ of the cylinder. As a result, when r_i/a = 0.145 (resp. 0.35), the WGM '1' and '2' fall in the middle of the Bragg (resp. low frequency) gap[39]. We also calculate the corresponding quality factor for

the WGM 1, $Q = f/\Delta f$, where f is the central frequency of the pass band and Δf is the full width at half maximum of the transmission peak. The right panel of Fig. 4.12 shows a significant increase in the quality factor when increasing the reduced-height l/a of the pillar basis. For l/a = 0.35, the quality factor is Q = 280, which is more than 10 times the value obtained without the additional cylinder, paving the way to a high resolved narrow pass band device for filtering applications[39].

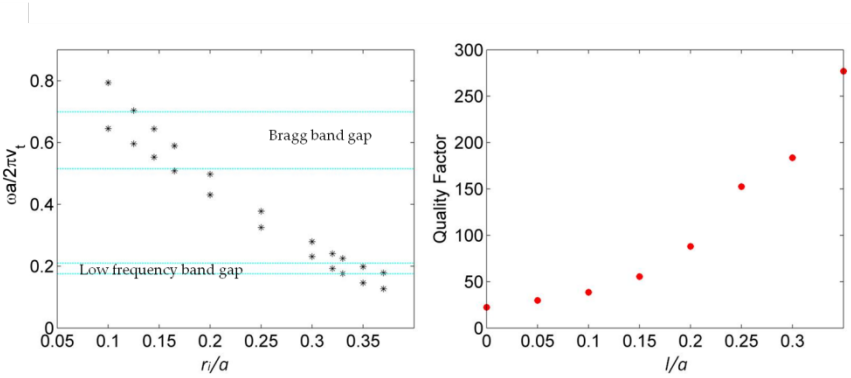

Figure 4.12 Left panel: the frequency evolution of the WGM 1 and 2 as a function of the inner radius of the hollow pillar. The upper frequency range limited by two horizontal cyan lines is the Bragg band gap of background full PnCs (*h/a*=0.45, *r/a*=0.4, *l/a*=0) and the lower one is the low frequency band gap. Right panel: The quality factor of the WGM 1 grows when increasing the confinement height *l/a*

The WGMs with high quality factors are applied to different kinds of multiplexers, based on monochannel or multichannel waveguides or cavity. In Fig.4.13, we show a multichannel waveguide consisting of waveguide i with inner radius r_i/a=0.12 and waveguide j with inner radius r_j/a=0.11. The transmission peaks for waveguide i and j are located at reduced frequency 0.654 and 0.678, respectively. Besides, an efficient sub-wavelength waveguide is also demonstrated as the WGMs can be tuned in the low frequency band gap[39].

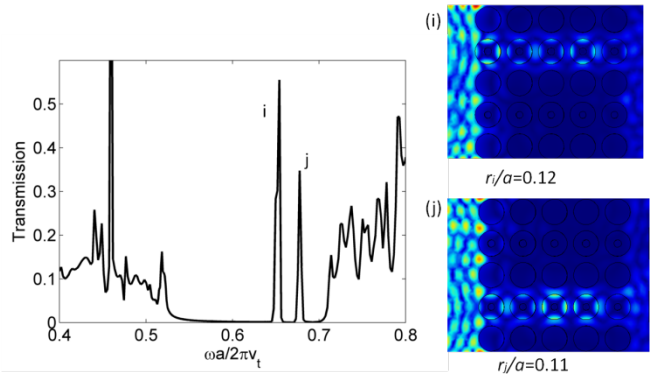

Figure 4.13 The multichannel wavelength multiplexer: Left panel: Transmission spectrum of the antisymmetric Lamb wave when the inner radius inside waveguides *i* and *j* are r_i/a =0.12 and r_j/a =0.11; Right panel: Displacement field distributions at the frequency of the two narrow pass bands *i* and *j*. The geometric parameters of the multiplexer are *h/a*=0.45, *r/a*=0.4, *l/a*=0.2, *e*/*a*=0.1

4.3.2 Active control of the WGMs and new localized modes

The objective of this section is to discuss how the filling of the holes with a liquid can affect or tune the WGMs and more interestingly gives rise to the occurrence of new localized modes in the band gap which are much sensitive to the presence of the fluid. The latter can be tuned with the physical and geometrical properties of the fluid, in particular its height. To avoid capillary or surface tension effects, it would be more adapted to work with holes of sub-millimeter size in the MHz regime. However, it should be pointed out that filling of few tens nm size holes in hypersonic PC has been performed by micro-fluid ejection technique and their phonon dispersion curves measured by Brillouin light scattering experiments (see for instance ref. [225, 226]).

In Fig. 4.14, we show the dispersion curves of the phononic crystal when the holes are filled with water for a few values of the inner radius r_i. For water, the mass density is ρ =998 kg m^{-3} and speed of sound is c = 1490ms^{-1}. Let us start with the inner radius r_i/a=0.17. The modes labeled 1 and 2 are the quadrupolar WGMs discussed in the previous section. However, the filling of the holes with water has the effect of giving rise to two new sets of localized modes in the band gap. One set, labeled M_{c1} and M_{c2}, corresponds to compressional vibrations inside the liquid column almost independently of the solid; they will be discussed in detail in

next part. The other set called M_{liq} is a doubly degenerate new mode which is essentially associated to the presence of the liquid and appears in the band gap under some conditions on the geometrical parameters. The strongest vibration of this mode occurs in the liquid where the displacement field is one order of magnitude higher than in the solid part. When decreasing the inner radius r_i/a of the pillars from 0.17 to 0.11 (Fig. 4.14), the WGM1,2 as well as M_{liq} see their frequency increasing and going outside the band gap, while the frequencies of M_{c1} and M_{c2} remain unchanged because they are dictated by the height of the fluid.

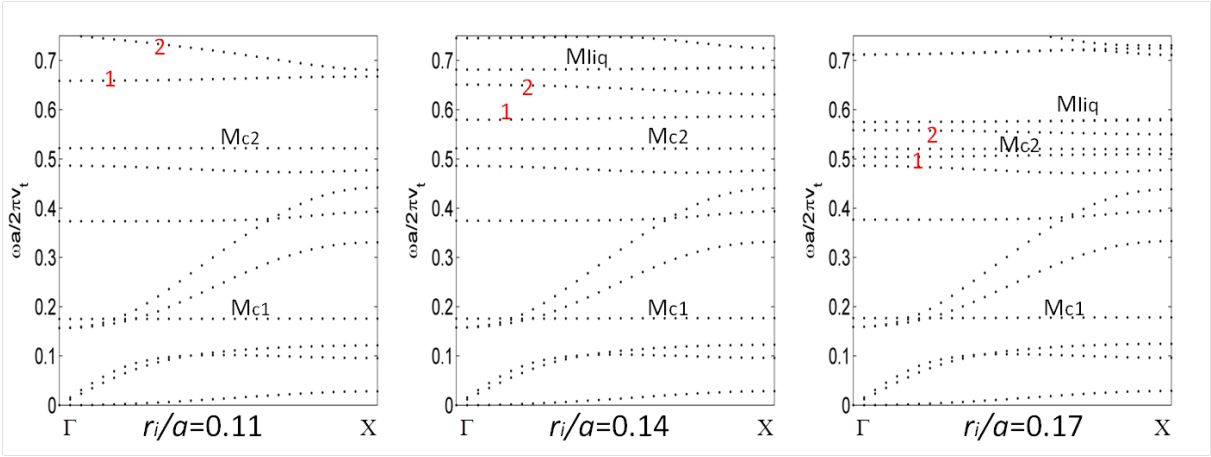

Figure 4.14 Dispersion curves of the hollow pillars on a thin silicon plate in the ΓX direction with different inner radii (left) r_i/a=0.11, (middle) r_i/a=0.14, (right) r_i/a=0.17. The other geometric parameters are h/a=0.45, r/a=0.4, l/a=0.2, e/a=0.1

As a complementary view, we show in upper panel of Fig. 4.15, how the localized modes, namely WGM1,2, $M_{c1,2}$ and M_{liq}, behave when changing either the inner radius of the hollow pillars or the height h_w of the fluid filling the hollow part of the pillar of total height h. In the upper-left panel, one can see in accordance with Fig.4.14 that with an increasing inner radius, WGM1,2 and M_{liq} decrease to lower frequencies, passing out of the Bragg band gap of the full PC (h/a=0.45, r/a=0.4, l/a=0). On the other hand, M_{c2} is practically insensitive to the inner radii, as the compressional mode in the liquid is only related to the height of the liquid (see discussion in next part). In the upper-right panel of Fig. 4.15, we present the evolution of

those localized modes as a function of the height h_w of water filling the pillar of total height h when the inner radius is $r_i/a = 0.19$. The liquid compressional modes $M_{c1,2}$ are very sensitive to h_w whereas the M_{liq} decreases through the Bragg band gap when h_w/h increases from 0.3 to 1. The latter mode can be then a good candidate to be tuned gradually by changing the height of water. The vibration of this mode is presented in the lower panel of Fig. 4.15, both in the solid and liquid part. One can see that the elastic and acoustic fields are mainly oriented along the diagonal direction of the square lattice. The vibration in the solid is mostly localized at the top of the pillar although there are still some displacements left in the plate. In the liquid part, the pressure field behaves like a dipolar motion, with -max and +max along the same diagonal direction.

Finally, let us notice that the quadrupolar WGM1,2 can also be tuned by the height of water, but with very small shifts. It should be noticed that WGM1,2 are essentially originating from the solid pillars in the absence of the liquid. Even with filling the holes, their acoustic energy remains mostly localized in the solid region surrounding the hollow part, although the vibration in the liquid becomes not negligible. This penetration of the wave into the liquid should soften the mode and decrease its frequency, although the effect remains small with water. In Fig. 4.19 we shall see that filling the holes with mercury which has a much higher impedance than water, and therefore comparable to silicon, will affect more strongly the frequency of WGMs.

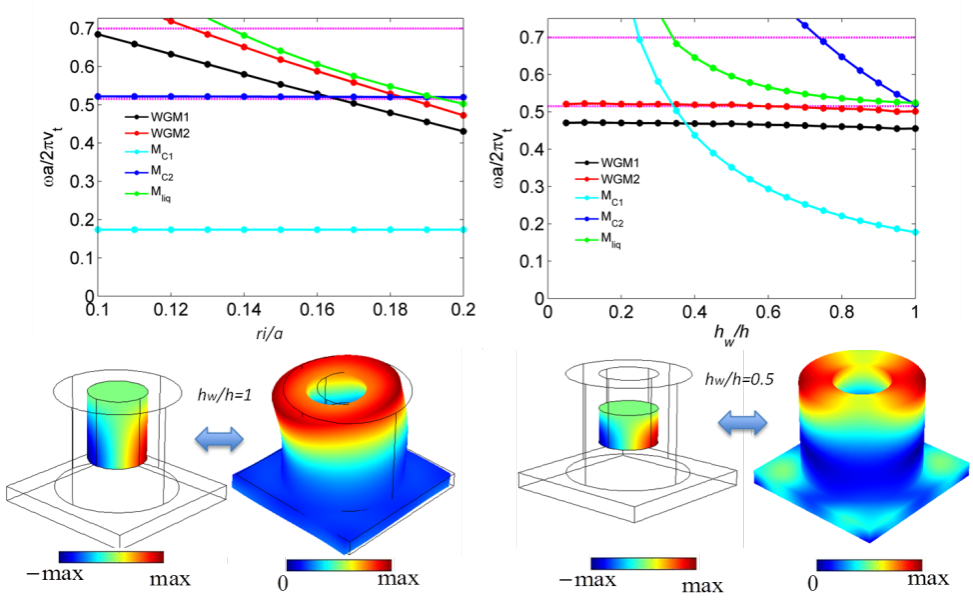

Figure 4.15 Upper-left panel: evolution of WGM1 (black dotted line), WGM2 (red dotted line), M_{c1} (cyan dotted line), M_{c2} (blue dotted line), M_{liq} (green dotted line) as a function of inner radius when the hollow pillars are fully filled with water ($h_w/h=1$). The two horizontal pink dotted lines are the limits of Bragg band gap of the full PnC; Upper-right panel: evolution of WGM1 (black dotted line), WGM2 (red dotted line), M_{c1} (cyan dotted line), M_{c2} (blue dotted line), M_{liq} (green dotted line) as a function of the height of filling water h_w/h when the inner radius is r_i/a=0.19. Lower panel: representation of the acoustic (pressure) and elastic (displacement) field of the mode M_{liq} respectively in the fluid and solid part for $h_w/h=1$ (left) and $h_w/h=0.5$ (right) when r_i/a=0.19. The other geometric parameters are h/a=0.45, r/a=0.4, l/a=0.2, e/a=0.1

4.3.3 Compressional modes along the height of the liquid

In this section, we discuss the modes called M_c in the previous section, which are associated to vertical motion inside the fluid. Due to the high impedance mismatch between most of the liquids and a hard solid, these modes are mainly localized inside the fluid. We give two illustrations about the sensitivity of these modes to the physical properties of the liquid and the variation of its parameters as a function of temperature.

First, it should be noticed that if the holes are filled with a liquid such as water which has a very smaller impedance than silicon, the frequency of the compressional modes are given with a very good precision by the resonance frequencies of a tube of height h_{liq} with rigid lateral boundaries, rigid bottom boundary and free upper boundary. The expressions of the frequencies are then $f_n = (2n+1)c / 4\, h_{liq}$, where n is the resonance number (0, 1, 2, 3, ...), c is

the speed of sound in the fluid; this means that the height can accommodate stationary waves at $\lambda/4$, $3\lambda/4$,…

In Fig.4.16, the hollow pillar filled with water has geometric parameters as h/a=0.4, r/a=0.39, r_i/a=0.1, h_w/h=1, l/a=0.1. The first and the second compressional liquid frequencies are f_{c1} = 0.197 and f_{c2} = 0.587, corresponding to a wavelength λ_{c1}/h = 4 and λ_{c2}/h = 4/3, respectively, as shown clearly in the pressure distributions in the left panel. The set of geometric parameters are chosen to move the WGMs to higher frequencies outside of the Bragg band gap. From the right panel, the first compressional liquid mode is at the edge of the low frequency band gap while the second one is in the middle of the Bragg band gap. We focus on the second compressional liquid mode, as the Bragg band gap is broader and more potential in the applications.

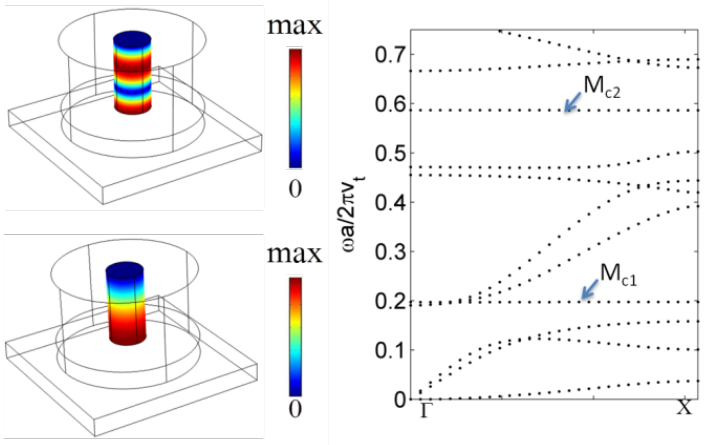

Figure 4.16 Left panel: 3D-schematic view of the pressure fields in water of the M_{c1} (left-lower) and M_{c2} (left-upper) compressional modes; Right panel: Dispersion curves of the PC with geometric parameters h/a=0.4, r/a=0.39, r_i/a=0.1, h_w/h=1, l/a=0.1, e/a=0.1 along ΓX direction

In a first example, we consider a set of mixtures of water and 1-propanol at different molar ratio x. We use the mass density and speed of sound at different molar ratio x as shown in Table 4.1 from refs[188, 189].

Molar Ratio x	Density ($kg \cdot m^{-3}$)	Speed of Sound (ms^{-1})
0 (water)	998	1490
0.021	990	1545
0.056	974	1588
0.230	908	1421
0.347	881	1367
0.596	841	1298

Table 4.1 Density and speed of sound of a mixture of water and 1-propanol at different molar ratio *x*

The M_{c2} in the Bragg band gap is isolated, allowing a phononic sensor application to sense the probed parameters on a sufficiently broad frequency range. The efficiency of the phononic sensor is detected by changing the physical properties of the filled liquid in the hollow pillar. Six kinds of liquids are employed to test the efficiency[188, 189]. Figure 4.17 left panel presents the evolution of the M_{c2} induced transmission peaks as a function of the acoustic velocity. It is observed that the transmission peaks are very sensitive to the acoustic velocity of the infiltrated liquid, with high quality factors $Q = f/\Delta f$ larger than 1000. Figure 4.17 right panel shows the relationship between the frequency of transmission peak and the corresponding acoustic velocity. In order to qualify the sensitivity, a common measurement is to calculate the slope of the lines in the right panel, named sensitivity S, as $S = \Delta f/\Delta c$, where Δf is the difference of the reduced frequencies of two infiltrated liquids and $\Delta c = (c_{liq}^{i} - c_{liq}^{j})/v_t$ is the difference of the reduced velocities of two infiltrated liquids by dividing to the transverse velocity of silicon v_t to have a dimensionless quantity. The average of S is 1.761, with a deviation 2.53% for the minimum and 0.87% for the maximum.

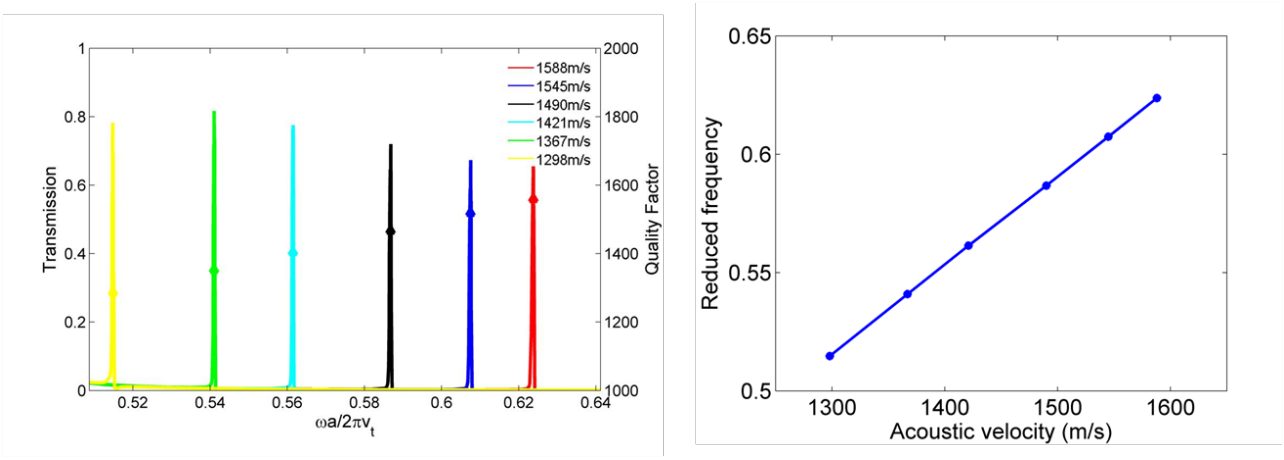

Figure 4.17 Left panel: Evolution of the second liquid compressional mode induced transmission peak (lines, corresponding to the left y-axis) and quality factor (dots, corresponding to the right y-axis) as a function of the acoustic velocity of filled liquid. The geometric parameters are *h/a*=0.4, *r/a*=0.39, r_i/a=0.1, h_{liq}/h=1, *l/a*=0.1, *e/a*=0.1. Right panel: The frequency of transmission peak corresponds to the acoustic velocity of different fluids

Furthermore, it is well known that the mass density and acoustic velocity of water will change if we vary the temperature of the liquid. We take the mass density and the acoustic velocity of water at different temperatures as shown in Table 4.2 from ref[41]. The temperature affects the elastic constant of silicon one order of magnitude lower than for the liquid[227] . So we assume that the temperature of solid background of the PC is kept fixed at the room temperature and the thermal property of the water in the hollow pillars is isolated from the solid background. The geometric parameters of the PC are *h/a*=0.4, *r/a*=0.39, r_i/a=0.1, h_w/h=1, *l/a*=0.1. By tuning the temperature of water from 0°C to 70°C, the frequency of the M_{c2} increases with its corresponding quality factor decreasing, as shown in Fig.4.18. In the range of [0°C; 50°C], the frequency moves significantly in the step of 10°C. Therefore, tuning the temperature of the infiltrated liquid is another way to actively control the M_{c2} induced transmission peak.

T (°C)	Mass Density (kg· m^{-3})	Speed of Sound (ms^{-1})
0	999	1405
10	999	1447
20	998	1482
30	997	1497
40	992	1529
50	986	1547
60	983	1550
70	977	1554

Table 4.2. Mass density and acoustic velocity of water at various temperatures

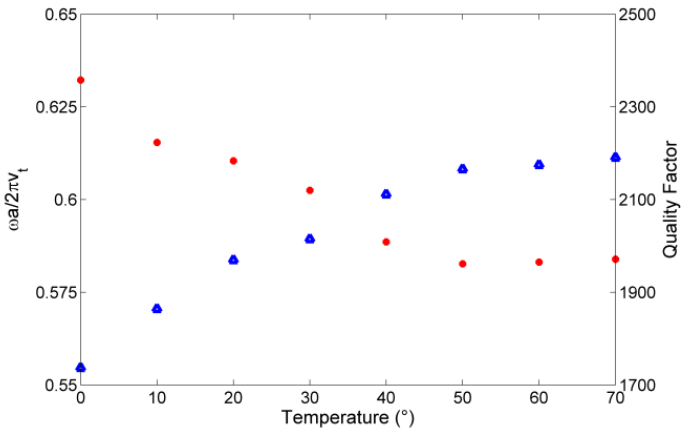

Figure 4.18 Varied frequencies (blue triangular dots) and corresponding quality factors (red circle dots) of the second liquid compressional mode by tuning the temperature of water in the holes. The geometric parameters are h/a=0.4, r/a=0.39, r_i/a=0.1, h_w/h=1, l/a=0.1, e/a=0.1

4.3.4 Influence of filling the holes with mercury on whispering gallery modes

The common liquids have very small impedance comparing to silicon. However, there is one liquid in nature, namely mercury, whose impedance is even a bit higher than silicon. We also studied the behavior of WGM1 as a function of the inner radius when the holes are filled with mercury of different heights and compare the results with the case of water. Fig.4.19 presents that at each inner radius, the upper end of the vertical bar is the frequency of WGM1 when the inner hole is empty and the lower end is the frequency when the inner hole is entirely filled with liquid; the red dotted bars are for mercury and, as a matter of comparison,

the blue dotted bars for water. For mercury, the mass density is ρ=13,600 kg m^{-3} and speed of sound is c = 1490ms^{-1}. The upper frequency range limited by two horizontal cyan lines is the Bragg band gap of background full PCs (h/a=0.45, r/a=0.4, l/a=0) and the lower one is the low frequency band gap. The tunable frequency range of the WGM1 increases when the inner radius becomes larger, as the corresponding filling ratio ϕ = A_{hole} / A_{pillar} increases, where A_{hole}, A_{pillar} are the area of inner hole and whole pillar, respectively. For a given inner radius, the tunable frequency range for mercury is wider than that for water due to the fact that the impedance $Z_m = \rho c$ of mercury is much larger than the impedance of water, even larger than that of silicon. In the Bragg band gap, mercury plays a more important role in actively controlling the WGM1.

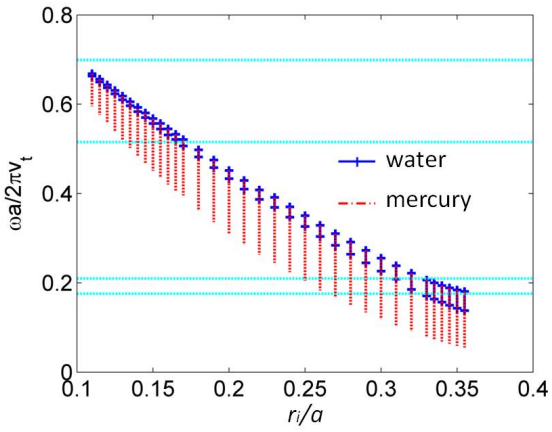

Figure 4.19 Varied range of WGM 1 frequency when the holes are respectively empty or fully filled with the liquid: water (blue dotted lines) and mercury (red dotted lines), corresponding to different inner radii. The other geometric parameters are *h/a*=0.45, *r/a*=0.4, *l/a*=0.2. The upper frequency range limited by two horizontal cyan lines is the Bragg band gap of background full PnCs (*h/a*=0.45, *r/a*=0.4, *l/a*=0) and the lower one is the low frequency band gap

Due to the fact that the property of the liquid is easier to control than that of the solid, we can realize an active control of the PC's functionalities, such as waveguiding or sensing. In Fig. 4.20, we present the evolution of the WGM1 frequency and its corresponding quality factor by changing the height of the fluid in the holes. To be specific, by increasing the height of mercury, the frequency of WGM1 moves to lower values, plotted in blue triangle dots,

especially in the range $h_m/h > 0.4$. The red dots show that the quality factor of WGM1 does not change too much within the range h_m/h =[0; 0.6] and increases from 140 at h_m/h=0.6 to 210 at h_m/h=1. The regime where the WGM1 changes significantly with respect to h_m still locates in the Bragg band gap, allowing for the realization of an actively tuned multichannel wavelength multiplexer.

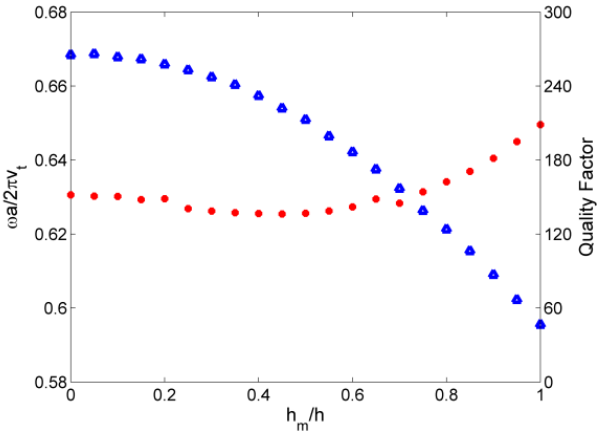

Figure 4.20 The evolutions of the WGM 1 frequency (blue triangle dots) and its corresponding quality factor (red circle dots) as a function of the filled mercury height. The geometric parameters are *h/a*=0.45, *r/a*=0.4, *l/a*=0.2, r_i/a=0.11

To illustrate the latter application, we consider a 5×6 super cell with periodic conditions applied in the *y* axis and Perfect Matched Layer applied in the direction of propagation *x*, as shown the inset of Fig.4.21 left panel. The PC contains two separated waveguides *c* and *d*, which are constituted by two rows of the same hollow pillars filled with mercury at h_m^c/h=0.4 and h_m^d/h=0.9, respectively. The geometric parameters for the two waveguides are *h/a*=0.45, *r/a*=0.4, *l/a*=0.2, r_i/a=0.11. The background full cylinders have parameters as *h/a*=0.45, *r/a*=0.4, *l/a*=0. The transmission is detected by exciting the anti-symmetric Lamb wave in front of the PC. In the left panel, two narrow pass bands *c* and *d* appear in the Bragg band gap at reduced frequency 0.66 and 0.61, respectively. The higher height of mercury significantly shifts the transmission frequency to a lower value inside the band gap. The corresponding

displacement field distributions in the solid silicon are presented in the right panel of Fig. 4.21, showing a multichannel wavelength multiplexer behavior.

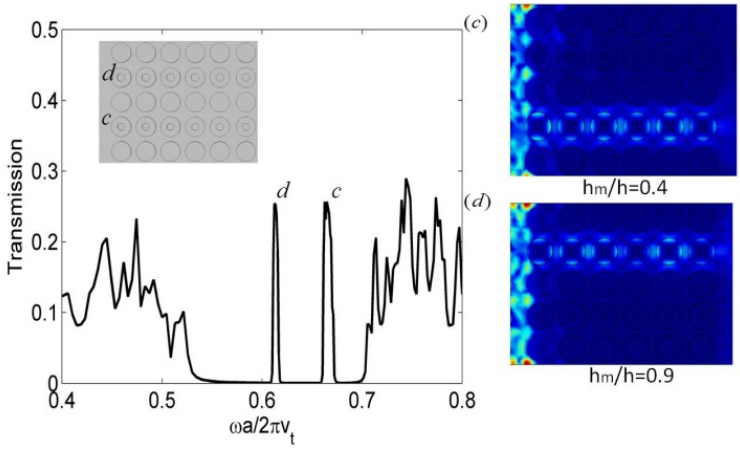

Figure 4.21 The multichannel wavelength multiplexer: Left panel: Transmission spectrum of the antisymmetric Lamb wave when the filled mercury heights inside waveguide *c* and *d* are h_m^c/h=0.4 and h_m^d/h=0.9; Right panel: Displacement field distributions at the frequency of the two narrow pass bands *c* and *d*. The geometric parameters of the multiplexer are *h/a*=0.45, *r/a*=0.4, *l/a*=0.2, r_f/a=0.11

4.4 Phononic crystal plate with hollow pillars connected by thin bars

4.4.1 Band structure and whispering-gallery modes

The phononic crystal studied in this paper is constituted by a square array of hollow pillars on a tailored plate where the pillars are connected to each other by a thin bar. A unit cell of the structure is depicted in Fig. 4.22. The confinement, and hence the quality factor, of the WGM localized at the top of the hollow pillars can be increased by possibly adding a full cylinder at their bottom. The geometrical parameters are the lattice constant a, the plate's thickness e, the width of the bars b, the height of confinement full pillar l, the height of hollow pillar h and their inner radius r_i and outer radius r. The whole unit cell is made of cubic silicon, with elastic constants c_{11}=166GPa, c_{12}=64GPa, c_{44}=79.6GPa and the mass density ρ=2330 kgm^{-3}. The crystallographic axes [100] and [010] of silicon are chosen parallel to the x and y axes, respectively. Periodic boundary conditions are set to each side of the unit cell in the (x, y) plane. Dispersion curves as well as transmission curves are calculated by the finite element code COMSOL Multiphysics® as a function of reduced frequency $\omega a/2\pi v_t$, where v_t =4678 ms^{-1} is the transverse velocity of acoustic wave in silicon along the [110] direction in the (001) plane.

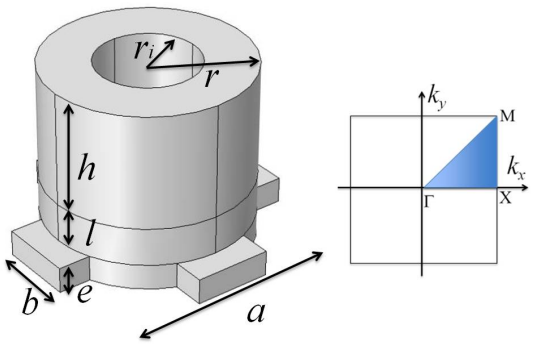

Figure 4.22 Left: 3D-schematic view of the unit cell: hollow pillar with inner radius r_i, outer radius r and height h, together with a confinement full cylinder with height l at its basis, deposited on a tailored plate (thickness e) with four identical bars (width b); Right: the irreducible Brillouin zone of the square lattice

The band structure of the phononic plate mainly depends on the width of the connecting bars b. In Fig. 4.23, we show the dispersion curves of the full pillar (r_i/a=0) deposited on tailored plate with b/a=1 (full plate) at left and b/a=0.1 at right, along both ΓX and ΓM directions. The other geometric parameters are r/a=0.4, h/a=0.45, e/a=0.1, l/a=0.2. At left for the case of b/a=1, an absolute Bragg band gap with center reduced frequency at $\omega_c a/2\pi v_t$ =0.593 and an absolute low frequency band gap with center reduced frequency at $\omega_c a/2\pi v_t$ =0.160 are presented. We define a relative size of a band gap[85] as $\Delta\omega/\omega_c$, where $\Delta\omega$ is the gap width. The relative sizes for the Bragg band gap and low frequency band gap are 0.359 and 0.111, respectively. Between the two gaps, there are two flat branches, named as branches '*aa*' and '*bb*', which are respectively associated with the rotation of the pillars and with vibrations localized at the corners of the unit cell. Two inserts clearly show the displacement fields of branch '*aa*' and '*bb*' at Γ point. The red and dark blue colors in the displacement fields represent the maximum and 0 values, respectively, which are the same for all the calculations in this paper.

In the right panel of Fig. 4.23, with a very narrow connecting bars b/a=0.1, the branch *'bb'* can be avoided because there is no matter at the corners of the unit cell contrary to the case considered in the left panel of Fig. 4.23. In addition, the unit cell with narrow bars makes the pillars easier to rotate or bend, so that the branch '*aa*' and those related with torsion or bending will move to lower frequency regions. Therefore, from the dispersion curves, one can notice an extra absolute wide gap (light pink colored area) and one extreme low frequency gap along ΓX direction (dark pink colored area). The extreme low frequency gap along ΓM direction cannot be maintained. Since the branch '*aa*' moves to a lower frequency and branches related with bending become more flat, the original absolute Bragg gap extends to a

very low frequency value (sub-wavelength region) with relative size increased to 1.223 and the low frequency band gap even moves to extreme low frequency regions in ΓX direction with the relative size 0.508. Such dispersion properties bring great potentials in sub-wavelength studies in the field of acoustic metamaterials.

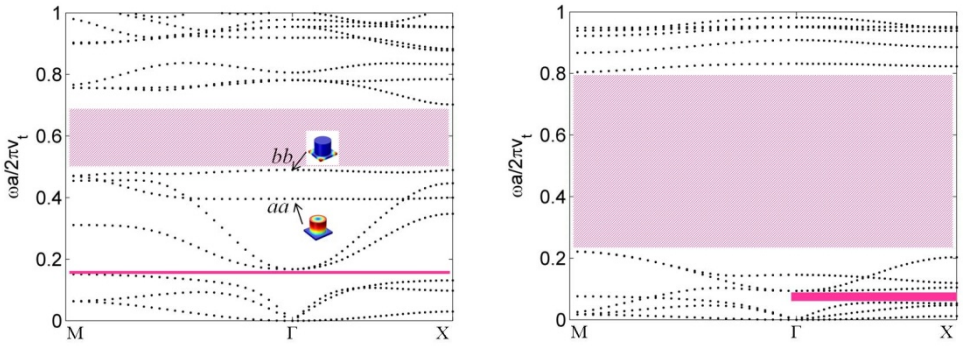

Figure 4.23 Dispersion curves of a phononic crystal plate consisting of the full cylinder (r_i/a=0) on the tailored plate with the width of bars as b/a=1 (left) and b/a=0.1 (right) in the ΓX and ΓM directions of the first irreducible Brillouin zone in the reduced frequency range [0; 1]. Two inserts are pointed to two branches labeled '*aa*' and '*bb*' at left, respectively, where the red and dark blue colors represent the maximum and 0 values, respectively. At right, the light pink colored area and dark pink colored area present the extra wide gap and extreme low frequency gap, respectively. The geometric parameters are r/a=0.4, h/a=0.45, e/a=0.1, l/a=0.2

The band gap diagram in Fig. 4.24 shows the evolutions of the Bragg band gap and low frequency gap in both ΓX (blue lines) and ΓM (red lines) directions as a function of the width of connecting bars *b*. For ΓX direction, as shown by blue lines, the lower edge of the Bragg gap continuously shifts downwards when decreasing *b/a* while its upper edge first shifts downwards until *b/a*=0.8, then increases to higher frequency ranges for lower values of *b/a*. As a result, the bandwidth of the Bragg gap turns to be much wider when *b/a* has a small value, for instance the width becomes about 0.6 in reduced frequency when *b/a*=0.1. On the other hand, the upper edge of low frequency gap keeps almost the same value when *b/a* is within [0.4; 1]. Then when *b/a* decreases to lower values, the low frequency gap moves to extreme low frequency range. For ΓM direction, as shown in red lines, the Bragg gap firstly becomes narrower when *b/a* changes from 1 to 0.8, then it even divides into two parts when *b/a*=0.7, afterward it significantly becomes wider (similar to the behavior along ΓX direction)

for lower values of *b/a* down to 0.1. The low frequency band gap can be maintained for *b/a* in the range [0.4; 1], whereas it disappears when *b/a* is smaller than 0.4. To conclude, by decreasing *b/a*, the absolute Bragg band gap firstly becomes narrower then turns to be much wider and extends to sub-wavelength range; the absolute low frequency band gap can be maintained when *b/a* is not smaller than 0.4, otherwise the gap is kept only along ΓX direction and moves to extreme low frequency ranges.

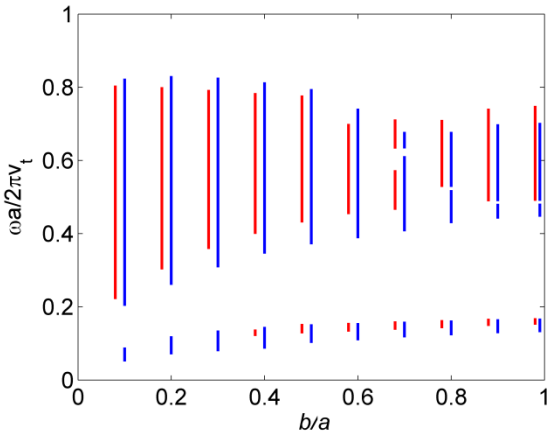

Figure 4.24 Band gap diagram of the phononic crystal plates with different widths of the bars (*b/a* is from 0.1 to 1). The blue lines stand for band gaps along ΓX direction and the red lines stand for band gaps along ΓM direction

To be noted, in Ref[86] , hybrid phononic crystal plates can also generate low and wide acoustic forbidden bands because the acoustic waves are scattered by both of the pillars and holes. The bottom limit of Bragg band gap can be extended to lower frequencies by a factor of 2 (from 52 kHz to 28 kHz), however the low frequency band gap becomes closed. In our new system, by narrowing the width of the connected bars, we allow the pillars to bend and rotate more easily, so the branches related with bending and torsion will become more flat and move to lower frequency range, such as branch '*aa*'. Meanwhile, in the narrowed tailored plate, there is no matter at the corners of original full square plate, so the branch '*bb*' can be suppressed. It results a widening and lowering the Bragg band gap whose bottom limit can be extended from reduced frequency 0.44 to 0.2. Meanwhile the low frequency band gap can be maintained and moved to lower frequency range. Let us also notice that, the Bragg band gap

can widened as much as 3 times (about 2 times in the Ref[86]) while remaining clean of any other branches inside.

In the following we shall investigate the properties and applications of the WGM confined at the top of hollow pillars in the case where the width of the connecting bars is fixed to b/a=0.1, considering a modulation of the inner radius of the pillars. Figure 4.25 summarizes the behavior of new modes that appear in the dispersion curve, i.e. quadrupolar (black dot-line), hexapolar (red dot-line) and octopolar (green dot-line) WGMs as a function of the inner radius r_i of the hollow pillar. Their corresponding displacement distributions are respectively given in Fig. 4.25. The quadrupolar WGM already falls at the top of the extra wide bang gap for a very small inner radius of r_i/a=0.05, then its frequency decreases until 0.165 when r_i/a=0.37 before slightly increasing for the highest radii. Hexapolar and octopolar WGM's penetrates into the band gap only when $r_i/a > 0.25$ and $r_i/a > 0.31$ respectively. Their frequencies also decrease when the inner radius increases until they leave the band gap for r_i/a around 0.38. It is worth noticing that the occurrence of several WGM's in the band gap is made possible by the new geometry adopted in this work where the pillars are connected by thin bars. In the case of pillars on a full plate[39, 228] only the quadrupolar WGM appear in the main band gap whereas the other WGM's remain always above the gap. Another point to mention is that all the three orders of WGMs reach the sub-wavelength domain with reduced frequencies about 0.2~0.3, but they do not enter the extreme low frequency band gap delimited by two solid pink lines. We shall see in section 4.4.2 that filling the hollows with a liquid can also give rise to localized modes in the low frequency gap.

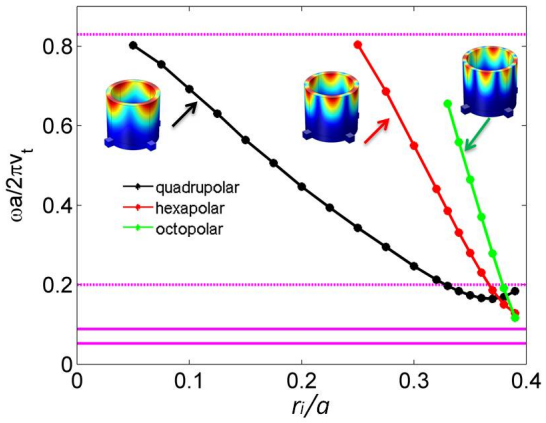

Figure 4.25 Evolution of WGMs frequencies with quadrupolar (black dot-line), hexapolar (red dot-line) and octopolar (green dot-line) shapes as a function of inner radius r_i/a. The wide (resp. low frequency) band gap in ΓX direction is delimited by two horizontal dotted (resp. solid) pink lines. The inserts show the displacement fields of the three polar-shapes of WGMs with inner radius r_i/a=0.35 at reduced frequency 0.176, 0.294 and 0.498, which corresponds to quadrupolar, hexapolar and octopolar shape, respectively. Other geometric parameters are b/a=0.1, r/a=0.4, h/a=0.45, e/a=0.1, l/a=0.2

Figure 4.26 presents the dispersion curves and transmission spectra of phononic crystal plates where the inner radius is chosen to respectively emphasize the quadrupolar, hexapolar and octopolar WGMs around the reduced frequency 0.35. In the transmission calculations, each phononic crystal contains 6 unit cells along the propagation direction x, whereas it is infinite along y direction with periodic conditions applied between neighboring cells. The calculation area along x is delimited by Perfect Matched Layers (PML) on both sides. The incident wave launched towards the phononic crystal is an A_0 Lamb mode of the plate. In the left dispersion curve of Fig. 4.26, two separate quadrupolar WGMs appear between the reduced frequency 0.3 and 0.4. That two modes present the same whispering-gallery shape inside the hollow cylinder but differentiate from each other by a rotation of 45 degree. However, the higher one cannot give rise to a transmission, as its displacement profile does not have the appropriate symmetry with respect to the incident plane wave[228]. Indeed it is to be noted that the localized bands in the dispersion of phononic crystal plate can be excited if the symmetry of the source is consistent with the symmetry of the localized mode. The transmitted peak of the lower mode appears at the reduced frequency 0.34. We also calculate its corresponding quality factor, $Q = f / \Delta f = 398$, where f is the central frequency of the pass

band and Δf is the full width at half maximum of the transmission peak. Below the dispersion and transmission spectra, we report the total displacement field calculated at the frequency of the peak from which one can clearly see the quadrupolar whispering-gallery mode which propagates through the hollow phononic crystal.

For the hexapolar WGMs shown in the middle of Fig. 4.26, two close branches exist but now almost at the same frequency. The difference between the two modes comes from a rotation of 30 degree in their displacement field. The transmitted peak appears at the reduced frequency of 0.329, inside the gap, and the quality factor reaches a theoretical value larger than 15,000, which is much higher than that of the quadrupolar WGM.

The same scheme of calculations has been followed for the octopolar WGM and is reported in the right panel of Fig. 4.26. In this case, keeping the same geometrical parameters than in the previous case, we get a quality factor higher than 15000. Moreover, this mode can still display a high quality factor of 2185 even if the height of the confinement *l/a* is reduced from 0.2 to only 0.05.

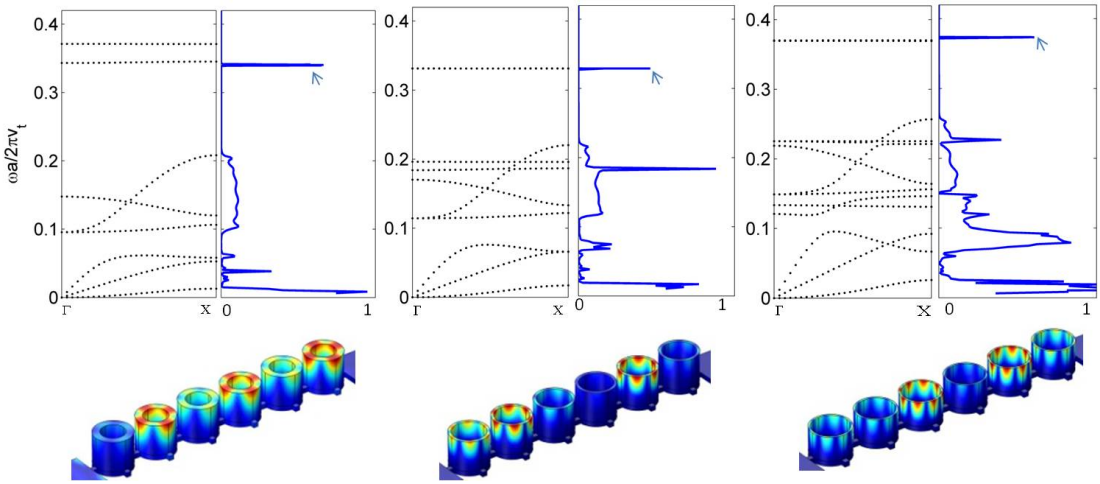

Figure 4.26 Dispersion curves and transmission spectra for respectively quadrupolar, hexapolar and octopolar WGM's. Left: r_i/a=0.25, l/a=0.2; Middle: r_i/a=0.34, l/a=0.2; Right: r_i/a=0.36, l/a=0.05. In each panel, the displacement field distributions at the bottom correspond to the arrowed transmitted peak. Other geometric parameters are r/a=0.4, h/a=0.45, e/a=0.1, b/a=0.1

To illustrate the functionality of the above structure for guiding and filtering applications, we design a multichannel wavelength multiplexer consisting of a 5×6 super cell as shown in

the insert of Fig. 4.27. If the localized mode of waveguide locates in the band gap of background phononic crystals and it has the same symmetry in displacement distribution as incident wave, then a pass band can be found in the corresponding transmission. The phononic crystal plate contains two different linear waveguides separated from each other by one row of full pillars to avoid leakage between the waveguides. The inner radius of the hollow pillars inside the waveguide $P1$ and $P2$ are respectively r_i^{P1}/a=0.27 and r_i^{P2}/a=0.34 with the other geometric parameters r/a=0.4, h/a=0.45, e/a=0.1, b/a=0.1, l/a=0.2. The transmission spectrum, displayed in the left panel of Fig. 4.27, features two narrow passing bands $P1$ and $P2$ located in the band gap at the reduced frequencies 0.299 and 0.329. In the right panel of Fig. 4.27, it is shown that the transmission pass bands $P1$ and $P2$ are induced by quadrupolar and hexapolar WGMs, respectively. This can be seen from the shape of the displacement fields in waveguides P1 and P2 which are quadrupolar WGM in waveguide P1 and hexapolar WGM in waveguide P2. Their respective quality factors are 180 and 19200. As the hexapolar WGM is more confined, its maximum displacement is much larger than quadrupolar WGM (by a factor of 17 for their maxima). For this reason the vibrations associated with the incident and transmitted fields in the plate are too small to be presented with the same color bars in the case of the hexapolar mode in waveguide P2.

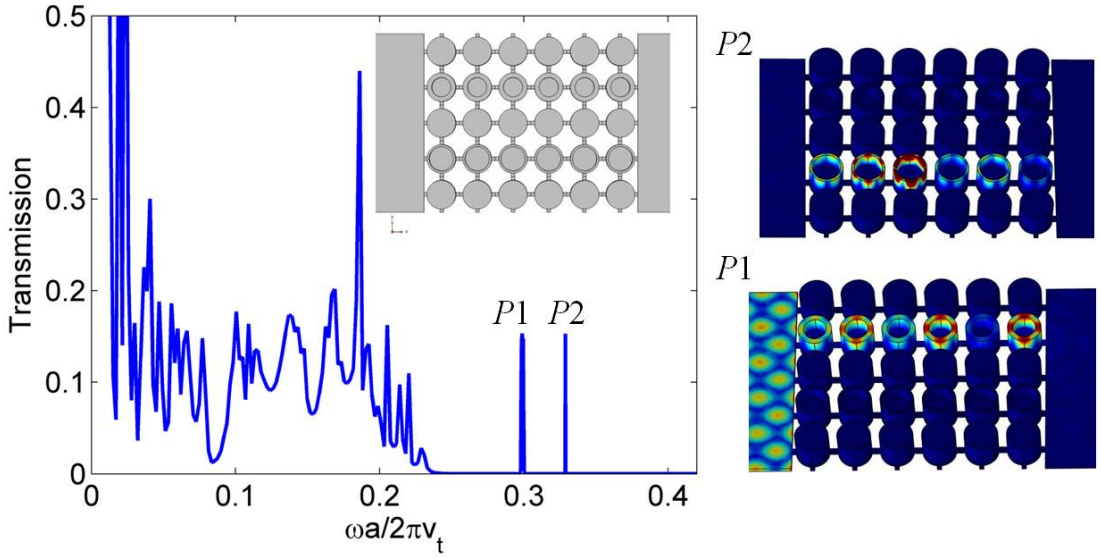

Figure 4.27 Left panel: (Inset) Schematic representation of the multichannel wavelength multiplexer; (Graph) The transmission spectrum of the anti-symmetric Lamb wave when the inner radius of the hollow pillars in the waveguides *P*1 and *P*2 are r_i^{P1}/a=0.27 and r_i^{P2}/a=0.34. Right panel: Displacement field distributions at the frequency of the two peaks *P*1 and *P*2, which correspond to quadrupolar and hexapolar WGMs, respectively

4.4.2 Tunable properties by liquid filling

In this section we investigate the existence and tuning of localized modes in the band gaps when the hollow parts of the pillars are partly or fully filled with a liquid. The tuning parameters may be the nature or the height of the fluid as well as the temperature, which can change the acoustic properties of the fluid. The localized modes may originate from the WGM's of the solid structure modified by the presence of the liquid or result essentially from the presence of the fluid. In a first part, we consider the special case of the mercury whose impedance is close to that of the solid silicon while having a much lower acoustic velocity and show the possibility of localized mode in the low frequency gap. In a second part, we investigate the case of usual fluids with density close to 1000 $kg.m^{-3}$ and acoustic velocities in the range of 1000~2000 m/s and discuss both the tuning of the WGM's as well as the existence of new modes induced by the fluid.

For mercury, the mass density is ρ=13,600 kg.m^{-3}, and the speed of sound is c =1490m.s^{-1}. In Fig. 4.28, the hollow parts of the pillars are fully filled with mercury, i.e. h_m/h=1. As can be seen in the band diagram, the two-close quadrupolar WGMs become very close to each other, moving to the center of the extreme low frequency band gap,. In the transmission spectrum, one can see only one transmitted peak at the reduced frequency of 0.057 and a Q factor of 134. This peak corresponds to the quadrupolar mode which presents the appropriate symmetry with respect to the incoming wave, as discussed above. So, for a constant value of the inner radius (r_i/a =0.37), the device presents the opportunity to tune the frequency of the quadrupolar mode in a wide range of frequency, from 0.165 when the hollow cylinders are empty (see figure 4.25) to 0.057 when the hollow cylinders are fully filled with mercury. The lower panel of Fig. 4.28 presents separately the displacement field distribution in the solid part (left) and the pressure field in the liquid (right) at the frequency of the transmission peak '*p*'. One can see that the quadrupolar whispering-gallery mode is localized, as previously, inside the solid but presents an interaction with the liquid via the interface. It means that the sensitivity of the mode depends strongly from the strength of that solid/liquid interaction.

The localized mode around 0.1 is hexapolar WGM which can also produce a very narrow transmission peak in the broad pass bands, with a quality factor more than 30 times than that of quadrupolar WGM, as also seen in the discussion of Fig. 5. At the frequency of 0.025, the S_0 and SH_0 branches deviate and also become flat near X point, however, they cannot generate a significant transmission as the dominant components of their displacement field are in plane while the dominant component of the A_0 incident wave is out of plane.

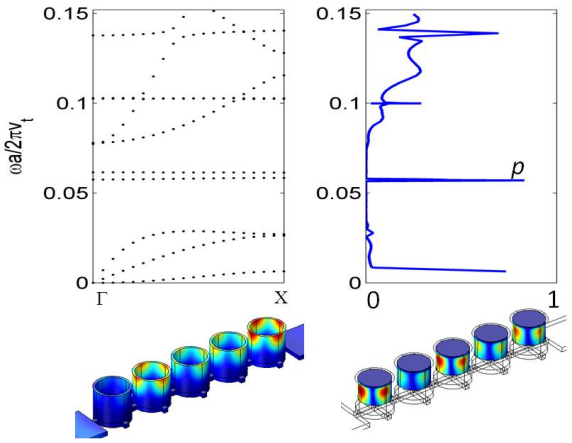

Figure 4.28 Upper panel: Dispersion curves (left) and transmission curve (right) for quadrupolar WGMs inside the extreme low frequency band gap when the hollow part is fully filled with mercury. The geometric parameters are r_i/a =0.35, r/a=0.4, h/a=0.45, e/a=0.1, b/a=0.1, l/a=0.2, h_m/h=1. Lower panel: displacement (left) and pressure (right) distributions in solid and liquid, respectively, for the reduced frequency at peak '*p*'

In the next part, we assume that the hollows are filled with water whose mass density ρ =998 kg.m^{-3} and speed of sound c =1490m.s^{-1} are close to those of most common liquids. Figure 4.29 gives the evolution of the localized modes in the main band gap as a function of the height h_{liq} of the water when the inner radius of the hollow is very small (r_i/a =0.05). First, one can recognize the quadrupolar WGM at the reduced frequency of 0.8 (black solid line) which is almost independent of the amount of liquid, owing to the large difference between the acoustic velocities and impedances in water and in silicon. For this small inner radius, the other orders of WGMs occur at higher frequencies, above the upper limit of the gap. Beside, two other localized branches appear in the gap which can be identified as the fundamental and first order compressional modes (Mc_0 and Mc_1) along the height of the liquid. Their frequencies can be easily identified as the resonance frequencies of a tube of height h_{liq} with rigid lateral boundaries, a rigid bottom boundary and a free upper boundary. The expression of resonances for such a simple model of acoustic tube is $f_n=(2n+1)c/4h_{liq}$, where n is the resonance order (0,1,2,3,…).

Because of the localization of the acoustic pressure, Mc_0 and Mc_1 are very sensitive to the liquid's height, with a good correspondence between the analytical expression and actual

behaviors. Mc_0 decreases throughout the extra wide band gap when h_w/h increases from 0.20 to 0.85, meaning that the device presents a good candidate for tuning gradually the frequency of the transmitted peak by changing the height of water.

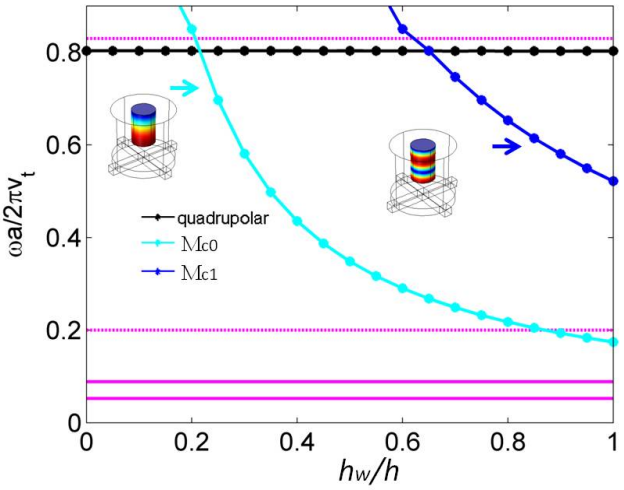

Figure 4.29 Evolution of quadrupolar WGMs (black dot-line), Mc_0 (cyan dot-line) and Mc_1 (blue dot-line) as a function of water filling height h_w/h. The inserts show the pressure distributions in the liquid for the fundamental and the first order compressional modes. The two horizontal dotted pink lines (resp. solid pink lines) show the limits of the extra wide band gap (resp. extreme low frequency band gap). Other geometric parameters are r_i/a =0.05, r/a=0.4, h/a=0.45, e/a=0.1, b/a=0.1, l/a=0.2

The above modes originated mainly either from the solid structure or from the filling liquid. We show now the occurrence of new coupled (Solid / Liquid) modes that result from the interaction between the solid and liquid when one increases the inner radius r_i/a. Figure 4.30 shows the evolution of the localized modes, including modes Mc_0, Mc_1, WGM4 (quadrupolar), WGM6 (hexapolar), WGM8 (octopolar), as well as two new branches called S/L1 and S/L2, when varying the inner radius of the hollow pillars. The quadrupolar, hexapolar and octopolar WGMs have similar shapes as the ones shown in Fig. 4.25. For compressional Mc_0 and Mc_1 modes, when the inner radius r_i/a is no larger than 0.3, the silicon hollow pillars can be regarded as rigid comparing to filled water, so that their frequencies do not depend on the inner radius. However, if r_i/a is larger than 0.3, the silicon wall of the hollow pillars become thinner, and cannot be regarded as totally rigid, which results in a slight decreasing of the frequencies of Mc_0 and Mc_1 modes. Besides, there are other localized Solid /

liquid modes, namely S/L1 and S/L2, whose pressure fields are presented in the liquid parts and displacement fields are presented in the solid parts, as shown in the right panel of Fig. 4.30. In general, the S/L1 and S/L2 also decrease when increasing the inner radius. These modes where the vibrations penetrate in both the solid and the liquid appear to be sensitive to both the inner radius of the pillars and the height of the fluid. This possibility of tuning them with two different parameters can make them useful in different applications such as sensing or waveguiding.

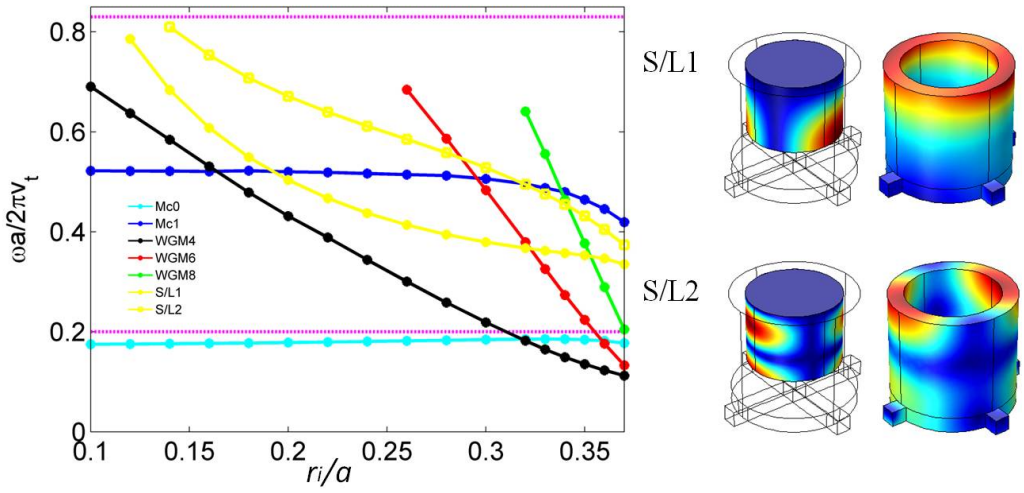

Figure 4.30 Left panel: Evolution of localized modes Mc_1, Mc_2, WGM4, WGM6, WGM8, S/L1 and S/L2as a function of the inner radius r_i when the hollow pillars are fully filled with water (h_w/h=1). The two horizontal dotted pink lines are the limits of the extra wide gap. Right panel: Representation of the pressure and displacement fields for the modes S/L1 and S/L2, respectively. Other geometric parameters are r/a=0.4, h/a=0.45, e/a=0.1, b/a=0.1, l/a=0.2

4.5 Conclusions

In this chapter, we firstly theoretically investigated the vibration properties of a phononic crystal plate with hollow pillars on top. The computed dispersion curves show the occurrence of two new branches of dispersion that do not appear in the native phononic crystal. These branches originate from the excitation of quadrupolar whispering gallery modes (WGM's) circulating around the upper boundary of the hollow pillar. By changing the inner radius of the hollow cylinder, we have been able to tune the frequencies of the WGM's inside the Bragg band gap. Through the computation of the transmission coefficient of an anti-symmetric Lamb wave, we have shown that one of the WGM gives rise to a transmitted pass band that can be used as a filter. The quality factor of the filter has been further improved by inserting a solid cylinder in between the plate and the hollow pillar. We then applied the high resolved filter to different kind of multiplexers, based on multichannel or monochannel waveguides or cavity. We also showed that the WGMs can reach the low frequency range, adding new type of elastic field localization inside the resonators, with the opportunity to perform interactions with the existing low frequency band gap. The demonstration of an efficient sub-wavelength waveguide with high quality factor has been done.

Then, we studied the dispersion and transmission excited by both anti-symmetric and symmetric Lamb waves along ΓX and ΓM directions, and found that the WGM1 can be well excited by anti-symmetric Lamb wave and generate a narrow pass band. Then we filled the inner holes with liquids and figured out that the frequency of WGM1 decreases while the corresponding quality factor increases with the height of liquid. We discussed a functionality to design an active multichannel wavelength multiplexer by tuning the height of liquids in the waveguides. Besides, a simple theoretical model is provided to explain the compressional liquid modes in the hollow pillars. These modes are isolated in the broad Bragg band gap with high quality factors larger than 1000, and applied to design a phononic sensor to sense a

mixture of water and 1-propanol at different molar ratio *x* with a high efficiency. By increasing the temperatures in the infiltrated liquid, the frequency of the second compressional mode moves to higher frequencies, realizing an active control.

Finally, we presented a new type of tailored phononic crystal plate whose unit cell is constituted by pillars connected by thin bars instead of being deposited on a full plate. By narrowing the bars, the Bragg band gap becomes much wider and extends to sub-wavelength region while the low frequency gap moves to extreme low frequency region. We have shown that the structure can generate several types of whispering-gallery modes (WGMs), namely quadrupolar, hexapolar and octopolar, inside the band gaps. Especially, the hexapolar or octopolar WGMs have very high quality factors. If the hollow pillars are filled with liquids, WGMs can further decrease to extreme low frequency gaps, and become useful in the applications of acoustic metamaterials. The localized compressional liquid modes can be tuned by changing the height of filling liquid and analyzed by a simple physical model, which proved to be a good candidate in applications as it can be gradually tuned through the whole extra wide gap. Finally we found that the liquid-filling hollow pillars give rise to other coupled modes, localized both in the solid and the liquid S/L1 and S/L2 in the extra wide band gap, with dipolar shape pressure fields in liquid. Each type of mode could find different physical applications with respect to the nature of the liquid and/or the solid. The phononic crystal plate with higher orders of WGMs and localized compressional and dispolar-shape liquid modes can be applied to wireless communication and sensing with the possibility of active control, such as tuning the filling liquid height and temperature.

Pillars or hollow pillars in micro/nano scale can be fabricated by various technologies, such as reactive ion etching[229], photoelectrochemical etching[230], and using chemically etched silica needles as templates[231]. The experimental technique can be carried out based on laser generation by Nd: YAG laser and detection of acoustic pluses by Michelson

interferometer[232] or interdigital transducers which can be fabricated by a standard lithography process[233].

Chapter 5

Scattering property by Pillar-Type Acoustic Metasurface

5.1 Introduction

Locally resonant sonic materials are artificially structured composites designed to exhibit negative effective mass density and/or elastic constants at some frequencies[2]. They are based onto the insertion into a background (3D) or on a free surface (2D) of local resonators having lateral sizes much smaller than the wavelength of the elastic wave so that homogenization theories applied. Unusual responses are then observed: the material expands upon compression when the compressibility gets negative and moves in the left when pushed toward the right if the mass density is negative. Although the periodicity is not a requirement, these resonators are generally regularly arranged and therefore Bragg scattering may occur when the acoustic wavelength is of the order of the spacing between the inclusions. Beside this expected feature, flat bands related to the normal modes of the resonators occur in the band structure at much lower frequencies as compared to the Bragg band gap. This property was first recognized in the seminal work of Liu *et al*.[12] and further exploited by Li and Chan[48] who demonstrated the double negativity in a phononic crystal made of rubber spheres arranged in a fcc lattice in water. In both systems, the negative compressibility resulted from a monopolar resonance of the rubber spheres, whereas a dipolar resonance yielded to the negative mass density. Very recently, negative density in a liquid foam[234] and negative acoustic index in Mie resonators made of random suspension of soft silicone rubber micro-beads[58, 235] have been demonstrated. Both parameters become negative when the motion of the centers of mass of the resonators is 180° out-of-phase with respect to the waves propagating in the background. If moreover the geometrical parameters of the crystal (diameter of the spheres, filling ratio…) are chosen in such a way that the mass density and the compressibility are both negative in the same frequency band, the elastic waves become propagative. However all these unique properties are achievable only because the speed of sound in the soft rubber or in the bubbly liquid is of a few tens of $m.s^{-1}$, lower by orders of

magnitude than the speed of sound in the epoxy matrix[12, 236] or in the water background[48]. Actually, the smaller is the contrast in sound speeds, the smaller is the wavelength in the embedding matrix at resonance and the phononic crystal can no longer be viewed as an effective medium. Very few materials exhibit such low elastic parameters and seeking for resonators made of a material commonly used in nano or micro-fabrication, whose lateral dimensions are much smaller than the wavelength, and that allow controlling the propagation of elastic waves in solids, is therefore of primary importance for designing new acoustical metamaterials.

Actually, these properties can be found in some phononic crystals that may exhibit local resonances at frequencies below the Bragg band gap, giving rise to one or several forbidden bands in a frequency range where the wavelength is much larger than the period. This has been demonstrated both numerically and experimentally, with 1D stripes periodically engraved on the surface of a lithium niobate substrate[237] and more recently with 2D phononic crystals made of a periodical array of cylindrical pillars deposited on a thin and homogeneous slab[81, 82, 195, 208, 238-240]. Inspired by the connection between negative dynamic properties and the symmetry of resonant modes[48], the latter structure deserves special attention as a pillar can exhibit both compressional (monopolar) and bending (dipolar) resonances. Moreover, the resonant frequencies can be easily tuned through a proper choice of the height and/or the diameter of the pillar. Finally, since the compressional resonant frequency (monopolar) and the bending resonant frequency (dipolar) are mainly sensitive to the height and to the diameter respectively, they can be tuned almost independently from each other.

Given their potential to serve as local resonators in an all-solid elastic metamaterial, we have investigated in this work their dynamic properties. The theoretical calculations are done in the collaboration with the experiments carried out by Rémi Marchal[241] . We have

successively considered a single pillar and a line of identical pillars on a thin plate. In both cases, the resonators as well as the plate were made of silicon. We have studied both numerically and experimentally their interaction with a Lamb wave propagating in the plate when the frequency is tuned to a resonant frequency. We more specifically point out how both the amplitude and the phase of the wave are affected by the scattering on top of single pillar, or one line of pillars, upon excitation on either a compressional or a bending eigenmode. We show in particular that for either of both modes, the pillars behave as secondary sources that emit in the plate a wave 180° out-of-phase with the Lamb wave. We investigate the conditions in which a zero, or on the contrary a maximum, of the transmission through the line of pillars, results from the superposition of both waves.

The main objectives and conclusions of this chapter are to clarify the scattering properties of an incident wave: amplitude and phase of the scattered wave as a function of the frequency especially in the vicinity of resonances.

5.2 Resonant property

The goal of this section is to provide in a comprehensive way a numerical study of the vibrationnal states of a single pillar deposited on a membrane with a thickness t (see Fig. 5.1). This study will be the fundament of the further investigation coming in the following sections. We have considered the effect of the usual geometrical parameters, namely the height h and the diameter d of the pillar. We also investigate the effect of the angle θ, varying from 0° for a straight cylinder to higher values then reaching to a truncated inverse conical shape of the pillars. The whole system is made of cubic silicon, with elastic constants c_{11}=166GPa, c_{12}=64GPa, c_{44}=79.6GPa and the mass density ρ=2330 kgm^{-3}. The crystallographic axis [100] and [010] are chosen parallel to the x and y axes, respectively. Dispersion curves as well as transmission curves are calculated by the finite element code COMSOL Multiphysics® as a

function of reduced frequency $\omega a/2\pi v_t$, where v_t =4678 m.s^{-1} is the transverse velocity of acoustic wave in silicon along the [110] direction in the (001).

The experimental technique we used is based on laser generation and detection of acoustic pulses within a broad spectrum. Ultrashort light pulses of 35 ps issued from a frequency-doubled (532 nm) Q-switched Nd:YAG laser were focused on the sample as a bright fringe ~5 mm long and ~50 μm across, through a cylindrical lens. As a result of photoelastic processes, elastic waves with a broad spectrum were excited in turn. The accurate determination of the excited spectrum is a challenging task that involves the knowledge of several physical parameters including the photoelastic tensor of silicon and the time dependence of the optical pulse. However, a rough estimation that does not account for the duration of the optical pulse consists of admitting that the largest acoustic wave number is related to the lateral size of the focus through $k_{\max} \approx \pi/l$; the highest frequency in the spectrum is therefore given by $\nu_{\max} \approx V/2l$ where V is the surface velocity in silicon; we thus estimate that the spectrum extended up to about 50 MHz. In all the experiments described in this article, the source was located a few millimeters ahead from the pillar or from the line of pillars.

The time dependence of the surface displacements was recorded at any point of the sample, on the plate as well as on top of a pillar, using a Michelson interferometer described in Ref[232]. In short, the technique consists of focusing one beam of the interferometer on the sample with a microscope objective to a spot of~5μm, whereas the reference beam is reflected by an actively stabilized mirror. A loop feedback device allowed the setting of optical path differences to $\lambda/4$ (modulo λ), therefore achieving optimum sensitivity and a linear response to the normal displacements at the surface of the sample. The microscope and the sample were both mounted on translation stages in such a way that the probe beam could be scanned across the sample over a maximum area of 25 × 25 mm^2, with absolute and relative precisions of

~10 and ~1 μm, respectively. The interference pattern was collected by a high-speed photodetector and digitized at 500 MSs^{-1} by a digital oscilloscope. The frequency response of the device was flat between 20 kHz and the cutoff frequency of the photodiode which was set to ~50 MHz in order to match the maximum frequency in the spectrum. This noncontact technique allowed us to record the displacements normal to the surface as small as a few pm and hence to resolve fine details of the interaction between the acoustic waves and a pillar or a line of pillars.

In the numerical model depicted in Fig.5.1, we have considered a full silicon model where the pillar is grafted at the middle of a circular membrane surrounded with a Perfectly Matched Layer (PML) to avoid any reflections from the boundary of the plate. We have investigated the behavior of the pillar under the excitation of anti-symmetric Lamb wave A_0, launched from an oscillating force applied normally to the surface of the plate, along the line 'AB' parallel to the crystallographic direction <100> of silicon. The numerical model used to compute the resonances of the pillar perfectly mimics the experimental scheme presented below: an oscillating force is applied normally to the surface of the plate, and the resulting displacements are monitored as a function of the frequency on five different points on top of the pillar. Experimentally only the component out-of-plane U_z of the displacement field can be measured and therefore we have investigated the propagation of the anti-symmetric Lamb mode A_0 since it features a large out-of-plane component. In the following results, only U_z is plotted as no conversion is observed after the interaction of the incident wave with the structure, *i.e.* the ratio U_z/U_x is conserved.

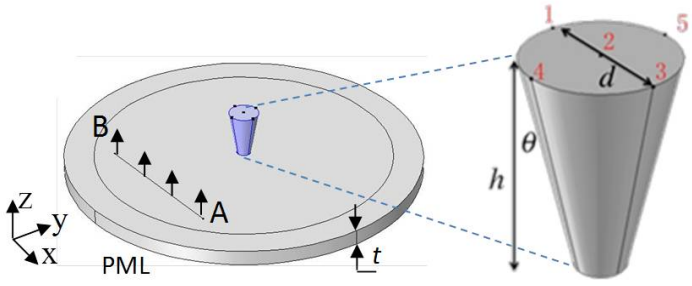

Figure 5.1 Numerical model used for the finite element calculation of a full silicon structure made of a pillar on top of a plate with a thickness *t*. The line 'AB' represents the incident source polarized with respect to the anti-symmetric Lamb wave A_0. Perfectly Matched Layers (PML) are applied all around the membrane. The inset magnifies the pillar and reports the geometrical parameters *h*, *d* and *θ* together with the different positions used for the detection

The excellent sensitivity of the experimental technique is a requirement to a complete characterization of the resonant frequencies of the single pillar. We show as a black line in Fig. 5.2a the time dependence of the normal displacements recorded close to the edge (point labeled 4 in Fig. 5.2b) on top of a single pillar (*d*=150µm, *h*=257µm) on a slab (*t*=145µm), after an anti-symmetric Lamb wave has been excited a few mm away from the pillar (red line in Fig. 5.2a). Similar measurements were taken in five different locations (black line in Fig. 5.2a), along a line either parallel to the excitation wave front (points 1, 2, 3 in Fig. 5.2b) or perpendicular to it (points 4, 2, 5). The spectral amplitudes, normalized to the amplitude of the excitation wave, are displayed in Fig.5.2c. As expected from the polarization of the normal modes, the line joining points 4 and 5 is a node for both the first bending mode (B_1) and second bending mode (B_2) and therefore the signals recorded in 1, 2, and 3 only result from the first compressional mode (C_1). It manifests itself in the spectrum by a broad peak centered at 6 MHz with amplitude twice the amplitude of the incident Lamb wave.

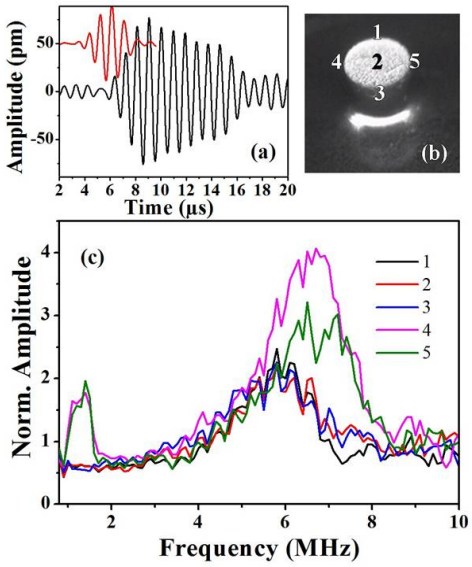

Figure 5.2 (Color online) (a) Normal displacement on the plate, measured close to the excitation area (red line – up shifted for clarity) and on the center of the pillar (black line). (b) Microscope image of the Silicon

pillar. The numbers indicate the points where measurements were made. (c) Spectral amplitudes measured on top of the pillar. The data are normalized by the amplitude of the Lamb wave on the plate

We first consider an isolated cylindrical pillar (θ = 0°) with the following set of geometrical parameters: h = 245 μm, t = 145 μm and d = 50 μm. Fig. 5.3(a) reports the displacement field U_z of single pillar as a function of the frequency in which the red curve reports the summation of the amplitudes $|U_z|$ recorded with the detectors (4 + 5) while the black curve represents the difference (4 - 5). The same implement is also carried out for one line of pillar (the distance between two pillars is e=200μm) as marked in blue and green curves, respectively. One can see the occurrence of three peaks of resonances. Each peak can be unambiguously ascribed to an eigenmode of the pillar with the help of the associated displacements. Actually, bending modes along y-axis are characterized by an out-of-phase displacement between points 4 and 5 while no displacement are expected along the line joining the points 1 and 3 which corresponds to a node. On the other hand, the normal displacements associated to a compression mode are uniform on top of the pillar, leading to zero displacement for the difference (4 - 5) and full amplitude for the summation (4 + 5). It results that the summation (4 + 5) highlights the compression mode of the pillar (labeled C_1) while the difference (4 - 5) is representative of the bending modes, labeled B_1 and B_2. For more details in the modes characterization, one can see Appendix E. Comparing the same modes of single pillar and one line of pillars, for diameter d=50μm, the frequencies of B_1 and B_2 are almost the same while the relative amplitude of single pillar is larger than that of one line of pillar; however, for the compression mode C_1, the frequency of one line of pillar is a bit larger and so is the relative amplitude.

The situation is more complex in Fig. 5.3(b), calculated for another set of geometrical parameters: h = 245 μm, t = 145 μm and d = 100 μm for which the mode B_2 gets close to C_1 and only the bending mode B_1 can be unambiguously detected. Actually, the second peak centered at ~7 MHz results from interplay of compression C_1 and bending B_2 modes and there

is no pure compression or bending anymore. The method based on the summation and the difference is the way to represent independently the contribution of each mode. For compression C_1 mode, the frequency of one line case is also a bit higher than single case and the relative amplitude of one line case is still a bit larger than single case. The frequencies of B_2 and C_1 are superposed for single case, while they are still separated for one line case. The results from the comparison of single and one line cases show that there is a slight coupling among neighboring pillars when the single pillar is arranged into a line.

Finally, Fig. 5.3(c) shows a representation of the bending mode B_1, B_2 and the compression mode C_1 when all frequencies are clearly separated (as parameters in Fig. 5.3(a)). In the following of the research, we will use the specific properties of the modes in term of monopolar for the compression mode and dipolar for the bending ones.

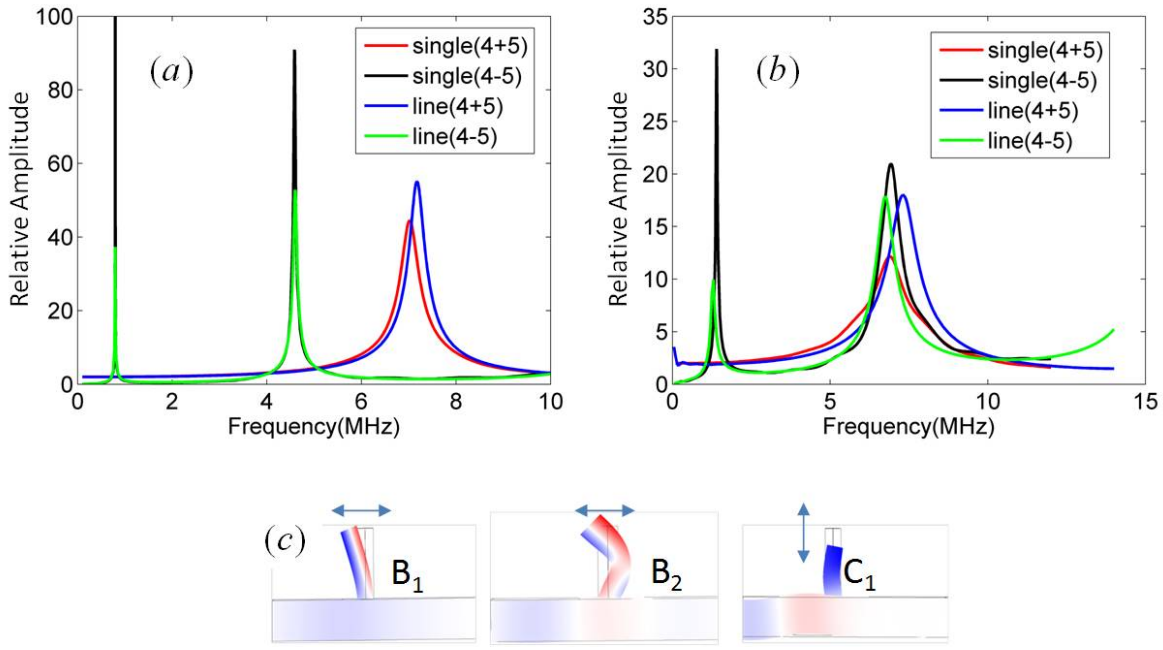

Figure 5.3 (a) Amplitude of the component U_z of the displacement field on top of the pillar considering the difference (4 -5) (black curve for single pillar and green curve for one line of pillar) and the summation (4 + 5) (red curve for single pillar and blue curve for one line of pillar) with the geometrical parameters *h* = 245 µm, *t* = 145 µm and *d* = 50 µm. (b) Same as (a) with the geometrical parameters *h* = 245 µm, *t* = 145 µm and *d* = 100 µm. (c) Snapshot of the involving bending and compression pillar modes when all frequencies are clearly separated (*h* = 245 µm, *t* = 145 µm and *d* = 50 µm)

Due to localization of the mechanical resonances inside the pillar, the frequencies and amplitudes of these modes depend on the geometrical parameters of the pillar. As seen Fig.

5.3(a) and (b), increasing the diameter of the pillar from 50 μm to 100 μm leads to widen the peaks, shifts the bending modes to higher frequencies and keeps almost unchanged the compression mode C_1. In other words, the three resonances strongly depend on the diameter and manifest themselves by sharp peaks, amplitude and frequencies variations in the spectrum.

To get an overview of the behavior of these modes with respect to the geometrical parameters, we start Fig. 5.4(a) with the evolution of their frequencies as a function of the diameter of the pillar for different heights (color scale). Looking at the black curves (h = 266 μm), one can see that the evolution of the bending mode B_2 is strongly dependent of the diameter while the compression mode C_1 stays almost at the same frequency. These two different behaviors result in the crossing of the two curves into a specific working point, W_p, for which the two modes B_2 and C_1 get the same frequency. For example, in this case, W_p is captured at 7.23MHz, for a diameter d = 78μm. The behavior of the frequencies of the modes, together with the evolution of W_p, is reported as a function of the height (Fig. 5.4(a)) and the thickness of the plate (Fig. 5.4(b)).

It will be shown in the next section that during the sample fabrication, etching process results in a quasi-conical shape of the silicon pillars, specially when the diameters are small. Therefore, we investigated the effect of the conicity on the eigen frequencies values (Fig. 5.4(c)). One can see that, changing θ from 0° to 6°, both the eigemodes and the working point W_p strongly shift to the low frequencies, showing how sensitive the eigen frequencies are with respect to this parameter.

Regardless of the modes, compression or bending, the eigen frequencies decrease for increasing height, increasing angle, and thinner plate. However, besides the effects of the dimensions of the pillar, the purpose of the research is to focus on the physical properties we can get when the modes are clearly separated or when the pillar works at the point W_p, *i.e.* when the two modes B_2 and C_1 are at the same value. It should be adressed that in Fig. 5.4 we

take out from the representation the torsional mode that appears in the same frequncey range. Such a mode cannot be characterized by U_z component and excited experimentally. We do not consider it in the following.

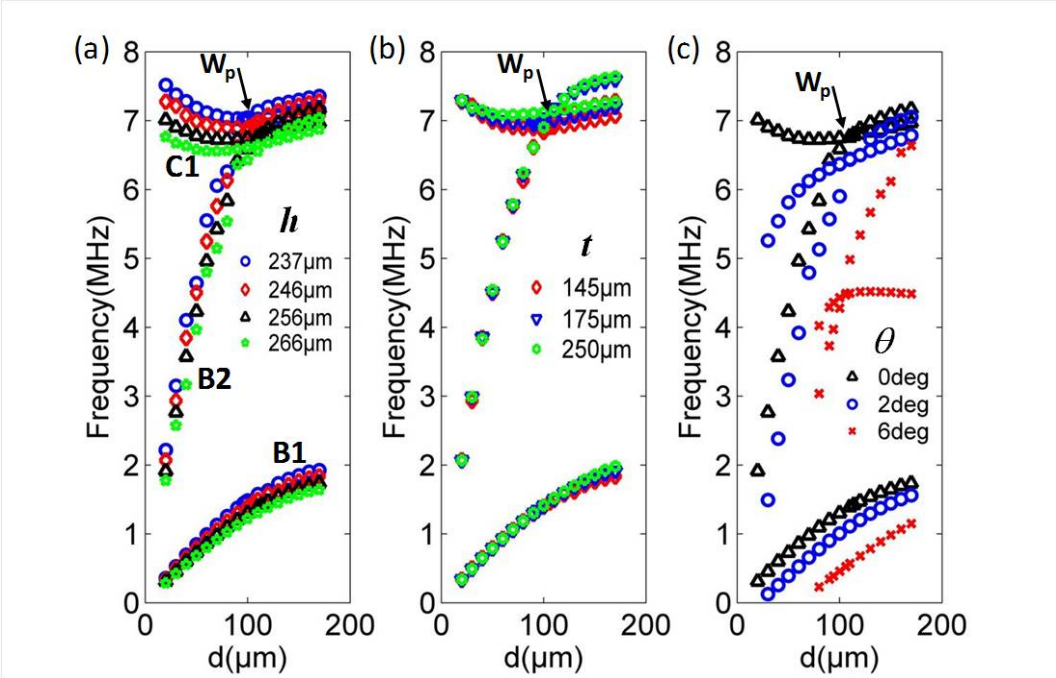

Figure 5.4 Evolution of the eigen frequencies of modes B_1, B_2, and C_1 of single pillar as a function of both the diameter (from 20 to 180 μm) and, in color scale, (a) the height h (t = 145 μm, θ = 0°), (b) the thickness t (h = 246 μm, θ = 0°), and (c) the angle θ (t = 145 μm, h = 256μm)

We mimic an experimental sample (d=96μm on top of pillar) in the numerical calculation and compare the superposed frequencies of B_2 and C_1. During the etching process, the sample pillar is a quasi-conical shape, which is also carefully sculptured for the numerical model, as shown insets in Fig 5.5. The characterized resonant frequency of bending (black line) and compression (red line) modes from experiment and simulation are displayed in the left and right panels of Fig 5.5, respectively, with a perfect match. To conclude, the quasi-conical shape only has an effect in resonant frequency, shifting to lower frequency range comparing to straight pillars ($\theta = 0^o$) with other same geometric parameters. Besides, comparing the right panel of Fig 5.5 and Fig. 5.3(b), for both B_2 and C_1, the width of the half peak of conical case is smaller than that of straight pillar. In the following part of numerical calculations, we study systems with straight pillars (without conical angle) in order to feature the physical

behaviors, including amplitude and phase information of scattered waves for isolated pillar and one line of pillars.

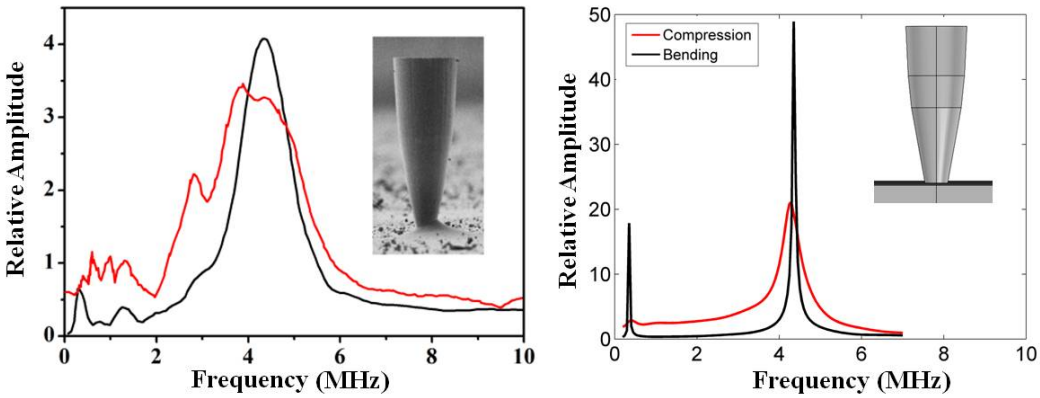

Figure 5.5 Comparison of superposed B_2 and C_1 frequencies between experimental sample and numerical model

We further complete the investigation of the far field transmission T of an anti-symmetric Lamb wave launched perpendicular to a periodic line of pillars. The Fig. 5.6(a) shows the unit cell used for the finite element calculation. PML are applied at the entrance and the exit of the slab to avoid any reflections from the external edges while periodic boundaries conditions (PBC) are applied along x-direction, on each side of the unit cell to build the infinite periodic line of pillars. The resonant frequencies of bending and compression modes are presented figure 5.6(b) for different values of the lattice parameter a. All calculations have been done with the geometrical parameters fixed to h = 256 µm, t = 145 µm, and θ = 0°. Fig. 5.6(b) shows that the resonances are almost independent of the lattice parameter a, indicating the idea of weak interaction between resonators.

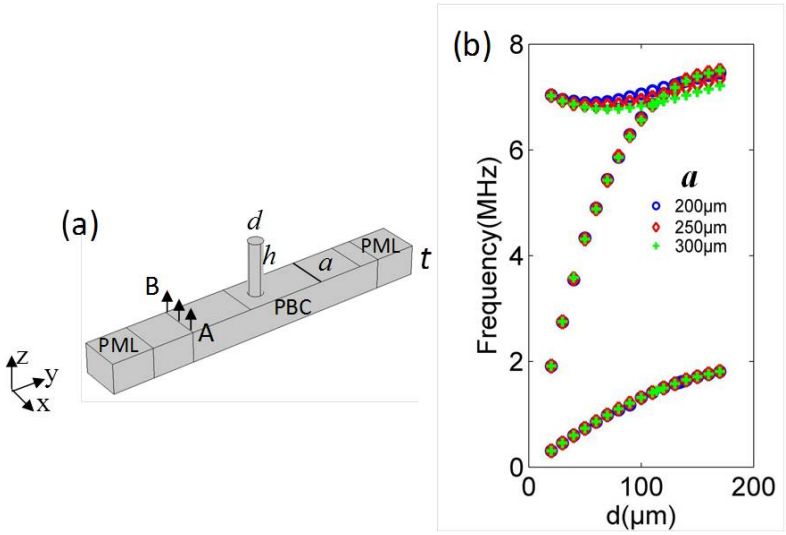

Figure 5.6 (a) 3D representation of the unit cell used for the calculation of the transmission through a line of pillar. The boundaries of the unit cell are defined with the usual periodic conditions (PBC) and the Perfectly Matched Layers (PML) (b) Evolution of the frequencies of modes B_1, B_2, and C_1 as a function of both the diameter (from 20 to 180 μm) and, in color scale, the lattice parameter *a* (*t* = 145 μm, *h* = 256 μm, and θ = 0°).

To clarify the interaction between B_2 and C_1 for one line of pillar, we calculate the evolution of their dispersion curves as a function of diameter. In the dispersion calculation, to mimic the situation of one line of pillars, the periodicity along *y* direction is chosen 10 *a*, making two neighboring pillars in *y* direction enough far away, where *a*=200μm. As shown in Fig. 5.7, the black arrow indicates the branch of B_2 and the brown arrow indicates the branch of C_1.When the diameter is 90μm, the two branches along ΓX direction cut each other. As the diameter increasing, the two branches get closer and their frequencies at Γpoint are superposed when the diameter is 112μm. Thereafter, the B_2 branch passes C_1, and they separate. The trend of the frequency evolution with diameter obeys the results in Fig. 5.6 (b). The behaviors of B_2 and C_1 dispersion curves show that these two modes are nearly independent to each other.

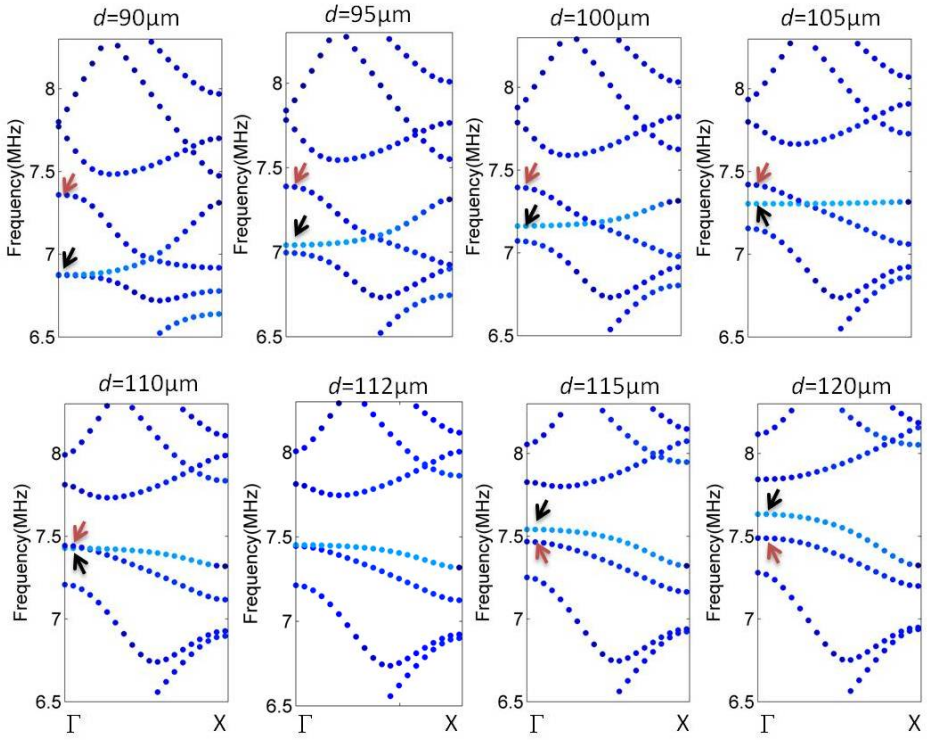

Figure 5.7 Evolution of B_2 (black arrow) and C_1 (brown arrow) dispersion branches as a function of diameter. B_2 first cut C_1, then pass by to higher frequency range

5.3 A single pillar with separated modes

First we consider a single pillar, which has separate bending and compression modes, with geometric parameters d =50µm, t =145µm, h =245µm, θ=0°. When an incident monochromatic A_0 wave is launched towards a single pillar, the amplitudes at the top of the pillar increase in the vicinity of a resonance frequency. In Fig. 5.8, the phase information of points 4 and 5 at the top of single pillar is displayed for separated modes when diameter is 50µm. For a bending mode (B_1 or B_2), points 4 and 5 are respectively in positive and negative quadrature with the incident wave. Their phase changes are π when traversing the resonance. For the compression mode, all the points including points 4 and 5 on top of the pillar vibrate in phase. They are also in phase with the incident wave for a frequency below the resonance, and become out of phase for a frequency after the resonance. Thus, their phase changes are also π when traversing the resonance.

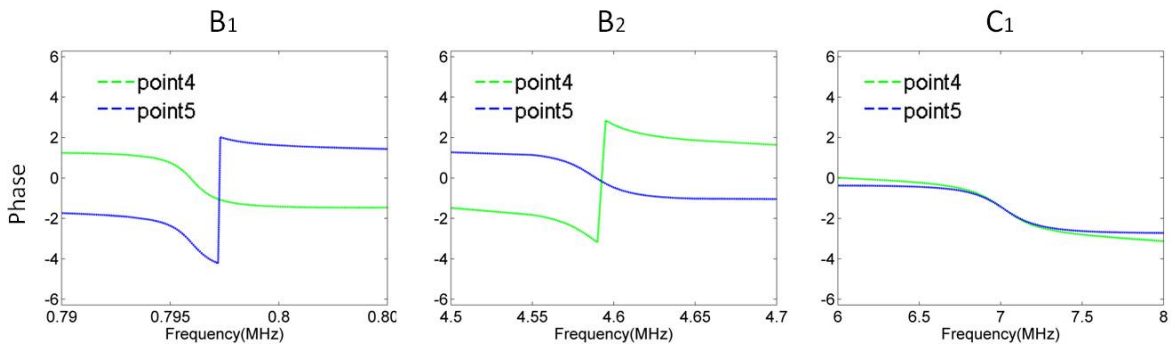

Figure 5.8 The phase of point 4 and 5 on top on the pillar when crossing B_1 (left), B_2 (middle) and C_1 (right)

From Fig. 5.3(a), one can see the separated modes of single pillar case, f_{B1}=0.796 MHz, f_{B2}=4.59 MHz and f_{C1}=7.02 MHz. The full wave field in the plate at each resonance can be regarded as a summation of the incident wave and an emitted wave by the vibrating pillar. So, emitted wave can be obtained as subtracting the full waves by the incident background wave. As the illustration in Fig. 5.1, the isolated pillar is located at the center of a plate. The diameter of the plate is 1600 μm, much larger than that of the pillar. The amplitude of emitted wave at B_1, B_2 and C_1 are displayed in Fig. 5.9 left, middle and right, respectively, where the circle is the region of the whole plate. For bending modes, the isolated pillar vibrates in *y* direction, so that it emits waves along *y* direction. From the left and middle of Fig. 5.9, the field distribution at B_1 is broader than that at B_2, because the wavelength of emitted wave at B_2 is smaller than that at B_1. For C_1 resonance, the emitted field distribution spreads in radiation along the distance to the center pillar.

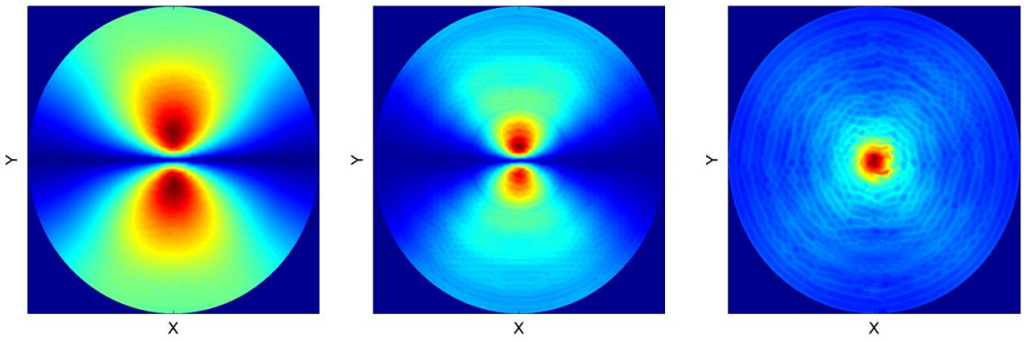

Figure 5.9 Amplitude of emitted wave by the vibrating pillar at the frequencies of B_1, B_2 and C_1, corresponding to the left, middle, and right panel, respectively. The geometric parameters are d =50μm, t =145μm, h =245μm, θ =0°.

At each resonance, the emitted wave behaves as a point source, so that its amplitude should decrease as a function of square root of the distance to the pillar sqrt(r). The normalized amplitude of emitted wave Amp/Amp$_{max}$ along the y direction crossing the pillar center at B_1, B_2 and C_1 are as shown in the left panel of Fig 5.10. We further multiply the normalized amplitude of emitted waves by sqrt(r) and get a numerical vibration near a constant. Such operations are implemented for B_1, B_2 and C_1 modes corresponding to right panel of Fig. 5.10, from which the numerical vibrations after operation for different modes are almost near a constant, demonstrating that the pillar in resonant vibration plays a role of point source to emit waves.

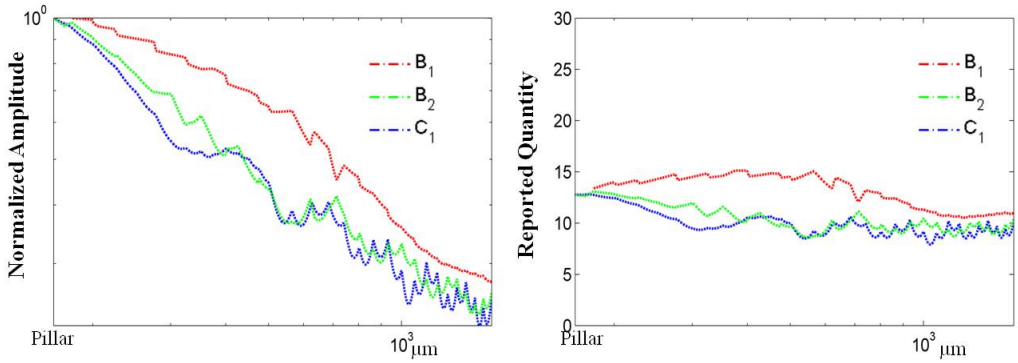

Figure 5.10 Left panel: Normalized amplitudes of emitted waves at B_1, B_2, and C_1; Right panel: Multiply the amplitudes by sqrt(r), getting numerical vibrations near a constant.

In order to study in more details about emitted waves, we detect a point 500μm away behind the pillar and plot real and imaginary values of the corresponding emitted waves at this position induced by B_1, B_2 and C_1, as shown in left panel of Fig. 5.11. Here, the emitted waves are normalized with respect to the incident wave. The red, green and blue curves are ellipse-like shapes. In this complex plot, if a point locates at the $+x$, $+y$, $-x$ and $-y$ axes, it means that the phase of emitted wave with respect to the incident wave at the corresponding frequency is 0, π/2, π/-π and –π/2, respectively. To show in more details, five frequencies in the vicinity of resonances are plotted for each resonance in the second, third and the last panel

of Fig. 5.11. The ellipse induced by B_1 is emitted wave in the frequency range (0.77, 0.81) MHz. It cuts the $-x$ axis at x = -1.03 when f=0.7962MHz (at this frequency the emitted wave is out of phase with respect to incident wave) with a maximum amplitude as 1.04, which shows that the amplitude of emitted wave is a bit larger than the amplitude of incident wave at this out of phase frequency. Therefore the vibration detected at this frequency is dominated by emitted wave after a cancellation between emitted and incident waves. Consequently, in the right panel we can observe clearly that the phase of total wave at f=0.7962MHz with respect to ranges far away from the resonance reaches π. In the vicinity of origin point, the B_1 induced ellipse approaches the origin point very closely, so that the phase shift of emitted wave before and after B_1 resonance is π, as shown the black curve in the right first panel.

For B_2 and C_1 resonances, the corresponding green (4.1~4.9MHz) and blue (6.15~9MHz) ellipses cut the $-x$ axis at x=-0.21 (f=4.59MHz) and x = -0.1 (f=7.3MHz), with maximum amplitudes as 0.31 and 0.17, respectively. After the interaction between the emitted wave and incident wave, the vibrations at the detected point are still dominated by the incident wave, but with some phase shift, as seen in the total waves curves in the right panel. These two ellipses are close to the origin point, but not as close as the B_1 induced ellipse, so the phase shift of emitted wave before and after B_2 or C_1 resonance is close to π, but not exactly π, as shown in the black curves in the right first panel.

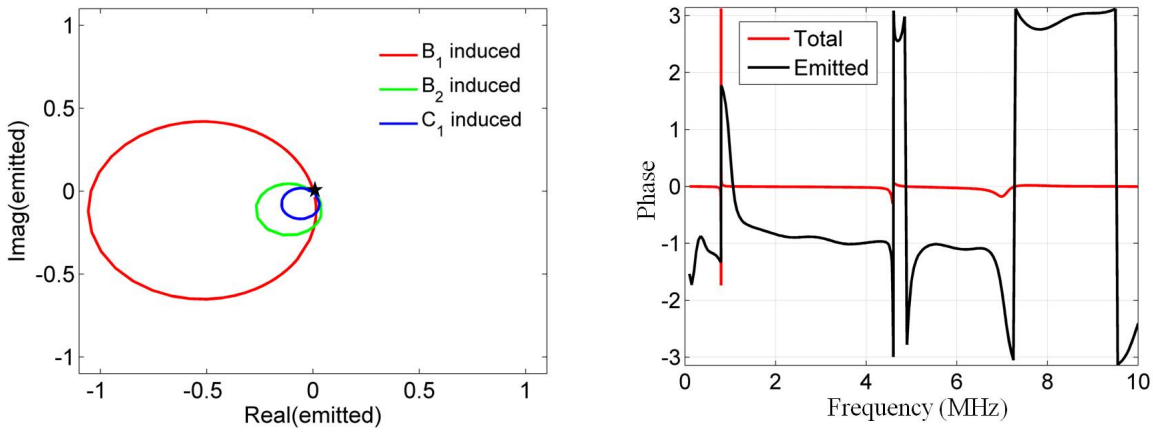

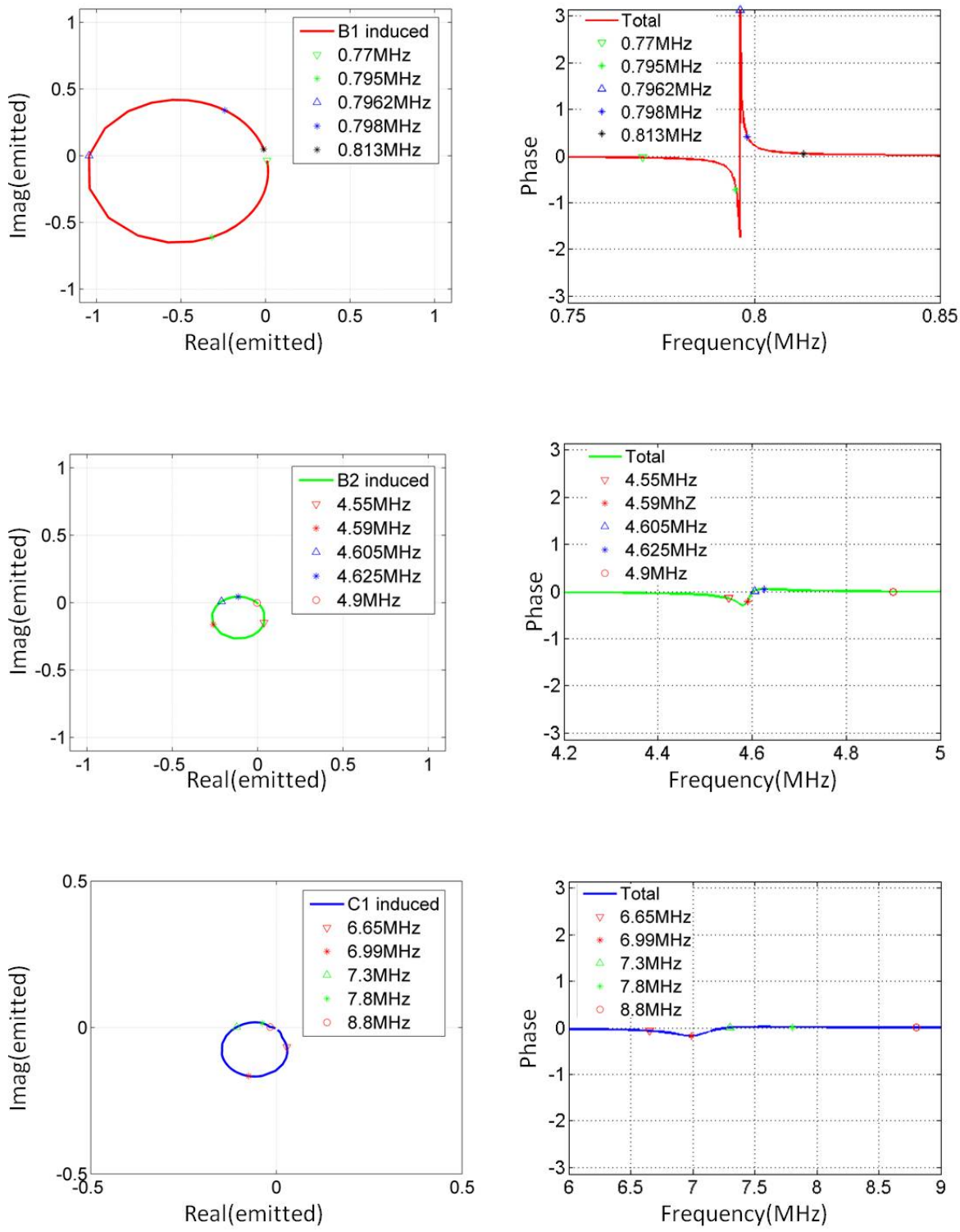

Figure 5.11 First panel: The left is complex plots of emitted wave induced by B_1 (red), B_2 (green) and C_1 (blue), the right is the phase of emitted (black) and total (red) waves; Second panel: The left is complex plots of emitted wave induced by B_1 (red), the right is the phase of total (red) waves; Third panel: Similar plot as in the second panel but for B_2; Last panel: Similar plot as in the second panel but for C_1

In Fig. 5.10, it is shown that the vibrating single pillar plays as a source emitting waves at the resonance and the amplitude of emitted wave decreases with the distance to the pillar. On

the other hand, the amplitude of incident wave is steady in a homogeneous plate without any pillar. Therefore, emitted waves induced by resonant pillar at different positions will have different amplitudes. To valid it, we especially detect a point 250μm away behind the single pillar (only for this figure), and the corresponding amplitude should be higher than that in Fig. 5.11. From the left panel of Fig. 5.12, the green and blue ellipses are obviously much bigger than those in Fig. 5.11. The red, green and blue ellipses cut the $-x$ axis at x=-1.04, x=-0.37 and x = -0.14, with maximum amplitudes as 1.05, 0.48, and 0.34, respectively. Similar results can be found as analyzed in Fig. 5.11.

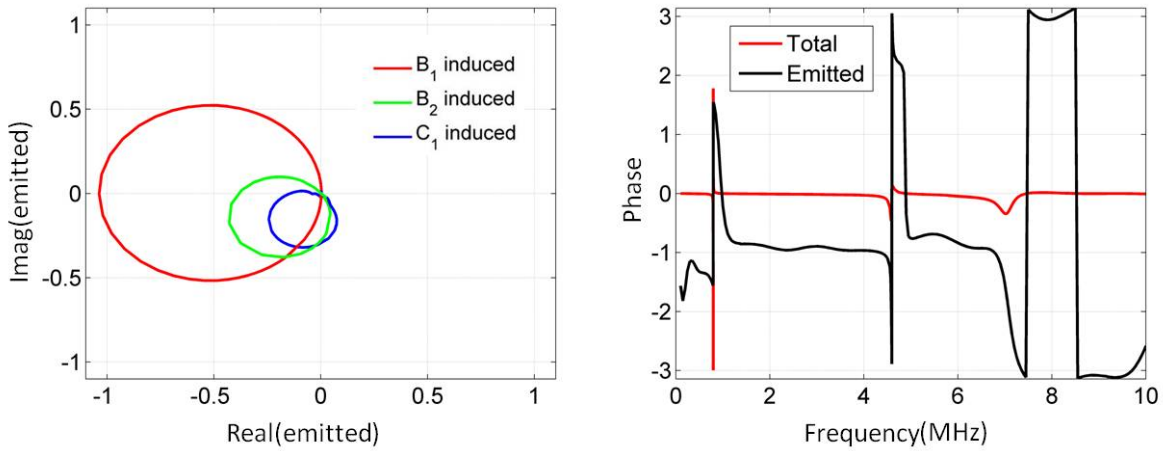

Figure 5.12 Same results as in Fig 5.11 but for a detected point 250μm away behind the single pillar

5.4 A single pillar with superposed modes

The situations of W_p point in Fig. 5.4 are the superposition of B_2 and C_1 modes. The localized modes of pillar, especially bending modes, are very sensitive to pillar's geometric parameters, such as diameter and height. By tuning the diameter of the pillar, keeping other geometric parameters fixed, we can achieve B_2 and C_1 in the superposition when diameter of single pillar is d=100 μm, with f_{B1}=1.42 MHz, $f_{B2/C1}$=6.93 MHz, as shown in Fig. 5.3(b).

Figure 5.13 presents the phase of points 4 and 5 on top of the single pillar in the vicinity of resonances. Their behaviors for B_1 resonance are similar to that in Fig. 5.8. However, the

B_2/C_1 resonance has aspects both of bending and compression modes, so that the vibrations of points at the top of pillar are not in phase any more, especially for points 4 and 5 due to the combination of bending and compression. When traversing the resonance, there is obvious phase difference between points 4 and 5, as clearly shown in the right panel.

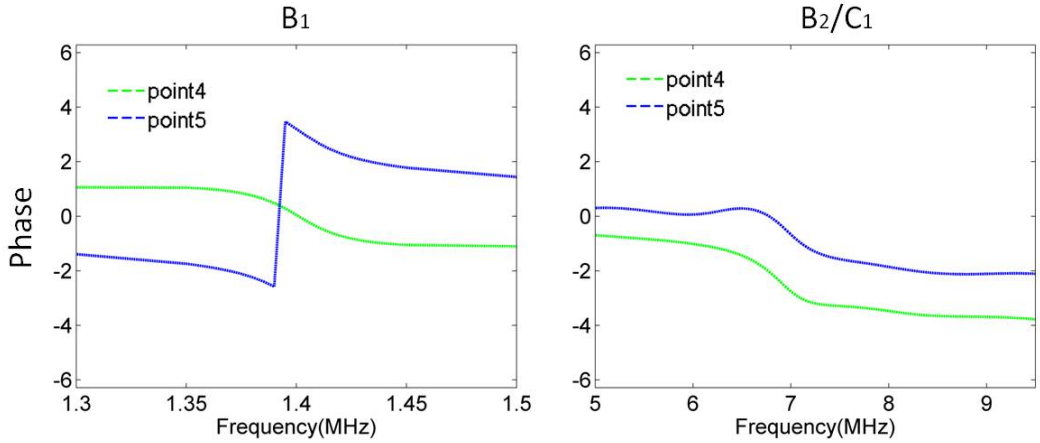

Figure 5.13 The phase of point 4 and 5 on top on the pillar when crossing B_1 (left) and B_2 / C_1 (right)

To evaluate the property of emitted waves by the B_2/C_1 mode, we show the normalized amplitudes of emitted waves by B_1 and B_2/C_1 modes in the left of Fig. 5.14. In the right panel, we also multiply their amplitudes by sqrt(*r*), obtaining numerical vibrations near a constant. The emitted waves by the superposition modes follow the same energy law, acting as waves generated from a point source and spending with a decrease in amplitude as a function of sqrt(*r*).

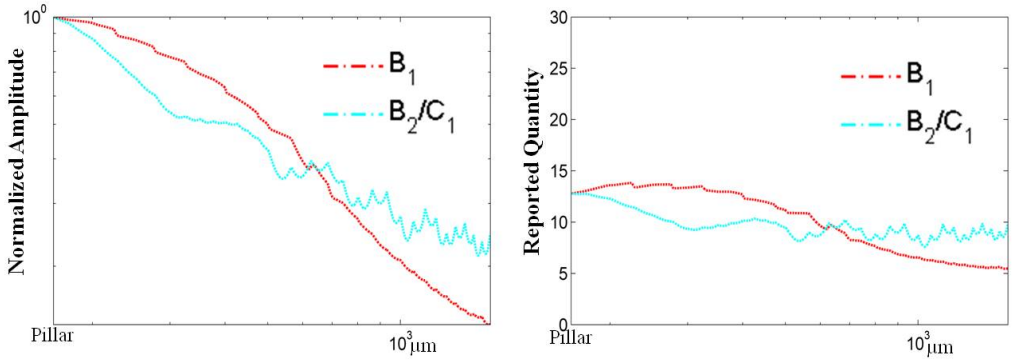

Figure 5.14 Left panel: Normalized amplitudes of emitted waves by B_1 and B_2/C_1 modes; Right panel: The results of multiplying their amplitudes by sqrt(*r*)

In Fig. 5.15, the maximum normalized amplitudes of emitted waves induced by B_1 and B_2/C_1 resonances are 0.92 and 0.41, respectively. They cut the $-x$ axis at x=-0.85 and x=-0.22, respectively. It is important to point out that the shape of cyan line is like one overlapped ellipse by two small ones. Its maximum amplitude 0.41 is larger than individual B_2 and C_1, as shown in Fig. 5.11. Besides, the 0.92 maximum amplitude of emitted wave induced by B_1 is smaller than that in Fig. 5.11, this is due to the fact that the vibration of the single pillar with d=100μm is less strong than that with d=50μm, as one can see the relative amplitude on top of pillar in Fig. 5.3. In the middle and lower panels of Fig. 5.15, we show 5 frequencies on the ellipse and the corresponding phase of total wave for B_1 and B_2/C_1 resonances.

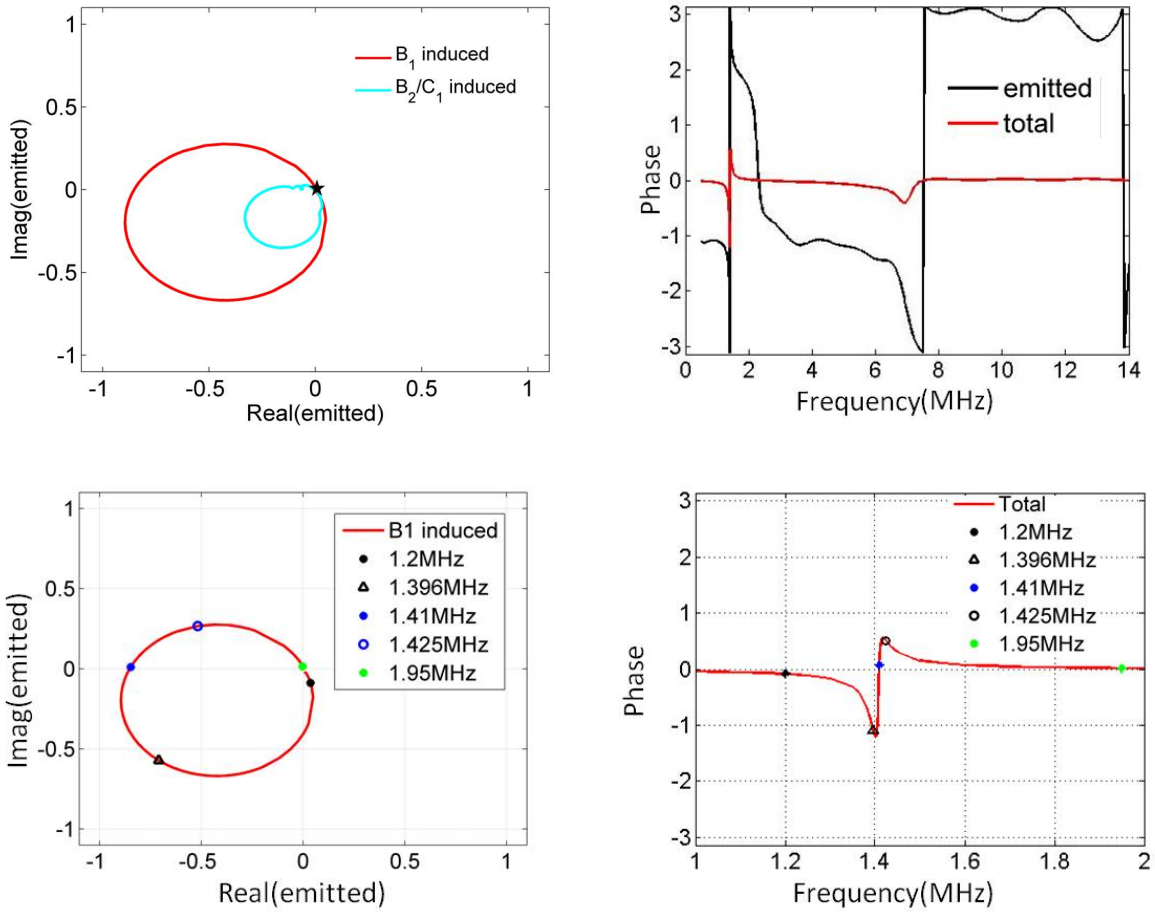

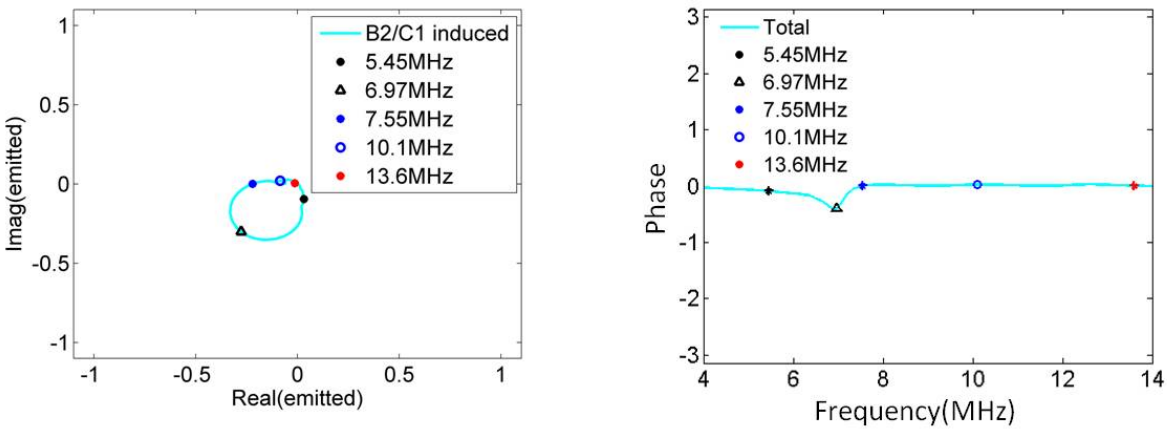

Figure 5.15 Upper panel: The left is complex plots of emitted wave induced by B_1 (red), B_2 / C_1 (cyan), the right is phase of emitted (black) and total (red) waves; Middle Panel: the left is complex plots of emitted wave induced by B_1 (red), the right is phase of total (red) waves; Lower panel: the left is complex plots of emitted wave induced by B_2 / C_1 (cyan), the right is phase of total (cyan) waves

5.5 One line of pillars with separated modes

For one line of pillars, with geometric parameters d =50μm, t =145μm, h= 245μm, θ=0°, bending and compression modes are separated as in case of isolated pillar. From Fig 5.16, the red line stands for compression mode and black line stands for bending mode. For each resonant mode, there is a dip in the transmission curve as marked by the green line. The color of dispersion curves indicates the quantity $\Omega = \int_{pillar} \sqrt{u_x^2+u_y^2+u_z^2}\,dV \,/\, \int_{unitcell} \sqrt{u_x^2+u_y^2+u_z^2}\,dV$, which means the percentage of elastic energy localized in the pillar over the whole unit cell. To mimic one line of pillar, the size of unit cell taken in the dispersion calculation is $a\times 10a$, with periodic boundary conditions applied in x and y axis. As one can see, the resonances in the left correspond well to the resonant flat branches in the right dispersion curves. The transmissions at each resonant frequency are T_{B1}=0.08, T_{B2}=0.41, T_{C1}=0.04. The color flat branch between B_2 and C_1 in the dispersion curve is the torsion mode, which cannot be excited by anti-symmetric Lamb incident waves.

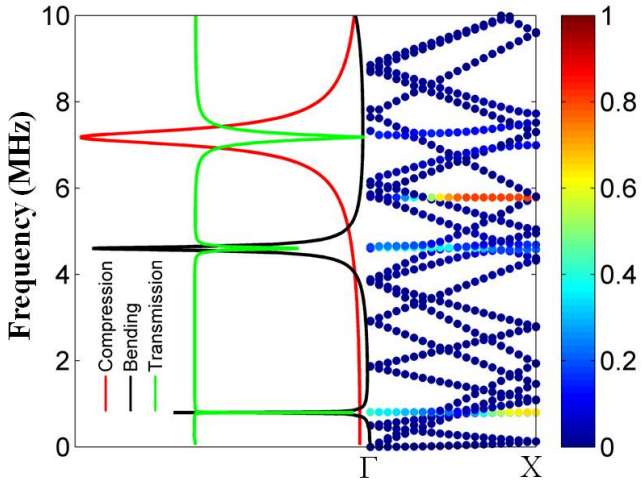

Figure 5.16 Transmission (green), compression mode (red) and bending mode (black) for one line of *d*=50 μm as well as the corresponding dispersion curve. The color bar means the percentage of vibration in the pillar part over the whole geometry. The black and red modes curves are divided by 33 in order to be shown with transmission in the same figure

For the phase of points 4 and 5 on top of the pillar shown in Fig. 5.17, they have almost the same behaviors as in the single pillar case in Fig. 5.8. For a bending mode (B_1 or B_2), points 4 and 5 are respectively in positive and negative quadrature with the incident wave. Their phases change also by π when traversing the resonance. For the compression mode, all the points including points4 and 5 on top of the pillar vibrate in phase. They are in phase with the incident wave for a frequency below the resonance, and become almost out of phase for a frequency after the resonance. Thus, their phase changes are also approximately π when traversing the resonance.

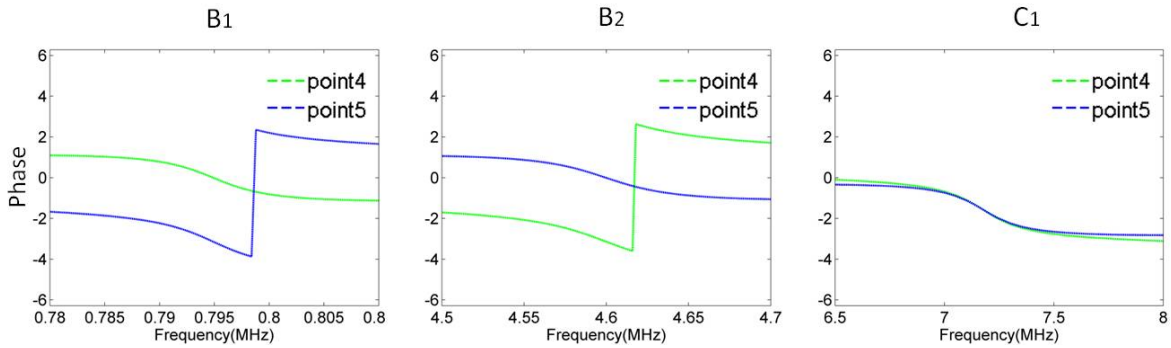

Figure 5.17 The phase of point 4 and 5 on top on the pillar when crossing B_1 (left), B_2 (middle) and C_1 (right)

The first row of Fig. 5.18 is the plot of complex value of emitted waves in the frequency range [0, 10] MHz, including B_1, B_2 and C_1 resonances, with respect to the incident waves. The shape of complex value for each resonance is also ellipse-like shape. The frequency ranges beyond resonances are located close to the origin point as the pillar almost does not emit waves, as marked by the black star in the center point. The maximum amplitudes of emitted waves induced by B_1, B_2 and C_1 resonance are 0.92, 0.59 and 0.96, respectively. Also, the three ellipses cut the $-x$ axis at x=-0.92, x=-0.59 and x=-0.96, respectively. Comparing the transmission values in the case of one line of pillars, we can claim that, at a given position, the incident and emitted waves at the resonant frequencies are out of phase, so that if the amplitude of emitted waves exactly equals that of incident waves, the resulted transmission is 0. With different amplitudes of emitted wave, the phases of transmitted waves have different shifts near resonances, as shown in the right panel of Fig. 5.18. One point to be noted, the three ellipses of emitted waves by one line of resonant pillars very closely approach the origin point (but not exactly cross the origin point), and they have well symmetries with respect to the x axis, thus the phase of emitted wave far from the resonances with very small amplitude is $\pi/2$ phase shifted with respect to the incident wave.

The second, third and last rows of Fig. 5.18 present several frequencies in the vicinity of B_1, B_2 and C_1 resonance, respectively, on the emitted ellipses as well as its corresponding phase of transmitted waves.

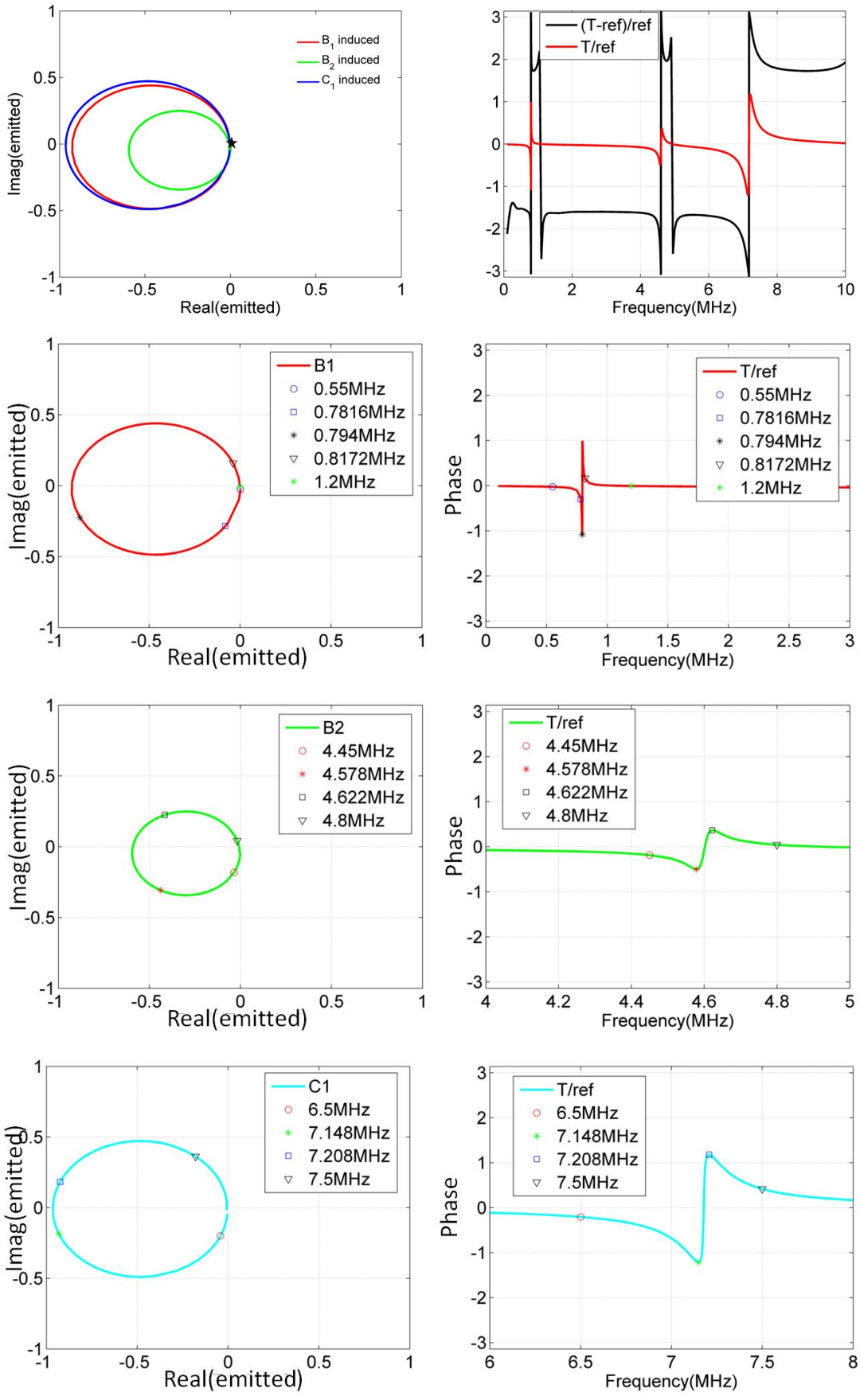

Figure 5.18 The first row: in the left is the complex plots of emitted wave induced by B_1 (red), B_2 (green) and C_1 (blue), in the right is the phase of emitted wave (black) and transmitted wave (red); The second,

third and forth rows are frequency dots in the vicinity of B_1, B_2 and C_1 resonances, respectively, on the emitted ellipses as well as the phase of transmitted wave

5.6 One line of pillars with superposed modes

For one line of pillar, with geometric parameters d=112μm, t =145μm, h= 245μm, θ=0°, B_2 and C_1 are superposed, which is clearly exhibited in the left panel of Fig. 5.20. The phase of points 4 and 5 on top of the pillar, as shown in Fig. 5.19, is similar to that in Fig. 5.13. Especially for B_2/C_1, points 4 and 5 are not in phase because of the aspect of bending vibration as compared to the compressional vibration.

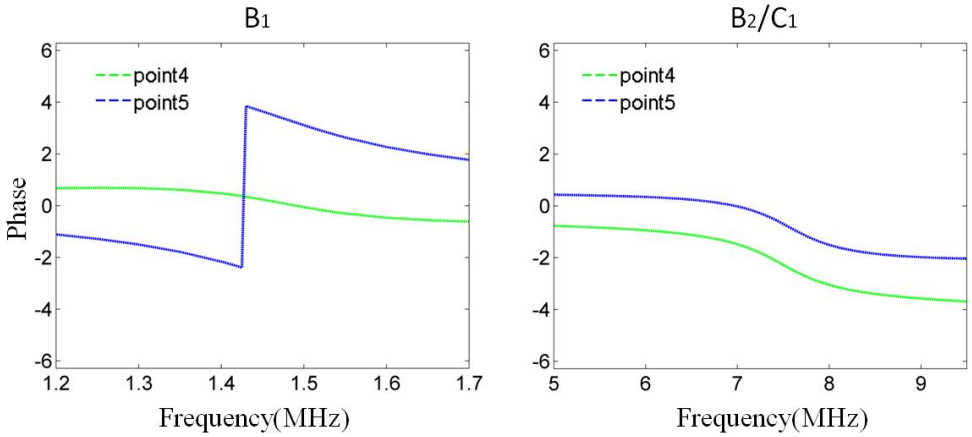

Figure 5.19 The phase of point 4 and 5 on top on the pillar when crossing B_1 (left) and B_2 / C_1 (right)

The amplitudes of transmission at B_1 and B_2/C_1 resonances are T_{B1}=0.21 and $T_{B2/C1}$=0.57. The amplitude characterizations at the top of pillars as black and red curves are divided by 10, in order to be presented in the same figure. In the right panel of Fig. 5.20, the shapes of complex plots for B_1 and B_2/C_1 induced emitted waves are ellipse-like, showing their maximum amplitudes as 0.79 and 1.57, respectively, which are also the points cutting the $-x$ axis. So the emitted wave at the resonant frequency is out of phase with incident wave. The most interesting point here is that the B_2/C_1 induced emitted waves at the out of phase frequency have bigger amplitude than incident waves, which enables transmission, but with a π phase shift with respect to the incident wave. The transmission at the B_2/C_1 resonant

frequency is 0.57 and its corresponding phase is π with respect to the incident wave as this transmission is dominated by emitted wave (as shown in Fig. 5.21). Besides, the phase shift of emitted wave induced by B_2/C_1 before and after the resonance is also about π, as the cyan ellipse approach very closely the origin point. Because of the symmetry with respect to *x* axis, the phase of emitted wave at all the non resonant frequency ranges is also about π/2 or -π/2, as shown in Fig. 5.21.

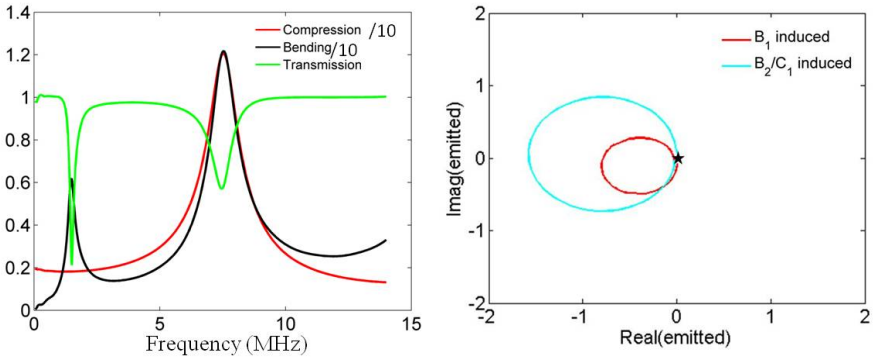

Figure 5.20 Left panel: Transmission and amplitude characterizations (divided by 10) of one line of pillars with *d*=112µm; Right panel: Complex plots of emitted wave induced by B_1 (red), B_2/C_1 (cyan) modes.

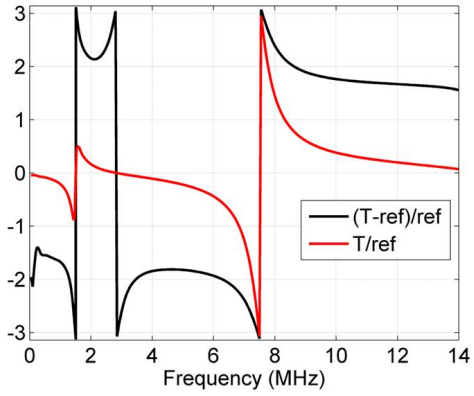

Figure 5.21 Black line is the phase of emitted wave; red line is the phase of the total wave at the same point in the far field

5.7 Discussion

To study in more details the case of B_2 and C_1 superposed resonances, we further show one line of pillars with diameters *d*=90, 92 95, 112, 115 and 120µm in Fig. 5.22. All mode

characterizations are divided by 80 in the left panel in order to compare with transmission. For d=90μm, the complex plot of emitted wave induced by this superposed resonance is heart-shape, which cut the $-x$ axis at x=-0.989 which causes a transmission dip 0.011 at f=7.15MHz. As the cut point does not reach x=-1, although the transmission is very small at this frequency, but the phase of transmitted wave cannot reach π or $-\pi$, as shown in the corresponding right panel. From d=92μm to 95 μm, the heart-shape merges into quasi-ellipse and cuts the $-x$ axis over x=-1, so that there is new transmission contributed by emitted wave and the phase of transmitted wave as correspond to the incident wave reaches π or $-\pi$ at the corresponding frequency where it cuts the $-x$ axis. When d=112μm, the mode characterization curves for B_2 and C_1 are exactly superposed which has a minimum value x=-1.57 for the cyan ellipse cutting the $-x$ axis, and contributes to a maximum new transmission 0.57 at the corresponding frequency. From d=112μm to 120 μm, the B_2 mode moves to a bit higher frequency than C_1 mode. When d= 120μm, the cyan ellipse cuts the $-x$ axis at x=-1.54 which contributes a new transmission 0.54.

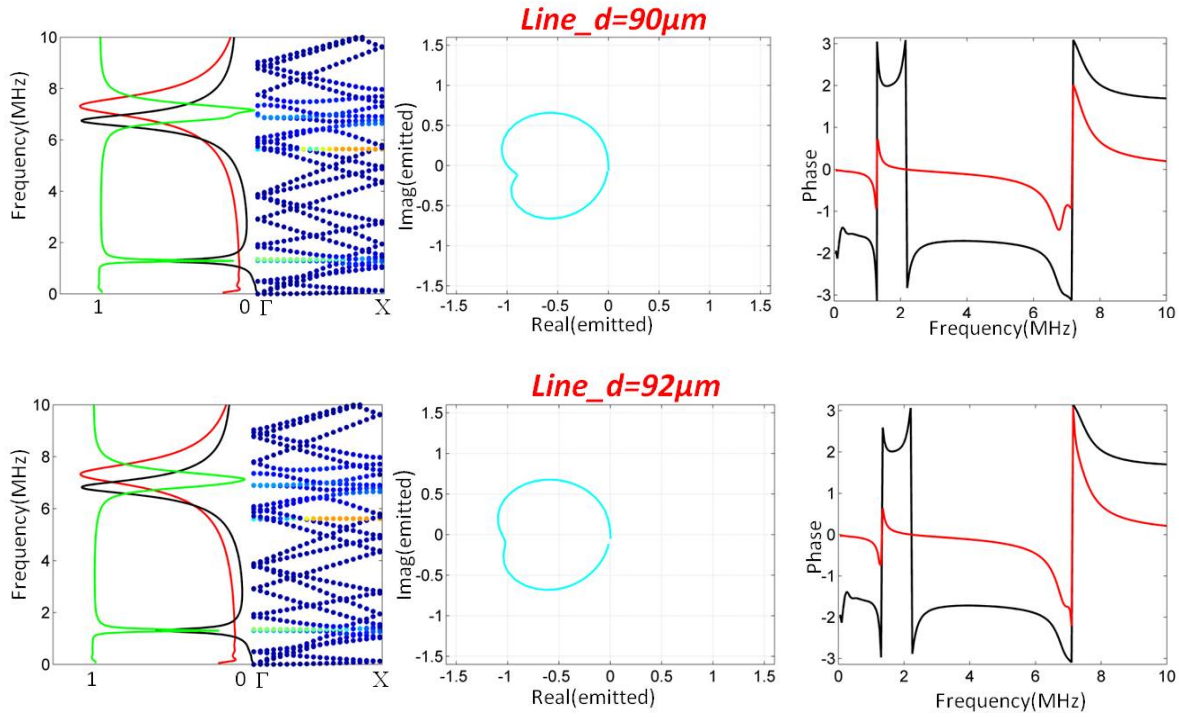

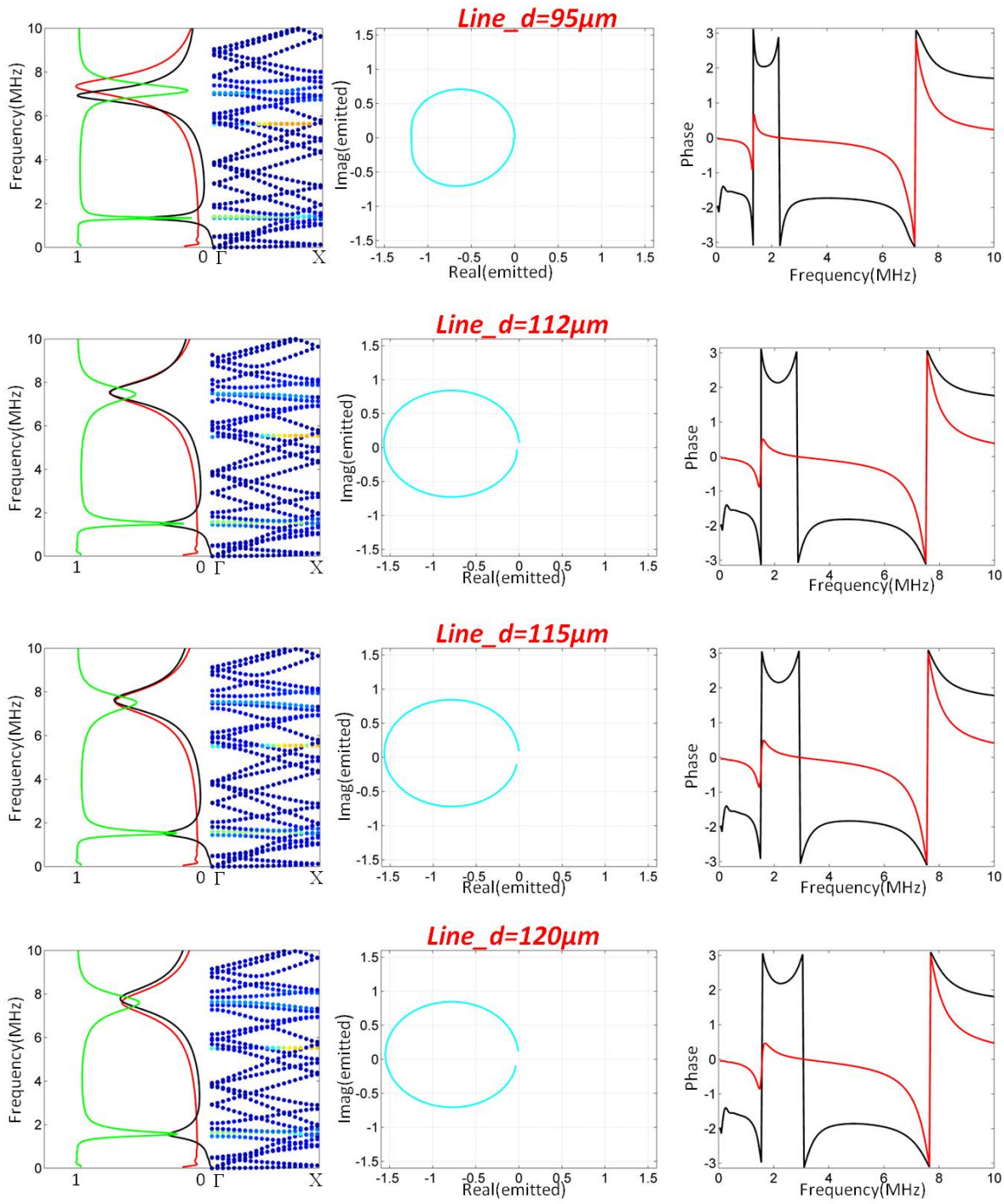

Figure 5.22 Left panel: Transmission (green) and modes characterization (divided by 80) (black for bending and red for compression) as well as dispersion curves of one line of pillars; Middle panel: complex plot for B_2/C_1 resonance; Right panel: phase of transmitted (red) and emitted (black) waves

From Fig. 5.6, one can observe that the resonant frequencies are very weakly sensitive to the lattice parameter. Therefore, the infinite adding of single emitted wave along *x* direction with a periodicity *a* will produce the similar result that from one real line of pillars, as

managed by Huygens-Fresnel principle[179]. Fig. 5.23(a) is the phase distribution of emitted wave by a single pillar at the frequency of C1, which corresponds to Fig.5.6. In Fig. 5.23(b), 5 of the same emitted waves are added with an inter-distance *a*. The central 5 dots stand for the positions of pillars. The adding of emitted waves makes the total emitted wave more flat at the middle. In Fig. 5.23(c), same operation is taken as in (b) but for 9 single emitted waves. From the phase in the middle 9-pillar part, we can see the total emitted wave at the edge in *y* direction is nearly a plane wave. Fig. 5.23(d) presents the real one line of 9 pillars located at the center and its lattice parameter is also *a*. The sizes of square for the all figures are the same, 6000μm×6000μm. From phase (upper panel) and amplitude (lower panel), the results of artificial 9 pillars and the real one line of 9 pillars are almost the same, producing a quasi-plane wave at 1 ~ 2 wavelength away from the center in *y* direction. The procedure in this figure proves that the resonances are almost independent of lattice parameter and the total emitted wave by adding infinite single emitted wave is a plane wave.

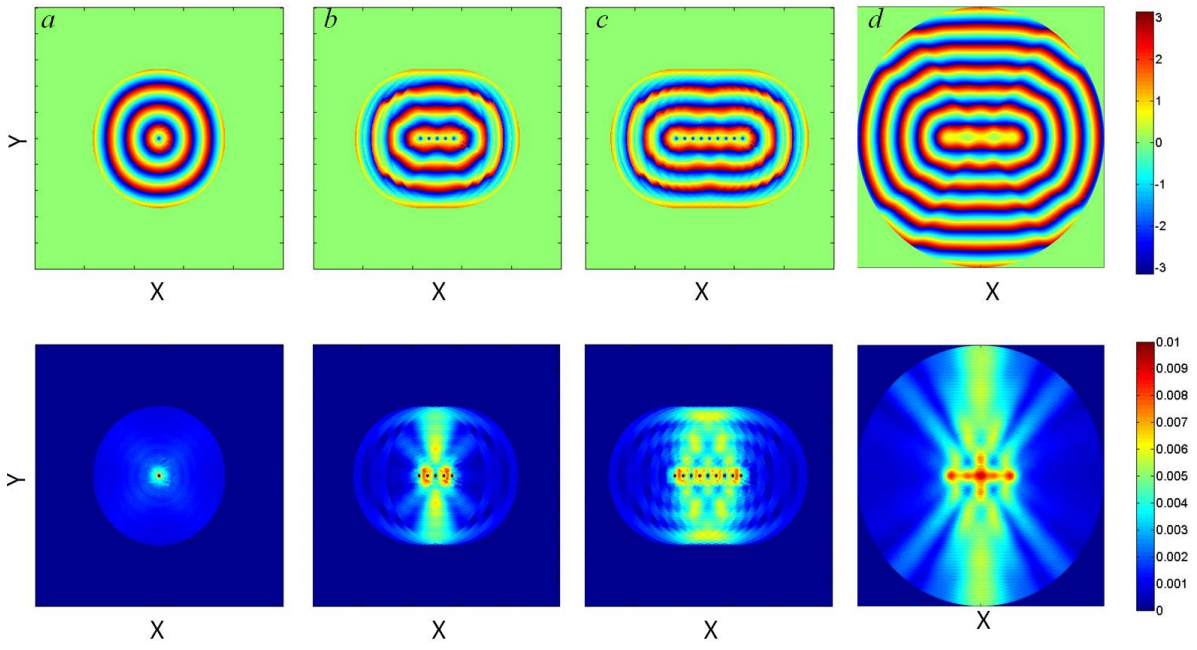

Figure5. 23 Phase (upper panel) and amplitude (lower panel) of (a) emitted wave at the frequency of C1 as shown in Fig. 5.9; (b) adding 5 single emitted wave at C1, with the inter-distance as lattice parameter *a*=200μm; (c) similar as in (b) but adding 9 single emitted wave at C1; (d) one real line of 9 pillars

5.8 Conclusion

In this chapter, we proposed acoustic metasurfaces consisting of a single pillar or one line of pillars deposited on a thin plate. Numerically and experimentally, we detected amplitude and phase information of points on top of pillar and in far field on the plate, characterizing the local resonances of bending and compression in the sub-wavelength ranges. The local resonances are very sensitive to the geometric parameters, such as the diameter, height and conical angle of pillars, making the superposition of bending and compression possible. For a single pillar, we studied the scattering properties when bending and compression resonances are separated and superposed, and found that the scattered waves in the close vicinity of resonances can have a π shift with respect to incident wave, which corresponding to the real-imaginary plot of emitted wave cutting the $-x$ axis. For the superposed resonance of bending and compression, the phase of scattering waves also has a π shift at the frequency of cutting the $-x$ axis, and the scattering wave has a larger amplitude than those in separated case. For one line of pillars, from both dispersion and transmission, it is found that local resonances cause transmission dips. Due to the different positions where the emitted wave complex plots cut the $-x$ axis, the transmission dips have differences in amplitude and phase. When the bending and compression resonances are superposed, the amplitude of scattering waves is bigger than that of incident waves at the corresponding out of phase frequency, resulting in a new transmission dominated by emitted wave with out of phase property respecting to the incident wave. Finally, we demonstrated that how the ellipses of bending and compression resonances get emerged from separated case for one line of pillars. Adding the compressional emitted wave by single pillar with a periodicity to mimic one line of pillars, the result of this artificial assembling approaches a plane wave, which is almost the same result of one real line of pillars, proving that the resonances of the pillar are almost independent to each other

Chapter 6

General Conclusions and Perspectives

6.1General conclusions

Acoustic artificial structured materials, namely phononic crystals and acoustic metamaterials, offer opportunities to control acoustic/elastic waves in limitless ways. In this thesis, we focus on the design and characterization of new kinds of these materials.

Firstly, an active acoustic metamaterial with piezoelectric resonant structures is proposed to exhibit double negativity (effective mass density and elastic modulus) over a certain frequency range. By switching the electric boundaries of the piezoelectric material, the negative properties can be actively controlled. The resonance could be strengthened to broaden the frequency band of the negative effective properties through the stacking of the multi units, also lowering the first resonant frequency. The number of resonances and segments of double negative bandwidth increase with the number of stacked units.

Secondly, we used newly developed homogenization method to discover the simultaneous control of S_0 and A_0 Lamb modes or even the full control of the fundamental Lamb modes. An approximating and simple method is proposed to fast calculate the effective phononic crystal plate by considering a plate as a finite slice of bulk medium. A GRIN flat lens, Luneburg lens and Maxwell lens are designed and numerically simulated to valid the simultaneous control of Lamb waves. Also, a more advanced device is shown which consists in a circular lens working as a Luneburg lens for the S_0 and SH_0 modes and as a Maxwell lens for the A_0 mode. Besides focusing energy, the method is further implemented to design beam splitters to diverge wave energy in different angles with respect to incident wave. The performance of these gradient index devices is broadband, since the method is based on homogenization theories in the quasi-static limit. The presented methods can be efficiently employed to the design of devices for the control or harvesting of mechanical energy, as it allows the full control of vibrations excited in a finite elastic plate.

The homogenization method employed to control the Lamb wave exhibits an additional coupling tensor $\boldsymbol{S}$, corresponding to the "Willis" term as proposed by J. R. Willis. We proved that the value of "Willis" term is non-zero if breaking the symmetry in the unit cell, realizing a "Willis" medium. However, in the local approximation, it is found that the "Willis" S terms do not affect the dispersion of bulk Willis medium as they appear in conjugate pair in dispersion equations. Due to the existing of boundary conditions, we showed the dispersion of SH_0 mode of "Willis" plate is different from the corresponding in-plane mode of "Willis" bulk medium, as the clear evidence of Willis plate. We further analytically developed the calculation of dispersion of "Willis" plate, and exhibited the significant changes to the dispersion curves if changing the value of the "Willis" S term.

Thirdly, we investigated the vibration properties of phononic crystal plates with hollow pillars deposited on top. Due to the introduction of inner hole in the pillars, new branches originating from the excitation of quadrupolar whispering-gallery modes (WGMs) appear in the both Bragg and low frequency band gaps. The frequency of the WGMs can be tuned by changing the inner radius, and the quality factor can be improved by inserting a full cylinder as a confinement between the hollow pillar and the plate. The occurrence of WGM gives rise to a transmitted pass band that can be used as a high resolved filter, which are further applied to design different kinds of multiplexers, based on multichannel or monochannel waveguide or cavity. By filling liquids in the hollow pillars, the phononic crystal plate exhibits new localized modes originating from the compression of liquids or coupling of the dipolar-shape vibration of liquid and solid. These localized modes can be actively tuned by controlling the kinds of liquid, the height of liquid or temperature, which can be applied to sense acoustic properties of different liquids.

A new type of tailored phononic crystal plate was also presented, whose unit cell is constituted by pillars connected by thin bars instead of being deposited on a full plate. By

narrowing the bars, the Bragg band gap becomes much wider and extends to sub-wavelength region while the low frequency gap moves to extreme low frequency region. Such new structure can generate high orders of WGMs, namely quadrupolar, hexapolar and octopolar shapes, inside band gaps. Higher order of WGMs has higher quality factor. The phononic crystal plate with higher orders of WGMs and localized compressional and dipolar-shape coupling modes can be applied to wireless communication and sensing with the possibility of active control.

Finally, we proposed acoustic metasurfaces consisting of a single pillar or one line of pillars deposited on a thin plate. Local resonances of dipolar and monopolar in the sub-wavelength ranges can be characterized, which are very sensitive to the geometric parameters of the pillar, such as diameter, height and conical angle. The scattered waves by resonances have a π shift with respect to incident wave. For one line of pillars, from both dispersion and transmission, it is found that local resonances cause transmission dips as the results of the interaction between out of phase scattering and incident waves. By tuning the pillar's geometric parameters, the dipolar and monopolar resonances can be superposed, which scattering waves have larger amplitude comparing to their separated cases. For one line of pillars, the amplitude of out of phase scattering waves at superposed resonance is bigger than that of incident waves at the corresponding resonant frequency, resulting in a new transmission with out of phase property.

6.2Perspective

The study of piezoelectric superlattice is carried out by the normal incidence in the Chapter 2. The case of oblique incidence is expected to be investigated in future, as it will bring more parameters, such as k_x, into the coupling matrix. The negative properties may also depend on the angle of incidence. Besides, bias voltage can be further applied to the piezoelectric materials to play an active role in tuning parameters.

The gradient index devices have much potential in controlling acoustic/elastic waves, such as absorption, focusing and deflection. The absorption application deserves to be further studied with structures like acoustic black hole. The method developed in this work for controlling all the fundamental Lamb waves can help to improve the absorbing functionality as the acoustic black hole can absorb all fundamental Lamb modes despite the fact that mode conversion happens during the source excitation or wave interaction with the devices. The experimental examples of GRIN devices with multimode control are expected to be carried out.

The study on Willis medium attracts more attention recently. The theory developed in this work offers a promising way to investigate the properties of Willis medium. The non-local phononic crystals are Willis medium, where the non-local property, including the behaviors along each dispersion curve, deserves to be studied in details. For local chiral phononic crystals, they also behave as Willis medium, especially in the case of a Willis plate. The symmetry of Willis term, as well as solving the dispersion eigen-equations with different Willis terms should be studied further. The essential properties of the symmetry in Willis term matrix is also deserve to be figured out. The transmission property between normal medium and Willis medium is also very interesting. It is expected that, even the longitudinal wave with normal incidence into the Willis medium will excite both of longitudinal and transverse waves, which is different from normal elastic case.

The phononic crystal plates with pillars have great physical potential in novel phenomena. By arranging the positions and shapes of two lines of pillars, Fano resonance is expecting to be observed. Instead of designing the geometry of a pillar with bending and compressional resonances at the same frequency, two different pillars at in the same unit cell which one's bending resonance and the other's compressional resonance are superposed can be studied further. Input external energy, such as force on top of pillars or bias voltage for piezoelectric pillars, how the resonant behaviors and scattering properties change is very interesting to be paid attention. Comparing with the periodic arrangement of pillars on the plate, the properties of band gaps, vibration and transmission of disordered pillars should be studied in next steps.

For one line of pillars, when the bending resonance is tuned to pass compressional resonances, the slope of B_2 dispersion changes from positive to negative, which is similar to the negative refraction property. Such possible connection can be further studied in future. In the current work, all the geometric systems are made of the same solid material. The different choices of materials for pillar and plate can also be studied. By introducing a hollow part in the single pillar or one line of pillars, the properties of bending and compressional resonances may change, and also new resonant mode can appear, such as whispering-gallery mode. Besides, the existing of hollow part can be filled by another solid material or liquid, their resonant properties can be further actively controlled by tuning the filling parameters, such as the kinds of material, the filling hight or even temperature.

Appendix A: Lamb waves in anisotropic plates

Let us consider the propagation of Lamb waves in tetragonal plates[149]. The wave is assumed to be propagating along the *x* axis with wave number *k*, but the wave-vector has also *z* component denoted by *b*. Thus, for a tetragonal material, the equations of motion are

$$\rho\omega^2 u_1 = (c_{11}k^2 + \beta^2 c_{44})u_1 + (c_{13} + c_{44})k\beta u_3 \tag{A1}$$

$$\rho\omega^2 u_2 = (c_{66}k^2 + \beta^2 c_{44})u_2 \tag{A2}$$

$$\rho\omega^2 u_3 = (c_{44}k^2 + \beta^2 c_{33})u_3 + (c_{13} + c_{44})k\beta u_1 \tag{A3}$$

The solutions of the above equations can be divided into the SH mode

$$\hat{u} = \sum_{s=+,-} u_2^s e^{ikx} e^{si\beta z}\hat{x}_2 \tag{A4}$$

where

$$\rho\omega^2 = c_{66}k^2 + c_{44}\beta^2 \tag{A5}$$

And

the mixed modes

$$\hat{u} = \sum_{a=1,2}\sum_{s=+,-} u_1^{as} e^{ikx} e^{si\beta_a z}\hat{x}_1 + \sum_{a=1,2}\sum_{s=+,-} sY_a u_1^{as} e^{ikx} e^{si\beta_a z}\hat{x}_3 \tag{A6}$$

Where the two values β_a with *a*=1, 2 are the positive solutions of the secular equation

$$(\rho\omega^2 - c_{11}k^2 - \beta_a^2 c_{44})(\rho\omega^2 - c_{44}k^2 - \beta_a^2 c_{33}) - (c_{13} + c_{44})^2 k^2 \beta_a^2 = 0 \tag{A7}$$

and

$$Y_a = u_3^a \Big/ u_1^a = \frac{\rho\omega^2 - c_{11}k^2 - \beta_a^2 c_{44}}{(c_{13} + c_{44})k\beta_a} \tag{A8}$$

From the mixed modes Equation (A6), we can use Euler equation and expend the equation

$$e^{i\beta_a z} = \cos(\beta_a z) + i\sin(\beta_a z) \tag{A9}$$

then the displacement can be separate into two uncoupled symmetry and anti-symmetry modes,

$$\begin{aligned}\hat{u}_S = &\left[\left(u_1^1 + u_1^{1-}\right)e^{ikx}\cos\left(\beta_1 z\right) + \left(u_1^2 + u_1^{2-}\right)e^{ikx}\cos\left(\beta_2 z\right)\right]\hat{x}_1 \\ &+\left[i\left(u_1^1 + u_1^{1-}\right)e^{ikx}Y_1\sin\left(\beta_1 z\right) + i\left(u_1^2 + u_1^{2-}\right)e^{ikx}Y_2\sin\left(\beta_2 z\right)\right]\hat{x}_3\end{aligned} \tag{A10}$$

$$\begin{aligned}\hat{u}_A = &\left[i\left(u_1^1 - u_1^{1-}\right)e^{ikx}\sin\left(\beta_1 z\right) + i\left(u_1^2 - u_1^{2-}\right)e^{ikx}\sin\left(\beta_2 z\right)\right]\hat{x}_1 \\ &+\left[\left(u_1^1 - u_1^{1-}\right)e^{ikx}Y_1\cos\left(\beta_1 z\right) + \left(u_1^2 - u_1^{2-}\right)e^{ikx}Y_2\cos\left(\beta_2 z\right)\right]\hat{x}_3\end{aligned} \tag{A11}$$

For the symmetry mode, boundary conditions are

$$\begin{aligned}\sigma_{33}\big|_{z=h/2} &= c_{33}\partial_3 u_3 + c_{13}\partial_1 u_1 = 0 \\ \sigma_{13}\big|_{z=h/2} &= c_{44}\left(\partial_3 u_1 + \partial_1 u_3\right) = 0\end{aligned} \tag{A12}$$

which in matrix form is

$$\begin{pmatrix} i\cos(\beta_1\frac{h}{2})\left(c_{33}Y_1\beta_1 + c_{13}k\right) & i\cos(\beta_2\frac{h}{2})\left(c_{33}Y_2\beta_2 + c_{13}k\right) \\ c_{44}\sin(\beta_1\frac{h}{2})\left(-\beta_1 - kY_1\right) & c_{44}\sin(\beta_2\frac{h}{2})\left(-\beta_2 - kY_2\right) \end{pmatrix}\begin{pmatrix}\left(u_1^1 + u_1^{1-}\right)e^{ikx} \\ \left(u_1^2 + u_1^{2-}\right)e^{ikx}\end{pmatrix} = 0 \tag{A13}$$

if the determinate of the left part matrix be zero, then we get the dispersion relation equation

$$\frac{c_{33}Y_1\beta_1 + c_{13}k}{\beta_1 + kY_1}\frac{\cos\left(\beta_1 h/2\right)}{\sin\left(\beta_1 h/2\right)} - \frac{c_{33}Y_1\beta_1 + c_{13}k}{\beta_1 + kY_1}\frac{\cos\left(\beta_2 h/2\right)}{\sin\left(\beta_2 h/2\right)} = 0 \tag{A14}$$

in the limit of low $\beta h, \cos\left(\beta_1 h/2\right) = 1, \sin\left(\beta_1 h/2\right) = \beta_1 h/2$, (A14) can be simplified as

$$c_{13}k\left(Y_2\beta_2 - Y_1\beta_1\right) = 0 \tag{A15}$$

Substitute the Y_1 and Y_2

$$\left[c_{13}\left(c_{33}\rho\omega^2 - c_{11}c_{33}k^2 + c_{13}^2k^2 + c_{13}c_{44}k^2\right) - \left(\rho\omega^2 - c_{11}k^2\right)c_{33}c_{44}\right]\left(\beta_2^2 - \beta_1^2\right) = 0 \tag{A16}$$

As $\beta_2^2 - \beta_1^2$ cannot be 0, its left part is 0

$$\left(c_{13} - c_{44}\right)\left(c_{33}\rho\omega^2 - \left(c_{13}^2 - c_{11}c_{33}\right)k^2\right) = 0 \tag{A17}$$

finally obtain the linear dispersion relation for symmetry mode

$$\rho\omega^2 = c_{11}\left(1 - \frac{c_{13}^2}{c_{11}c_{33}}\right)k^2 \tag{A18}$$

Or

$$\omega^2 = v_p^2 k^2 \tag{A19}$$

With

$$v_p^2 = \frac{c_{11}}{\rho}(1 - \frac{c_{13}^2}{c_{11}c_{33}}) \tag{A20}$$

which for an isotropic material recovers the well known plate velocity for the symmetric Lamb mode.

For the anti-symmetry mode, imposing the same boundary conditions, we have

$$\begin{pmatrix} \sin(\beta_1 \frac{h}{2})(-c_{33}Y_1\beta_1 - c_{13}k) & \sin(\beta_2 \frac{h}{2})(-c_{33}Y_2\beta_2 - c_{13}k) \\ ic_{44}\cos(\beta_1 \frac{h}{2})(\beta_1 + kY_1) & ic_{44}\cos(\beta_2 \frac{h}{2})(\beta_2 + kY_2) \end{pmatrix} \begin{pmatrix} (u_1^1 - u_1^{1-})e^{ikx} \\ (u_1^2 - u_1^{2-})e^{ikx} \end{pmatrix} = 0 \tag{A21}$$

if the determinate of the left part matrix be zero, then we get the dispersion relation equation

$$\frac{c_{33}Y_1\beta_1 + c_{13}k}{\beta_1 + kY_1}\frac{\sin(\beta_1 h/2)}{\cos(\beta_1 h/2)} - \frac{c_{33}Y_1\beta_1 + c_{13}k}{\beta_1 + kY_1}\frac{\sin(\beta_2 h/2)}{\cos(\beta_2 h/2)} = 0 \tag{A22}$$

Substitute Y_1 and Y_2, it can be arranged as

$$\sum_a (-1)^a \left[\frac{(c_{13}^2 + c_{44}c_{13} - c_{33}c_{11})k^2 - c_{33}c_{44}\beta_a^2 + c_{33}\rho\omega^2}{c_{13}\beta_a^2 - c_{11}k^2 + \rho\omega^2} \right] \beta_a \tan(\beta_a h/2) = 0 \tag{A23}$$

Multiplying the above equation by

$$(c_{13}\beta_a^2 - c_{11}k^2 + \rho\omega^2)(c_{13}\beta_b^2 - c_{11}k^2 + \rho\omega^2) \tag{A24}$$

and defining the functions

$$P_1(\omega, k) = c_{33}\rho\omega^2 + (c_{13}^2 + c_{44}c_{13} - c_{33}c_{11})k^2 \tag{A25}$$

$$P_2(\omega, k) = \rho\omega^2 - c_{11}k^2 \tag{A26}$$

The dispersion relation becomes

$$\sum_a (-1)^a \left[P_1P_2 + P_1c_{13}\beta_b^2 - P_2c_{33}c_{44}\beta_a^2 - c_{13}c_{33}c_{44}\beta_a^2\beta_b^2 \right] \beta_a \tan(\beta_a h/2) = 0 \tag{A27}$$

Given that β_a and β_b are the solutions of the secular equation (A7), they satisfy

$$\beta_a^2\beta_b^2 = \frac{P_2\left(\rho\omega^2 - c_{44}k^2\right)}{c_{33}c_{44}} \tag{A28}$$

$$\beta_a^2 + \beta_b^2 = \frac{c_{44}\left(\rho\omega^2 - c_{44}k^2\right) + c_{33}P_2 + \left(c_{13}+c_{44}\right)^2 k^2}{c_{33}c_{44}} \tag{A29}$$

Then the dispersion relation can be cast as

$$\sum_a (-1)^a \left[\left(\left(c_{13}^2 - c_{33}c_{11}\right)k^2 + c_{33}\rho\omega^2\right)\beta_b^2 - \rho\omega^2\left(\rho\omega^2 - c_{11}k^2\right)\right]\beta_a \tan\left(\beta_a h/2\right) = 0 \tag{A30}$$

In the low limit of ω and k, the dispersion relation $\omega - k$ is not linear. ω approaches to 0 faster than k. Expanding the tangent function, we have

$$\frac{h^2}{12}\left(c_{13}^2 - c_{33}c_{11}\right)\beta_b^2\beta_a^2\left(\beta_a^2 - \beta_b^2\right) + \rho\omega^2 c_{11}\left(\beta_a^2 - \beta_b^2\right)\left(1 + \frac{h^2}{12}\left(\beta_a^2 + \beta_b^2\right)\right) = 0 \tag{A31}$$

Neglecting the $\beta_a^2 + \beta_b^2$ in the second term, it is simplified as

$$\frac{h^2}{12}\left(c_{13}^2 - c_{33}c_{11}\right)\beta_a^2\beta_b^2 + \rho\omega^2 c_{11} = 0 \tag{A32}$$

If we approximate

$$\beta_a^2\beta_b^2 \approx \frac{c_{11}}{c_{33}}k^4 \tag{A33}$$

The final dispersion relation is

$$\rho\omega^2 = c_{11}\left(1 - \frac{c_{13}^2}{c_{11}c_{33}}\right)\frac{h^2}{12}k^4 \tag{A34}$$

Or

$$\omega^2 = \frac{v_p^2 h^2}{12}k^4 \tag{A35}$$

which for an isotropic plate is the well known dispersion relation for anti-symmetric or flexural waves.

Appendix B: Properties of the Eigenvectors of *M*

The matrix *M* is a Hermitian matrix, therefore its eigenvalues are real. Also, it is known that the Fourier components satisfy $F_{-G} = F_G^*$, means that

$$M_{-G-G'} = M_{GG'}^* \tag{B1}$$

$$M_{-GG'} = M_{G-G'}^* \tag{B2}$$

We can now express the eigenvalue equation for *M* as

$$\begin{pmatrix} M_{GG'} & M_{G-G'} \\ M_{G-G'}^* & M_{GG'}^* \end{pmatrix} \begin{pmatrix} u_{G'} \\ u_{-G'} \end{pmatrix} = \lambda \begin{pmatrix} u_{G'} \\ u_{-G'} \end{pmatrix} \tag{B3}$$

or to simplify the notation

$$\begin{pmatrix} M_{aa} & M_{ab} \\ M_{ab}^* & M_{aa}^* \end{pmatrix} \begin{pmatrix} u \\ v \end{pmatrix} = \lambda \begin{pmatrix} u \\ v \end{pmatrix} \tag{B4}$$

The above eigenvalue equation can be expressed as

$$M_{aa}u + M_{ab}v = \lambda u \tag{B5}$$

$$M_{ab}^*u + M_{aa}^*v = \lambda v \tag{B6}$$

taking the complex conjugate of the above and exchanging the order of the equations, we get

$$M_{aa}v^* + M_{ab}u^* = \lambda v^* \tag{B7}$$

$$M_{ab}^*v^* + M_{aa}^*u^* = \lambda u^* \tag{B8}$$

which shows that the eigenvector (v^*, u^*) has the same eigenvalue as the eigenvector (u, v), so that they differ only in a phase factor $e^{i\phi}$, then we have

$$v = e^{i\phi}u^* \tag{B9}$$

or

$$u_{-G} = e^{i\phi}u_G^* \tag{B10}$$

For the specific case of a symmetric lattice, that is, if we can find a unit cell such that $F_{-G} = F_G$, we have that the matrix M becomes real symmetric, so that it is possible to find always real eigenvectors, so that the phase factor should be π or 0, in other words, in this case we have that

$$u_{-G} = \pm u_G \tag{B11}$$

Appendix C: Equation of motions of bulk Willis medium

Re-call the constitutive equation and the equation of motion in Eq. (3.76) and (3.77),

$$\boldsymbol{\sigma} = C\boldsymbol{\varepsilon} + i\omega S\boldsymbol{u} \tag{3.76}$$

$$\mathrm{div}\boldsymbol{\sigma} + \rho\omega^2\boldsymbol{u} + i\omega S^{\dagger}\boldsymbol{\varepsilon} = 0 \tag{3.77}$$

substitute Eq. (3.76) into Eq. (3.77), the first equation component is

$$\begin{aligned}&\frac{\partial\sigma_{11}}{\partial x_1}+\frac{\partial\sigma_{12}}{\partial x_2}+\frac{\partial\sigma_{13}}{\partial x_3}+\rho\omega^2u_1\\&+i\omega[s_{11}^{\dagger}\frac{\partial u_1}{\partial x_1}s_{12}^{\dagger}\frac{\partial u_2}{\partial x_2}+s_{13}^{\dagger}\frac{\partial u_3}{\partial x_3}+s_{14}^{\dagger}(\frac{\partial u_3}{\partial x_2}+\frac{\partial u_2}{\partial x_3})+s_5^{\dagger}(\frac{\partial u_3}{\partial x_1}+\frac{\partial u_1}{\partial x_3})+s_{16}^{\dagger}(\frac{\partial u_2}{\partial x_1}+\frac{\partial u_1}{\partial x_2})]=0\end{aligned} \tag{C1}$$

Expand the stress, we have

$$\begin{aligned}&c_{11}\frac{\partial^2u_1}{\partial x_1^2}+c_{12}\frac{\partial^2u_2}{\partial x_1\partial x_2}+c_{13}\frac{\partial^2u_3}{\partial x_1\partial x_3}+i\omega(s_{11}\frac{\partial u_1}{\partial x_1}+s_{12}\frac{\partial u_2}{\partial x_1}+s_{13}\frac{\partial u_3}{\partial x_1})+i\omega(s_{11}^{\dagger}\frac{\partial u_1}{\partial x_1}+s_{16}^{\dagger}\frac{\partial u_2}{\partial x_1}+s_{15}^{\dagger}\frac{\partial u_3}{\partial x_1})\\&+c_{66}(\frac{\partial^2u_2}{\partial x_1\partial x_2}+\frac{\partial^2u_1}{\partial x_2^2})+i\omega(s_{61}\frac{\partial u_1}{\partial x_2}+s_{62}\frac{\partial u_2}{\partial x_2}+s_{63}\frac{\partial u_3}{\partial x_2})+i\omega(s_{16}^{\dagger}\frac{\partial u_1}{\partial x_2}+s_{12}^{\dagger}\frac{\partial u_2}{\partial x_2}+s_{14}^{\dagger}\frac{\partial u_3}{\partial x_2})\\&+c_{44}(\frac{\partial^2u_3}{\partial x_1\partial x_3}+\frac{\partial^2u_1}{\partial x_3^2})+i\omega(s_{51}\frac{\partial u_1}{\partial x_3}+s_{52}\frac{\partial u_2}{\partial x_3}+s_{53}\frac{\partial u_3}{\partial x_3})+i\omega(s_{15}^{\dagger}\frac{\partial u_1}{\partial x_3}+s_{14}^{\dagger}\frac{\partial u_2}{\partial x_3}+s_{13}^{\dagger}\frac{\partial u_3}{\partial x_3})\\&+\rho\omega^2u_1=0\end{aligned} \tag{C2}$$

Arrange the above equation as

$$\begin{aligned}&c_{11}\frac{\partial^2u_1}{\partial x_1^2}+c_{12}\frac{\partial^2u_2}{\partial x_1\partial x_2}+c_{13}\frac{\partial^2u_3}{\partial x_1\partial x_3}+i\omega[(s_{11}+s_{11}^{\dagger})\frac{\partial u_1}{\partial x_1}+(s_{12}+s_{16}^{\dagger})\frac{\partial u_2}{\partial x_1}+(s_{13}+s_{15}^{\dagger})\frac{\partial u_3}{\partial x_1}]\\&+c_{66}(\frac{\partial^2u_2}{\partial x_1\partial x_2}+\frac{\partial^2u_1}{\partial x_2^2})+i\omega[(s_{61}+s_{16}^{\dagger})\frac{\partial u_1}{\partial x_2}+(s_{62}+s_{12}^{\dagger})\frac{\partial u_2}{\partial x_2}+(s_{63}+s_{14}^{\dagger})\frac{\partial u_3}{\partial x_2}]\\&+c_{44}(\frac{\partial^2u_3}{\partial x_1\partial x_3}+\frac{\partial^2u_1}{\partial x_3^2})+i\omega[(s_{51}+s_{15}^{\dagger})\frac{\partial u_1}{\partial x_3}+(s_{52}+s_{14}^{\dagger})\frac{\partial u_2}{\partial x_3}+(s_{53}+s_{13}^{\dagger})\frac{\partial u_3}{\partial x_3}]\\&+\rho\omega^2u_1=0\end{aligned} \tag{C3}$$

For each group of Willis terms in the above equation, we have

$$s_{11}^{\dagger}=s_{111}^{\dagger}, s_{11}=s_{111}$$

$$s_{16}^{\dagger}=s_{112}^{\dagger}, s_{12}=s_{112}$$

$$s_{15}^{\dagger}=s_{113}^{\dagger}, s_{13}=s_{113}$$

$$s_{16}^{\dagger} = s_{121}^{\dagger}, s_{61} = s_{121}$$

$$s_{12}^{\dagger} = s_{122}^{\dagger}, s_{62} = s_{122}$$

$$s_{14}^{\dagger} = s_{123}^{\dagger}, s_{63} = s_{123}$$

$$s_{15}^{\dagger} = s_{131}^{\dagger}, s_{51} = s_{131}$$

$$s_{14}^{\dagger} = s_{132}^{\dagger}, s_{52} = s_{132}$$

$$s_{13}^{\dagger} = s_{133}^{\dagger}, s_{53} = s_{133}$$

For each pair of the above group,

$$s_{ijk}^{\dagger} + s_{ijk} = 0 \tag{C4}$$

The above expression means that although the Willis terms appear in the equation of motion for bulk Willis medium, it always exist with its conjugated term and the summation of them is zero.

Thus, the equation of motion becomes

$$c_{11}\frac{\partial^2 u_1}{\partial x_1^2} + c_{12}\frac{\partial^2 u_2}{\partial x_1 \partial x_2} + c_{13}\frac{\partial^2 u_3}{\partial x_1 \partial x_3} + c_{66}\left(\frac{\partial^2 u_2}{\partial x_1 \partial x_2} + \frac{\partial^2 u_1}{\partial x_2^2}\right) + c_{44}\left(\frac{\partial^2 u_3}{\partial x_1 \partial x_3} + \frac{\partial^2 u_1}{\partial x_3^2}\right) + \rho\omega^2 u_1 = 0 \tag{C5}$$

As one can see, the equation of motion finally is independent of Willis terms.

The second equation component of the results of substituting Eq. (3.76) into Eq. (3.77) is

$$\begin{aligned}
&c_{66}\left(\frac{\partial^2 u_2}{\partial x_1^2} + \frac{\partial^2 u_1}{\partial x_1 \partial x_2}\right) + i\omega\left[\left(s_{61} + s_{21}^{\dagger}\right)\frac{\partial u_1}{\partial x_1} + \left(s_{62} + s_{26}^{\dagger}\right)\frac{\partial u_2}{\partial x_1} + \left(s_{63} + s_{25}^{\dagger}\right)\frac{\partial u_3}{\partial x_1}\right] \\
&+ c_{12}\frac{\partial^2 u_1}{\partial x_1 \partial x_2} + c_{11}\frac{\partial^2 u_2}{\partial x_2^2} + c_{13}\frac{\partial^2 u_3}{\partial x_2 \partial x_3} + i\omega\left[\left(s_{21} + s_{26}^{\dagger}\right)\frac{\partial u_1}{\partial x_2} + \left(s_{22} + s_{22}^{\dagger}\right)\frac{\partial u_2}{\partial x_2} + \left(s_{23} + s_{24}^{\dagger}\right)\frac{\partial u_3}{\partial x_2}\right] \\
&+ c_{44}\left(\frac{\partial^2 u_3}{\partial x_2 \partial x_3} + \frac{\partial^2 u_2}{\partial x_3^2}\right) + i\omega\left[\left(s_{41} + s_{25}^{\dagger}\right)\frac{\partial u_1}{\partial x_3} + \left(s_{42} + s_{24}^{\dagger}\right)\frac{\partial u_2}{\partial x_3} + \left(s_{43} + s_{23}^{\dagger}\right)\frac{\partial u_3}{\partial x_3}\right] \\
&+ \rho\omega^2 u_2 = 0
\end{aligned} \tag{C6}$$

For each group of Willis terms in the above equation, we have

$$s_{21}^{\dagger} = s_{211}^{\dagger}, s_{61} = s_{211}$$

$$s_{26}^{\dagger} = s_{212}^{\dagger}, s_{62} = s_{212}$$

$$s_{25}^{\dagger} = s_{213}^{\dagger}, s_{63} = s_{213}$$

$$s_{26}^{\dagger} = s_{221}^{\dagger}, s_{21} = s_{221}$$

$$s_{22}^{\dagger} = s_{222}^{\dagger}, s_{22} = s_{222}$$

$$s_{24}^{\dagger} = s_{223}^{\dagger}, s_{23} = s_{223}$$

$$s_{25}^{\dagger} = s_{231}^{\dagger}, s_{41} = s_{231}$$

$$s_{24}^{\dagger} = s_{232}^{\dagger}, s_{42} = s_{232}$$

$$s_{23}^{\dagger} = s_{233}^{\dagger}, s_{43} = s_{233}$$

Similarly, the equation of motion finally becomes

$$c_{66}\left(\frac{\partial^2 u_2}{\partial x_1^2} + \frac{\partial^2 u_1}{\partial x_1 \partial x_2}\right) + c_{12}\frac{\partial^2 u_1}{\partial x_1 \partial x_2} + c_{11}\frac{\partial^2 u_2}{\partial x_2^2} + c_{13}\frac{\partial^2 u_3}{\partial x_2 \partial x_3} + c_{44}\left(\frac{\partial^2 u_3}{\partial x_2 \partial x_3} + \frac{\partial^2 u_2}{\partial x_3^2}\right) + \rho\omega^2 u_2 = 0 \quad \text{(C7)}$$

The third equation component of the results of substituting Eq. (3.76) into Eq. (3.77) is

$$\begin{aligned}
&c_{44}\left(\frac{\partial^2 u_3}{\partial x_1^2} + \frac{\partial^2 u_1}{\partial x_1 \partial x_3}\right) + i\omega\left[(s_{51} + s_{31}^{\dagger})\frac{\partial u_1}{\partial x_1} + (s_{52} + s_{36}^{\dagger})\frac{\partial u_2}{\partial x_1} + (s_{53} + s_{35}^{\dagger})\frac{\partial u_3}{\partial x_1}\right] \\
&+c_{44}\left(\frac{\partial^2 u_2}{\partial x_2 \partial x_3} + \frac{\partial^2 u_3}{\partial x_2^2}\right) + i\omega\left[(s_{41} + s_{36}^{\dagger})\frac{\partial u_1}{\partial x_2} + (s_{42} + s_{32}^{\dagger})\frac{\partial u_2}{\partial x_2} + (s_{43} + s_{34}^{\dagger})\frac{\partial u_3}{\partial x_2}\right] \\
&+c_{13}\frac{\partial^2 u_1}{\partial x_1 \partial x_3} + c_{13}\frac{\partial^2 u_2}{\partial x_2 \partial x_3} + c_{33}\frac{\partial^2 u_3}{\partial x_3^2} + i\omega\left[(s_{31} + s_{35}^{\dagger})\frac{\partial u_1}{\partial x_3} + (s_{32} + s_{34}^{\dagger})\frac{\partial u_2}{\partial x_3} + (s_{33} + s_{33}^{\dagger})\frac{\partial u_3}{\partial x_3}\right] \\
&+\rho\omega^2 u_3 = 0
\end{aligned} \quad \text{(C8)}$$

$$s_{31}^{\dagger} = s_{311}^{\dagger}, s_{51} = s_{311}$$

$$s_{36}^{\dagger} = s_{312}^{\dagger}, s_{52} = s_{312}$$

$$s_{35}^{\dagger} = s_{313}^{\dagger}, s_{53} = s_{313}$$

$$s_{36}^{\dagger} = s_{321}^{\dagger}, s_{41} = s_{321}$$

$$s_{32}^{\dagger} = s_{322}^{\dagger}, s_{42} = s_{322}$$

$$s_{34}^{\dagger} = s_{323}^{\dagger}, s_{43} = s_{323}$$

$$s_{35}^{\dagger} = s_{332}^{\dagger}, s_{31} = s_{331}$$

$$s_{34}^{\dagger} = s_{332}^{\dagger}, s_{32} = s_{332}$$

$$s_{33}^{\dagger} = s_{333}^{\dagger}, s_{33} = s_{333}$$

$$c_{44}\left(\frac{\partial^2 u_3}{\partial x_1^2} + \frac{\partial^2 u_1}{\partial x_1 \partial x_3}\right) + c_{44}\left(\frac{\partial^2 u_2}{\partial x_2 \partial x_3} + \frac{\partial^2 u_3}{\partial x_2^2}\right) + c_{13}\frac{\partial^2 u_1}{\partial x_1 \partial x_3} + c_{13}\frac{\partial^2 u_2}{\partial x_2 \partial x_3} + c_{33}\frac{\partial^2 u_3}{\partial x_3^2} + \rho\omega^2 u_3 = 0 \qquad \text{(C9)}$$

As a conclusion, from (C5), (C7) and (C9), the final form of equation of motion for bulk Willis medium is not affected by Willis terms.

Appendix D: Dispersion eigenequations of Willis plate

For the eigen equation of symmetric mode

$$D^s = \begin{vmatrix} Q_1^s & Q_2^s & Q_3^s \\ Q_4^s & Q_5^s & Q_6^s \\ Q_7^s & Q_8^s & Q_9^s \end{vmatrix} = 0 \tag{D1}$$

where

$$Q_1^s = ic_{13}k_1 \cos\beta h + ic_{33}f_\beta \beta \cos\beta h + i\omega s_{31}\cos\beta h - \omega s_{33}f_\beta \sin\beta h$$

$$Q_2^s = i\omega s_{32}\cos\alpha h$$

$$Q_3^s = ic_{13}k_1 \cos\gamma h + ic_{33}f_\gamma \gamma \cos\gamma h + i\omega s_{31}\cos\gamma h - \omega s_{33}f_\gamma \sin\gamma h$$

$$Q_3^s = ic_{13}k_1 \cos\gamma h + ic_{33}f_\gamma \gamma \cos\gamma h + i\omega s_{31}\cos\gamma h - \omega s_{33}f_\gamma \sin\gamma h$$

$$Q_5^s = -c_{44}\alpha \sin\alpha h + i\omega s_{42}\cos\alpha h$$

$$Q_6^s = i\omega s_{41}\cos\gamma h - \omega s_{43}f_\gamma \sin\gamma h$$

$$Q_7^s = -c_{44}k_1 f_\beta \sin\beta h - c_{44}\beta \sin\beta h + i\omega s_{51}\cos\beta h - \omega s_{53}f_\beta \sin\beta h$$

$$Q_8^s = i\omega s_{52}\cos\alpha h$$

$$Q_9^s = -c_{44}k_1 f_\gamma \sin\gamma h - c_{44}\gamma \sin\gamma h + i\omega s_{51}\cos\gamma h - \omega s_{53}f_\gamma \sin\gamma h$$

Assume *s* terms are zero in the expression and consider it as a normal medium.

$$Q_1^s = ic_{13}k_1 \cos\beta h + ic_{33}f_\beta \beta \cos\beta h$$

$$Q_2^s = 0$$

$$Q_3^s = ic_{13}k_1 \cos\gamma h + ic_{33}f_\gamma \gamma \cos\gamma h$$

$$Q_4^s = 0$$

$$Q_5^s = -c_{44}\alpha \sin\alpha h$$

$$Q_6^s = 0$$

$$Q_7^s = -c_{44}k_1 f_\beta \sin\beta h - c_{44}\beta \sin\beta h$$

$$Q_8^s = 0$$

$$Q_9^s = -c_{44}k_1 f_\gamma \sin\gamma h - c_{44}\gamma \sin\gamma h$$

Then

$$D^s = Q_1^s Q_5^s Q_9^s - Q_3^s Q_5^s Q_7^s = Q_5^s (Q_1^s Q_9^s - Q_3^s Q_7^s) = 0 \tag{D2}$$

$$Q_5^s = c_{44}\alpha \sin\alpha h = 0,\ \ \alpha = \frac{n\pi}{h}, n = 0, \pm 1, \pm 2, ... \tag{D3}$$

Eq. (D3) is the dispersion relation for the SH mode.

$$Q_1^s Q_9^s - Q_3^s Q_7^s = 0 \tag{D4}$$

$$(c_{13}k_1 + c_{33}f_\beta\beta)(k_1 f_\gamma + \gamma)\tan\gamma h = (c_{13}k_1 + c_{33}f_\gamma\gamma)(k_1 f_\beta + \beta)\tan\beta h \tag{D5}$$

We have

$$c_{33}f_\gamma\gamma + c_{13}k_1 = \frac{c_{33}\rho\omega^2 - c_{11}c_{33}k_1^2 - c_{33}c_{44}\gamma^2 + (c_{13}^2 + c_{13}c_{44})k_1^2}{(c_{13} + c_{44})k_1}$$

$$c_{33}f_\beta\beta + c_{13}k_1 = \frac{c_{33}\rho\omega^2 - c_{11}c_{33}k_1^2 - c_{33}c_{44}\beta^2 + (c_{13}^2 + c_{13}c_{44})k_1^2}{(c_{13} + c_{44})k_1}$$

$$k_1 f_\gamma + \gamma = \frac{\rho\omega^2 - c_{11}k_1^2 + c_{13}\gamma^2}{(c_{13} + c_{44})\gamma}$$

$$k_1 f_\beta + \beta = \frac{\rho\omega^2 - c_{11}k_1^2 + c_{13}\beta^2}{(c_{13} + c_{44})\beta}$$

So

$$\begin{aligned}&(\rho\omega^2 - c_{11}k_1^2 + c_{13}\gamma^2)[c_{33}\rho\omega^2 - c_{11}c_{33}k_1^2 - c_{33}c_{44}\beta^2 + (c_{13}^2 + c_{13}c_{44})k_1^2]\tan\gamma h - \\ &(\rho\omega^2 - c_{11}k_1^2 + c_{13}\beta^2)[c_{33}\rho\omega^2 - c_{11}c_{33}k_1^2 - c_{33}c_{44}\gamma^2 + (c_{13}^2 + c_{13}c_{44})k_1^2]\tan\beta h = 0\end{aligned} \tag{D6}$$

Eq. (D6) gives the exact dispersion of symmetric Lamb mode.

In the limit of low $\beta h / \gamma h, \omega, k_1$, the expression can be simplified as

$$[c_{33}\rho\omega^2 + (c_{13}^2 - c_{33}c_{11})k_1^2](\gamma^2 - \beta^2) = 0 \tag{D7}$$

A linear dispersion relation is also obtained as

$$\rho\omega^2 = c_{11}(1-\frac{c_{13}^2}{c_{11}c_{33}})k_1^2 \tag{D8}$$

For the eigen equation of anti-symmetric mode

$$D^a = \begin{vmatrix} Q_1^a & Q_2^a & Q_3^a \\ Q_4^a & Q_5^a & Q_6^a \\ Q_7^a & Q_8^a & Q_9^a \end{vmatrix} = 0 \tag{D9}$$

where

$$Q_1^a = -c_{13}k_1 \sin\beta h - c_{33}f_\beta \beta \sin\beta h - \omega s_{31}\sin\beta h + i\omega s_{33}f_\beta \cos\beta h$$

$$Q_2^a = -\omega s_{32}\sin\alpha h$$

$$Q_3^a = -c_{13}k_1 \sin\gamma h - c_{33}f_\gamma \gamma \sin\gamma h - \omega s_{31}\sin\gamma h + i\omega s_{33}f_\gamma \cos\gamma h$$

$$Q_4^a = -\omega s_{41}\sin\beta h + i\omega s_{43}f_\beta \cos\beta h$$

$$Q_5^a = ic_{44}\alpha\cos\alpha h - \omega s_{42}\sin\alpha h$$

$$Q_6^a = -\omega s_{41}\sin\gamma h + i\omega s_{43}f_\gamma \cos\gamma h$$

$$Q_7^a = ic_{44}k_1 f_\beta \cos\beta h + ic_{44}\beta\cos\beta h - \omega s_{51}\sin\beta h + i\omega s_{53}f_\beta \cos\beta h$$

$$Q_8^a = -\omega s_{52}\sin\alpha h$$

$$Q_9^a = ic_{44}k_1 f_\gamma \cos\gamma h + ic_{44}\gamma\cos\gamma h - \omega s_{51}\sin\gamma h + i\omega s_{53}f_\gamma \cos\gamma h$$

Assume *s* terms are zero in the expression and consider it as a normal medium.

$$Q_1^a = -c_{13}k_1 \sin\beta h - c_{33}f_\beta \beta \sin\beta h$$

$$Q_2^a = 0$$

$$Q_3^a = -c_{13}k_1 \sin\gamma h - c_{33}f_\gamma \gamma \sin\gamma h$$

$$Q_4^a = 0$$

$$Q_5^a = ic_{44}\alpha\cos\alpha h$$

$$Q_6^a = 0$$

$$Q_7^a = ic_{44}k_1 f_\beta \cos\beta h + ic_{44}\beta\cos\beta h$$

$$Q_8^a = 0$$

$$Q_9^a = ic_{44}k_1 f_\gamma \cos\gamma h + ic_{44}\gamma\cos\gamma h$$

Then

$$D^a = Q_1^a Q_5^a Q_9^a - Q_3^a Q_5^a Q_7^a = Q_5^a (Q_1^a Q_9^a - Q_3^a Q_7^a) = 0 \tag{D10}$$

$$Q_5^a = ic_{44}\alpha\cos\alpha h = 0,\ \alpha = \frac{(1/2+n)\pi}{h}, n = 0,\pm1,\pm2,... \tag{D11}$$

Eq. (D11) is also the dispersion relation for the SH mode.

$$Q_1^a Q_9^a - Q_3^a Q_7^a = 0 \tag{D12}$$

gives the dispersion for anti-symmetric Lamb mode.

Appendix E Modes Characterization

1. Define two orthogonal states $|\alpha\rangle$ and $|\beta\rangle$ which correspond to a compression and a bending, respectively. Assume that these two states are coupled into two other states:

$$|\psi_1\rangle = \cos\theta|\alpha\rangle + \sin\theta|\beta\rangle \tag{E1}$$

$$|\psi_2\rangle = -\sin\theta|\alpha\rangle + \cos\theta|\beta\rangle \tag{E2}$$

For instance, if $\theta = 0$, we have $|\psi_1\rangle = |\alpha\rangle$ and $|\psi_2\rangle = |\beta\rangle$, indicating that they are separated.

2. Assume that the coupling of these states with an incident field induces at the top of pillar a vibration defined by

$$|\psi\rangle = Ae^{i\psi_1}|\psi_1\rangle + Be^{i\psi_2}|\psi_2\rangle \tag{E3}$$

Which depends on the strength of the coupling and the phase shift.

Substitute Eqs. (E1) and (E2) into Eq. (E3), $|\psi\rangle$ can be written as

$$|\psi\rangle = \left[Ae^{i\psi_1}\cos\theta - Be^{i\psi_2}\sin\theta\right]|\alpha\rangle + \left[Ae^{i\psi_1}\sin\theta + Be^{i\psi_2}\cos\theta\right]|\beta\rangle \tag{E4}$$

3. Since $|\alpha\rangle$ has the same displacement at points “4” and “5”, while $|\beta\rangle$ has the opposite displacement at the points “4” and “5”.

For point “4”, we can write like $|\psi\rangle$ in Eq. (E4).

$$|\psi_{(4)}\rangle = |\psi\rangle \tag{E5}$$

For point “5”, there is

$$|\psi_{(5)}\rangle = \left[Ae^{i\psi_1}\cos\theta - Be^{i\psi_2}\sin\theta\right]|\alpha\rangle - \left[Ae^{i\psi_1}\sin\theta + Be^{i\psi_2}\cos\theta\right]|\beta\rangle \tag{E6}$$

Therefore,

$$\frac{|\psi_{(4)}\rangle + |\psi_{(5)}\rangle}{2} = \left[Ae^{i\psi_1}\cos\theta - Be^{i\psi_2}\sin\theta\right]|\alpha_{(4)}\rangle \tag{E7}$$

$$\frac{\left|\psi_{(4)}\right\rangle-\left|\psi_{(5)}\right\rangle}{2}=\left[Ae^{i\psi_1}\sin\theta+Be^{i\psi_2}\cos\theta\right]\left|\beta_{(4)}\right\rangle \tag{E8}$$

The above two equations mean that with <4+5> and <4-5>, we recover the displacement of the compressional and bending modes at point "4". The only point is that there is a coefficient (complex number) in front of $\left|\alpha_{(4)}\right\rangle$ and $\left|\beta_{(4)}\right\rangle$ that define the strength of the two quantities.

4. For simplicity, if we assume that the two modes comressional and bending do not couple to each other and behave as independent modes, that means $\theta=0$ results in $\left|\psi_1\right\rangle\equiv\left|\alpha\right\rangle$ and $\left|\psi_2\right\rangle\equiv\left|\beta\right\rangle$. Then

$$\frac{\left|\psi_{(4)}\right\rangle+\left|\psi_{(5)}\right\rangle}{2}=Ae^{i\psi_1}\left|\alpha_{(4)}\right\rangle \tag{E9}$$

$$\frac{\left|\psi_{(4)}\right\rangle-\left|\psi_{(5)}\right\rangle}{2}=Be^{i\psi_2}\left|\beta_{(4)}\right\rangle \tag{E10}$$

$\left|A\right|$ and $\left|B\right|$ express the strength of the compressional and bending modes couple with the incident waves. These excitations can have a phase shift between them.

Biography and Publications

I was born on 18 May, 1990 in Taizhou, Zhejiang Province, China. After two and a half years study in Taizhou No.1 Middle School, I was admitted to Tongji University in Department of Mechanics in advance in 2008. From March 2012 to June 2012, I did an internship at the Lab of Applied Mechanics, ENSTA_Bretagne. In 2012, I was admitted to the direct doctoral program in the same department. In 2014, I was successfully enrolled in the Ecole doctorale Sciences Pour l'Ingénieur at Institut d'Electronique, et Microélectronique et de Nanotechnologie, Université de Lille 1, in the framework of double doctoral diplomas agreement of Tongji University and Université de Lille 1. In the same year, I also successfully won a scholarship provided by China Scholar Council, supporting my study in France. Under the direction of Prof Yongdong Pan and Prof Bahram Djafari-Rouhani, I conducted research in phononic crystals and acoustic metamaterials. Until now, I have published several papers and given several conference presentations among which I won the 3rd prize in the "Best Oral Presentation" in Phononics2015.

Referee Serve for Journals: Scientific Reports

Journal Publication:

[1]. **Yabin Jin**, Yan Pennec, Yongdong Pan, Bahram Djafari-Rouhani. *Phononic crystal plate with hollow pillars connected by thin bars.* J. Phys. D: Appl. Phys. 50(3), 035301, 2016;

[2]. **Yabin Jin**, Daniel Torrent, Yan Pennec, Gaëtan Lévêque, Yongdong Pan, Bahram Djafari-Rouhani. *Multimodal and omnidirectional beam splitter for Lamb modes in elastic plates.* AIP Adv. 6(12), 121602, 2016;

[3]. **Yabin Jin**, Yan Pennec, Yongdong Pan, Bahram Djafari-Rouhani. *Phononic crystal plate with hollow pillars actively controlled by fluid filling*. Crystals. 6(6), 64, 2016;

[4]. **Yabin Jin**, Daniel Torrent, Yan Pennec, Yongdong Pan, Bahram Djafari-Rouhani. *Gradient index devices for the full control of elastic waves in plates.* Sci. Rep, 6, 24437, 2016;

[5]. **Yabin Jin**, Nicolas Fernez, Yan Pennec, Bernard Bonello, Rayisa. P. Moiseyenko, Stephane Hemon, Yongdong Pan, Bahram Djafari-Rouhani. *Tunable waveguide and cavity in*

a phononic crystal plate by controlling whispersing-gallery modes in hollow pillars, Phys. Rev. B. 93(5), 054109, 2016;

[6]. **Yabin Jin**, Daniel Torrent, Yan Pennec, Yongdong Pan, Bahram Djafari-Rouhani. *Simultaneous control of the S0 and A0 Lamb modes by graded phononic crystal plates*. J. Appl. Phys. 117(24), 244904, 2015;

[7]. **Yabin Jin**, Bernard Bonello, Yongdong Pan, *Acoustic metamaterials with piezoelectric resonant structures*. J. Phys. D: Appl. Phys. 47(24), 245301, 2014;

French Conference or Seminar

[1].Yabin Jin. Université de Bordeaux seminar on metamaterials and metasurface, Oct. 26 2016, Bordeaux, France (oral)

[2].Yabin Jin, et al. GDR's workshop on Thermal Nanosciences and Nanoengineering, Nov. 12-13, 2015, Paris, France (oral)

[3].Yabin Jin, et al. GDR Ondes Assemblée Générale, Oct. 19-21, 2015, Lyon, France (poster)

[4].Yabin Jin, et al. Workshop of the IEMN department 'Materials and Nanostructures', Apr. 23-24, 2015, Hardelot, France (poster)

International Conference:

[1]. Yabin Jin, et al. Metamaterials' 2016, Sept. 19-22, Crete, Greece. (oral)

[2]. Yabin Jin, et al. META'16, Jul. 25-28, Malaga, Spain. (oral)

[3]. Yabin Jin, et al. ASME 2015 International Mechanical Engineering Congress & Exposition, Nov. 13-19, 2015, Houston, US

[4]. Yabin Jin, et al. Metamaterials'2015 The 9th International Congress on Advanced Electromagnetic Materials in Microwaves and Optics, Sep. 7-12, 2015, Oxford, UK

[5]. Yabin Jin, et al. Phononics 2015 3rd International Conference on Phononic Crystals/Metamaterials, Phonon Transport and Phonon Coupling, May 31-Jun 5, 2015, Paris, France (oral)

[6]. Yabin Jin, et al. 17th International Conference on Photoacoustic and Photothermal Phenomena, Oct. 20-24, 2013, Suzhou, China. (poster)

[7]. Yabin Jin, et al. International Symposium on the Theory and Application of Artificial Periodic Structures, Oct 18-20, 2013, Changsha, China. (oral)

Reference

[1]Sánchez-Dehesa, J. & Krokhin, A. 2016. Introduction to Acoustics of Phononic Crystals. Homogenization at Low Frequencies. *In:* KHELIF, A. & ADIBI, A. (eds.) *Phononic Crystals: Fundamentals and Applications.* New York, NY: Springer New York.

[2]Ma, G. & Sheng, P. Acoustic metamaterials: From local resonances to broad horizons. Science Advances,2016, 2 (2):

[3]Yablonovitch, E. Inhibited spontaneous emission in solid-state physics and electronics. Physical Review Letters,1987, 58 (20): 2059

[4]Sajeev, J. Strong localization of photons in certain disordered dielectric superlattices. Physical Review Letters,1987, 58 (23): 2486

[5]Sigalas, M. M. & Economou, E. N. Elastic and acoustic wave band structure. Journal of Sound and Vibration,1992, 158 (2): 377-382

[6]Sigalas, M. & Economou, E. N. Band structure of elastic waves in two dimensional systems. Solid State Communications,1993, 86 (3): 141-143

[7]Kushwaha, M. S., Halevi, P., Dobrzynski, L. & Djafari-Rouhani, B. Acoustic band structure of periodic elastic composites. Physical Review Letters,1993, 71 (13): 2022-2025

[8]Hussein, M. I., Leamy, M. J. & Ruzzene, M. Dynamics of Phononic Materials and Structures: Historical Origins, Recent Progress, and Future Outlook. Applied Mechanics Reviews,2014, 66 (4): 040802-040802

[9]Taras, G., Martin, M., Chaitanya, U. & Edwin, T. Sound ideas. Physics World,2005, 18 (12): 24

[10]Pennec, Y. & Djafari-Rouhani, B. 2016. Fundamental Properties of Phononic Crystal. *In:* KHELIF, A. & ADIBI, A. (eds.) *Phononic Crystals: Fundamentals and Applications.* New York, NY: Springer New York.

[11]Alonso-Redondo, E., Schmitt, M., Urbach, Z., Hui, C. M., Sainidou, R., Rembert, P., Matyjaszewski, K., Bockstaller, M. R. & Fytas, G. A new class of tunable hypersonic phononic crystals based on polymer-tethered colloids. Nat Commun,2015, 6

[12]Liu, Z., Zhang, X., Mao, Y., Zhu, Y. Y., Yang, Z., Chan, C. T. & Sheng, P. Locally Resonant Sonic Materials. Science,2000, 289 (5485): 1734-1736

[13]Still, T., Cheng, W., Retsch, M., Sainidou, R., Wang, J., Jonas, U., Stefanou, N. & Fytas, G. Simultaneous Occurrence of Structure-Directed and Particle-Resonance-Induced Phononic Gaps in Colloidal Films. Physical Review Letters,2008, 100 (19): 194301

[14]Vasseur, J. O., Djafari-Rouhani, B., Dobrzynski, L. & Deymier, P. A. Acoustic band gaps in fibre composite materials of boron nitride structure. Journal of Physics: Condensed Matter,1997, 9 (35): 7327

[15]Wang, Y.-Z., Li, F.-M., Huang, W.-H. & Wang, Y.-S. Effects of inclusion shapes on the band gaps in two-dimensional piezoelectric phononic crystals. Journal of Physics: Condensed Matter,2007, 19 (49): 496204

[16]Maldovan, M. Sound and heat revolutions in phononics. Nature,2013, 503 (7475): 209-217

[17]Pennec, Y., Vasseur, J. O., Djafari-Rouhani, B., Dobrzyński, L. & Deymier, P. A. Two-dimensional phononic crystals: Examples and applications. Surface Science Reports,2010, 65 (8): 229-291

[18]Khelif, A. & Adibi, A. Phononic Crystals: Fundamentals and Applications. Springer New York, 2015

[19]Laude, V. Phononic Crystals, Artificial Crystals for Sonic, Acoustic, and Elastic Waves. 2015

[20]Colombi, A., Guenneau, S., Roux, P. & Craster, R. V. Transformation seismology: composite soil lenses for steering surface elastic Rayleigh waves. Scientific Reports,2016, 6 25320
[21]Gorishnyy, T., Ullal, C. K., Maldovan, M., Fytas, G. & Thomas, E. L. Hypersonic Phononic Crystals. Physical Review Letters,2005, 94 (11): 115501
[22]Cheng, W., Wang, J., Jonas, U., Fytas, G. & Stefanou, N. Observation and tuning of hypersonic bandgaps in colloidal crystals. Nat Mater,2006, 5 (10): 830-836
[23]Edwin, T. L., Taras, G. & Martin, M. Phononics: Colloidal crystals go hypersonic. Nat Mater,2006, 5 (10): 773-774
[24]Maldovan, M. & Thomas, E. L. Simultaneous complete elastic and electromagnetic band gaps in periodic structures. Applied Physics B,2006, 83 (4): 595-600
[25]Maldovan, M. & Thomas, E. L. Simultaneous localization of photons and phonons in two-dimensional periodic structures. Applied Physics Letters,2006, 88 (25): 251907
[26]Djafari-Rouhani, B., El-Jallal, S. & Pennec, Y. Phoxonic crystals and cavity optomechanics. Comptes Rendus Physique,2016, 17 (5): 555-564
[27]Ma, T.-X., Wang, Y.-S. & Zhang, C. Investigation of dual photonic and phononic bandgaps in two-dimensional phoxonic crystals with veins. Optics Communications,2014, 312 68-72
[28]Ma, T.-X., Wang, Y.-S., Zhang, C. & Su, X.-X. Simultaneous guiding of slow elastic and light waves in three-dimensional topology-type phoxonic crystals with a line defect. Journal of Optics,2014, 16 (8): 085002
[29]Yu, J.-K., Mitrovic, S., Tham, D., Varghese, J. & Heath, J. R. Reduction of thermal conductivity in phononic nanomesh structures. Nat Nano,2010, 5 (10): 718-721
[30]Bolmatov, D., Zhernenkov, M., Zav'yalov, D., Stoupin, S., Cunsolo, A. & Cai, Y. Q. Thermally triggered phononic gaps in liquids at THz scale. Scientific Reports,2016, 6 19469
[31]Yang, S., Page, J. H., Liu, Z., Cowan, M. L., Chan, C. T. & Sheng, P. Focusing of Sound in a 3D Phononic Crystal. Physical Review Letters,2004, 93 (2): 024301
[32]Sukhovich, A., Jing, L. & Page, J. H. Negative refraction and focusing of ultrasound in two-dimensional phononic crystals. Physical Review B,2008, 77 (1): 014301
[33]Bucay, J., Roussel, E., Vasseur, J. O., Deymier, P. A., Hladky-Hennion, A. C., Pennec, Y., Muralidharan, K., Djafari-Rouhani, B. & Dubus, B. Positive, negative, zero refraction, and beam splitting in a solid/air phononic crystal: Theoretical and experimental study. Physical Review B,2009, 79 (21): 214305
[34]Xu, Z., Qian, M.-L., Cheng, Q. & Liu, X.-J. Manipulating Backward Propagation of Acoustic Waves by a Periodical Structure. Chinese Physics Letters,2016, 33 (11): 114302
[35]Liang, B., Yuan, B. & Cheng, J.-C. Acoustic Diode: Rectification of Acoustic Energy Flux in One-Dimensional Systems. Physical Review Letters,2009, 103 (10): 104301
[36]Liang, B., Guo, X. S., Tu, J., Zhang, D. & Cheng, J. C. An acoustic rectifier. Nat Mater,2010, 9 (12): 989-992
[37]Khelif, A., Choujaa, A., Benchabane, S., Djafari-Rouhani, B. & Laude, V. Guiding and bending of acoustic waves in highly confined phononic crystal waveguides. Applied Physics Letters,2004, 84 (22): 4400-4402
[38]Sun, J.-H. & Wu, T.-T. Propagation of acoustic waves in phononic-crystal plates and waveguides using a finite-difference time-domain method. Physical Review B,2007, 76 (10): 104304
[39]Jin, Y., Fernez, N., Pennec, Y., Bonello, B., Moiseyenko, R. P., Hémon, S., Pan, Y. & Djafari-Rouhani, B. Tunable waveguide and cavity in a phononic crystal plate by

controlling whispering-gallery modes in hollow pillars. Physical Review B,2016, 93 (5): 054109
[40]Pennec, Y., Djafari-Rouhani, B., Vasseur, J. O., Khelif, A. & Deymier, P. A. Tunable filtering and demultiplexing in phononic crystals with hollow cylinders. Physical Review E,2004, 69 (4): 046608
[41]Rostami-Dogolsara, B., Moravvej-Farshi, M. K. & Nazari, F. Acoustic add-drop filters based on phononic crystal ring resonators. Physical Review B,2016, 93 (1): 014304
[42]Gomis-Bresco, J., Navarro-Urrios, D., Oudich, M., El-Jallal, S., Griol, A., Puerto, D., Chavez, E., Pennec, Y., Djafari-Rouhani, B., Alzina, F., Martínez, A. & Torres, C. M. S. A one-dimensional optomechanical crystal with a complete phononic band gap. Nat Commun,2014, 5
[43]Fang, K., Matheny, M. H., Luan, X. & Painter, O. Optical transduction and routing of microwave phonons in cavity-optomechanical circuits. Nat Photon,2016, 10 (7): 489-496
[44]Zen, N., Puurtinen, T. A., Isotalo, T. J., Chaudhuri, S. & Maasilta, I. J. Engineering thermal conductance using a two-dimensional phononic crystal. Nat Commun,2014, 5
[45]Davis, B. L. & Hussein, M. I. Nanophononic Metamaterial: Thermal Conductivity Reduction by Local Resonance. Physical Review Letters,2014, 112 (5): 055505
[46]Liu, Z., Chan, C. T. & Sheng, P. Analytic model of phononic crystals with local resonances. Physical Review B,2005, 71 (1): 014103
[47]Fang, N., Xi, D., Xu, J., Ambati, M., Srituravanich, W., Sun, C. & Zhang, X. Ultrasonic metamaterials with negative modulus. Nat Mater,2006, 5 (6): 452-456
[48]Li, J. & Chan, C. T. Double-negative acoustic metamaterial. Physical Review E,2004, 70 (5): 055602
[49]Ding, Y., Liu, Z., Qiu, C. & Shi, J. Metamaterial with Simultaneously Negative Bulk Modulus and Mass Density. Physical Review Letters,2007, 99 (9): 093904
[50]Yang, M., Ma, G., Yang, Z. & Sheng, P. Coupled Membranes with Doubly Negative Mass Density and Bulk Modulus. Physical Review Letters,2013, 110 (13): 134301
[51]Lee, S. H., Park, C. M., Seo, Y. M., Wang, Z. G. & Kim, C. K. Composite Acoustic Medium with Simultaneously Negative Density and Modulus. Physical Review Letters,2010, 104 (5): 054301
[52]Wu, Y., Lai, Y. & Zhang, Z.-Q. Elastic Metamaterials with Simultaneously Negative Effective Shear Modulus and Mass Density. Physical Review Letters,2011, 107 (10): 105506
[53]Shelby, R. A., Smith, D. R. & Schultz, S. Experimental Verification of a Negative Index of Refraction. Science,2001, 292 (5514): 77-79
[54]Shalaev, V. M. Optical negative-index metamaterials. Nat Photon,2007, 1 (1): 41-48
[55]Fang, N., Lee, H., Sun, C. & Zhang, X. Sub-Diffraction-Limited Optical Imaging with a Silver Superlens. Science,2005, 308 (5721): 534-537
[56]Schurig, D., Mock, J. J., Justice, B. J., Cummer, S. A., Pendry, J. B., Starr, A. F. & Smith, D. R. Metamaterial Electromagnetic Cloak at Microwave Frequencies. Science,2006, 314 (5801): 977-980
[57]Cai, W., Chettiar, U. K., Kildishev, A. V. & Shalaev, V. M. Optical cloaking with metamaterials. Nat Photon,2007, 1 (4): 224-227
[58]Brunet, T., Leng, J. & Mondain-Monval, O. Soft Acoustic Metamaterials. Science,2013, 342 (6156): 323
[59]Liang, Z. & Li, J. Extreme Acoustic Metamaterial by Coiling Up Space. Physical Review Letters,2012, 108 (11): 114301

[60]Xie, Y., Popa, B.-I., Zigoneanu, L. & Cummer, S. A. Measurement of a Broadband Negative Index with Space-Coiling Acoustic Metamaterials. Physical Review Letters,2013, 110 (17): 175501
[61]Liu, F., Huang, X. & Chan, C. T. Dirac cones at k→=0 in acoustic crystals and zero refractive index acoustic materials. Applied Physics Letters,2012, 100 (7): 071911
[62]Jing, Y., Xu, J. & Fang, N. X. Numerical study of a near-zero-index acoustic metamaterial. Physics Letters A,2012, 376 (45): 2834-2837
[63]Liang, Z., Feng, T., Lok, S., Liu, F., Ng, K. B., Chan, C. H., Wang, J., Han, S., Lee, S. & Li, J. Space-coiling metamaterials with double negativity and conical dispersion. Scientific Reports,2013, 3 1614
[64]Frenzel, T., David Brehm, J., Bückmann, T., Schittny, R., Kadic, M. & Wegener, M. Three-dimensional labyrinthine acoustic metamaterials. Applied Physics Letters,2013, 103 (6): 061907
[65]Xie, Y., Wang, W., Chen, H., Konneker, A., Popa, B.-I. & Cummer, S. A. Wavefront modulation and subwavelength diffractive acoustics with an acoustic metasurface. Nat Commun,2014, 5
[66]Xie, Y., Konneker, A., Popa, B.-I. & Cummer, S. A. Tapered labyrinthine acoustic metamaterials for broadband impedance matching. Applied Physics Letters,2013, 103 (20): 201906
[67]Wang, W., Xie, Y., Konneker, A., Popa, B.-I. & Cummer, S. A. Design and demonstration of broadband thin planar diffractive acoustic lenses. Applied Physics Letters,2014, 105 (10): 101904
[68]Tang, K., Qiu, C., Ke, M., Lu, J., Ye, Y. & Liu, Z. Anomalous refraction of airborne sound through ultrathin metasurfaces. Scientific Reports,2014, 4 6517
[69]Li, Y., Jiang, X., Liang, B., Cheng, J.-C. & Zhang, L. Metascreen-Based Acoustic Passive Phased Array. Physical Review Applied,2015, 4 (2): 024003
[70]Li, Y., Qi, S. & Assouar, M. B. Theory of metascreen-based acoustic passive phased array. New Journal of Physics,2016, 18 (4): 043024
[71]Li, Y. & Assouar, B. M. Acoustic metasurface-based perfect absorber with deep subwavelength thickness. Applied Physics Letters,2016, 108 (6): 063502
[72]Li, Y. & Assouar, M. B. Three-dimensional collimated self-accelerating beam through acoustic metascreen. Scientific Reports,2015, 5 17612
[73]Zhang, L., Ren, J., Wang, J.-S. & Li, B. Topological Nature of the Phonon Hall Effect. Physical Review Letters,2010, 105 (22): 225901
[74]Wang, P., Lu, L. & Bertoldi, K. Topological Phononic Crystals with One-Way Elastic Edge Waves. Physical Review Letters,2015, 115 (10): 104302
[75]Mousavi, S. H., Khanikaev, A. B. & Wang, Z. Topologically protected elastic waves in phononic metamaterials. Nat Commun,2015, 6
[76]Nash, L. M., Kleckner, D., Read, A., Vitelli, V., Turner, A. M. & Irvine, W. T. M. Topological mechanics of gyroscopic metamaterials. Proceedings of the National Academy of Sciences,2015, 112 (47): 14495-14500
[77]Kane, C. L. & Lubensky, T. C. Topological boundary modes in isostatic lattices. Nat Phys,2014, 10 (1): 39-45
[78]Xiao, M., Ma, G., Yang, Z., Sheng, P., Zhang, Z. Q. & Chan, C. T. Geometric phase and band inversion in periodic acoustic systems. Nat Phys,2015, 11 (3): 240-244
[79]Xiao, M., Chen, W.-J., He, W.-Y. & Chan, C. T. Synthetic gauge flux and Weyl points in acoustic systems. Nat Phys,2015, 11 (11): 920-924
[80]Ding, K., Ma, G., Xiao, M., Zhang, Z. Q. & Chan, C. T. Emergence, Coalescence, and Topological Properties of Multiple Exceptional Points and Their Experimental Realization. Physical Review X,2016, 6 (2): 021007

[81]Pennec, Y., Djafari-Rouhani, B., Larabi, H., Vasseur, J. O. & Hladky-Hennion, A. C. Low-frequency gaps in a phononic crystal constituted of cylindrical dots deposited on a thin homogeneous plate. Physical Review B,2008, 78 (10): 104105
[82]Wu, T.-T., Huang, Z.-G., Tsai, T.-C. & Wu, T.-C. Evidence of complete band gap and resonances in a plate with periodic stubbed surface. Applied Physics Letters,2008, 93 (11): 111902
[83]Wang, Y.-F., Laude, V. & Wang, Y.-S. Coupling of evanescent and propagating guided modes in locally resonant phononic crystals. Journal of Physics D: Applied Physics,2014, 47 (47): 475502
[84]Assouar, B. & Oudich, M. Enlargement of a locally resonant sonic band gap by using double-sides stubbed phononic plates. Applied Physics Letters,2012, 100 (12): 123506
[85]Bilal, O. R. & Hussein, M. I. Trampoline metamaterial: Local resonance enhancement by springboards. Applied Physics Letters,2013, 103 (11): 111901
[86]Assouar, B., Sun, J.-H., Lin, F.-S. & Hsu, J.-C. Hybrid phononic crystal plates for lowering and widening acoustic band gaps. Ultrasonics,2014, 54 (8): 2159-2164
[87]Coffy, E., Lavergne, T., Addouche, M., Euphrasie, S., Vairac, P. & Khelif, A. Ultra-wide acoustic band gaps in pillar-based phononic crystal strips. Journal of Applied Physics,2015, 118 (21): 214902
[88]Shu, F., Liu, Y., Wu, J. & Wu, Y. Band gap in tubular pillar phononic crystal plate. Ultrasonics,2016, 71 172-176
[89]Zhao, J., Bonello, B. & Boyko, O. Focusing of the lowest-order antisymmetric Lamb mode behind a gradient-index acoustic metalens with local resonators. Physical Review B,2016, 93 (17): 174306
[90]Addouche, M., Al-Lethawe, M. A., Choujaa, A. & Khelif, A. Superlensing effect for surface acoustic waves in a pillar-based phononic crystal with negative refractive index. Applied Physics Letters,2014, 105 (2): 023501
[91]Krokhin, A. A., Arriaga, J. & Gumen, L. N. Speed of Sound in Periodic Elastic Composites. Physical Review Letters,2003, 91 (26): 264302
[92]Torrent, D. & Sánchez-Dehesa, J. Acoustic metamaterials for new two-dimensional sonic devices. New Journal of Physics,2007, 9 (9): 323
[93]Huang, H. H., Sun, C. T. & Huang, G. L. On the negative effective mass density in acoustic metamaterials. International Journal of Engineering Science,2009, 47 (4): 610-617
[94]Martin, T. P., Layman, C. N., Moore, K. M. & Orris, G. J. Elastic shells with high-contrast material properties as acoustic metamaterial components. Physical Review B,2012, 85 (16): 161103
[95]Martin, Š. & Tomáš, T. Spherical media and geodesic lenses in geometrical optics. Journal of Optics,2012, 14 (7): 075705
[96]Lin, S.-C. S., Huang, T. J., Sun, J.-H. & Wu, T.-T. Gradient-index phononic crystals. Physical Review B,2009, 79 (9): 094302
[97]Zhao, J., Marchal, R., Bonello, B. & Boyko, O. Efficient focalization of antisymmetric Lamb waves in gradient-index phononic crystal plates. Applied Physics Letters,2012, 101 (26): 261905
[98]Climente, A., Torrent, D. & Sánchez-Dehesa, J. Sound focusing by gradient index sonic lenses. Applied Physics Letters,2010, 97 (10): 104103
[99]Climente, A., Torrent, D. & Sánchez-Dehesa, J. Omnidirectional broadband acoustic absorber based on metamaterials. Applied Physics Letters,2012, 100 (14): 144103
[100]Li, R.-Q., Zhu, X.-F., Liang, B., Li, Y., Zou, X.-Y. & Cheng, J.-C. A broadband acoustic omnidirectional absorber comprising positive-index materials. Applied Physics Letters,2011, 99 (19): 193507

[101]Naify, C. J., Martin, T. P., Layman, C. N., Nicholas, M., Thangawng, A. L., Calvo, D. C. & Orris, G. J. Underwater acoustic omnidirectional absorber. Applied Physics Letters,2014, 104 (7): 073505
[102]Zheng, L.-Y., Wu, Y., Zhang, X.-L., Ni, X., Chen, Z.-G., Lu, M.-H. & Chen, Y.-F. A new type of artificial structure to achieve broadband omnidirectional acoustic absorption. AIP Advances,2013, 3 (10): 102122
[103]Climente, A., Torrent, D. & Sánchez-Dehesa, J. Omnidirectional broadband insulating device for flexural waves in thin plates. Journal of Applied Physics,2013, 114 (21): 214903
[104]Yuan, B., Tian, Y., Cheng, Y. & Liu, X. An acoustic Maxwell's fish-eye lens based on gradient-index metamaterials. Chinese Physics B,2016, 25 (10): 104301
[105]Torrent, D., Pennec, Y. & Djafari-Rouhani, B. Omnidirectional refractive devices for flexural waves based on graded phononic crystals. Journal of Applied Physics,2014, 116 (22): 224902
[106]Nicolaou, Z. G. & Motter, A. E. Mechanical metamaterials with negative compressibility transitions. Nat Mater,2012, 11 (7): 608-613
[107]Cummer, S. & Schurig, D. One path to acoustic cloaking. New Journal of Physics,2007, 9 (3): 45
[108]Cummer, S. A., Popa, B.-I., Schurig, D., Smith, D. R., Pendry, J., Rahm, M. & Starr, A. Scattering Theory Derivation of a 3D Acoustic Cloaking Shell. Physical Review Letters,2008, 100 (2): 024301
[109]Chen, H. & Chan, C. T. Acoustic cloaking and transformation acoustics. Journal of Physics D: Applied Physics,2010, 43 (11): 113001
[110]Zhang, S., Xia, C. & Fang, N. Broadband Acoustic Cloak for Ultrasound Waves. Physical Review Letters,2011, 106 (2): 024301
[111]Popa, B.-I., Zigoneanu, L. & Cummer, S. A. Experimental Acoustic Ground Cloak in Air. Physical Review Letters,2011, 106 (25): 253901
[112]Torrent, D. & Sánchez-Dehesa, J. Acoustic cloaking in two dimensions: a feasible approach. New Journal of Physics,2008, 10 (6): 063015
[113]Yang, Z., Dai, H. M., Chan, N. H., Ma, G. C. & Sheng, P. Acoustic metamaterial panels for sound attenuation in the 50–1000 Hz regime. Applied Physics Letters,2010, 96 (4): 041906
[114]Mei, J., Ma, G., Yang, M., Yang, Z., Wen, W. & Sheng, P. Dark acoustic metamaterials as super absorbers for low-frequency sound. Nat Commun,2012, 3 756
[115]Zhang, Y., Wen, J., Xiao, Y., Wen, X. & Wang, J. Theoretical investigation of the sound attenuation of membrane-type acoustic metamaterials. Physics Letters A,2012, 376 (17): 1489-1494
[116]Zhang, S., Yin, L. & Fang, N. Focusing Ultrasound with an Acoustic Metamaterial Network. Physical Review Letters,2009, 102 (19): 194301
[117]Li, J., Fok, L., Yin, X., Bartal, G. & Zhang, X. Experimental demonstration of an acoustic magnifying hyperlens. Nat Mater,2009, 8 (12): 931-934
[118]Guenneau, S., Movchan, A., Pétursson, G. & Anantha Ramakrishna, S. Acoustic metamaterials for sound focusing and confinement. New Journal of Physics,2007, 9 (11): 399
[119]Ao, X. & Chan, C. T. Far-field image magnification for acoustic waves using anisotropic acoustic metamaterials. Physical Review E,2008, 77 (2): 025601
[120]Bonello, B., Belliard, L., Pierre, J., Vasseur, J. O., Perrin, B. & Boyko, O. Negative refraction of surface acoustic waves in the subgigahertz range. Physical Review B,2010, 82 (10): 104109

[121]Psarobas, I. E., Stefanou, N. & Modinos, A. Scattering of elastic waves by periodic arrays of spherical bodies. Physical Review B,2000, 62 (1): 278-291
[122]Tanaka, Y., Tomoyasu, Y. & Tamura, S.-I. Band structure of acoustic waves in phononic lattices: Two-dimensional composites with large acoustic mismatch. Physical Review B,2000, 62 (11): 7387-7392
[123]Fokin, V., Ambati, M., Sun, C. & Zhang, X. Method for retrieving effective properties of locally resonant acoustic metamaterials. Physical Review B,2007, 76 (14): 144302
[124]Nemat-Nasser, S., Willis, J. R., Srivastava, A. & Amirkhizi, A. V. Homogenization of periodic elastic composites and locally resonant sonic materials. Physical Review B,2011, 83 (10): 104103
[125]Akl, W. & Baz, A. Stability analysis of active acoustic metamaterial with programmable bulk modulus. Smart Materials and Structures,2011, 20 (12): 125010
[126]Akl, W. & Baz, A. Analysis and experimental demonstration of an active acoustic metamaterial cell. Journal of Applied Physics,2012, 111 (4): 044505
[127]Baz, A. The structure of an active acoustic metamaterial with tunable effective density. New Journal of Physics,2009, 11 (12): 123010
[128]Malinovsky, V. S. & Donskoy, D. M. Electro-magnetically controlled acoustic metamaterials with adaptive properties. The Journal of the Acoustical Society of America,2012, 132 (4): 2866-2872
[129]Pope, S. A., Laalej, H. & Daley, S. Performance and stability analysis of active elastic metamaterials with a tunable double negative response. Smart Materials and Structures,2012, 21 (12): 125021
[130]Pope, S. A. Double negative elastic metamaterial design through electrical-mechanical circuit analogies. IEEE Transactions on Ultrasonics, Ferroelectrics, and Frequency Control,2013, 60 (7): 1467-1474
[131]Pope, S. A. & Daley, S. Viscoelastic locally resonant double negative metamaterials with controllable effective density and elasticity. Physics Letters A,2010, 374 (41): 4250-4255
[132]Popa, B.-I., Zigoneanu, L. & Cummer, S. A. Tunable active acoustic metamaterials. Physical Review B,2013, 88 (2): 024303
[133]Yan, X., Zhu, R., Huang, G. & Yuan, F.-G. Focusing guided waves using surface bonded elastic metamaterials. Applied Physics Letters,2013, 103 (12): 121901
[134]Zhao, J., Pan, Y. & Zhong, Z. Theoretical study of shear horizontal wave propagation in periodically layered piezoelectric structure. Journal of Applied Physics,2012, 111 (6): 064906
[135]Rokhlin, S. I. & Wang, L. Stable recursive algorithm for elastic wave propagation in layered anisotropic media: Stiffness matrix method. The Journal of the Acoustical Society of America,2002, 112 (3): 822-834
[136]Every, A. G. & Mccurdy, A. K. Phonon focusing in piezoelectric crystals. Physical Review B,1987, 36 (3): 1432-1447
[137]Zhao, J., Pan, Y. & Zhong, Z. A study of pressure-shear vertical wave propagation in periodically layered fluid and piezoelectric structure. Journal of Applied Physics,2013, 113 (5): 054903
[138]Wang, L. & Rokhlin, S. I. Stable reformulation of transfer matrix method for wave propagation in layered anisotropic media. Ultrasonics,2001, 39 (6): 413-424
[139]Zhu, R., Huang, G. L. & Hu, G. K. Effective Dynamic Properties and Multi-Resonant Design of Acoustic Metamaterials. Journal of Vibration and Acoustics,2012, 134 (3): 031006-031006

[140]Martin, T. P., Nicholas, M., Orris, G. J., Cai, L.-W., Torrent, D. & Sánchez-Dehesa, J. Sonic gradient index lens for aqueous applications. Applied Physics Letters,2010, 97 (11): 113503
[141]Zigoneanu, L., Popa, B.-I. & Cummer, S. A. Design and measurements of a broadband two-dimensional acoustic lens. Physical Review B,2011, 84 (2): 024305
[142]Climente, A., Torrent, D. & Sánchez-Dehesa, J. Gradient index lenses for flexural waves based on thickness variations. Applied Physics Letters,2014, 105 (6): 064101
[143]Umnova, O. & Zajamsek, B. Omnidirectional graded index sound absorber. *In:* Acoustics 2012, 2012 Nantes, France.
[144]Norris, A. N. & Shuvalov, A. L. Elastic cloaking theory. Wave Motion,2011, 48 (6): 525-538
[145]Vasseur, J. O., Deymier, P. A., Chenni, B., Djafari-Rouhani, B., Dobrzynski, L. & Prevost, D. Experimental and Theoretical Evidence for the Existence of Absolute Acoustic Band Gaps in Two-Dimensional Solid Phononic Crystals. Physical Review Letters,2001, 86 (14): 3012-3015
[146]Zhang, X. & Liu, Z. Negative refraction of acoustic waves in two-dimensional phononic crystals. Applied Physics Letters,2004, 85 (2): 341-343
[147]Deymier, P. A. Acoustic Metamaterials and Phononic Crystals. Springer Berlin Heidelberg, 2013
[148]Lin, S.-C. S., Tittmann, B. R. & Huang, T. J. Design of acoustic beam aperture modifier using gradient-index phononic crystals. Journal of Applied Physics,2012, 111 (12): 123510
[149]Royer, D., Morgan, D. P. & Dieulesaint, E. Elastic Waves in Solids I: Free and Guided Propagation. Springer Berlin Heidelberg, 1999
[150]Wu, T.-T., Chen, Y.-T., Sun, J.-H., Lin, S.-C. S. & Huang, T. J. Focusing of the lowest antisymmetric Lamb wave in a gradient-index phononic crystal plate. Applied Physics Letters,2011, 98 (17): 171911
[151]Rupin, M., Lemoult, F., Lerosey, G. & Roux, P. Experimental Demonstration of Ordered and Disordered Multiresonant Metamaterials for Lamb Waves. Physical Review Letters,2014, 112 (23): 234301
[152]Williams, E. G., Roux, P., Rupin, M. & Kuperman, W. A. Theory of multiresonant metamaterials for A0 Lamb waves. Physical Review B,2015, 91 (10): 104307
[153]Torrent, D., Pennec, Y. & Djafari-Rouhani, B. Effective medium theory for elastic metamaterials in thin elastic plates. Physical Review B,2014, 90 (10): 104110
[154]Jin, Y., Torrent, D., Pennec, Y., Pan, Y. & Djafari-Rouhani, B. Simultaneous control of the S0 and A0 Lamb modes by graded phononic crystal plates. Journal of Applied Physics,2015, 117 (24): 244904
[155]Graff, K. F. Wave Motion in Elastic Solids. Dover Publications, 1975
[156]Vemula, C. & Norris, A. N. Flexural wave propagation and scattering on thin plates using Mindlin theory. Wave Motion,1997, 26 (1): 1-12
[157]Zabelin, V., Dunbar, L. A., Le Thomas, N., Houdré, R., Kotlyar, M. V., O'faolain, L. & Krauss, T. F. Self-collimating photonic crystal polarization beam splitter. Optics Letters,2007, 32 (5): 530-532
[158]Ao, X., Liu, L., Wosinski, L. & He, S. Polarization beam splitter based on a two-dimensional photonic crystal of pillar type. Applied Physics Letters,2006, 89 (17): 171115
[159]Bayindir, M., Temelkuran, B. & Ozbay, E. Photonic-crystal-based beam splitters. Applied Physics Letters,2000, 77 (24): 3902-3904
[160]Lawall, J. & Prentiss, M. Demonstration of a novel atomic beam splitter. Physical Review Letters,1994, 72 (7): 993-996

[161]Cassettari, D., Hessmo, B., Folman, R., Maier, T. & Schmiedmayer, J. Beam Splitter for Guided Atoms. Physical Review Letters,2000, 85 (26): 5483-5487
[162]Li, J., Wu, F., Zhong, H., Yao, Y. & Zhang, X. Acoustic beam splitting in two-dimensional phononic crystals using self-collimation effect. Journal of Applied Physics,2015, 118 (14): 144903
[163]Li, B., Guan, J.-J., Deng, K. & Zhao, H. Splitting of self-collimated beams in two-dimensional sonic crystals. Journal of Applied Physics,2012, 112 (12): 124514
[164]Kaya, O. A., Cicek, A., Salman, A. & Ulug, B. Acoustic Mach–Zehnder interferometer utilizing self-collimated beams in a two-dimensional phononic crystal. Sensors and Actuators B: Chemical,2014, 203 197-203
[165]Willis, J. R. Variational principles for dynamic problems for inhomogeneous elastic media. Wave Motion,1981, 3 (1): 1-11
[166]Willis, J. R. The nonlocal influence of density variations in a composite. International Journal of Solids and Structures,1985, 21 (7): 805-817
[167]Milton, G. W., Briane, M. & Willis, J. R. On cloaking for elasticity and physical equations with a transformation invariant form. New Journal of Physics,2006, 8 (10): 248
[168]Milton, G. W. & Willis, J. R. On modifications of Newton's second law and linear continuum elastodynamics. Proceedings of the Royal Society A: Mathematical, Physical and Engineering Science,2007, 463 (2079): 855
[169]Norris, A. N., Shuvalov, A. L. & Kutsenko, A. A. Analytical formulation of three-dimensional dynamic homogenization for periodic elastic systems. Proceedings of the Royal Society A: Mathematical, Physical and Engineering Science,2012,
[170]Willis, J. R. Effective constitutive relations for waves in composites and metamaterials. Proceedings of the Royal Society A: Mathematical, Physical and Engineering Science,2011, 467 (2131): 1865
[171]Srivastava, A. & Nemat-Nasser, S. Overall dynamic properties of three-dimensional periodic elastic composites. Proceedings of the Royal Society A: Mathematical, Physical and Engineering Science,2011, 468 (2137): 269
[172]Nassar, H., He, Q. C. & Auffray, N. Willis elastodynamic homogenization theory revisited for periodic media. Journal of the Mechanics and Physics of Solids,2015, 77 158-178
[173]Xiang, Z. H. & Yao, R. W. Realizing the Willis equations with pre-stresses. Journal of the Mechanics and Physics of Solids,2016, 87 1-6
[174]Willis, J. R. Exact effective relations for dynamics of a laminated body. Mechanics of Materials,2009, 41 (4): 385-393
[175]Nemat-Nasser, S. & Srivastava, A. Overall dynamic constitutive relations of layered elastic composites. Journal of the Mechanics and Physics of Solids,2011, 59 (10): 1953-1965
[176]Shuvalov, A. L., Kutsenko, A. A., Norris, A. N. & Poncelet, O. Effective Willis constitutive equations for periodically stratified anisotropic elastic media. Proceedings of the Royal Society A: Mathematical, Physical and Engineering Science,2011, 467 (2130): 1749
[177]Torrent, D., Pennec, Y. & Djafari-Rouhani, B. Resonant and nonlocal properties of phononic metasolids. Physical Review B,2015, 92 (17): 174110
[178]Hsu, J.-C. & Wu, T.-T. Efficient formulation for band-structure calculations of two-dimensional phononic-crystal plates. Physical Review B,2006, 74 (14): 144303
[179]Born, M., Wolf, E. & Bhatia, A. B. Principles of Optics: Electromagnetic Theory of Propagation, Interference and Diffraction of Light. Cambridge University Press, 1999

[180]Soukoulis, C. M. & Wegener, M. Past achievements and future challenges in the development of three-dimensional photonic metamaterials. Nat Photon,2011, 5 (9): 523-530
[181]Kwon, D.-H., Werner, P. L. & Werner, D. H. Optical planar chiral metamaterial designs for strong circular dichroism and polarization rotation. Optics Express,2008, 16 (16): 11802-11807
[182]Zhao, R., Zhang, L., Zhou, J., Koschny, T. & Soukoulis, C. M. Conjugated gammadion chiral metamaterial with uniaxial optical activity and negative refractive index. Physical Review B,2011, 83 (3): 035105
[183]Kafesaki, M., Sigalas, M. M. & García, N. Frequency Modulation in the Transmittivity of Wave Guides in Elastic-Wave Band-Gap Materials. Physical Review Letters,2000, 85 (19): 4044-4047
[184]Celli, P. & Gonella, S. Manipulating waves with LEGO® bricks: A versatile experimental platform for metamaterial architectures. Applied Physics Letters,2015, 107 (8): 081901
[185]Wu, T.-T., Wu, L.-C. & Huang, Z.-G. Frequency band-gap measurement of two-dimensional air/silicon phononic crystals using layered slanted finger interdigital transducers. Journal of Applied Physics,2005, 97 (9): 094916
[186]Qiu, C., Liu, Z., Mei, J. & Shi, J. Mode-selecting acoustic filter by using resonant tunneling of two-dimensional double phononic crystals. Applied Physics Letters,2005, 87 (10): 104101
[187]Zhao, J., Bonello, B., Marchal, R. & Boyko, O. Beam path and focusing of flexural Lamb waves within phononic crystal-based acoustic lenses. New Journal of Physics,2014, 16 (6): 063031
[188]Amoudache, S., Pennec, Y., Djafari Rouhani, B., Khater, A., Lucklum, R. & Tigrine, R. Simultaneous sensing of light and sound velocities of fluids in a two-dimensional phoXonic crystal with defects. Journal of Applied Physics,2014, 115 (13): 134503
[189]Lucklum, R. & Li, J. Phononic crystals for liquid sensor applications. Measurement Science and Technology,2009, 20 (12): 124014
[190]Wu, T.-T., Huang, Z.-G. & Lin, S. Surface and bulk acoustic waves in two-dimensional phononic crystal consisting of materials with general anisotropy. Physical Review B,2004, 69 (9): 094301
[191]Khelif, A., Achaoui, Y., Benchabane, S., Laude, V. & Aoubiza, B. Locally resonant surface acoustic wave band gaps in a two-dimensional phononic crystal of pillars on a surface. Physical Review B,2010, 81 (21): 214303
[192]Khelif, A., Aoubiza, B., Mohammadi, S., Adibi, A. & Laude, V. Complete band gaps in two-dimensional phononic crystal slabs. Physical Review E,2006, 74 (4): 046610
[193]Vasseur, J. O., Hladky-Hennion, A.-C., Djafari-Rouhani, B., Duval, F., Dubus, B., Pennec, Y. & Deymier, P. A. Waveguiding in two-dimensional piezoelectric phononic crystal plates. Journal of Applied Physics,2007, 101 (11): 114904
[194]Bloch, F. Über die Quantenmechanik der Elektronen in Kristallgittern. Zeitschrift für Physik,1929, 52 (7): 555-600
[195]Pennec, Y., Djafari Rouhani, B., Larabi, H., Akjouj, A., Gillet, J. N., Vasseur, J. O. & Thabet, G. Phonon transport and waveguiding in a phononic crystal made up of cylindrical dots on a thin homogeneous plate. Physical Review B,2009, 80 (14): 144302
[196]Cummer, S. A., Christensen, J. & Alù, A. Controlling sound with acoustic metamaterials. Nature Reviews Materials,2016, 1 16001
[197]Lemoult, F., Fink, M. & Lerosey, G. Acoustic Resonators for Far-Field Control of Sound on a Subwavelength Scale. Physical Review Letters,2011, 107 (6): 064301

[198]Lemoult, F., Kaina, N., Fink, M. & Lerosey, G. Wave propagation control at the deep subwavelength scale in metamaterials. Nat Phys,2013, 9 (1): 55-60
[199]Zhu, J., Christensen, J., Jung, J., Martin-Moreno, L., Yin, X., Fok, L., Zhang, X. & Garcia-Vidal, F. J. A holey-structured metamaterial for acoustic deep-subwavelength imaging. Nat Phys,2011, 7 (1): 52-55
[200]Ma, G., Yang, M., Xiao, S., Yang, Z. & Sheng, P. Acoustic metasurface with hybrid resonances. Nat Mater,2014, 13 (9): 873-878
[201]Chen, H. & Chan, C. T. Acoustic cloaking in three dimensions using acoustic metamaterials. Applied Physics Letters,2007, 91 (18): 183518
[202]Oudich, M., Li, Y., Assouar, B. & Hou, Z. A sonic band gap based on the locally resonant phononic plates with stubs. New Journal of Physics,2010, 12 (8): 083049
[203]Midtvedt, D., Isacsson, A. & Croy, A. Nonlinear phononics using atomically thin membranes. Nat Commun,2014, 5
[204]Hsu, J.-C. Local resonances-induced low-frequency band gaps in two-dimensional phononic crystal slabs with periodic stepped resonators. Journal of Physics D: Applied Physics,2011, 44 (5): 055401
[205]Achaoui, Y., Khelif, A., Benchabane, S., Robert, L. & Laude, V. Experimental observation of locally-resonant and Bragg band gaps for surface guided waves in a phononic crystal of pillars. Physical Review B,2011, 83 (10): 104201
[206]Graczykowski, B., Sledzinska, M., Alzina, F., Gomis-Bresco, J., Reparaz, J. S., Wagner, M. R. & Sotomayor Torres, C. M. Phonon dispersion in hypersonic two-dimensional phononic crystal membranes. Physical Review B,2015, 91 (7): 075414
[207]Vitalyi, E. G. & Oliver, B. W. Double-negative flexural acoustic metamaterial. New Journal of Physics,2014, 16 (12): 123053
[208]Oudich, M., Djafari-Rouhani, B., Pennec, Y., Assouar, M. B. & Bonello, B. Negative effective mass density of acoustic metamaterial plate decorated with low frequency resonant pillars. Journal of Applied Physics,2014, 116 (18): 184504
[209]El Hassouani, Y., Li, C., Pennec, Y., El Boudouti, E. H., Larabi, H., Akjouj, A., Bou Matar, O., Laude, V., Papanikolaou, N., Martinez, A. & Djafari Rouhani, B. Dual phononic and photonic band gaps in a periodic array of pillars deposited on a thin plate. Physical Review B,2010, 82 (15): 155405
[210]Rayleigh, L. CXII. The problem of the whispering gallery. Philosophical Magazine Series 6,1910, 20 (120): 1001-1004
[211]Foreman, M. R., Swaim, J. D. & Vollmer, F. Whispering gallery mode sensors. Advances in Optics and Photonics,2015, 7 (2): 168-240
[212]Grandidier, J., Callahan, D. M., Munday, J. N. & Atwater, H. A. Light Absorption Enhancement in Thin-Film Solar Cells Using Whispering Gallery Modes in Dielectric Nanospheres. Advanced Materials,2011, 23 (10): 1272-1276
[213]Li, F., Xuan, M., Wu, Y. & Bastien, F. Acoustic whispering gallery mode coupling with Lamb waves in liquid. Sensors and Actuators A: Physical,2013, 189 335-338
[214]Kaproulias, S. & Sigalas, M. M. Whispering gallery modes for elastic waves in disk resonators. AIP Advances,2011, 1 (4): 041902
[215]Tomes, M. & Carmon, T. Photonic Micro-Electromechanical Systems Vibrating at X-band (11-GHz) Rates. Physical Review Letters,2009, 102 (11): 113601
[216]Ding, L., Baker, C., Senellart, P., Lemaitre, A., Ducci, S., Leo, G. & Favero, I. High Frequency GaAs Nano-Optomechanical Disk Resonator. Physical Review Letters,2010, 105 (26): 263903
[217]Sturman, B. & Breunig, I. Acoustic whispering gallery modes within the theory of elasticity. Journal of Applied Physics,2015, 118 (1): 013102

[218]Jin, Y., Bonello, B. & Pan, Y. Acoustic metamaterials with piezoelectric resonant structures. Journal of Physics D: Applied Physics,2014, 47 (24): 245301
[219]Popa, B.-I. & Cummer, S. A. Non-reciprocal and highly nonlinear active acoustic metamaterials. Nat Commun,2014, 5
[220]Wang, P., Casadei, F., Shan, S., Weaver, J. C. & Bertoldi, K. Harnessing Buckling to Design Tunable Locally Resonant Acoustic Metamaterials. Physical Review Letters,2014, 113 (1): 014301
[221]Wu, Y., Lai, Y. & Zhang, Z.-Q. Effective medium theory for elastic metamaterials in two dimensions. Physical Review B,2007, 76 (20): 205313
[222]Lai, Y., Wu, Y., Sheng, P. & Zhang, Z.-Q. Hybrid elastic solids. Nat Mater,2011, 10 (8): 620-624
[223]Sánchez-Pérez, J. V., Caballero, D., Mártinez-Sala, R., Rubio, C., Sánchez-Dehesa, J., Meseguer, F., Llinares, J. & Gálvez, F. Sound Attenuation by a Two-Dimensional Array of Rigid Cylinders. Physical Review Letters,1998, 80 (24): 5325-5328
[224]Laude, V., Moiseyenko, R. P., Benchabane, S. & Declercq, N. F. Bloch wave deafness and modal conversion at a phononic crystal boundary. AIP Advances,2011, 1 (4): 041402
[225]Demirci, U. & Montesano, G. Single cell epitaxy by acoustic picolitre droplets. Lab on a Chip,2007, 7 (9): 1139-1145
[226]Sato, A., Pennec, Y., Shingne, N., Thurn-Albrecht, T., Knoll, W., Steinhart, M., Djafari-Rouhani, B. & Fytas, G. Tuning and Switching the Hypersonic Phononic Properties of Elastic Impedance Contrast Nanocomposites. ACS Nano,2010, 4 (6): 3471-3481
[227]Tilli, M., Motooka, T., Airaksinen, V.-M., Franssila, S., Paulasto-Krockel, M. & Lindroos, V. Handbook of silicon based MEMS materials and technologies. William Andrew, 2015
[228]Jin, Y., Pennec, Y., Pan, Y. & Djafari-Rouhani, B. Phononic Crystal Plate with Hollow Pillars Actively Controlled by Fluid Filling. Crystals,2016, 6 (6):
[229]Jang, S. G., Yu, H. K., Choi, D.-G. & Yang, S.-M. Controlled Fabrication of Hollow Metal Pillar Arrays Using Colloidal Masks. Chemistry of Materials,2006, 18 (26): 6103-6105
[230]Li, X., Seo, H.-S., Um, H.-D., Jee, S.-W., Cho, Y. W., Yoo, B. & Lee, J.-H. A periodic array of silicon pillars fabricated by photoelectrochemical etching. Electrochimica Acta,2009, 54 (27): 6978-6982
[231]Zhu, M. W., Li, H. W., Chen, X. L., Tang, Y. F., Lu, M. H. & Chen, Y. F. Silica needle template fabrication of metal hollow microneedle arrays. Journal of Micromechanics and Microengineering,2009, 19 (11): 115010
[232]Marchal, R., Boyko, O., Bonello, B., Zhao, J., Belliard, L., Oudich, M., Pennec, Y. & Djafari-Rouhani, B. Dynamics of confined cavity modes in a phononic crystal slab investigated by in situ time-resolved experiments. Physical Review B,2012, 86 (22): 224302
[233]Yankin, S., Talbi, A., Du, Y., Gerbedoen, J.-C., Preobrazhensky, V., Pernod, P. & Bou Matar, O. Finite element analysis and experimental study of surface acoustic wave propagation through two-dimensional pillar-based surface phononic crystal. Journal of Applied Physics,2014, 115 (24): 244508
[234]Pierre, J., Dollet, B. & Leroy, V. Resonant Acoustic Propagation and Negative Density in Liquid Foams. Physical Review Letters,2014, 112 (14): 148307
[235]Brunet, T., Merlin, A., Mascaro, B., Zimny, K., Leng, J., Poncelet, O., Aristégui, C. & Mondain-Monval, O. Soft 3D acoustic metamaterial with negative index. Nat Mater,2015, 14 (4): 384-388

[236]Still, T., Oudich, M., Auerhammer, G. K., Vlassopoulos, D., Djafari-Rouhani, B., Fytas, G. & Sheng, P. Soft silicone rubber in phononic structures: Correct elastic moduli. Physical Review B,2013, 88 (9): 094102
[237]Laude, V., Robert, L., Daniau, W., Khelif, A. & Ballandras, S. Surface acoustic wave trapping in a periodic array of mechanical resonators. Applied Physics Letters,2006, 89 (8): 083515
[238]Wu, T.-C., Wu, T.-T. & Hsu, J.-C. Waveguiding and frequency selection of Lamb waves in a plate with a periodic stubbed surface. Physical Review B,2009, 79 (10): 104306
[239]Pennec, Y., Beaugeois, M., Djafari-Rouhani, B., Sainidou, R., Akjouj, A., Vasseur, J. O., Dobrzynski, L., El Boudouti, E. H., Vilcot, J. P., Bouazaoui, M. & Vigneron, J. P. Microstubs resonators integrated to bent Y-branch waveguide. Photonics and Nanostructures - Fundamentals and Applications,2008, 6 (1): 26-31
[240]Pourabolghasem, R., Mohammadi, S., Eftekhar, A. A., Khelif, A. & Adibi, A. Experimental evidence of high-frequency complete elastic bandgap in pillar-based phononic slabs. Applied Physics Letters,2014, 105 (23): 231908
[241]Marchal, R. 2014. *Active acoustical metamaterials.* Université Pierre et Marie Curie - Paris VI.